On the Detection of Polycyclic Aromatic Hydrocarbons within Dynamic Surface Features on Mars

Jacqueline D. Campbell

A thesis submitted for the degree of Doctor of Philosophy

Mullard Space Science Laboratory

Department of Space and Climate Physics

University College London

October 2020

I, Jacqueline D. Campbell, confirm that the work presented in this thesis is my own. Where information has been derived from other sources, I confirm that this has been indicated in the thesis.

Abstract

The aim of this thesis is to identify suitable environments for the detection of organic signatures on the Martian surface, to produce diagnostic spectra for organics in various Mars analogues, to establish the detectability limit of those organics using laboratory experiments and then compare laboratory results to measurements from Mars.

The organics searched for in this work are Polycyclic Aromatic Hydrocarbons (PAHs), which are considered to be 'building blocks' for life, and can be a biomarker for extant life; they are abundant on Earth and throughout the universe, but so far are conspicuously absent on Mars, likely due to the high levels of ultra-violet radiation present on the Martian Surface. Therefore, dynamic processes on Mars that uncover previously shielded material on the Martian surface are identified, and various sites examined, to look at their suitability as potential candidates for PAH detection.

The Martian South Polar Residual Cap (SPRC) has been chosen as a primary study site due to the abundance of CO_2 ice sublimation features known as Swiss Cheese Terrain (SCT). These quasi-circular pits exhibit seasonal and long term retreat, exposing dust that had previously been trapped within the ice. The morphology and compositional changes of SCT over time are examined, and laboratory experiments in environmental cells have been carried out to establish base-line spectra for PAHs in SPRC and Mars regolith analogues, as well as the

minimum amount of PAH necessary for detection from orbit by the Compact Reconnaissance Imaging Spectrometer for Mars (CRISM).

In addition, Recurring Slope Lineae (RSL) sites and analogues have been examined to provide baseline spectra and detectability limits for PAHs in non-polar dynamic features.

This work intends to shed light on the question of these 'missing' organic molecules on Mars, and assist in the search for life on the Red Planet.

Impact Statement

The novel research in this thesis contributes to the field of astrobiology and Mars geoscience in several different ways. Several publications (Appendix D) have arisen from this research and are either published, under review or in preparation. This section outlines the impact of this work both inside and outside of academia.

Firstly, it establishes new, freely and publicly available short-wave infrared spectral data for Mars. Analysis of Earth observation spectral reflectance data relies heavily on ground truthing for calibration and validation. Given the paucity of data we have for the Martian surface in general, and in particular regions that rovers and landers have never been to, such as the polar caps and steep canyons, laboratory experiments are crucial. A set of new reflectance spectra for a mix of PAHs pertinent to Mars, recorded using instrument parameters comparable to the Compact Reconnaissance Imaging Spectrometer for Mars (CRISM) has been recorded. These spectra can be applied as endmembers for all components and mixtures of interest for SPRC analogues and magnesium chloride brines and from these, the detectability limit for PAHs within CO_2 ice and RSL analogues has been established. All of these data will be publicly available for anyone to download from the SSHADE database (see section 3) for free upon publication of the papers resulting from this research. This open access approach will aid researchers looking for PAHs not only in other regions of Mars, but on any astronomical object, including icy moons, comets, asteroids and even exoplanets. The availability of these data will prevent the need for repetition of experiments, saving time, money and many other resources, and it is my hope

that this PAH spectrum becomes the go-to spectra in searches for this molecule on Mars.

The infrared spectral analysis of SCT mesas supports findings about the source of dust being from within ice, and this of great interest to the search for life on Mars. The ill-fated Mars Polar Lander mission (Albee et al., 2000) really put a nail in the coffin of in-situ Mars Polar Research, and I hope that these findings, along with the recent news on subsurface lakes, in some small way reignites interest in Martian polar regions as important to the study of Mars in general and the search for life in particular. Work from this thesis has been presented at numerous conferences, workshops and seminars across the globe (see Appendix D).

More broadly, I have found that CRISM imagery of the poles is particularly effective in teaching students and the general public about hyperspectral imaging; the high reflectance values over ice, and summary product colour maps, make beautiful, clear pictures that make spectroscopy accessible and fun. I have used the imagery from this thesis many times in outreach events for schools, undergraduate and MSc courses, and at careers events for space science; it's proved an excellent way to inspire interest in planetary geology.

Finally, and in my own personal view most importantly, the completion of this thesis by someone from a council estate, who failed their humanities A Levels and worked as a train driver, sales assistant and care worker until their mid-30s before embarking on a career as space scientist (something that I never thought

was possible) serves as a reminder that it is never too late to try something new

and contribute to humanity's collective knowledge of how the universe works.

Acknowledgements

Table of Contents

List of Figures

21

List of Tables

List of Abbreviations

BD1435	Viviano-Beck et al. (2014) summary product for CO_2 ice
BD1500	Viviano-Beck et al. (2014) summary product for H_2O ice
BDCARB	Pelkey et al. (2007) summary product for carbonates
CAT	CRISM Analysis Tool
CCD	Charge-Coupled Device
CRISM	Compact Reconnaissance Imaging Spectrometer for Mars
CTX	Context Camera on Mars Reconnaissance Orbiter
DEM	Digital Elevation Model
DTM	Digital Terrain Model
ENVI	Environment for Visualising Images (software)
ESA	European Space Agency
FRT	Full Resolution Targeted
GIS	Graphical Information Systems
HCPINDEX	Viviano-Beck et al. (2014) summary product for pyroxene
HiRISE	High Resolution Imaging Science Experiment on Mars Reconnaissance Orbiter
HRSC	High Resolution Stereo Camera on Mars Express
ICER2	Viviano-Beck et al. (2014) summary product for ice
IDL	Interactive Data Language (programming language)
IPAG	L'Institut de Planétologie et d'Astrophysique de Grenoble
IR	Infrared
ISM	Interstellar Medium

JGR	Journal of Geophysical Research
JMARS	Java Mission-planning and Analysis for Remote Sensing (software)
JSC Mars-1	Martian regolith simulant from Hawai'i
LCPINDEX2	Viviano-Beck et al. (2014) summary product for low-calcium pyroxene
MOC	Mars Orbiter Camera on Mars Global Surveyor
MOLA	Mars Orbiter Laser Altimeter on Mars Global Surveyor
MRO	Mars Reconnaissance Orbiter
MSSL	Mullard Space Science Laboratory
MY	Mars Year
NASA	National Aeronautics and Space Administration
N-FINDR	Endmember extraction algorithm (Winter 1999)
NIR	Near-Infrared
NPRC	North Polar Residual Cap
OLINDEX2	Viviano-Beck et al. (2014) summary product for olivine
OMEGA	Observatoire pour la Minéralogie l'Eau les Glaces et l'Activité
PAH	Polycyclic Aromatic Hydrocarbons
PDS	Planetary Data System
PLD	Polar Layered Deposits
RGB	Red Green Blue image bands
ROI	Region of Interest
RSL	Recurring Slope Lineae
SAM	Sample Analysis at Mars instrument on Mars Science Laboratory rover
SCT	Swiss Cheese Terrain
SHADOWS	Spectrophotometer with cHanging Angles for the Detection Of Weak Signals

SHINE	The SpectropHotometer with variable INcidence and Emergence
SMACC	Sequential Maximum Angle Convex Cone
SPRC	South Polar Residual Cap
SSHADE	Solid Spectroscopy Hosting Architecture of Databases and Expertise
STFC	Science and Technology Facilities Council
TES	Thermal Emission Spectrometer on Mars Global Surveyor
THEMIS	Thermal Emission Imaging System on Mars Odyssey
UCL	University College London
UV	Ultraviolet
VIMS	Visual and Infrared Mapping Spectrometer on Cassini

1: Introduction

Mars has long been the subject of scientific exploration, with a focus on the investigation of conditions on ancient Mars, searches for evidence of life, and for corresponding habitable environments (Fairén et al., 2010). During the last 2 decades, the polar regions have emerged as sites of increased scientific interest. Mars polar regions, both in the northern and southern hemispheres, have residual caps that survive throughout each hemisphere's respective summer; the North Polar Residual Cap (NPRC) registers as predominately water ice (Langevin et al., 2005), while the longer, colder winter in the southern hemisphere (due to the Martian orbital obliquity) means that the higher altitude South Polar Residual Cap (SPRC) is largely composed of CO_2 ice (Douté et al., 2007; Byrne, 2009). The SPRC overlays, and is surrounded by, water ice layers known as Polar Layered Deposits (Piqueux et al., 2008).

While the Martian climate is postulated to have been more 'Earth-like' in the past, with warmer, wetter conditions and an active magnetosphere (Jakosky and Phillips, 2001), conditions on present day Mars are much less habitable. The attenuation of Mars' magnetosphere, along with Mars's low gravity, led to a loss of atmosphere through solar wind interactions, leaving the average temperatures and atmospheric surface pressures much lower than on the Earth (Jakosky et al., 2015; Kass and Yung, 1995; Melosh and Vickery, 1989). Liquid water generally cannot exist on the surface of Mars due to low atmospheric temperatures and pressures and both water and CO_2 ice sublimate directly from the solid to vapour phase (Hecht, 2002; Blackburn et al., 2010). The lack of a dense atmosphere or

ozone layer on present-day Mars means that the surface is exposed to high levels of short-wave ultraviolet (UV) radiation, which would have a deleterious effect on any biological material on the planetary surface (Cockell et al., 2000). Galactic cosmic rays also reach the surface of Mars, but their effect on PAHs is negligible compared to the UV radiation of solar origin (Dartnell et al., 2012), and has resulted in the complexification rather than destruction of PAHs in interstellar nebulae (Allamandola, 2011). The annual, seasonal sublimation and deposition of CO_2 ice on the SPRC leads to a unique surface feature known colloquially as 'Swiss Cheese Terrain' (SCT), characterised by flat floored, circular depressions that can intersect to form intricate patterns reminiscent of Emmental Swiss Cheese (Malin et al., 2001). These SCT features are of particular interest as their sublimation cycles expose material previously shielded from deep solar UV within the SPRC (Jian & Ip, 2009). More specifically, it would be of great interest to look for evidence of one particular class of organic molecules, Polycyclic Aromatic Hydrocarbons (PAHs), that may have been afforded protection from this harmful radiation within the SPRC.
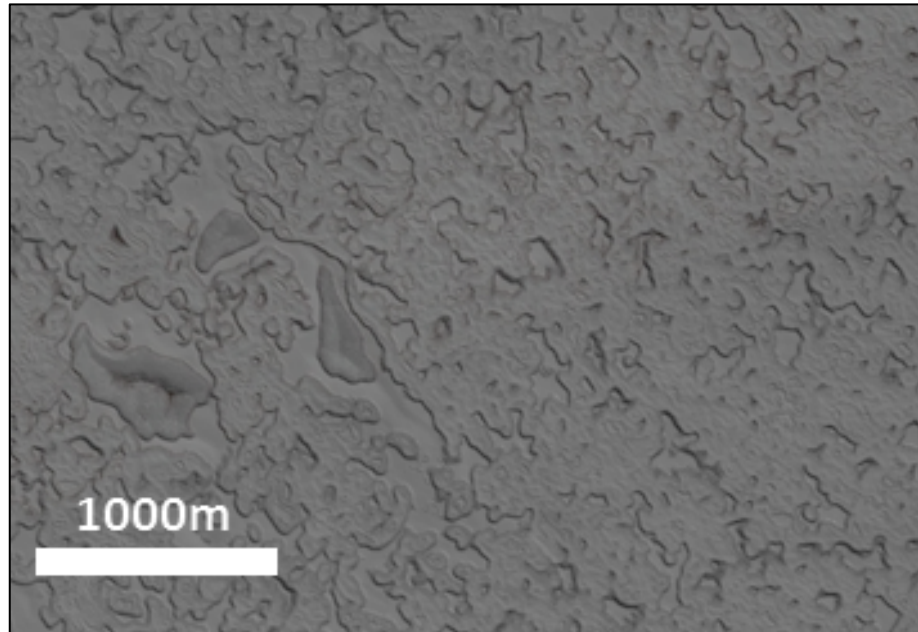
Figure 1.1: Example of Swiss Cheese Terrain (HiRISE image

ESP_014380_0945)

The detection of organics has been a primary objective of orbiters and landers since the Viking missions (Klein, 1978). Despite apparent negative results for the detection of extant life by the Viking landers in the 1970s, which searched for traces of biologically important compounds (Klein, 1978; Schuerger and Clark, 2008), perchlorates were discovered by the 2008 Phoenix lander (Hecht et al., 2009). More recently, organics were discovered by the Sample Analysis at Mars (SAM) instrument on NASA's 2012 rover mission, Mars Science Laboratory (Freissinet et al., 2015), known as "Curiosity". Perhaps of even more interest, the reanalysis of the 1976 Viking Lander data by Navarro-Gonzalez et al. (2010) using modern laboratory techniques suggested that there were both perchlorates and organic carbon present at the Viking Lander sample sites, although they were not identified at the time. As well as SCT, we will also look at the dynamic

Recurring Slope Lineae (RSL), whose exact cause remains a matter of debate, but are certainly seasonally active and a 'hot topic' in Mars science.

The use of spectrometers started in 1969, with Mariners 6 and 7 (Herr et al., 1972). Regarding SPRC dust, the first analysis was conducted by Douté et al, (2007). This work used data from the Mars Express instrument Observatoire pour la Minéralogie, l'Eau, les Glaces et l'Activité (OMEGA). The spatial resolution limitations of OMEGA (~2 km/pixel; Bibring et al., 2004b) meant that Douté et al.'s study of the SPRC was holistic in nature and was not able to observe these small features. Since the aim of this work is to look for regions of interest that might provide protection for fragile organic molecules, but also allow periodic exposure in order to be detectable from space, a finer spatial resolution is required. As a result, we use data from the Compact Reconnaissance Imaging Spectrometer for Mars (CRISM) on board NASA's Mars Reconnaissance Orbiter (MRO), which attains surface spatial resolution of around ~20m/pixel (Murchie et al., 2007). Using CRISM allows local analysis of regions of the SPRC with various morphologies, and in particular, thin SCT and RSL features, to establish whether PAHs can be detected in dynamic features on Mars.

The following questions will need to be addressed throughout this thesis:

- Why are polycyclic aromatic hydrocarbons (PAHs) considered to be important in planetary science?
- Why has Mars (and in particular SPRC and RSL features) been chosen as a study site?
- Why is the detection of PAHs on Mars problematic?

- Where else, other than on Earth, have PAHs been detected?

- What would PAHs look like if they were present in these environments on Mars, and how much PAH would have to be there to be detectable at all?

- What processes occur, and what chemical and mineralogical components are present, on the SPRC and in RSL, and how might they affect attempts to detect PAHs?

- What implications does this study have on future work?

Some of these themes will be discussed in detail throughout the rest of the following chapter, and hopefully form a solid basis for the original research that follows to answer the rest of them.

2. Background

The purpose of this thesis is to search for previously undetected organics on Mars. In order to do this, we must learn what those organics are, what environments would be the best place to look for them, and what they might look like to our remote sensing instruments if they are present in detectable amounts. What follows is a review on existing literature on what is already known about these elusive molecules, about conditions on Mars, and the resulting rationale for why particular sites and methods are discussed and utilised throughout the rest of the thesis.

The organic molecules in question are Polycyclic Aromatic Hydrocarbons (PAHs). The environments looked at include dynamic surface features on the Martian South Polar Residual Cap (SPRC) and seasonal surface streak features

called Recurring Slope Lineae (RSL), and the method used is (shortwave) infrared spectroscopy.

2.1. The Importance of Polycyclic Aromatic Hydrocarbons (PAHs) in Astrobiology

The primary motivation for this project is the detection of PAHs; it is necessary to understand some of their characteristics in order to understand their importance in astrobiology and how best to detect them.

PAHs are a group of chemical compounds consisting of benzene rings of hydrogen and carbon that are particularly stable compared to aliphatic (non-ring-like) hydrogen-carbon molecules (Arey and Atkinson, 2003). Some examples of PAH structures are shown below.

Naphthalene ($C_{10}H_8$)   Anthracene ($C_{14}H_{10}$)

Phenanthrene ($C_{14}H_{10}$)   Pyrene ($C_{16}H_{10}$)

Benzo(a)pyrene ($C_{20}H_{12}$)   Coronene ($C_{24}H_{12}$)
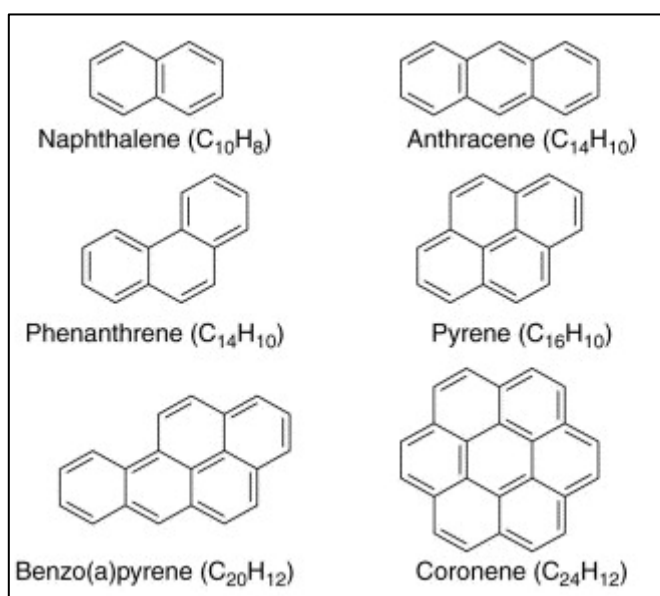
Figure 2.1: Structure of common PAHs. (Samanta et al., 2002)

PAHs are considered to be one of the smallest forms of dust particle, with the simplest species, naphthalene, containing only 18 atoms (Parker et al., 2012), though some species can contain >100 atoms (Joblin et al., 2011). There are hundreds of species of PAH (Ifegwu and Anyakora, 2015); they are abundant on Earth, and are a by-product of incomplete combustion of organic materials such as wood, tar and coal, and they are present in crude oil and cooked food (Samanta et al., 2002; Finlayson-Pitts and Pitts Jr, 1997).

PAHs occur not only on Earth, but throughout the universe; they have been found to coalesce in space within dust clouds; spectral signatures indicative of PAHs, such as anthracene ($C_{14}H_{10}$) and pyrene ($C_{16}H_{10}$) were detected by Mulas et al., (2005) during their investigation of infrared emissions from the Red Rectangle Nebula. Indications of PAHs have also been found on three of Saturn's moons; Iapetus and Phoebe (Cruikshank et al., 2013) and in the upper atmosphere of Titan (Waite et al., 2007; Coates et al., 2007). The exact process by which they are formed is not well understood, but laboratory and computational experiment results published in 2019 suggest a series of high-temperature reactions in the circumstellar envelopes of carbon-rich stars may be responsible (Zhao et al., 2019). Whatever their origin, there are close to 120 known interstellar PAH species, which may account for up to 30% of total cosmic carbon (Ehrenfreund and Charnley, 2000; Herbst and van Dishoeck, 2009). PAHs are also thought to be linked to the unidentified infrared emission bands observed at wavelengths from 3–14 μm (Ricks et al., 2009); unidentified emission bands have been

observed in the direction of galaxy M82 (the Cigar Galaxy), hinting at the ubiquitous nature of PAHs (Sironi and Draine, 2009).

PAHs are thought to accumulate spontaneously in the Interstellar Medium (ISM) and can become frozen within ice particles in dense molecular clouds in space, then undergo processing by UV light and cosmic rays to produce more complex species (Dartnell et al., 2012). These eventually rain down on primordial planets directly from planetary accretion discs, or are delivered on comets and meteorites (Allamandola, 2011). PAHs can also form in-situ on planetary bodies through Fischer-Tropsch reactions of hydrogen and carbon-monoxide rich igneous material (Zolotov and Shock, 1999). Therefore, PAHs should be present, or have been present in the past, on all planetary bodies in the solar system (Dullemond et al., 2007).

The delivery of complex organic compounds to planets via bolide impact is a very important concept in astrobiology and could be instrumental in explaining abiogenesis (the origin of life). Carbon's propensity to catenate (form long chains), and the carbon-based nature of all life on Earth, means that the presence of carbon compounds is considered an important factor in any potentially habitable environment (Plaxco and Gross, 2011).

Monnard and Deamer (2002) put forward the argument that some of these complex molecules are amphiphilic, creating vesicles analogous to cell membranes that are capable of creating a stable, protected environment for emerging biochemistry. In addition, these 'membranes' can trap photo-

luminescent molecules formed by UV radiation, resulting in complex organic chains that are capable of absorbing and emitting energy, a crucial step in theories on the origin of life (Dworkin et al., 2001).

The presence of PAHs could indicate the degradation of organisms (Mckay et al. 1996) and could therefore be a biomarker for extinct or even extant life. The ability to identify PAHs using remote sensing could prove a critical tool in the search for extra-terrestrial organisms. PAHs have not been detected on Mars (Benner et al., 2000), and so the decision to choose Mars as a possible environmental host for PAHs must be justified. Before we take a closer look at Mars, we will cover some of the ways that PAHs have been detected elsewhere in the universe.

2.2. Detection of PAHs

Detection of PAHs outside Earth has been possible for many years, historically in interstellar space, which we will discuss first.

2.2.1. PAHs in Interstellar Space

Spectral signatures in interstellar regions were first attributed to PAHs in the mid-1980s (Leger and Puget, 1984; Allamandola et al., 1985). While there are signatures diagnostic of PAHs at 6.2, 7.7, 8.7, 11.3 and 12.7 µm (Salama, 2008), it is the signature at 3.29 µm and its accompanying weaker bands and underlying structures between 3.1 and 3.7 µm (Tokunaga et al., 1991) that were of initial interest to this investigation due to the laboratory data available, and the

parameters of the CRISM instrument (see section 3.1.4) used for data acquisition and processing. Figure 2.2 shows the emission feature at 3.29 μm.
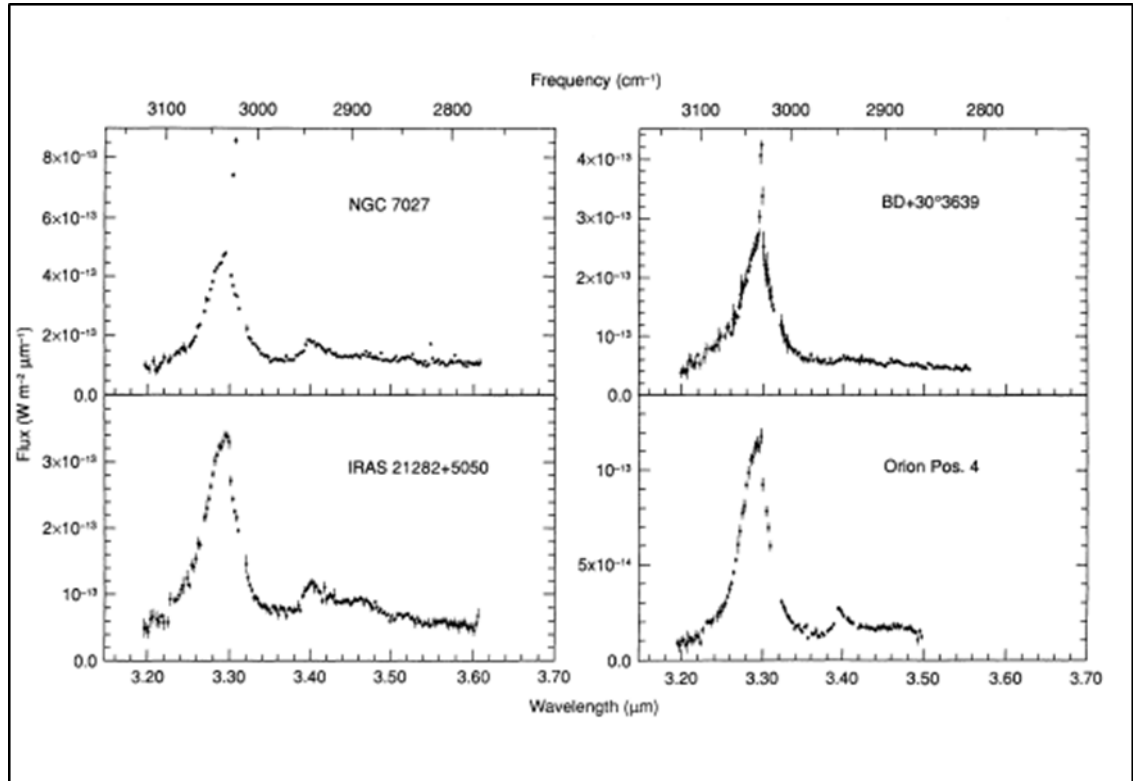
Figure 2.2: Emission spectra diagnostic of PAHs in interstellar dust clouds

(Tokunaga et al., 1991)

Note that infrared emission and reflectance spectra are inversely correlated, therefore peaks in emission spectra of PAHs correspond to troughs in reflectance spectra (Stuart, 2004); ergo, PAH emission signatures from interstellar nebulae manifest as peaks while PAH reflectance signatures from planetary bodies manifest as troughs.

PAHs are most often identified through their near and mid-infrared bands (Joblin et al., 2011). PAHs have been detected in interstellar medium nebulae

(Allamandola, 1990), circumstellar discs (Lovas et al., 2005), in regions of planet formation (Acke, 2011), and in meteorites and comets (Wing, 1991; Li, 2009); they appear to be virtually ubiquitous throughout our own Milky Way galaxy (Draine, 2011), and even in other galaxies (Draine and Li, 2007). However, PAHs have only been detected on a small number of solar system bodies.

2.2.3. Detection of PAHs on extra-terrestrial Bodies

The *Visual and Infrared Mapping Spectrometer (VIMS)* on board the *Cassini* orbiter is an imaging spectrometer spanning the 0.3-5.1 µm wavelength range (Brown et al., 2004). *VIMS* was used to analyse the surface of several of Saturn's moons, and then compared to spectral models of various compounds for best fit to ascertain surface and atmospheric composition.

As a result and as mentioned earlier, spectral signatures indicative of PAHs have been found on the surfaces of both Iapetus and Phoebe (Cruikshank et al., 2008; Cruikshank et al., 2014), and in the upper atmosphere of Saturn's moon Titan (Lopez-Puertas et al., 2013; Waite et al., 2007; Coates et al., 2007). Cruikshank et al.'s (2008, 2014) findings on icy moon surfaces are more pertinent to this study (in comparison to Lopez-Puertas et al.'s findings in Titan's atmosphere) as the detection techniques and analysis methods used on Iapetus and Phoebe are better suited to investigating the Martian icy polar caps.

While Iapetus contains large amounts of water ice (Cruikshank et al., 2008), it is unique in that one hemisphere is covered in dark material, possibly swept up by the moon during its orbit, resulting in two distinct hemispheres of high and low

albedo (Owen et al., 2001). Spectral mapping revealed a noticeable, broad absorption feature on the light coloured, icy hemisphere, between 2.5 and 3.5 µm that is attributed to H_2O ice, which makes up 78% of the high albedo surface (Buratti et al., 2005). Cruikshank et al., (2008) posit that the spectral region of interest for PAHs (3.29 µm) sits within the signature of water ice, so the presence of water ice precludes the effective detection of PAH signatures. Obscuration of organic signatures by water ice was overcome by Cruikshank et al., (2008) by analysing dark material (which completely covers the ice beneath) on the low albedo hemisphere of Iapetus. The low albedo region exhibits an absorption feature between 2.5 and 3.5 µm that is shallower and narrower than that of the higher albedo ice regions, and that has been identified as tholin-rich material (Buratti et al., 2005).
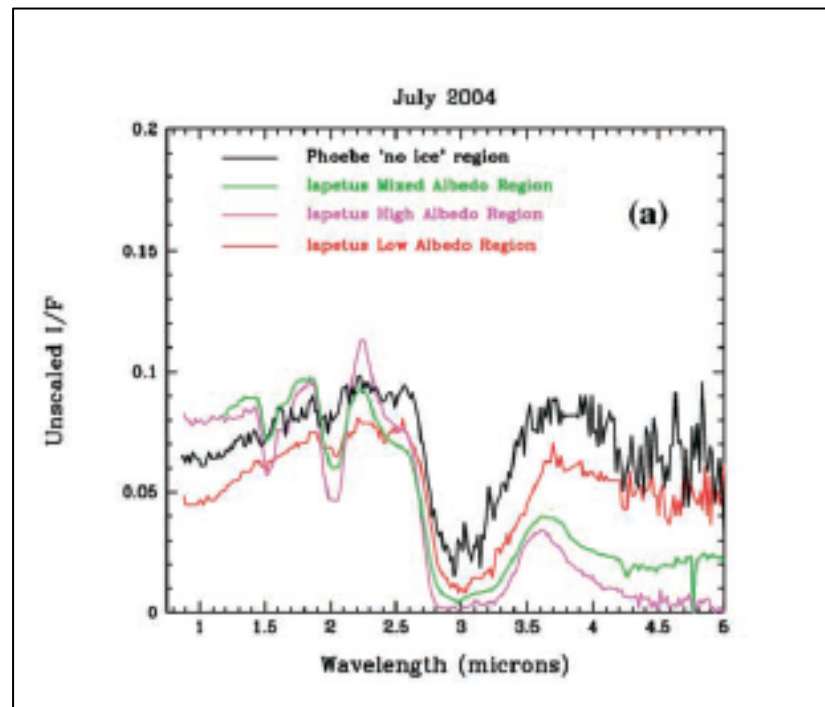
Figure 2.3: Spectral response of regions of Iapetus and Phoebe (Buratti et al., 2005)

46

Tholins are a class of organic compound that do not form naturally on Earth, but rather result from the irradiation of simple compounds like ethane and methane (Sagan and Khare, 1979; Poch et al., 2016); they are carbon and nitrogen containing compounds that have a characteristic reddish/brown colour (Derenne et al., 2012).

Cruikshank et al., (2008) identified some of the organic content of the tholin material as PAHs based on spectral comparisons with the averaged spectral profile of 6 astrobiologically significant PAHs (Colangeli et al., 1992) measured in laboratories (chrysene, triphenylene, perylene, benzo (α) pyrene, pentacene and coronene). The similarities in absorption features between signatures from the 6 PAH mix and Iapetus can be seen in Figure 2.4.
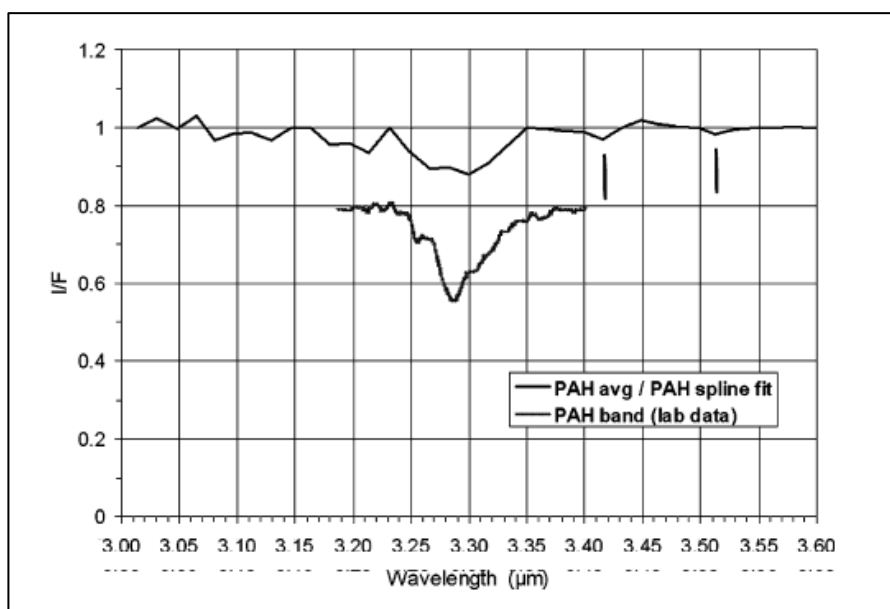
Figure 2.4: Iapetus average of 130 pixels with strongest PAH signatures (top line) compared with average of 6 PAHs of astrobiological interest (bottom line; Cruikshank et al., 2008)

What is considered to be a relatively strong signature for PAHs on Iapetus is still a very subtle absorption feature (Figure 2.5).
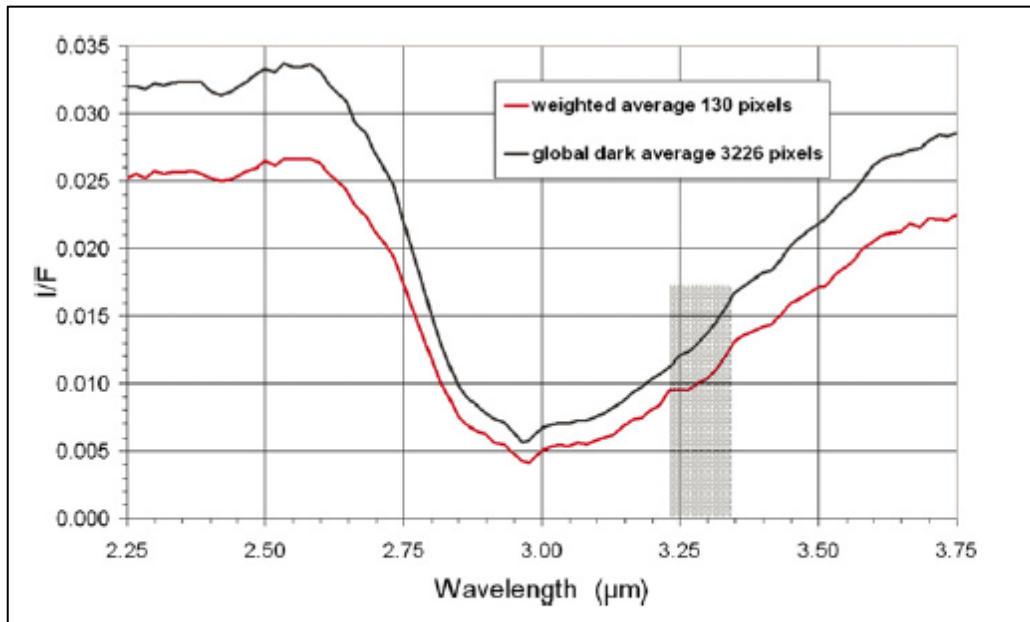
Figure 2.5: Comparison of global average of dark material on Iapetus with 130 pixels with PAH signature (Cruikshank et al., 2008)

The evidence for PAHs is compelling for Iapetus; however, unlike on the Martian SPRC, Iapetus has extensive, uninterrupted areas of dark material that mask the effects of ice on IR spectra. Nevertheless, it is useful to see the successful identification of PAHs in a comparatively ideal environment like Iapetus to gain an understanding of the type of spectral feature that is being sought after on Mars.

Another Saturnian moon, Phoebe, was spectrally mapped by *VIMS* (Clark et al., 2005). Phoebe does not exhibit the dichotomous albedo of Iapetus; it has uniformly low albedo and is thought to contain large volumes of water ice covered

by a layer of surface deposits made up of iron bearing minerals and silicates (Clark et al., 2005; Johnson and Lunine, 2005). Clark et al., (2005) also detected weak spectral signatures suggesting organics at 3.2-3.3 µm (Figure 2.6).
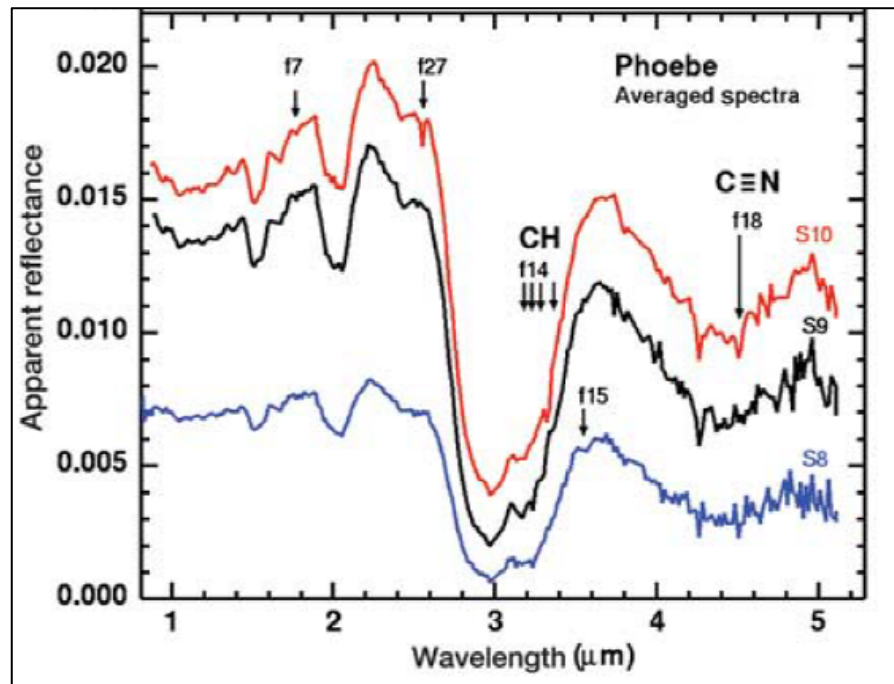
Figure 2.6: Phoebe spectra showing hydrocarbon absorption feature at ~3.3 µm

(Clark et al., 2005)

Cruikshank et al., (2008) also found evidence of a weak absorption feature indicative of PAHs on Phoebe (Fig. 2.7).
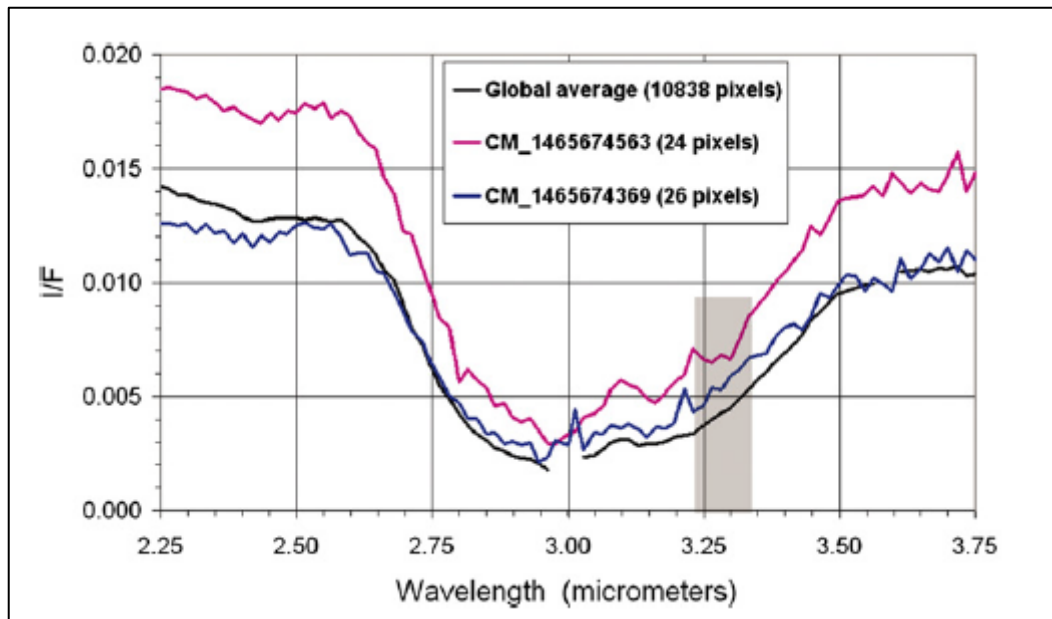
Figure 2.7: Absorption feature at 3.3 µm in dark material on Phoebe

(Cruikshank et al., 2008)

While Phoebe exhibits a weak PAH signature relative to Iapetus, Phoebe still has much larger areas of dark material to analyse compared with depression rims on the Martian SPRC, which means comparisons between Saturnian moons and Mars have their limitations. If PAHs are present at all on Mars, they are likely to be in very low concentrations, as they would be only a component of the very small regions of dust on scarp walls. This is explored further in Chapter 6.

PAHs have also been detected on comets, demonstrating a link between comet formation and the composition of the ISM (Li, 2009). Re-examination of signatures from Hale-Bopp showed possible evidence of PAHs, (Lisse et al., 2007), although this has been disputed (Crovisier et al., 2008), but there is certainly more recent evidence of PAHs on comet 67P/Churyumov-Gerasimenko from the Rosetta mission (Schuhmann et al., 2019). The presence of PAHs on

comets provides a possible delivery mechanism for PAHs to Mars throughout the history of the solar system up to present day.

2.2.4. Detection of PAHs on Mars

Like Earth, Mars has been bombarded with bolides throughout the history of the solar system, and 2.5×10^5 kg/year of unaltered organic material has been postulated as being delivered to the Martian surface, which when extrapolated at a constant rate over the history of the solar system, outweighs present-day terrestrial biomass (Flynn, 1996).

With regard to PAHs on Mars, while they have not been detected in-situ, they have been detected in meteorites of Martian origin found on Earth. Shergottites are basaltic (see section 2.3) meteorites that once formed part of the Martian crust and became dislodged through impact events, then landed on Earth (Becker and Pepin, 1984). Two such examples of Martian meteorites, (EETA79001 and ALH84001) were found to contain PAHs (Botta et al., 2008) but the origin of the PAHs remains in contention as terrestrial contamination cannot be ruled out (Gibson et al., 2001). Organic detection within carbonate globules has been used in previous analyses of the Martian meteorite ALH 84001 (Flynn et al., 1998), and CRISM has been used to identify carbonates with success by Harner and Gilmore (2015), with various carbonates sharing an absorption feature with PAHs at 3.3 µm, though that has a double trough, making it easier to separate from PAH features upon more detailed analysis

The lack of any evidence of PAHs on the surface of Mars is likely to be because they would be rapidly destroyed by exposure to UV radiation, or by the chemical reactivity of the Martian regolith (Quinn and Zent, 1999; Benner et al. 2000). Following experiments in 'Mars chambers' that emulate environmental conditions on Mars, Dartnell et al., (2012) found that PAHs can be destroyed by exposure to UV radiation in as little as 3 Martian days (one Mars day is 24 hours 37 mins).

Dartnell et al., (2012) propose that PAHs might be protected from the deleterious effects of UV radiation and oxidisation chemistry if they were within the subsurface of Mars, inside rocks, or in areas of permanent shadow. Additionally, ice can act as a barrier to UV radiation (Vincent, 1998) reducing the harm caused to microbial communities on Earth (Cockell et al., 2011; Perovich, 2006), and this could allow organic compounds to become more complex where partial shielding of UV radiation occurs (Herbst and van Dishoek, 2009; Oberg et al., 2009). In-situ astrobiological detection of the subsurface will be carried out in the future, for example on the ESA ExoMars Rover mission scheduled for launch in 2022, which will carry a drill unit capable of penetrating up to 2 m in depth (Vago et al., 2017; Ciarletti et al., 2011). This will tell us more about drill-sites, but remote sensing technology can be used to study the whole of Mars, targeting material previously shielded from UV that has been uncovered by natural dynamic processes.

The hostile environment on Mars does not mean searching for PAHs is futile (ten Kate, 2010). As we have seen, revisiting of old data from the Viking and Phoenix Landers using modern techniques means that previous results can become redundant, and historical data can become significant in new ways (Schuerger

and Clark, 2008; Hecht et al., 2009). The recent discovery of what may be biomarkers in the clouds of Venus show us that we must keep an open mind as to what constitutes a habitable environment, even in the most hostile of surroundings (Greaves et al., 2020).

2.3. The Martian Environment

We touched briefly on the present-day conditions on Mars in the introduction, and we will now go into more detail.

Figure 2.8: The planet Mars. (Photo credit: NASA/J. Bell [Cornell U.] and M. Wolff)

Since the earliest days of space exploration, Mars has been a target for scientific missions to investigate its geological history and to look for evidence of life, due to its proximity and similarities to Earth (Fairén et al., 2010).

Mars has its own annual eccentricity in orbit, and uses a metric called Solar Longitude[1] (L_s) to divide its seasons and its own year system of Mars Years[2]

---

[1] http://www-mars.lmd.jussieu.fr/mars/time/solar_longitude.html
[2]https://mars.nasa.gov/resources/21392/mars-in-a-minute-how-long-is-a-year-on-mars.

(MY). Mars also has its own Areoid (Burke, 2012) that is used as a baseline instead of a geoid to contextualise surface feature heights.

Based on orbital remote sensing, surface rover and landing measurements, Mars' surface is thought to be made up chiefly from basalt (a mix of the minerals plagioclase feldspar, pyroxene and olivine), not dissimilar from the composition of Earth's oceanic crust (Herd et al., 2002; Taylor, 2009), although there is a much richer mineral diversity across the surface due to the Earth's climatic history (Carroll, 2012; Press et al., 2004). Rocks on the Martian surface are largely of igneous origin, having crystallised from magma following Mars' formation and periods of volcanism in the distant past (Baratoux, 2013), but there is evidence of secondary minerals produced by hydrothermal alteration and weathering, such as clay minerals, opaline silica and evaporites, like gypsum (Bibring et al., 2005; Rice et al., 2017).

Mars is of particular interest to astrobiology for a number of reasons. Mars shares many characteristics with Earth, including seasons, an atmosphere, ice caps, volcanoes, clouds and dust storms (de Pater and Lissauer, 2007). There is also evidence of liquid water having been present in large quantities on the surface of Mars; for example, remote sensing satellites, landers and rovers have captured images of valleys, deltas and the aforementioned indications of hydrothermal alteration (Lammer et al., 2005). While there are other bodies in the solar system of perhaps even greater astrobiological interest, (such as Jupiter's moon Europa, and Saturn's moons Titan and Enceladus [Ball, 2004]) Mars is closer and therefore less of a logistical challenge to investigate (Squyres, 2005). Mars also

shares more similarities in conditions with early Earth than distant icy moons (Vita-Finzi and Fortes, 2013).

As mentioned earlier, the Martian climate was undoubtedly more 'Earth-like' in the past (Fassett and Head, 2010), but the temperatures and atmospheric surface pressures are now much lower than on Earth, averaging -63 °C; highs of 20 °C have been recorded at the equator, and lows of -153 °C at the poles (Johnson et al., 1996; Kass and Yung, 1995; Melosh and Vickery, 1989). With the notable exception of possible evidence of briny liquid water flows discussed in section 2.4.1 (Ojha et al., 2015), liquid water generally cannot exist on the surface of Mars due to low pressures and temperatures; both water and CO_2 ice sublimates directly from the solid to vapour phase rather than melts (Blackburn et al., 2010). The lack of any significant atmosphere on present-day Mars results in high UV flux on the Martian surface, which would quickly destroy any PAHs on the surface (Patel et al., 2002; Cockell et al., 2000). Therefore, we are interested in dynamic features that may expose material that has been protected from UV. Some of the most dynamic regions on Mars are the polar caps, which we will look at now.

2.3.1. The Martian Polar Caps

Mars has both North and South Polar ice caps made up of CO_2 ice and water (H_2O) ice. As mentioned earlier, Mars has seasons, though they are longer and colder than those on Earth due to Mars lying, on average, 52% further from the Sun than Earth (Couper and Henbest, 2001). Seasonal variation in the amount

of solar radiation in the polar regions causes regular patterns of sublimation and condensation during spring and autumn respectively (Jian and Ip, 2009). The lower altitude, warmer northern cap loses its CO_2 ice layer entirely during Northern hemisphere spring and summer (Calvin et al., 2015); conversely, the colder southern cap retains a permanent 8-10 m thick CO_2 layer, the SPRC (Byrne, 2009). While the South Pole registers as predominantly CO_2 ice when examined by spacecraft spectrometers, it overlays, and is surrounded by, water ice layers known as Polar Layered Deposits (PLD; Paige et al., 1990; Piqueux et al., 2008).

Mars' obliquity, (the angle at which its axis is tilted) has changed many times over the history of the solar system and isn't stable, unlike Earth's which is kept relatively consistent due to the gravitational effects of the moon (Ward, 1973; Touma and Wisdom, 1993). These changes in axial orientation over the scale of hundreds of thousands of years, on the one hand, mean that the ice caps are relatively young having melted/sublimated and refrozen many times over Mars' history, which could be bad news for searching for ancient signs of organics. On the other hand, this could be advantageous, meaning that what are currently the poles would have been warmer and perhaps the site of liquid water repeatedly throughout history, which is good for the search for life (Cockell et al., 2011). In addition, the recent findings about sub-surface bodies of saltwater make the poles and perhaps other areas of Mars extremely interesting, astrobiologically speaking (Orosei et al., 2018; Lauro et al., 2019 and 2020).

The annual, seasonal sublimation and deposition of CO_2 ice on the SPRC leads to a unique surface feature known broadly as 'Swiss Cheese Terrain' (SCT), characterised by flat floored, circular depressions that can intersect to form intricate patterns reminiscent of Emmental Swiss Cheese (Malin et al., 2001). It is the South Pole SCT terrain that is of interest to this study as it is much dustier than the North Pole water ice deposits (Milkovich et al., 2008), and we will now discuss these SPRC features in more detail.

2.3.2. Swiss Cheese Terrain

NASA's *CTX Context Camera* on board *MRO* has attained complete summer coverage of the SPRC with a spatial resolution of ~6 m/pixel, allowing detailed mapping of the various SCT units over the entire polar cap (Thomas et al., 2009). The dynamic nature of the SPRC has been established by comparing current maps made from *CTX* imagery to earlier images from the *Mars Orbital Camera (MOC)* on Mars Global Surveyor, and by comparing images obtained during different orbits from the *High Resolution Imaging Science Experiment (HiRISE)* on *MRO* (Thomas et al., 2005; Pommerol et al., 2011). The SCT features are of particular interest to this study as their seasonal sublimation cycles may expose previously shielded dust particles (Jian et al., 2009).

SCT is an overarching term widely used by NASA, but that some argue is too broad to effectively describe the myriad morphologies present on the SPRC, and various sub-categories of SCT morphology have since been described (Thomas et al., 2009) .

Figure 2.9 shows the different features and textures that are informally grouped under the term SCT, though as mentioned earlier, Thomas et al., 2009 argue that this term, coined by James et al., (1992) when the features were first identified using 100 m spatial resolution, is now too broad and vague. Distinct morphologies have now been identified and named; a comprehensive account of the SPRC sub-units can be found in two papers by Thomas et al., (2005 and 2009), the two most extensive studies of SPRC morphology ever carried out; the classifications designated in these seminal works will be used to describe study sites throughout this thesis.
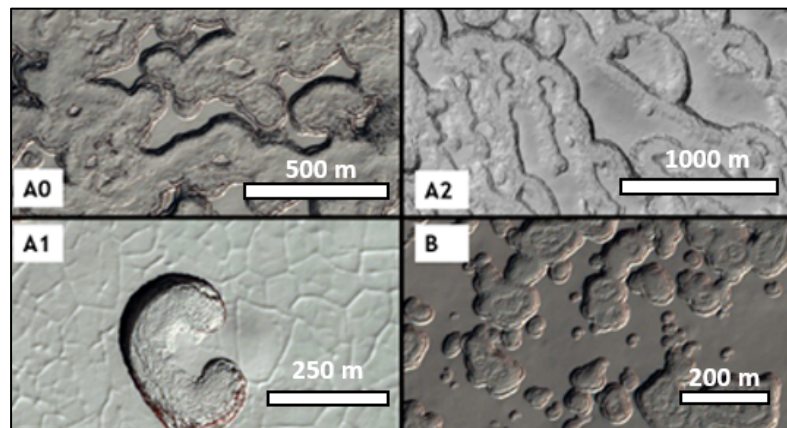
Figure 2.9: Examples of SCT feature morphologies. HiRISE product IDs clockwise from top left: ESP_014380_0945, PSP_005386_0930, ESP_012271_0940, ESP_014141_0930. Morphology designations A0-B follow the terminology of Thomas et al. (2009)

The SPRC consists of two distinct units; the upper unit (B) is made up of a series of 1-2 m thick layers superposed over a lower, older, 8-10m thick unit (A) that has undergone significant erosion (Thomas et al., 2005).

Unit A has 3 subdivisions that are differentiated by morphology. Unit A0 (Figure 2.10) covers <1% of the SPRC, and is largely restricted to dwindling mesas left behind as sublimation depressions expand and meet (Thomas et al., 2009).
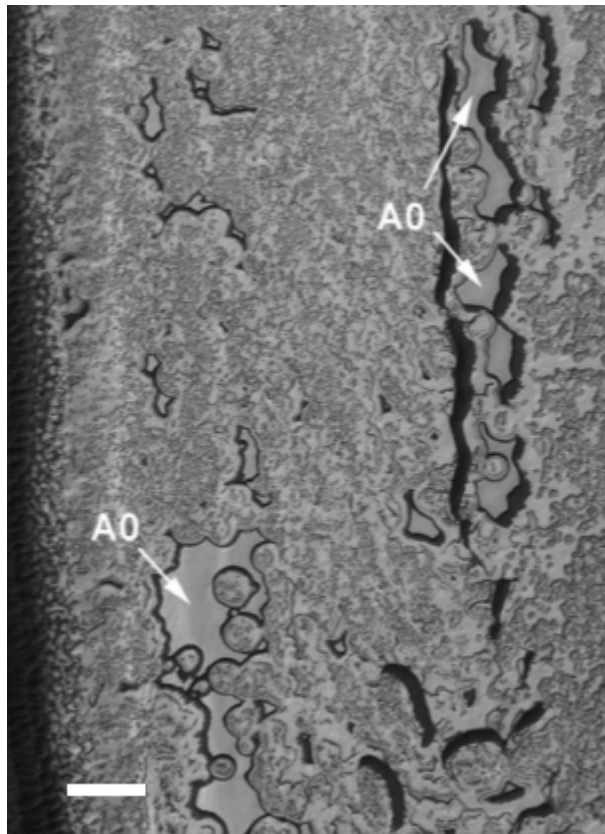
Figure 2.10: SPRC Unit A0 morphology. White scale bar = 1 km. (Thomas et al., 2009)

Examination of time series imagery has shown that dark fans can appear seasonally, adjacent to these A0 mesas, and may be the result of the ejection of entrained dust that is spread around the margins of the mesas as sublimation occurs within the body of the ice plateaus, with material then forcefully ejected out of the mesa walls by escaping CO_2 gas (Buhler et al., 2017). An example of these dark fans can be seen in a Figure 2.11 below, taken from Buhler et al.'s 2017 paper.
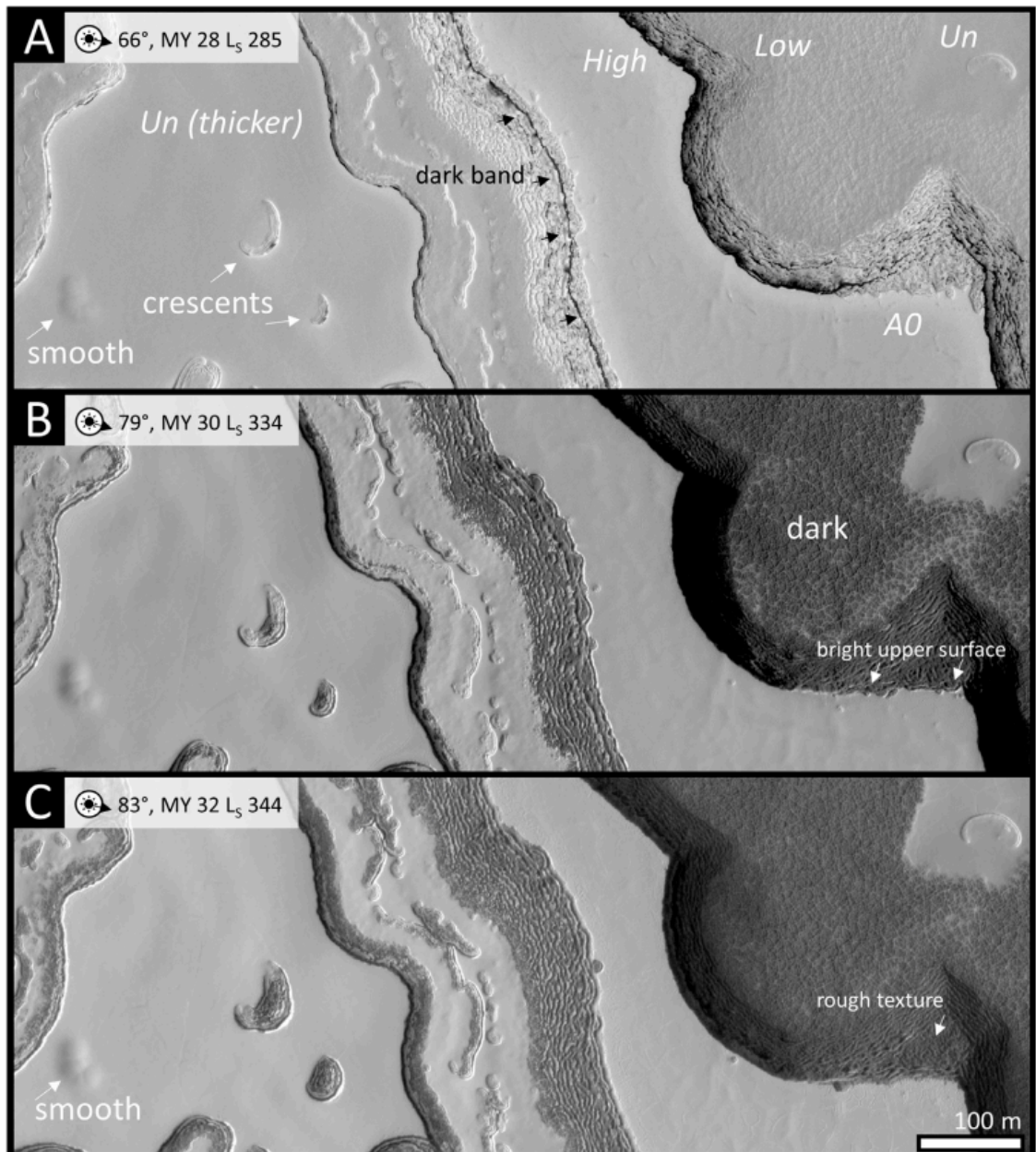
Figure 2.11: Example of fans appearing over time around a unit of A0 morphology. HiRISE images (A) PSP_004686_0930, (B) ESP_023410_0930, (C) ESP_041278_0930. Taken from Buhler et al., (2017)

Next up is A1 type morphology (Figure 2.12). This type of morphology is thought to be the earliest stage of SCT pit formation (Thomas et al., 2009).
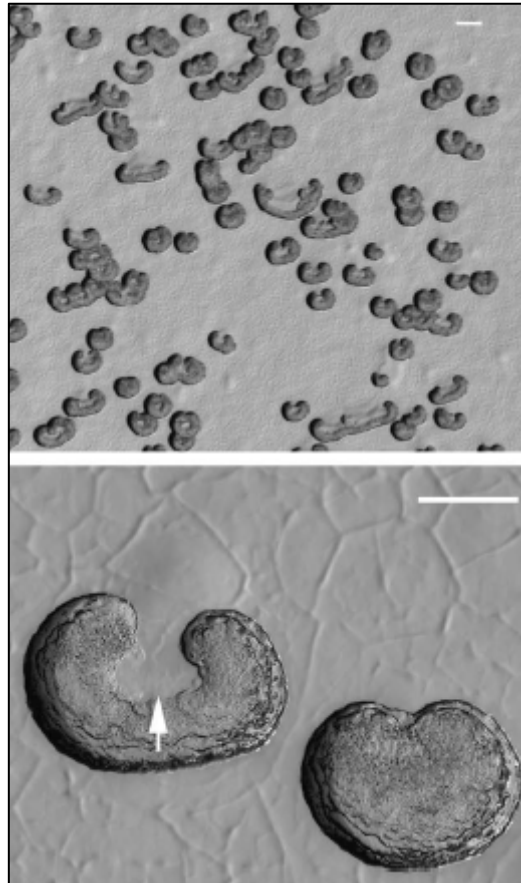
Figure 2.12: SPRC Unit A1 morphology. White scale bar = 1 km. (Thomas et al., 2009)

It's thought that these proto-pit, heart and bean-shaped curls undergo not only sublimation but also cliff collapse, where chunks of ice are calved from the scarps and tumble to the base of the pit (Buhler et al., 2017).

Unit A2 is known as the 'Fingerprint Terrain' (Figure 2.13), essentially a more mature, elongated version of Unit A1 (Thomas et al., 2005).
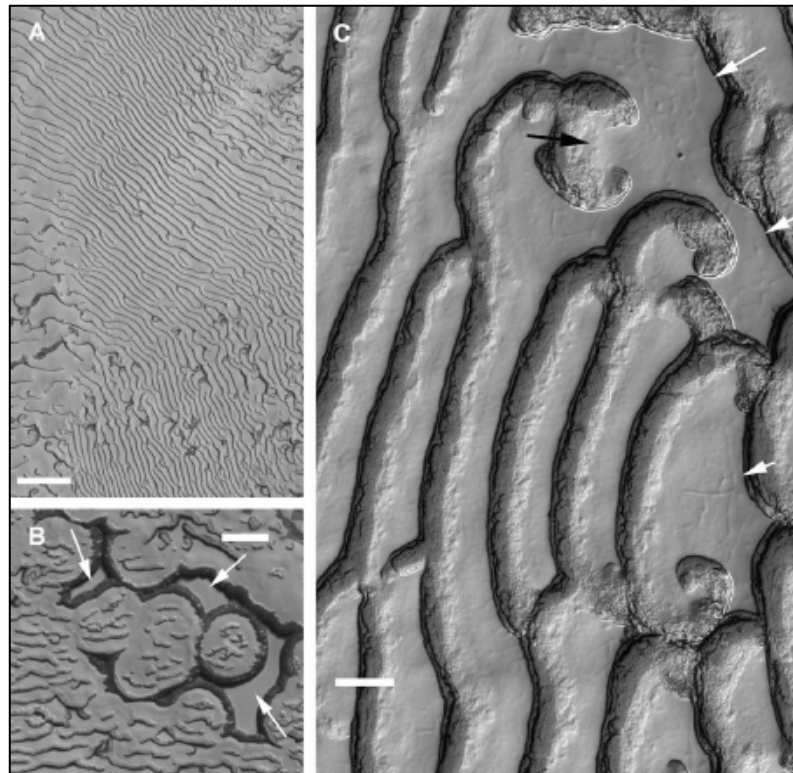
Figure 2.13: SPRC Unit A2 morphology. White scale bar = 1 km. (Thomas et al., 2009)

The vast majority of the cap is covered by Unit B terrain, made up of a series of younger, smoother, thinner (~1 m) layers which overlay eroded areas of unit A (Thomas, 2009). Unit B displays the widest range of morphologies (Figure 2.14) but much of it is made up of almost circular pits that have not yet widened so much that they have eaten away at the mesas leaving thin plateaued regions, as is the case for A0 type morphology.
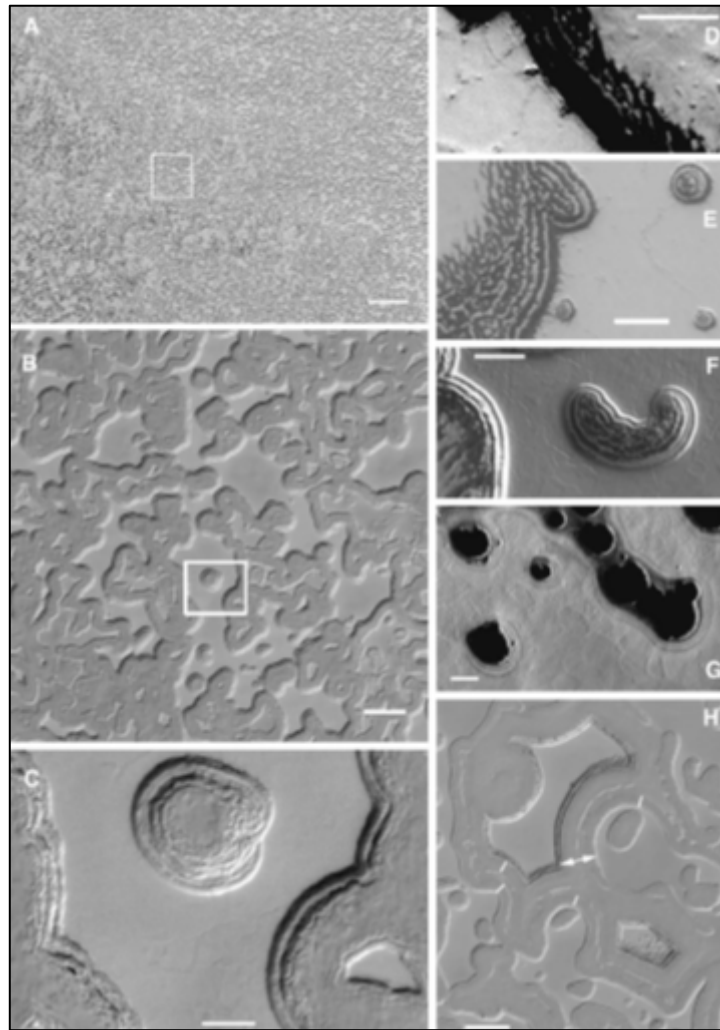
Figure 2.14: SPRC Unit B morphology. (Thomas et al., 2009)

The characteristics of the different SPRC morphologies are summarised in Table 2.1 (Thomas et al., 2005 and 2009). The distribution of these units is shown in Figure 2.15, copied from Thomas et al.'s 2009 paper.

Table 2.1: Attributes of SPRC Terrain Units (based on Thomas et al.,

(2005,2009)

Unit	Features
A0	Quasi-circular depressions >500 m diameter <1% of surface ~10-14 m thick
A1	Curl or heart-shaped depressions ~200 m diameter
A2	'Fingerprint' terrain: elongate, asymmetric depressions. Merges into unit A1 60-120 m across
B	Wide range of surface morphologies, but mostly circular depression features ranging from 10s to 100s of metres diameter. ~1 m thick layers overlying Unit A terrain
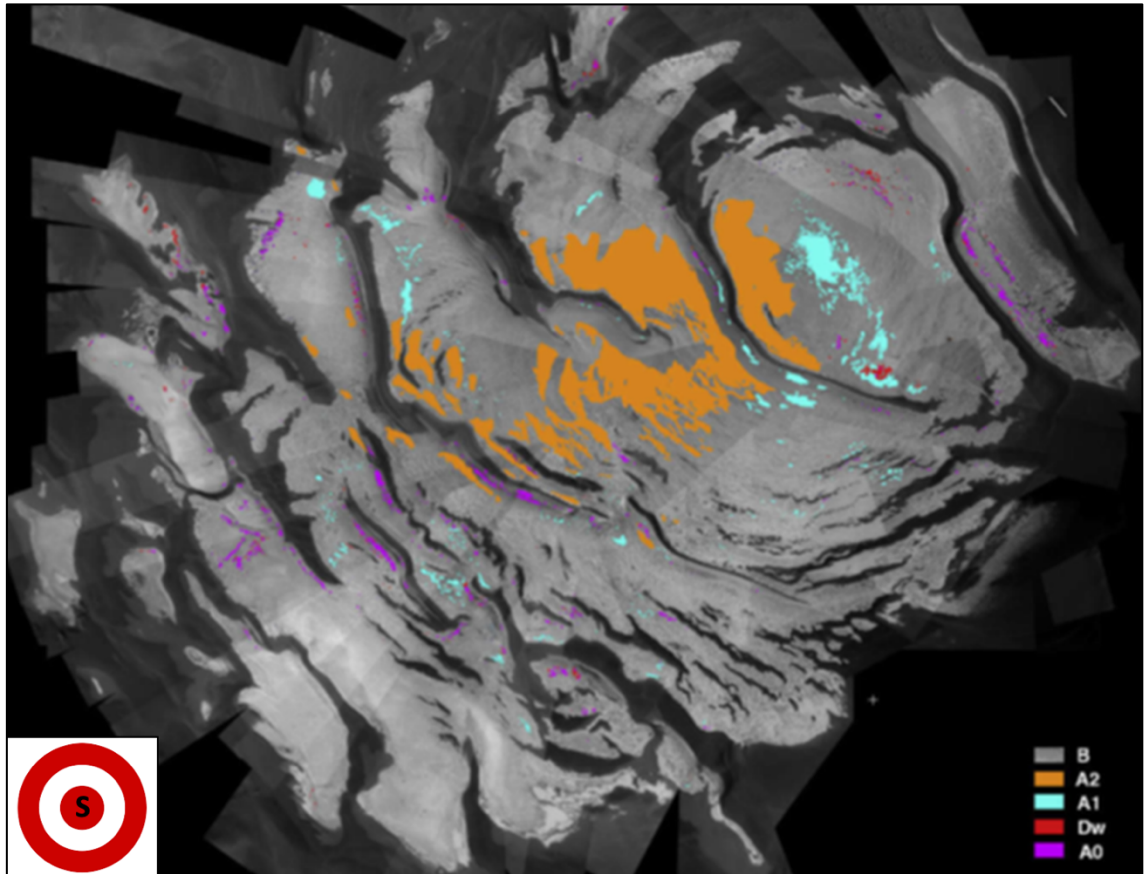
Figure 2.15: Distribution of SPRC terrain units (Thomas et al., 2009). 'S' target marks position of the South Pole

We can see that the various morphology types are constrained to certain areas of the cap, and the reasons for this are still unclear. While SCT has not been observed over long periods due the lack of high resolution imagery available over the cap for more than 2 decades, models by Byrne (2003) show that, at current rates, the metres thick top layer of CO_2 ice would have completely sublimated away within a century or two, and so it is thought that the CO_2 ice layer must be continually redistributed around the cap where the whole process starts all over again. The 'life cycle' of SCT is shown below in Figure 2.16 using HiRISE imagery examples.
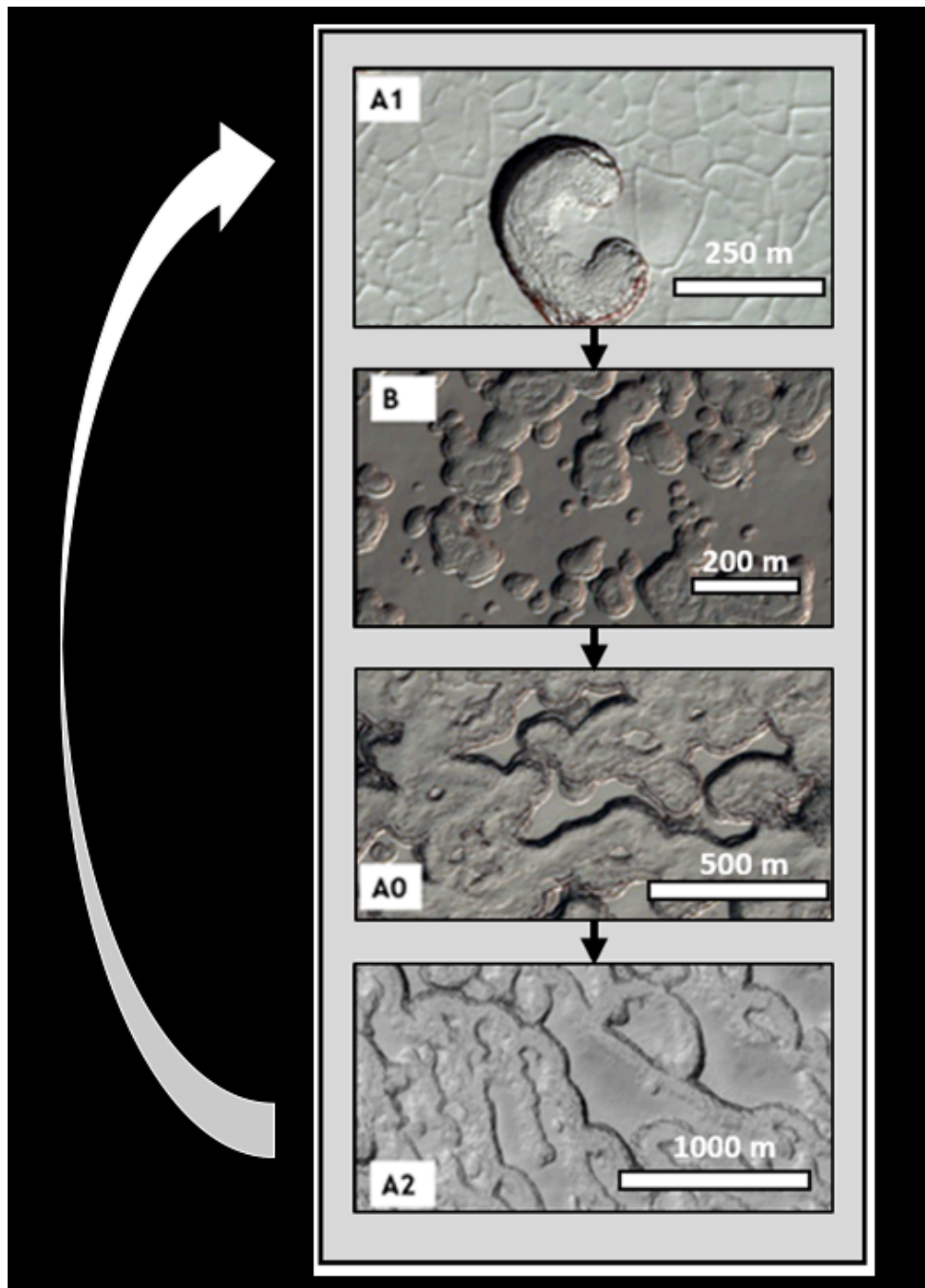
Figure 2.16: 'Life Cycle' of SCT through types of morphology A1, B, A0 to A2.

Made using HiRISE imagery ESP_014141_0930, ESP_012271_0940,

ESP_014380_0945 and , PSP_005386_0930 (top to bottom)

It is posited that the surface begins to crack, then insolation triggers sublimation

and cliff collapse which starts to form irregular bean and heart-shaped pits (A1),

which eventually become wider and close to circular (B) and then erode the mesas away through sublimation (A0) until eventually the mesas dwindle and elongate (A2) until almost smooth, then begin to crack, and the process repeats (Thomas et al., 2009; Byrne, 2003).

While there is some evidence of vertical erosion or 'down-wasting', into the depression floors (Thomas et al., 2005) the majority of erosion occurs through scarp retreat of depression walls (Byrne et al., 2009) or block fall (Buhler et al., 2017). The depression features within the lower, older unit exhibit a scarp retreat rate of ~3 m/MY, while the younger layers show scarp retreat rates of 2.2 m/MY (Thomas et al., 2009).

The surface layer of the SPRC predominantly registers as CO_2 ice when analysed using either THEMIS (Thermal Emission Imaging System) multispectral imager or the OMEGA spectrometer, with depressions and SPRC edges exposing a small amount of water ice beneath (Bibring et al., 2004a; Titus et al., 2003). The strongest signatures for water ice originate from around the margins of the SPRC (Titus et al., 2006). It is the retreating walls of depression features, and fans on the floors of these depressions, containing dark materials that are the principal study sites in Chapters 4 and 6 where we look for dust previously entrained within ice. Regions of flat, high albedo ice on mesas and featureless terrain are also examined for contrast to establish the impact of dusty rims on spectra obtained using the CRISM instrument.

Next we will look at the equatorial RSL features that will be discussed later in Chapter 7.

2.4. Valles Marineris

The second region examined for evidence of PAHs will be around the margins of Valles Marineris, a huge canyon system near the equator of Mars. It was first observed by the Mariner 9 orbiter in 1972 (Sagan and Fox, 1975). It is over 4,000 km long and up to 7 km deep and is many times larger than the Grand Canyon on Earth. Its scale can be seen in the Viking Orbiter Mosaic shown below in Figure 2.17.
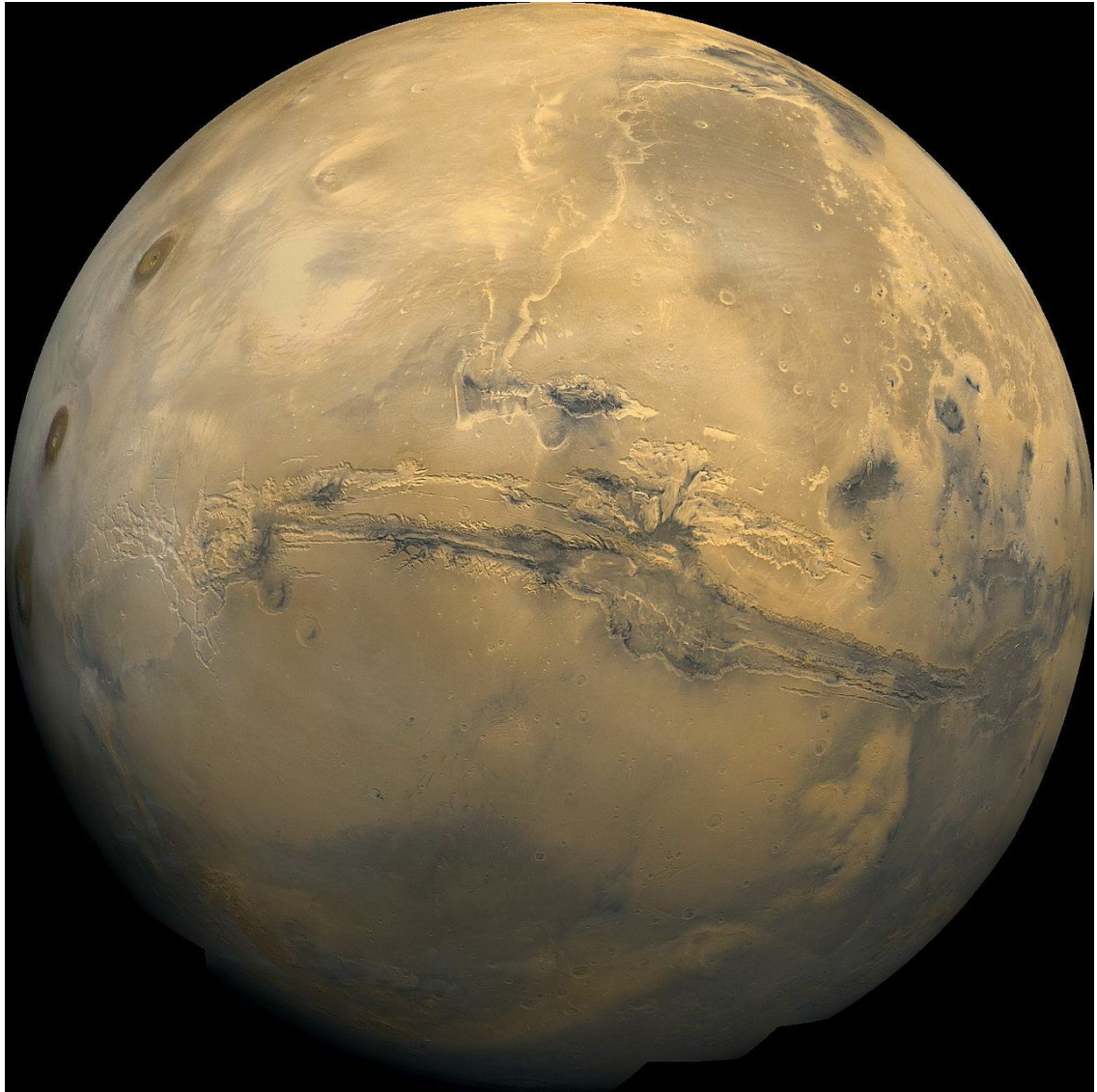
Figure 2.17: Viking 1 Orbiter global mosaic of Mars showing Valles Marineris

(MG07S078-334SP)

It's thought that the rift may have formed alongside the formation of the Tharsis

Bulge, a region to the north west of Valles Marineris that experienced extended

periods of volcanism in early Mars history and is the home to several massive

volcanoes including the tallest known in the solar system, Olympus Mons (~22

km high) which is also used in the processing of CRISM imagery (see Section

3.3). The key point is that Valles Marineris is home to many slopes that exhibit RSL activity, which we will discuss next.

2.4.1. Recurring Slope Lineae

Recurring Slope Lineae (RSL) are narrow (0.5-5 m) surface features that look like dark streaks on downward sloping surfaces of 25-40 ° that extend and darken during spring and summer in warmer temperatures of 250-300 K (McEwen et al., 2011) and then fade and shorten in autumn and winter, re-occurring each year (Stillman et al., 2016). They have been observed in various southern mid-latitudes and equatorial regions and are present all around the margins of Valles Marineris (Stillman et al., 2017). Figure 2.18 shows the global distribution of RSL sites (ibid). The sites are colour coded according to those that meet one, two or three of the criteria for RSL activity; incremental lengthening, recurring and fading.
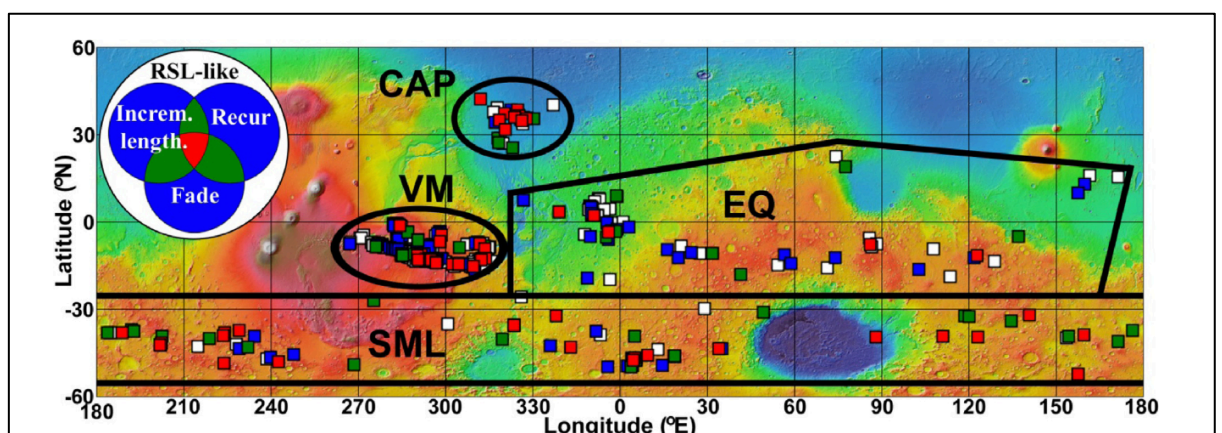
Figure 2.18: Global distribution of RSL sites, grouped into 4 main regions (black lines) over MOLA 463 m colourised elevation map (Stillman et al., 2017).

71

It's clear that Valles Marineris is home to a large number of RSLs, and Figure 2.19 shows RSL distribution in more detail around the region.
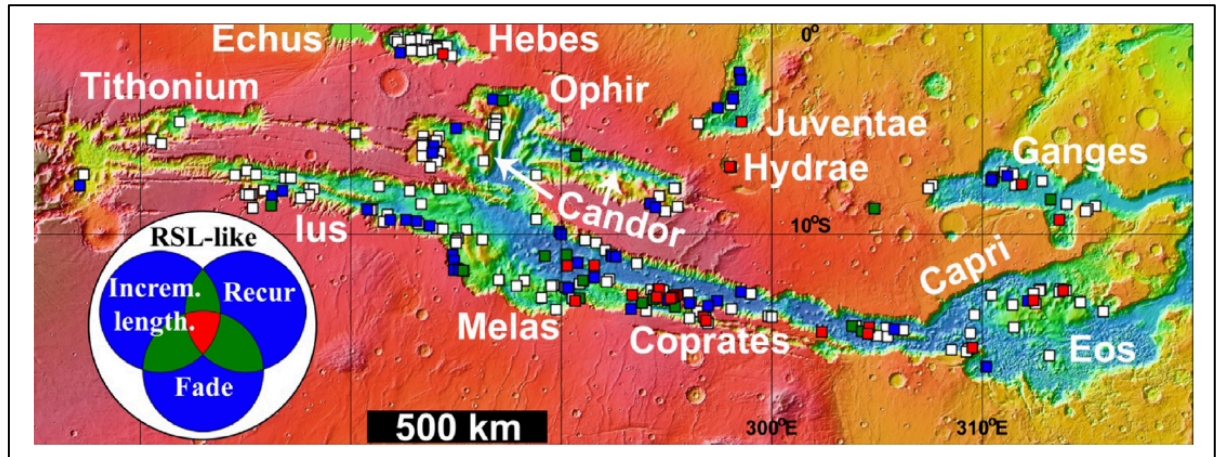
Figure 2.19: Distribution of RSL around Valles Marineris over MOLA 463 m elevation map (Stillman et al., 2017)

RSLs in Valles Marineris typically have a 'spur and gulley' configuration (McEwen et al., 2014) and appear to start from a region of bedrock and then extend downhill across the adjacent sandy floor (Figure 2.20).
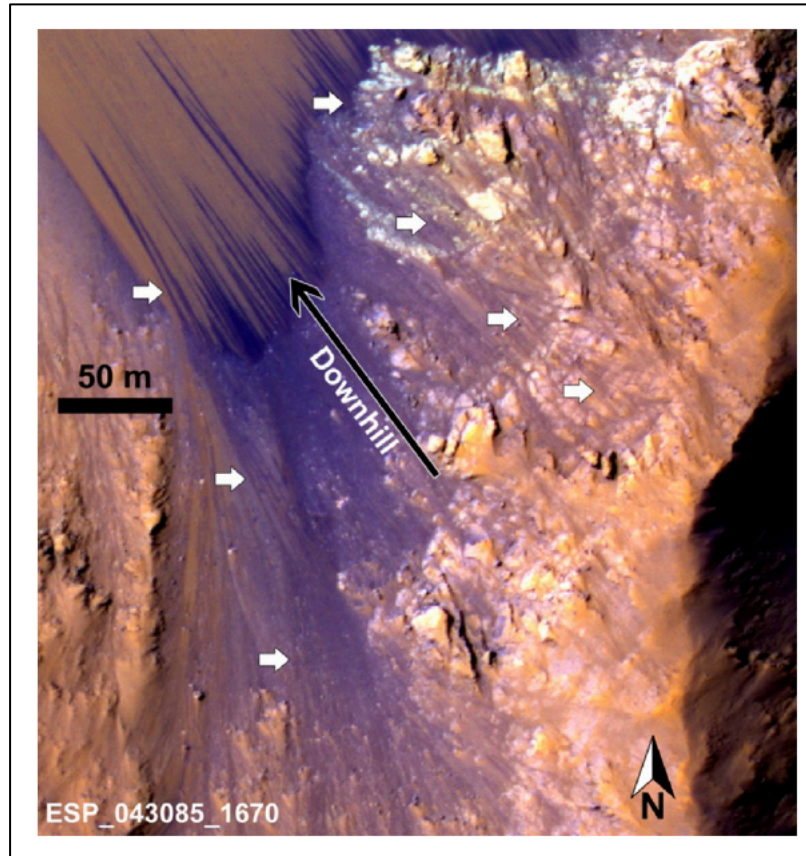
Figure 2.20: Typical spur and gully RSL feature (HiRISE image

ESP_043085_1670; Stillman et al., 2017)

Figure 2.21 shows a time series of images capturing the seasonal changes in RSL.
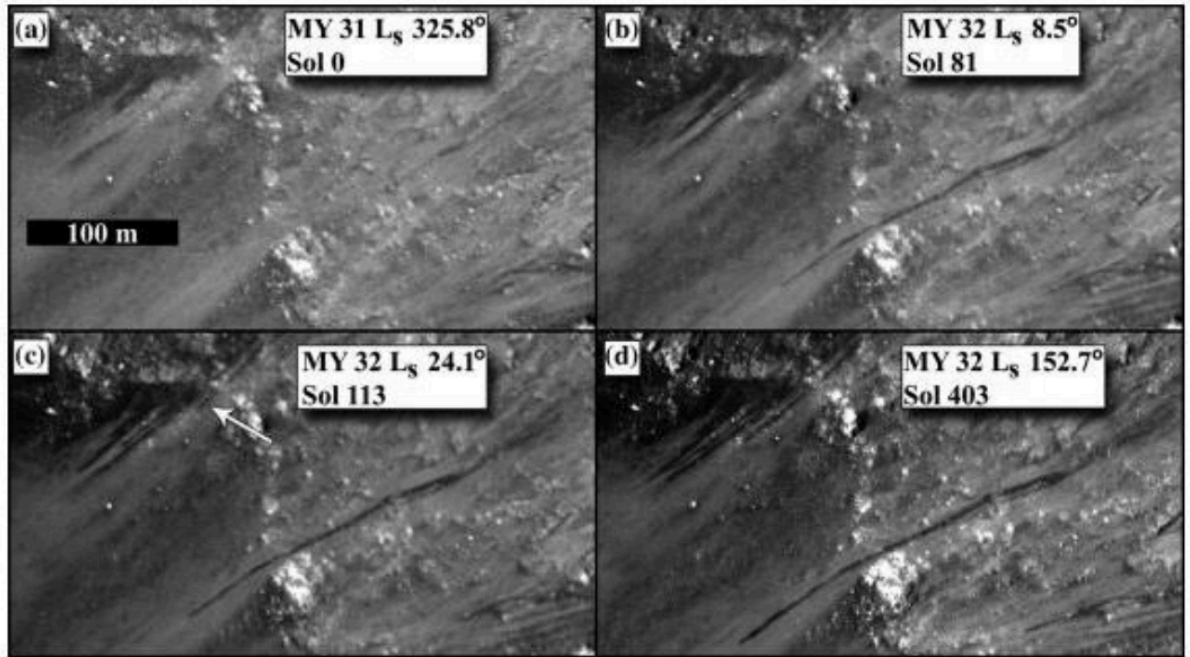
Figure 2.21: Rauna Crater RSL feature showing appearance and lengthening of streaks over the course of Mars Year 32 (Stillman et al., 2016)

The transient nature of these features suggests some dynamic process that could be caused by volatiles, and a 2015 paper by Ojha et al. posited that briny water was responsible for RSL activity.

Modelling by Chevrier and Rivera-Valentin (2012) showed that the presence of various salts could be enough to keep water in its liquid phase at typical Martian surface pressures and temperatures. While liquid water itself has not been identified using either CRISM or OMEGA infrared spectrometers nor Odyssey neutron spectrometer (Ojha et al., 2015; Wilson et al., 2018), work has been done to find the spectral features of the hydration and dehydration of salts including magnesium chloride ($MgCl_2$), which has been detected by THEMIS at a range of

RSL locations (Massé et al., 2014) and was shown to have unique features at 1.45 μm, 1.95 μm, 2.5 μm and 3 μm (Figure 2.22).
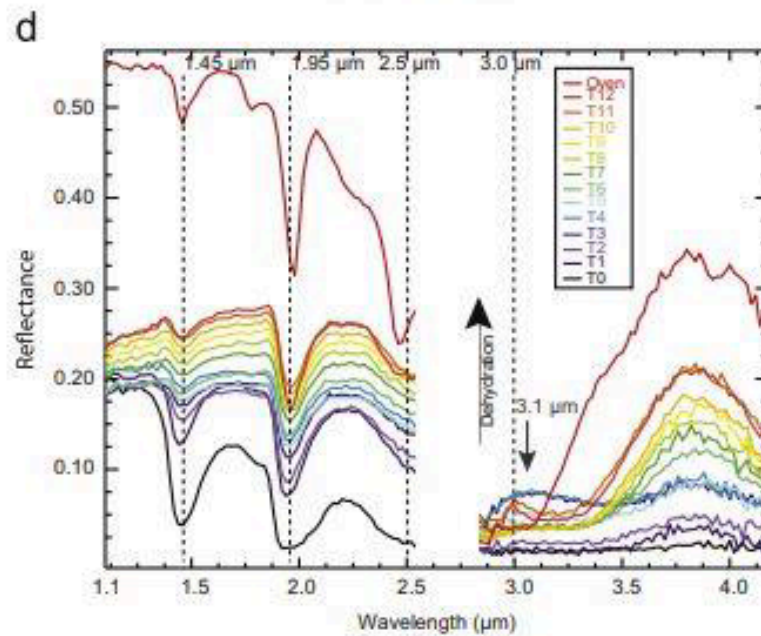
Figure 2.22: Spectral features of magnesium Chloride (MgCl₂) brines undergoing dehydration (Massé et al., 2014). Spectra move upwards in reflectance as the samples dehydrate (black arrow)

Analysis of densely packed RSL features at Palikir Crater by Ojha et al., (2015), showed these tell-tale features at ~1.45, 1.9 and 3 μm during summer and indicate a mix of Martian regolith with magnesium chloride and perchlorate salts (Figure 2.23).
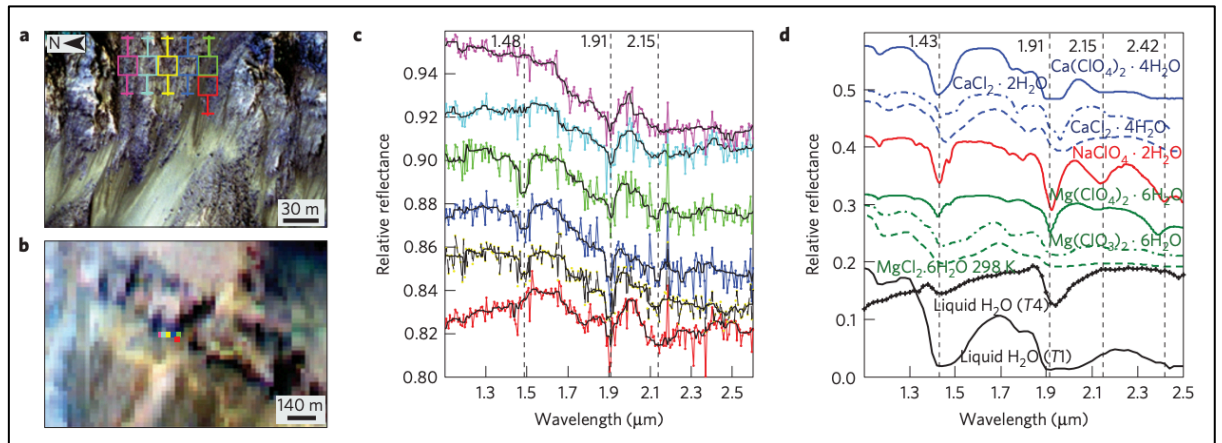
Figure 2.23: Locations of RSL features at Palikir Crater (HiRISE, top left, CRISM, bottom left). CRISM spectra of RSL regions (centre) and laboratory salt spectra (right). Taken from Ojha et al., (2015).

Despite these findings, it is not conclusive that RSLs are created by any known wet process, and there is still much contention regarding their origin. Dundas et al., (2017) argue that RSL are formed through a dry process of granular flow, and that their darkening and lengthening is caused by grain-sorting. This, however, does not explain their seasonal nature nor their contemporaneous and very similar characteristics in neighbouring sites, which could be explained by ambient temperature changes if it is indeed a wet process. However, numerical models published by Schmidt et al., (2017), argue that seasonal changes in temperature can cause rarefied (low-density) gas to flow through the Martian soil and trigger RSL activity. Even if RSL are the result of a wet process, it is unclear what the source of water may be; in the case of Valles Marineris it could be from groundwater seeps as these RSL occur near rock/regolith boundaries (Levy, 2012; McEwen et al., 2014) but some other RSL occur in permeable sand environments and it is proposed that these could be triggered by the absorption

of water from the atmosphere by hygroscopic (moisture absorbing) salts (McEwen et al., 2015). When the laboratory experiments described in Chapter 5 were devised, the more recent work on dry-hypotheses was not published, and a wet-process explanation was more favoured at that time; if I were to start this research again now, I may choose to do things differently, but such is the nature of scientific research. All hope is not lost though, as RSL are still dynamic features and thermal creep causing upwelling of gas from the subsurface is still of interest to this study. There is also recent research indicating that RSLs may in fact be a combination of wet and dry processes, being formed by a brine-triggered granular flow (Wang et al., 2019). It is also possible that RSLs in different regions are caused by different mechanisms, which may explain why some RSL meet all three of Stillman et al.'s (2017) criteria, and others only one or two. The debate continues, and the RSL portion of this thesis will work on the assumption that brines are a possible cause of dynamic RSL features and are worth investigating for signs of PAHs. RSLs are worth investigation as any sign of liquid water, or upwelling or movement of material from the subsurface even if dry, could be extremely important to the search for life.

I have attempted to address some of the questions posed at the start of the chapter regarding whether PAHs are important to the search for extra-terrestrial life, whether they should exist/have existed on Mars but have not yet been detected, whether it is possible to detect them on planetary bodies and whether dynamic features on the SPRC and RSLs are worthwhile candidate sites within which to search for PAHs.

To answer the rest of the questions, original work is required, and the next section will outline the tools and processes employed to undertake this research.

3. Data and Tools

In order to study the dynamic phenomena described in Section 2.3, and search for organics on Mars, a variety of orbital cameras, laboratory instruments, and software packages are used. In this chapter, the data and tools used to carry out the research are described in detail. Much of the identification of imagery and mapping for figures was done using JMARS[3] which has been used to identify intersecting scenes from multiple instruments and datasets (Christensen et al., 2009).

The spectra obtained through laboratory experiments will be archived using the Solid Spectroscopy Hosting Architecture of Databases and Expertise (SSHADE)[4] upon publication of the associated papers. The orbital imagery from CRISM, HRSC, CTX and HiRISE was obtained through the NASA Planetary Data System (PDS) Geosciences Node[5]

3.1. Mars remote sensing instruments

This section outlines the specifications of the various remote sensing and laboratory instruments used in this study. It is worthwhile to note that whilst not used for any scientific analysis, many figures in this work use the Mars Orbital Laser Altimeter (MOLA) 463 m/pixel Global map (Smith et al., 2001;

---

[3] https://jmars.asu.edu
[4] https://www.sshade.eu/db/ghosst
[5] http://pds-geosciences.wustl.edu

Neumann et al., 2001) and occasionally the Mars Orbital Camera (MOC) 230 m/pixel global mosaic (Malin and Edgett, 2001). As they are not used for analysis, they are not mentioned in the following instrument description subsections.

3.1.1. Mars Express High Resolution Stereo Camera (HRSC)

The High Resolution Stereo Camera (HRSC) is a camera on board the European Space Agency's (ESA's) Mars Express, which was launched in July 2002 and arrived at Mars in December 2003 (Jaumann et al., 2007). HRSC is a multi-view push broom sensor composed of 9 lines of charge-coupled device (CCD) line sensors, which enable simultaneous high-resolution stereo, multicolour, and multi-phase imaging (Neukum and Jaumann, 2004). HRSC can obtain images with a spatial resolution of ~10 m/pixel at its nominal periapsis altitude of 250 km. HRSC acquires imagery from 9 viewing angles from which stereo photogrammetric retrieval of surface Digital Terrain Models (DTMs; see section 3.1.3 for more information on these) can be made (Jaumann et al., 2007). As of 2019, HRSC has ~79.1% <20 m/pixel resolution global surface coverage (Gwinner, 2016 and 2019).

3.1.2. MRO Context Camera (CTX)

NASA's Mars Reconnaissance Orbiter (MRO) mission was launched from Cape Canaveral, Florida on 12th August 2005, and arrived at its final Mars Orbit insertion on the 10th March 2006 (Zurek and Smrekar, 2007). The

Context Camera (CTX) is part of the payload of MRO. From an altitude of 400 km, CTX attains image with ~6 m/pixel resolution (Malin et al., 2007), and has 100% global coverage, with many regions having repeat coverage (Dickson et al., 2018; Sidiropoulos and Muller, 2015); in particular, the poles, due to the sun-synchronous orbit of MRO (Johnston et al., 2005). CTX is designed to obtain coarser resolution context images to compliment the finer resolution HiRISE camera, also on-board MRO.

3.1.3. MRO HiRISE Camera

The High Resolution Imaging Science Experiment (HiRISE), mentioned in the previous section, is also on-board MRO and provides very detailed ~25-30 cm/pixel spatial resolution imagery (McEwen et al., 2007). HiRISE has much more restricted global coverage as a result of its finer resolution and smaller swath-width, with around 2.4% global coverage as of 2016 (UoA, 2016). However, as a result of targeted observations on regions of interest, and MRO's polar orbital track, there is good coverage of dynamic surface features including the poles and Valles Marineris. Figure 3.1 shows the mapped repeat coverage at <20 m/pixel of polar regions and targeted surface features.

HiRISE can also be used to create Digital Terrain Models (DTMs; Tao et al., 2018; Putri et al., 2019), 3D representations made by correlating two HiRISE images taken from slightly different angles, to allow a height value to be assigned to each pixel. Height values are shown relative to a baseline elevation (datum) called the Areoid, the Martian equivalent of the Geoid (Burke

et al., 2012). HIRISE DTMs can then be displayed using Geographical Information System (GIS) software (in this case, ArcGis[6]). The spatial resolution of the original 25 cm/pixel is reduced for the DTMs used in this study to ~1 m/pixel. The DTM used later in Section 6.3 was produced by Putri and Yu (private communication).
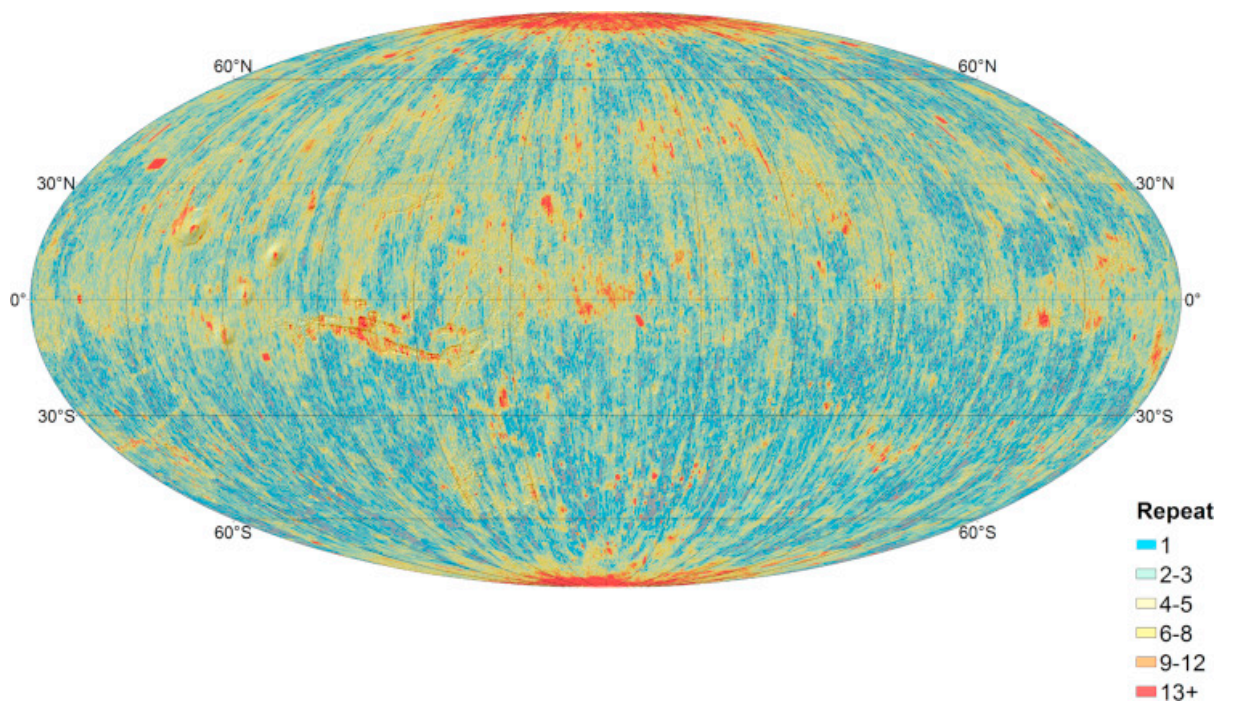
Figure 3.1: Overall repeat coverage of Mars with resolution finer than 20 m/pixel (from Sidiropoulos and Muller, 2016).

---

[6] https://www.arcgis.com

3.1.4. MRO CRISM

MRO's mission objective is to study the history of water on Mars and, among other instruments including HiRISE and CTX, carries on board the Compact Reconnaissance Imaging Spectrometer for Mars, known as CRISM (Figure 3.2).
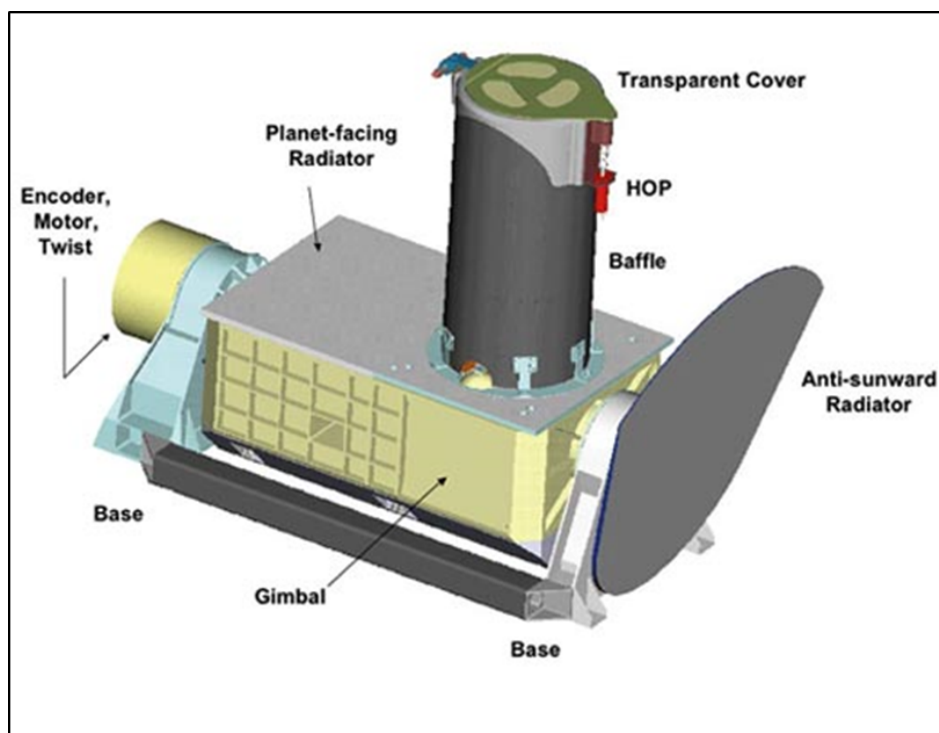
Figure 3.2: The CRISM instrument 2005 (NASA MRO Website)

CRISM is a visible to infrared hyperspectral imager, capable of producing visible and infrared spectral measurements of Mars. CRISM's three main objectives are:

1. To characterise crustal mineralogy with data collected at 72 wavelengths and examine key mineralogical features at a spatial resolution of 100-200 m/pixel

2. To map key areas of mineralogical interest using targeted mode, (<1% surface coverage) at a spatial resolution of ~20 m/pixel, and spectral range of 362-3920 nm for 545 channels at 6.55 nm/channel

3. To measure seasonal and spatial atmospheric variations

(Murchie et al., 2007).

It is objective No. 2 that is of most interest to this investigation, as the narrower spectral channels are required to be sensitive enough to pick out subtle spectral features, along with the higher spatial resolution needed to resolve the small scale SCT depression rim and RSL surface streak features.

The CRISM instrument is not designed with the identification of organics as a primary objective. However, the large number of channels means the instrument has a high sensitivity to carbonates (ibid), which can be used to identify low abundances of carbon rich material and the ability to discern various mineralogies.

In a paper on utilising CRISM data, Pelkey et al., (2007) and in the follow up by Viviano-Beck et al., (2014) spectral 'summary products' are devised by using 'band math', where different bands are combined mathematically to develop a new band that is then indicative of a particular substance; this new band can then be used as a targeting tool to identify areas of mineralogical

interest for further analysis (Pelkey et al., 2007). The product most useful for the identification of carbon-rich material, (BDCARB, indicative of carbonate overtones, giving the strongest response where it detects the vibrational spectrum of a carbonate molecule transitioning from a ground to an excited state (Gaffey, 1986) is shown in Table 3.1 with an example of the band-math employed. The use of summary products is described in more detail in Section 3.4.

Table 3.1: Spectral Summary Product for Identification of Carbonate-rich Materials (Pelkey et al., 2007)

Name	Parameter	Formulation[b]	Rationale
BDCARB	2.33 & 2.53 μm band depth	$1 - (\text{sqrt } [(R2330/(a*R2230 + b*R2390)) *(R2530/(c*R2390 + d*R2600))])$	carbonate overtones

For the purposes of this research, the images with the highest spatial resolution are required in order to resolve small scale features of SCT and RSLs; therefore, images obtained using Full Resolution Targeted (FRT) mode are used, with ~20 m/pixel spatial resolution at 300 km altitude with a swath width of 9.4-11.9 km (Murchie et al., 2007). It should be noted that masks at the edge of transitions between different detector types for CRISM result in small portions of missing or meaningless data, and these are replaced with a missing data value of 65535 (ibid). This must be accounted for in later data analysis as the image 'despike' function in the CRISM Analysis Tool (CAT) for ENVI does not remove these anomalous spikes as it should (Morgan et al., 2009) and this is discussed further in Section 3.3.

In terms of the reliability of CRISM data, IR calibration readings are taken several times a day, with a closed shutter, and thermal background measurements accounted for by extrapolating for zero exposure using a step function, with the results used to remove any bias from the data (Murchie et al., 2007). This seems to have been quite successful, with comparisons to synthetic data showing a maximum wavelength shift of 1.10 nm in IR CRISM data, (Ceamanos et al., 2010) which is negligible in terms of the µm scale spectral measurements discussed in this work. The CRISM instrument, (like all space instrumentation) is protected from the thermal effects of the sun and spacecraft eclipse by using cryogenic systems. However, it is gradually getting warmer, increasing the noise in acquired imagery (Murchie et al., 2007; Seelos, 2017) leading to the decision to used imagery from 2007 in the first analysis from Chapter 4; later imagery is used in Chapter 6 as a time series was needed and this problem doesn't really affect the imaging mode used in this research (see section 3.3). The spectral range and resolution parameters of CRISM were taken into account when choosing what instruments and facility should be used to generate laboratory spectra.

3.2. Spectro-goniometer radiometers and CarboN-IR Environmental Cell

The Cold Surfaces Spectroscopy Facility at the Institut de Planetologie et d'Astrophysique de Grenoble (IPAG) has instrumentation for in-situ formation of ices, and cold rooms capable of keeping ambient room temperature down to -40 °C. This allows for stable thermal conditions during preparation of

materials for experiments. These samples are subsequently analysed in the Carbon-IR environmental cell, which can maintain very low temperatures and pressures, using a spectro-goniometer radiometer to record reflectance spectra in visible and near-mid infrared wavelengths.

3.2.1. SHINE Spectro-goniometer radiometer

The SpectropHotometer with variable INcidence and Emergence (SHINE) spectro-goniometer radiometer was developed at IPAG, and is designed to measure bidirectional reflectance and polarisation distribution functions of planetary-type material. These measurements enable the production of accurate models to help describe surface composition, roughness and texture (Brissaud et al., 2004). In particular, the spectro-goniometer radiometer is able to use spectral bidirectional reflectance and polarization functions to characterise the light scattering properties of snows of various grain-size, and the compactness and surface roughness of materials at different stages of metamorphism. The instrument is able to acquire spectral radiance measurements from 310-4800 nm, with a spectral resolution of between 6-48 nm, dependent on wavelength (ibid), making it ideal for emulating CRISM's FRT acquisition mode. The instrument schematic is shown below in Figure 3.3.
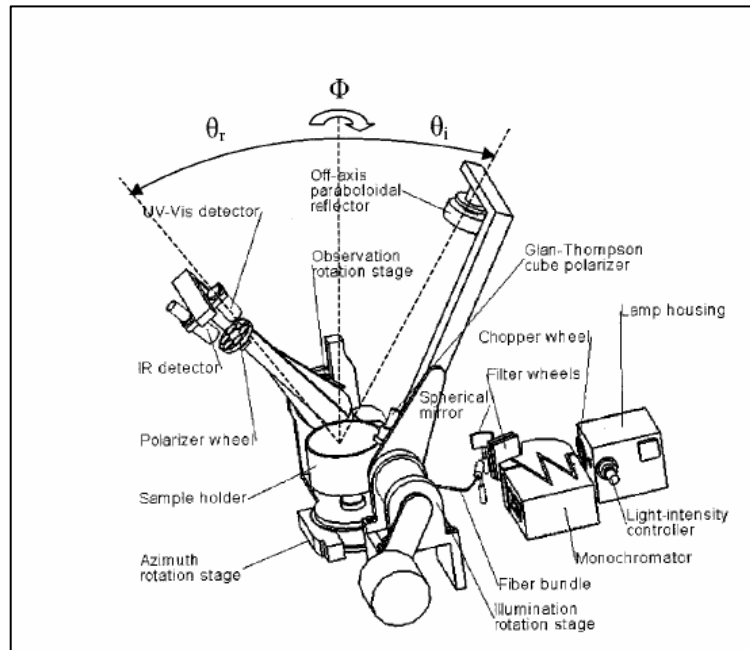
Figure 3.3: Schematic view of spectro-goniometer radiometer (taken from

Brissaud et al., 2004)

The characteristics of the instrument are summarised in Table 3.2.

Table 3.2: Instrument Characteristics for Spectro-Goniometer Radiometer

(Brissaud et al., 2004)

Characteristics	Quantities
Spectral characteristics	
Range unpolarized	310–4800 nm (measurable signal)
	380–3900 nm (S/N > 100 in 1 s)
Polarized illumination	320–3000 nm
Polarized observation	320–4800 nm
Resolution	Minimum: <0.1 nm (but S/N limited)
	Maximum: 6 nm (<500 nm), 12 nm (<1000 nm), 24 nm (<2000 nm), 48 nm (>2000 nm)
Wavelength accuracy	0.2–0.6 nm (grating dependent)
Angular characteristics	
Incidence angle (θ_i)	0°–90°
	Resolution: 0.1°
	Maximum sampling: 0.1°
Emergence angle (θ_r)	0°–80° (to 83° for dark or fine-grained samples)
	Resolution: $\pm 2°$ (may be reduced to $<\pm 0.5°$, but S/N limited)
	Maximum sampling: 0.1°
Azimuth angle (Φ)	0°–180°
	Resolution: $\pm 2°$ (may be reduced to $<\pm 0.5°$, but S/N limited)
	Maximum sampling: 0.1°
Phase angle (g)	g_{min} to 165°
	$g_{min} = 8°$ for bright or large-grained samples
	$g_{min} = 4.5°$ for dark or fined-grained samples
Reproducibility	0.002°
Illumination characteristics	
Diameter (nadir)	200 mm
Parallelism	<0.1°
Homogeneity	$\pm 1\%$ within 60-mm diameter ($\theta_r < 70°$)
	$\pm 4\%$ within 120-mm diameter ($\theta_r \leq 80°$)
Observation characteristics	
Detectors	Si (300–1200 nm) (room temperature)
	InSb (800–4800 nm) (cooled 80 K)
Diameter (nadir)	20 mm
Field of view	$\pm 2.05°$ (may be reduced to $\leq \pm 0.5°$)
Radiometry	
Absolute accuracy	(see Part 2[17])
	<1%, 400–1000 nm, % Spectralon (fully calibrated)
	<2%, 1000–2500 nm, % Spectralon (partly calibrated)
	<?%, 2500–4800 nm, % sulfur (under calibration)
Relative accuracy	<0.5% (400–2500 nm)
Polarimetry (optional)	
Illumination	Linear polarization: variable 0° to 90°
	Extinction ratio: 10^{-5}
Observation	S and P components
	Extinction ratio: $<10^{-3}$
Samples	
Type	Rocks, minerals, snow or ice, etc. (from bright to dark)
Texture	Compact or granular
Grain size	Micrometer to a few millimeters
Size	Maximum: 300-mm diameter, 250-mm deep (translucent and coarse grained)
	Maximum: 120-mm diameter, 2–10-mm deep (dark or fine-grained samples)
	Minimum: 25 mm × 120 mm ($\theta_r \leq 80°$, all Φ)
	Minimum: 25 mm × 45 mm ($\theta_r \leq 60°$, all Φ)
Temperature	Room temperature or heated
	Down to -35 °C (in cold room)

The spectro-goniometer radiometer is used in conjunction with the CarboN-IR environmental cell (Section 3.2.3) to analyse materials at low temperatures.

3.2.2. SHADOWS Spectro-goniometer radiometer

The SHADOWS (Spectrophotometer with cHanging Angles for the Detection Of Weak Signals; Potin et al., 2018) instrument is similar to the SHINE instrument at IPAG, but is designed for use with materials that do not need to be used in conjunction with the CarboN-IR Environmental Cell and that do not need samples to be kept at extremely cold temperatures or in a vacuum. Therefore, the SHADOWS instrument was used for some of the RSL analogue experiments discussed in Chapter 5. SHADOWS has a spectral range of 350-5000 nm, and can achieve spectral resolution of <1 nm, which is more than sufficient to emulate the parameters of the CRISM instrument.

Figure 3.4 shows a schematic of the SHADOWS instrument, while Table 3.3 outlines its characteristics, both taken from Potin et al., (2018).
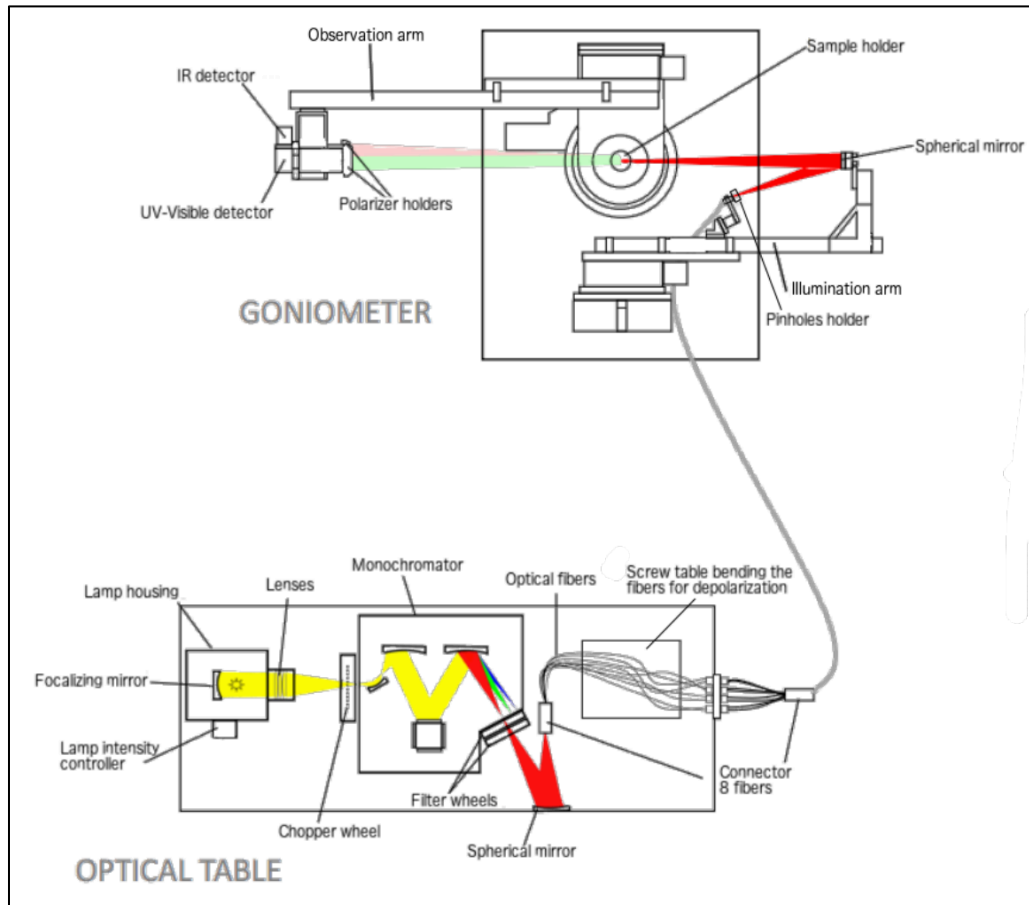
Figure 3.4: Schematic view of the SHADOWS spectro-goniometer

radiometer (taken from Potin et al., 2018)

Table 3.3: Instrument Characteristics for SHADOWS Spectro-Goniometer

Radiometer

Characteristics	Quantities
SPECTRAL RANGE	
Nominal range	400 - 4700 nm
Low SNR ranges (factor of 100 lower)	300 - 400 nm and 4700 - 5000 nm
CO_2 absorption band	between 4200 - 4300 nm
for opposition effect	400 - 1700 nm
LAMP AND LAMP HOUSING	
Intensity stabilizer	0.1% over 24h
Chopper frequency	413 Hz
MONOCHROMATOR	
Input & output slits	Height: 15mm, width: from 4 μm to 2 mm
Gratings	1) 350 - 680 nm, 1200 lines/mm - Max resolution: 6.4 nm
	2) 680 - 1400 nm, 600 lines/mm - Max resolution: 12.8 nm
	3) 1400 - 3600 nm, 300 lines/mm - Max resolution: 25.8 nm
	4) 3600 - 5000 nm, 150 lines/nm - Max resolution: 51.3 nm
Wavelength accuracy	Gratings 1 and 2 : 0.2 nm, Grating 3: 0.4 nm, Grating 4: 0.6 nm
BIDIRECTIONAL REFLECTANCE	
Incidence angle	0° to 75° (60° for bright samples)
	Resolution (solid angle of illumination): ±2.9°
	Minimum sampling: 0.001°
Emergence angle	0° to ±85°
	Resolution: ±2.05° (options: 0.8°, 1.25°, 1.65° but lower SNR)
	Minimum sampling: 0.001°
Azimuth angle	0° to 180°
	Resolution: ±2.05° (options: 0.8°, 1.25°, 1.65° but lower SNR)
	Minimum sampling: 0.001°
Phase angle	5° to 160°
	for bright samples ≈ 8° to 140°.
Illumination spot size on sample	5.2 mm (nadir) (option: 1.7 by 1.2mm or less, but lower SNR)
Observation FOV on sample	diameter 20 mm (nadir)
TRANSMISSION	
Incidence angle	0° to 75°
	Resolution: ±2.9°
Emergence angle	0° to 85° in both H & V planes (direct transmission at 0°)
	Resolution: ±2.05° (options: 0.8°, 1.25°, 1.65° but lower SNR)
	Minimum sampling 0.001°

The absolute reflectance uncertainty of both spectro-goniometer radiometers is about 0.5% at fixed angle after calibration. Inside the cell (Section 3.2.3) with double sapphire windows (which decrease the apparent reflectance of samples) the uncertainty reaches close to 1%. Samples with the lowest

reflectance, such as samples 4 and 5 in Chapter 5 have the highest levels of uncertainty, but at most have an error margin around the thickness of the plot line in the figures presented in this work, so remain very reliable (Brissaud et al., 2004).

3.2.3. CarboN-IR Environmental Cell

The CarboN-IR environmental cell system (Figure 3.5) allows for the study of planetary material samples in stable conditions; the chamber is designed to enable visible and near-IR monitoring throughout the physical evolution of ice samples (Bonnefoy et al., 2000).
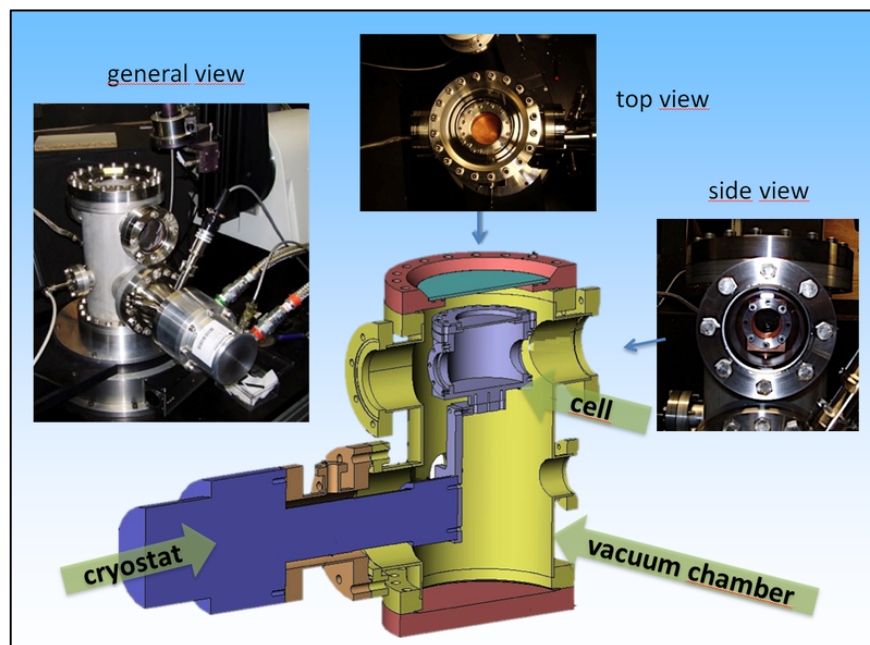
Figure 3.5: Photographs of CarboN-IR system and schematic diagram of interior of vacuum chamber (IPAG)

The cell is made from copper of high thermal conductivity (~400 $Wm^{-1} K^{-1}$ at 200 K) and is able to hold samples 8 cm in diameter and up to 6 cm thick. The covers of the cell and vacuum chamber consist of a transparent corundum window (which offers good transmission, > 80% for 310-4800 nm wavelengths) surrounded by a metal flange, which can be hermetically sealed using screws and a high vacuum, low temperature suitable grease (Apiezon N[7], suitable for -273 – 30 °C) to create an effective volume of Martian-type atmosphere of 312 cm^3 which can be pumped to high vacuum (~$1x10^{-4}$ Pa). The Sumitomo cryostat can be cooled as low as -196 °C (Bonnefoy et al., 2000). In order to prevent condensation and overly rapid ice sublimation, the sapphire window was pre-heated with a hair-dryer and the window sealed by three people at once to expedite the implementation of the vacuum. The arrangement of the spectro-goniometer radiometer and CarboN-IR cell used in conjunction is shown in Figure 3.6.
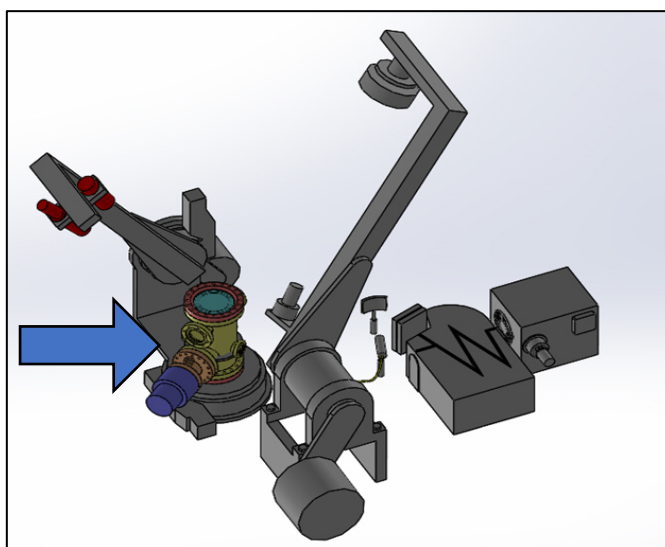
Figure 3.6: Schematic diagram of the spectro-goniometer radiometer and CarboN-IR environmental cell (blue arrow; IPAG)

[7] https://www.apiezon.com/index.php/products/vacuum-greases/n-grease

Using a combination of data from all the above instruments, this study attempts to characterise SPRC and RSL-like environments to establish whether PAHs can indeed be detected on Mars. These methods, tools and instruments will be mentioned again many times throughout the thesis, and where appropriate, a cross-reference will be given to the relevant section in this chapter.

3.3. Data Calibration and Processing

The Harris® ENVI+IDL®[8] image processing software was used for calibration, pre-processing and analysis of the CRISM data, additionally using the CRISM Analysis Tool[9] (CAT) plug-in when required. The image processing pipeline was based on "best practices" guidelines, which were presented at the CRISM Data User's Workshop (Morgan et al., 2009).

More specifically, after ingestion into CAT, Top-of-atmosphere radiances can be converted to bi-directional reflectance factors to minimise the effects of different view and solar angles and levels of solar illumination. This 'photometric correction', (Africano et al., 2005), employs a simple normalisation step, which was done by dividing by the cosine of the incidence angle. Atmospheric correction (McGuire et al., 2009) is then carried out using 'division by scaled volcano', i.e. by dividing the readings from the image being processed by the ratio of the highest altitude point on Mars (the summit of

---

[8] https://www.l3harrisgeospatial.com/Software-Technology/ENVI
[9] http://geo.pds.nasa.gov/missions/mro/crism.htm#Tools

Olympus Mons, ~22 km) and its base, then multiplying by a factor dependent on the altitude and season of image acquisition in order to remove some of the effects of atmospheric gases from surface spectra. However, this doesn't account for local differences in atmospheric conditions, especially related to scattering and absorption (i.e. dust content) at the time of acquisition.

Lastly, destriping and despiking is used to remove residual artefacts from the imagery, as well as anomalous features in the spectra, which are caused by various sources of noise. These include the Poisson noise inherent in the detector counts for the short and long visible and IR sensors (S and L detectors), as well as thermal noise for the L detectors. Due to cryogenic cooler degradation (resulting in detectors reaching temperatures ~15 K hotter than their nominal operating range at the beginning of the mission), thermal noise has worsened for more recent acquisitions. Fortunately, this has had little effect on the CRISM data used for this research, as the highest spatial resolution FRT mode utilised to analyse fine scale features ceased functioning in 2012 due to a gimbal malfunction (Seelos, 2017). Additionally, observation and column-dependent noise caused by calibration errors has resulted in vertical striping in the image and spikes in spectra which are manifested as a result of crossing a sharp surface brightness boundary. This causes detectors to record erroneous spectral information, being biased by the preceding acquisition (Kreisch et al., 2017).

Almost all of these anomalies are accounted for within the CAT_ENVI software. However, CAT does not remove any 'no data' values caused by

masks situated in between detector types in the CRISM instrument (Murchie et al., 2007); therefore, these need to be removed manually in a post-processing step, but this is easy to do as these anomalous data points are several orders of magnitude higher than one would expect and therefore easily recognised, and are unlikely to be confused with genuine spectral features. Once corrections are completed, diagnostic summary products can be generated.

3.4. Spectral Mapping of CRISM Scenes

Summary products (Pelkey et al., 2007; Viviano-Beck et al., 2014) are then input into the next stage of the processing chain, wherein spectral mapping is conducted to identify those pixels with the best spectral responses for the composition of interest, on any given surface feature. Each of these summary products can be stored as one colour channel in a Red/Green/Blue (RGB) composite summary. The employed summary products are:

- BD1435; diagnostic of CO_2 ice
- BD1500; diagnostic of H_2O ice
- ICER2; diagnostic of CO_2/H_2O ice mixtures
- BDCARB; diagnostic of carbonate overtones
- OLINDEX2; diagnostic of the mineral olivine
- LCPINDEX; diagnostic of the mineral low-calcium pyroxene
- HCPINDEX; diagnostic of the mineral high-calcium pyroxene

These summary product bands were chosen in order to highlight ice content, and any regions that may be rich in carbonates or dust with significant spectral differences to the (CO_2 and water) ice signatures which are the two most abundant units on the SPRC. They are not so useful for RSL regions, which appear as uniformly basaltic, and where individual spectral analysis of pixels is more efficacious. As an example of how the RGB composite summary product arrangement may be used, a colour map of BD1435=Red, BD1500=Green, BDCARB=Blue results in the areas with a spectral response indicative of CO_2 ice showing up as red, H_2O ice as green, and carbonate overtones as blue, with mixtures showing up as blends of these colours, and many examples of this particular arrangement can be seen in Chapter 4 (see Figure 4.5). It is important to note that blue colours do not indicate definitive carbonate content, but this method certainly differentiates areas with varying spectral responses (and thus chemical compositions) from each other.

Moreover, in order to permit the visual inspection of the morphological features of each CRISM scene, the original CRISM data have been used to create a second composite image, using RGB bands close to the default (in ENVI) bands, i.e. bands 230 (2509.7 nm), 75 (1486.9 nm) and 10 (1060.3 nm) for red, green and blue channels, respectively.

For the SPRC analysis in Chapter 4, composite RGB images were produced for different regions of interest (ROIs). More specifically, for each CRISM product examined in detail, at least one depression rim and one area of featureless ice was selected for further analysis. Finally, statistics for each ROI

were generated through ENVI, while minimum and maximum values were recorded to compare variation in spectral reflectance across each ROI. A more targeted approach was used in Chapter 6, based on what was learned from the more systematic approach in Chapter 4. As mentioned earlier, summary products were not particularly useful for RSL regions, and so pixel by pixel spectral analyses of original CRISM bands were employed instead.

3.5. Identifying Spectral Signatures

Gaffey (1986) posits that Gaussian decomposition is a useful tool for identifying diagnostic peaks. This process involves using statistical techniques to identify and separate peaks in reflectance. Gaffey (1986) and Cruikshank et al., (2008) expound the benefits of using spectral ratios to accentuate spectral features, i.e. dividing one spectrum by another to remove similarities, with any residual peaks representing unique features. Examination and comparison of archetypal spectra for Martian measurements of ices and other minerals is invaluable in this kind of investigation. Viviano-Beck et al., (2014) have created a library[10] of spectra for Martian mineralogical absorption features which also includes the effects of water and CO_2 ice.

For the SPRC, ROI band thresholds were used to identify the strongest 10% of CO_2 and H_2O ice signatures from each scene, and then ROIs with a minimum of 25 pixels chosen from the same across-track region of the scene as the SCT dark-rim features to provide the local 'purest' ice spectra.

---

[10] https://crismtypespectra.rsl.wustl.edu/

Laboratory, local and library spectra can be used to compare more ambiguous spectra and identify diagnostic features. On the basis of minerals mentioned in (Yung et al., 2010), the Viviano-Beck et al., (2014) spectra for jarosite ($KFe_3^{+3}[OH]_6[SO_4]_2$), magnesium carbonate ($MgCO_3$), magnesium-rich olivine ($[Mg^{+2}, Fe^{+2}]2SiO_4$), high-calcium pyroxene ($Ca_2Si_2O_6$), magnesium rich smectite clays, and talc ($H_2Mg_3[SiO_3]_4$) are of particular interest the SPRC, along with CO_2 and water ice.

To remove the effects of water and CO_2 ice, data from the Viviano-Beck spectral library data for CO_2 and water ice, as well as the local 'purest' spectra, were plotted alongside each site's spectra, and the reflectance spectra were divided by the corresponding wavelength reflectance values for water ice; this water corrected spectrum was then divided by the spectra for CO_2 ice to remove the effects of both types of ice on the data.

Subsequently, the Peak-Fit[11] software was used to carry out Gaussian decomposition to find individual peaks that could be compared to peak-fitted CRISM spectra derived from Viviano-Beck et al., (2014) for CO_2, water ice, and the 6 minerals chosen by Yung et al., (2010). Peak-Fit applies an algorithm designed to smooth out noise and statistically negligible features that could be identified as peaks to the human eye. After denoising, 'numerical fitting', which automatically carries out statistical fitting of the input raw data to the output Gaussian peaks, while additionally generating an R^2 value of reliability, was used. For this study, only fits with R^2 above 0.95 were deemed

---

[11]http://www.sigmaplot.co.uk/products/peakfit/peakfit.php

acceptable. The output of the above process is a graph with a series of peaks that accentuate individual spectral features, examples of which can be seen in Chapter 4 (Figure 4.18).

3.5.1. Endmember Analysis

In strict geological terms, an endmember is a mineral that is at the extreme end of a mineral series in terms of purity. However, in the context of this study, an endmember is a constituent material of a given study area that may make up part of a particular pixel. More specifically, it may be a mineral, a rock type, a blend of organics, or a type of ice. The relatively coarse spatial resolution of CRISM (20 m/pixel) means that it is often difficult to find completely pure pixels of fine-scale features. Therefore, many pixels of interest to this study are most likely to be mixtures of spectra of materials in a scene. This means unmixing of pixels is required to find and identify their constituent endmembers. Unmixing will result in an estimate of the number of different endmembers, their spectral signatures, and the relative abundance of each endmember within a given pixel or region of interest.

3.5.2. Types of Spectral Unmixing

There are two general models for unmixing; linear and non-linear (Keshava et al., 2002). Linear unmixing is useful for looking at features that are too small to be resolved by an instrument because of relatively low spatial resolution and the mixing occurs within the instrument itself (Clark and Roush, 1984). This type of unmixing is useful to differentiate H_2O and CO_2 ice from dusty rim

features within SCT features. Non-linear spectral unmixing is more appropriate where the targeted material is mixed together at an intimate level, and is mixed all together at grain-size scales (Borel and Gerstl, 1994). The non-linear is therefore of more use when looking at the component endmembers of the dust content of SCT rims, and when looking for organic material that may be blended within the dust.

3.5.3. ENVI Linear Spectral Unmixing

The Linear Spectral Unmixing tool in ENVI software is used first to see how many endmembers it can identify, then with the Matched Filtering function, results are compared to spectral libraries for known ices and minerals on Mars to assess the composition of entire scenes as well as regions of interest to this study. It works on the assumption that the reflectance of a pixel is a linear combination of the reflectance of each constituent material, which is derived from spectral libraries to eke out each individual spectrum based on how well it matches the library spectra. In addition, the Sequential Maximum Angle Convex Cone (SMACC) tool[12] is used, which does not require any spectral library input and automatically discerns discrete endmember components using residual minimisation. Essentially, it finds the brightest pixel in a given scene, then finds the pixel that is the most spectrally different; it then finds a third pixel most different from the first two. This process is then repeated until the SMACC tool finds a pixel that is already included in the first two groups of

---

[12] https://www.harrisgeospatial.com/docs/SMACC.html

pixels (brightest and most different from the brightest) or until it has reached the specified number of unique endmembers.

3.5.4. N-FINDR Endmember Extraction

The N-FINDR algorithm was developed by Winter (1999) and has been through many updates and adaptations over the years by various people, including R. Song at UCL MSSL (private communication), who has applied the method to CRISM imagery at my behest in order to compare the result to the ENVI spectral unmixing. It works by randomly selecting a set of pixels from a scene as initial endmembers and then comparing it to others until it finds a pixel with a purer signature than any other combination of pixels in any given group, and then replaces the endmember pixel with this new purest pixel. The process repeats until all pixels have been evaluated and all unique endmembers identified and relative abundances for each pixel can then be calculated. (Ibid). The results of the applications of these methods can be seen in Chapters 6 and 7, and a more generalised workflow for the processing and analysis of CRISM data can be found in Appendix A. The next chapter describes an initial analysis of five regions of the SPRC in a preliminary assessment of dust-rich rim features, and was done prior to (and in fact led to) the laboratory analogue experiments that will then be described in Chapter 5.

4. First Analysis of 5 SCT Pit Features from 2007-2012

Having established in Section 2.3.2 that SPRC features may expose dust previously shielded ice, the next step was to carry out a small-scale study of suitable candidate features on the SPRC, and examine in detail the dust on the rims of pit features. This chapter details the first analysis of compositional mapping of SCT features within 5 CRISM scenes, and the attempt to detect PAH signatures based on the prominent spectral feature at 3.29 µm. The work from this chapter was adapted into paper that was published in a peer-reviewed journal (Campbell et al., 2018).

4.1. Selecting Regions of Interest

Having decided that the CRISM instrument will be used to analyse areas of the SPRC due to its high spatial resolution capabilities (20 m/pixel) compared with the OMEGA spectrometer on Mars Express (<300 m/pixel; Bibring et al., 2004b), the next step was to select CRISM scenes for investigation.

4.1.1. ROI initial selection

A discussed 3.1.4, only Full Resolution Targeted (FRT) products (~20 m/pixel) were utilised, to see the most detail possible for thin rim features, as FRT provides the highest spatial resolution. Using the JMARS software (Christensen et al., 2009) the field of view was constrained to the area covering the Martian SPRC (Southern Latitudes >75° and centred at 83.9°S, 160.0°E),

and all FRT footprints (image outlines) within this region were displayed onto a map of hill-shaded topography derived from MOLA (Smith et al., 2001) . A total of 1,703 FRT products ranging from acquisition years 2007-2012 are included in this area.

Due to inconsistent nomenclature and subcategories of sublimation features on the SPRC, it was not possible to simply search for CRISM images featuring SCT, or to distinguish between morphologies, and so a more systematic approach was required.

The Arizona Lunar and Planetary Laboratory website for HiRISE[13] had labelled 50 images as 'Swiss Cheese' or 'Swiss Cheese-Like', and by visually checking these images, it was clear they covered a range of different SCT morphologies as described by Thomas at al., (2009).

This list of 50 HiRISE product IDs was entered into JMARS, and the software was used to search for footprints intersecting with CRISM scenes. This yielded only 15 FRT footprints. Additional instruments were then used to broaden the target area. Footprints from MOC Narrow Angle (MOC-NA) and CTX orbiter cameras that intersected with the 50 initial HiRISE footprints were entered into JMARS, and then the coverage of all 3 of these instruments was used to look for intersecting FRT CRISM scenes (Figure 4.1).

---

[13] https://www.uahirise.org/
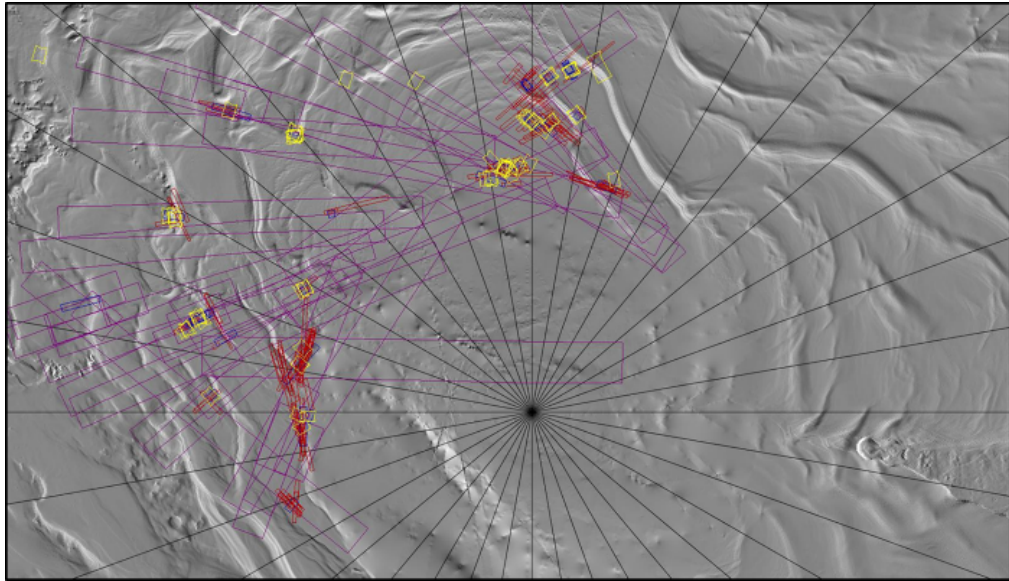
Figure 4.1: Footprints of HiRISE, MOC-NA, CTX and CRISM that cover SCT

(Produced using JMARS)

This method yielded 72 CRISM footprints, from which 17 were discarded due to either poor quality or limited coverage of SCT, leaving 55 images divided into 13 separate groups, where each group covers a corresponding SPRC region-of-interest with multiple products, acquired between 2007 and 2012 (the period in which CRISM FRT mode was operational, see Section 3.3).

4.1.2. Generation of Polar Stereographic Map

As JMARS uses the MOLA topographic digital elevation model (DEM) as a base layer, ice and land are not differentiated and it is difficult to see the extent of the ice cap using this software. To ensure CRISM images were within the SPRC, a polar stereographic map of the South Pole was created using ~12m

resolution HRSC images to produce a mosaic base map showing the extent of the south polar cap.

Using JMARS, the field of view was constrained to the total extent of the SPRC, and all HRSC footprints from this region loaded. HRSC 25-50 m/pixel images covering the largest area were chosen to provide maximum coverage with the fewest possible footprints. The images were visually checked for quality using the Planetary Data System[14] (PDS) archive and any poor-quality images replaced with better quality footprints covering the same region.

Once full polar coverage was achieved, the images were downloaded from the PDS and loaded into the GIS software Arcmap®[15], which allows the user to generate maps with image files. The HRSC Level 3 products had been georeferenced using 5 x 5km MOLA DTM, meaning they should have been tied to the correct Martian co-ordinates when loaded into the map; however subsequent analysis showed that there were some discrepancies, and the geo-referencing tool in Arcmap® was used to identify matching morphological features common to overlapping portions of images to more accurately position the footprints to create as smooth a map as possible.

The area covered by the SPRC as defined by Thomas et al., (2009) was added as a layer, as were the 13 CRISM groups identified with JMARS, and overlain over with the HRSC mosaic, shown below in Figure 4.2.

---

[14] https://pds-geosciences.wustl.edu/
[15] https://desktop.arcgis.com/en/arcmap/
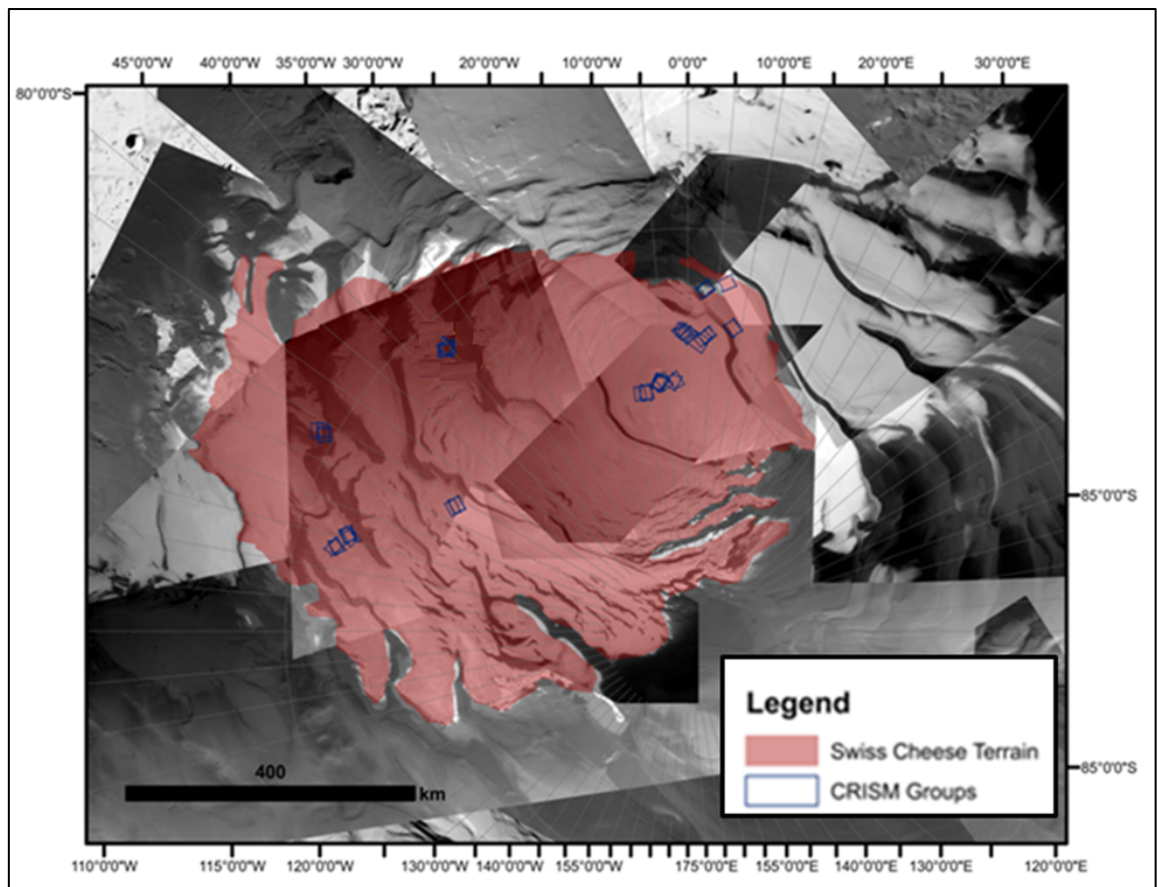
Figure 4.2: Polar stereographic map of the Martian SPRC based on extent mapping from Thomas et al., (2009) using a manually generated mosaic of HRSC images, showing 13 CRISM groups of interest (blue boxes)

4.1.3. Narrowing Down the Scenes of Interest

The CRISM footprints were further narrowed down to only those taken in 2007 (MY 27), in order to capitalise on the most effective operating period (see section 3.1.4) of the CRISM instrument, and ensure similar Martian spring/summer environmental conditions. This resulted in 13 images ready to be processed and used for initial spectral analysis. RGB composites were generated for the 13 sites, and those that showed rim regions with the

strongest spectral response for carbonates were chosen, resulting in 5 sites covering the various SCT morphologies (see section 2.3.2). More specifically:

- Site 1 is located at the edge of the SPRC and covers Unit B morphology.

- Site 2 is situated near the edge of the SPRC but does not include any ice-free surfaces, and covers Unit A0 and Unit B SPRC morphology

- Site 3 is located closer to the South Pole, well within the limits of the SPRC, and exhibits Unit A0 and B morphology.

- Site 4 is covered by characteristic 'curl features' of Unit A1.

- Site 5 covers Unit A0 and A2 morphology and is situated near the South Pole, adjacent to Site 4, supporting the idea that Unit A1 and A2 features represent different stages of the same sublimation morphology

A reminder of the morphologies can be seen in Figure 4.3.
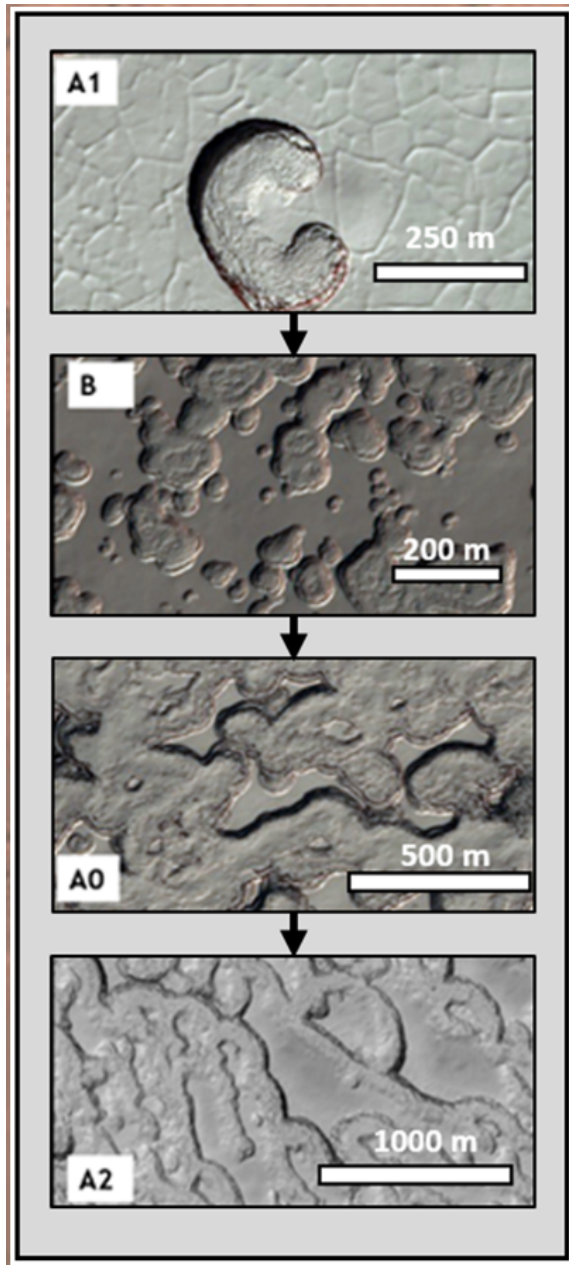
Figure 4.3: SCT through types of morphology A1, B, A0 to A2. Made using HiRISE imagery ESP_014141_0930, ESP_012271_0940, ESP_014380_0945 and , PSP_005386_0930 (top to bottom)

Table 4.1 shows the product details, and Figure 4.4 shows their context (top), details of their morphology can be seen in more detail using CTX imagery (bottom).

Table 4.1: Details of 5 CRISM scene sites

Site No.	Product ID	Acquisition Date	Lat	Long
1	FRT00007E26	26/09/2007	-84.9	298.4
2	FRT00006EEE	04/09/2007	-85.5	284.7
3	FRT00007CE5	21/09/2007	-86.8	297.8
4	FRT00005AE3	14/05/2007	-87.0	354.2
5	FRT000075F0	29/08/2007	-86.9	359.2
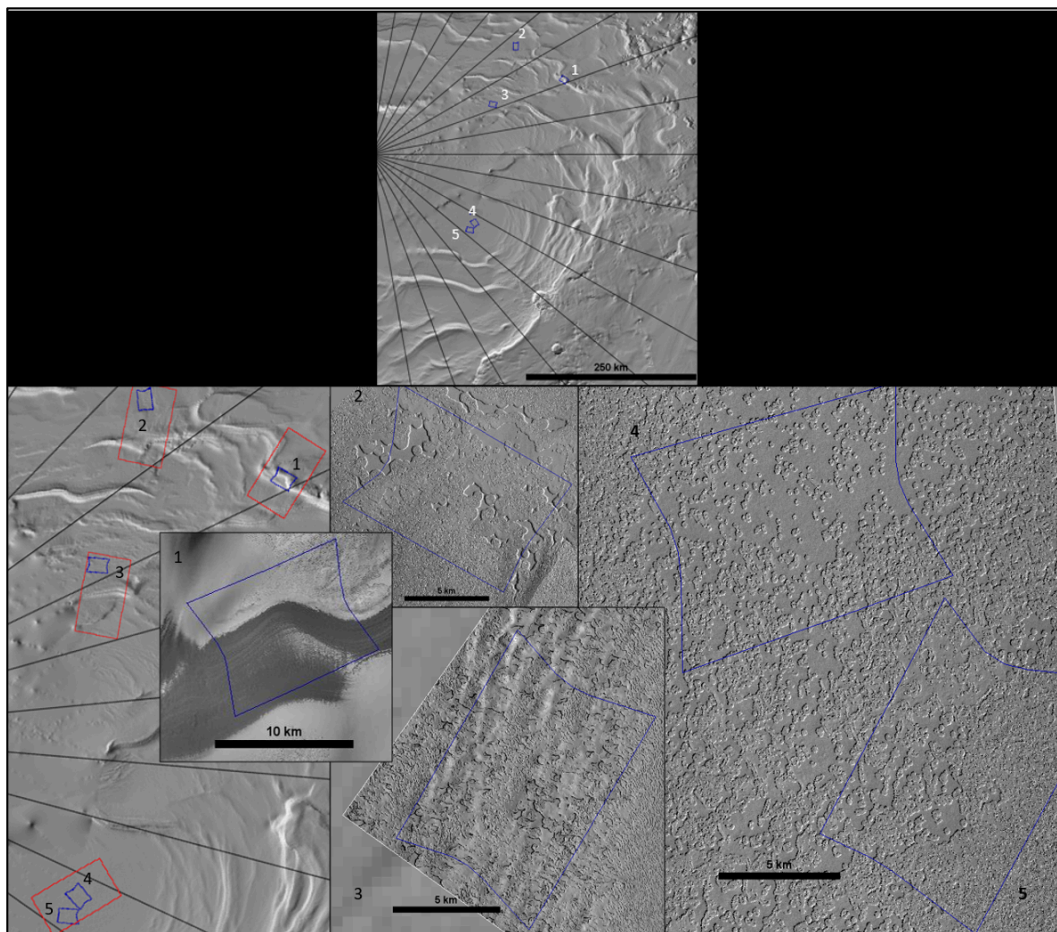
Figure 4.4: Locations of 5 CRISM sites over MOLA 463 m hillshade (top; produced in JMARS), with CTX imagery used to show morphology (bottom): Site 1: CTX B11_014076_0952_XN_84S061W. Site 2: CTX B05_011756_0944_XN_85S074W. Site 3: B11_014090_0932_XI_86S057W. Sites 4 & 5: CTX B07_012374_0931_XN_86S00

111

From these 5 sites, more specific regions of interest were chosen by looking at the summary product spectral maps, and selecting rim features that showed a strong spectral response for carbonates (rationale described in Section 3.4), as well as regions that showed a strong response for H_2O and CO_2 ice for comparison.

4.2. Results

Spectral maps of the 5 CRISM scenes listed in Table 4.1 were produced, and rim features and areas of featureless ice examined in more detail using multi-pixel regions of interest.

4.2.1. Site 1

Figure 4.5 shows the spectral difference between the SPRC and surrounding area. The low-albedo, non-icy area is dark purple in colour in the right-hand image, indicating a mix of carbonates (blue) and CO_2 ice in low amounts, possibly in the form of permafrost within the regolith. The margin of the SPRC is turquoise, indicating a mix of water and carbonates, as would be expected from a higher water ice content (green) at the edge of the SPRC described by Thomas et al., (2009). The SPRC itself in the bottom left of the image shows the higher CO_2 content typical of the SPRC.
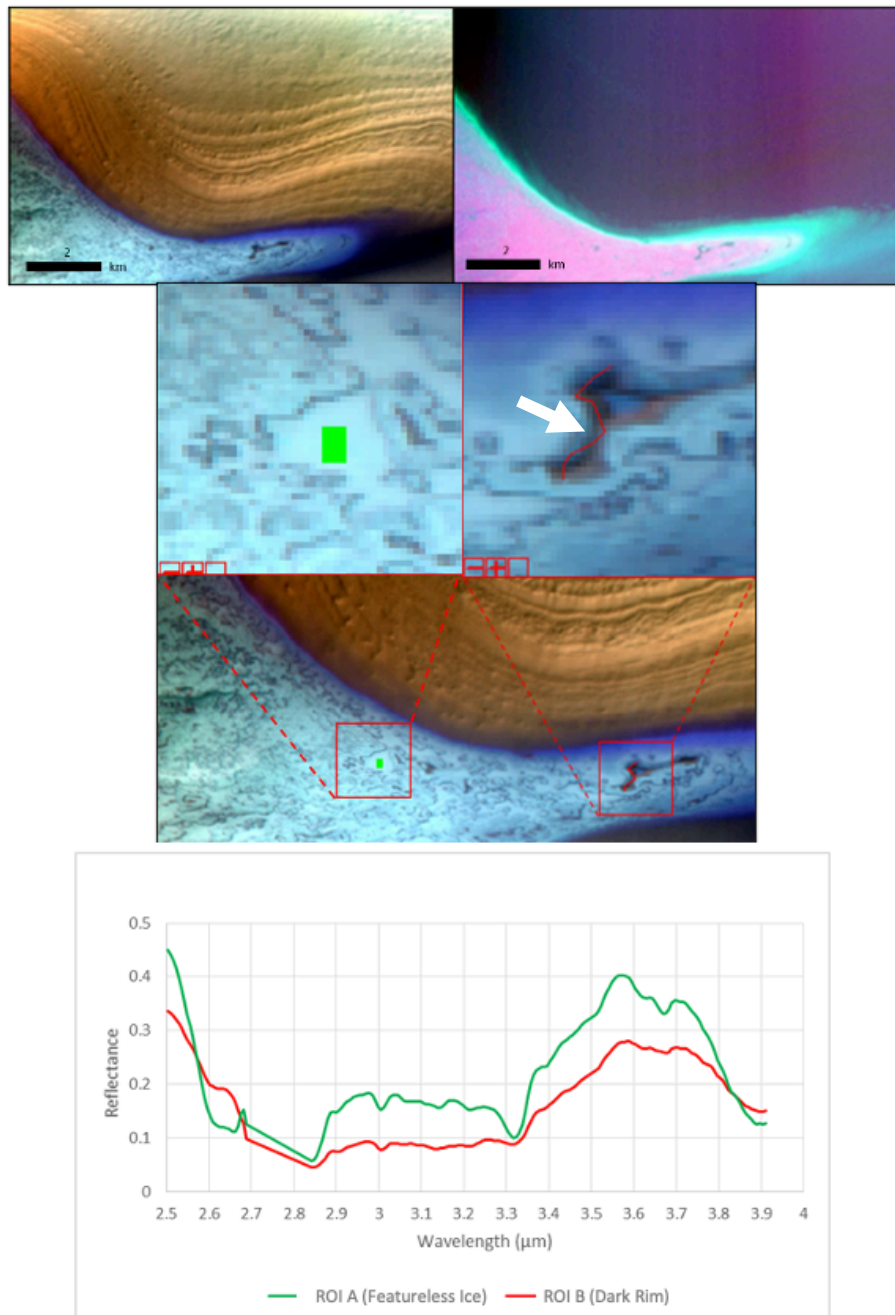
Figure 4.5: (Top left) False colour visualisation of Site 1 from CRISM bands R = 230 G = 75 B = 10. (Top right) False colour visualisation of Site 1 using Pelkey (2007) summary products R = 1435 (CO_2 ice) G = 1500 (H_2O ice) B = BDCARB (carbonate overtones). (Centre) Locations and close ups of Site 1, ROI A (green rectangle) and B (red line, highlighted by white arrow). Red squares are 1x1km. (Bottom) Reflectance spectra of Site 1 ROIs

Region of interest A (green rectangle) is situated on a featureless patch of ice, while ROI B (red line) is around a dark rim feature. The lower overall reflectance values of ROI B in comparison to ROI A, are likely to be a consequence of the lower albedo of the dust covered, textured scarp features, and because of possible lower solar irradiance in the topographically low shadowed rims. The trough just above 3.3µm is much more pronounced in featureless ice.

4.2.2. Site 2

At site 2, (Figure 4.6) the spectral mapping shows scarp features in shadow in the left-hand image manifest as blue (carbonates) when the 3 summary products are applied, whereas the illuminated scarps are green, suggesting water ice. This difference between shadowed and illuminated areas is unlikely to be due to any actual compositional difference, but may be because of variations in spectral response due to areas that receive more sunlight. This highlights limitation of the summary products; they don't show definitive compositions, only indications of what the surface might be made of, and in this particular instance the local conditions show an unreliable result.
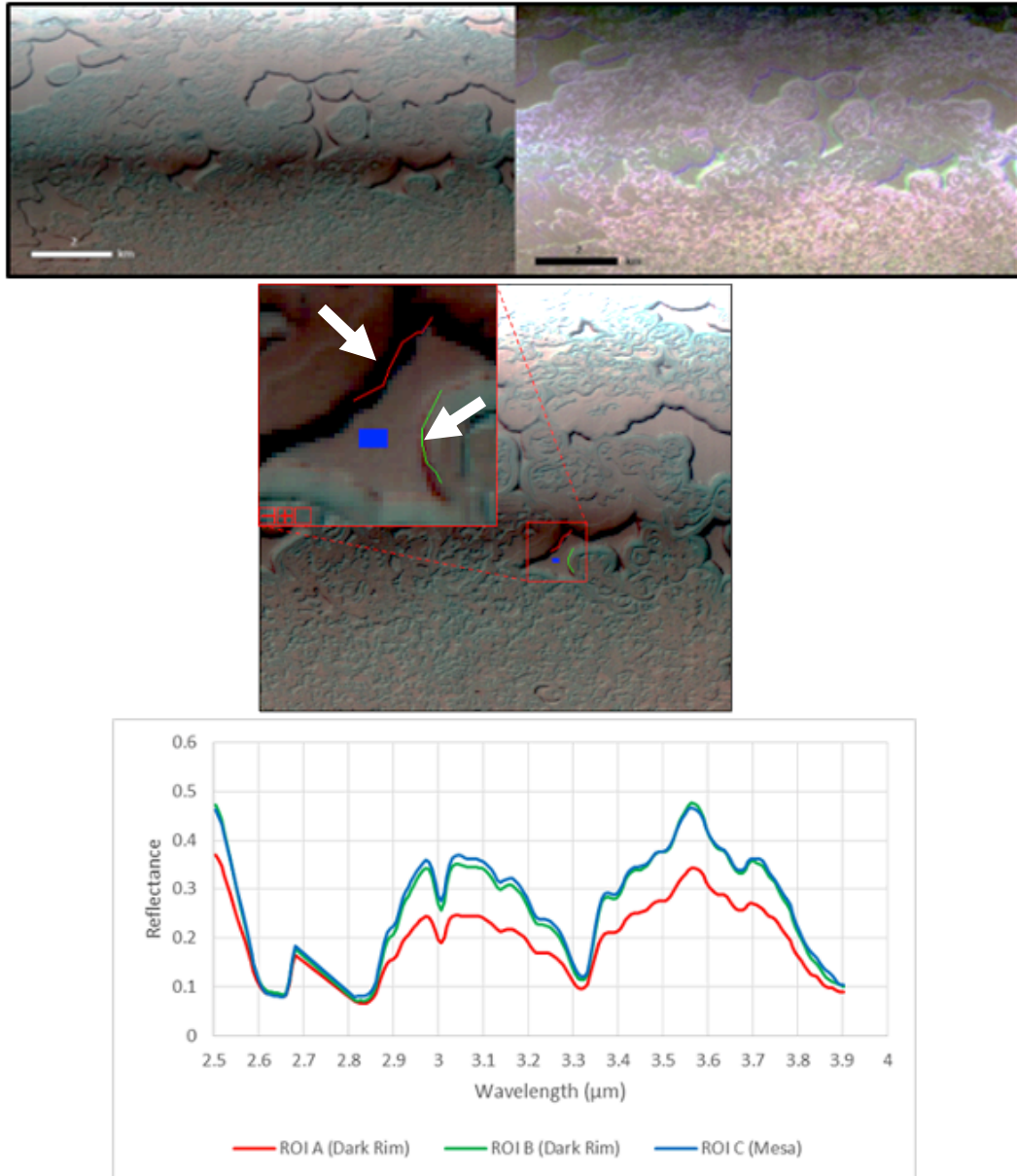
Figure 4.6: (Top left) False colour visualisation of Site 2 from CRISM bands R = 230 G = 75 B = 10. (Top right) False colour visualisation of Site 1 using Pelkey (2007) summary products R = 1435 (CO_2 ice) G = 1500 (H_2O ice) B = BDCARB (carbonate overtones). (Centre) Locations and close ups of Site 2, highlighted by white arrow, ROI A (red line) ROI B (green line) and ROI C (blue rectangle). Red squares are 1x1km. (Bottom) Reflectance spectra of Site 2 ROIs

ROIs from both red and green summary product highlighted areas were recorded, as well as from a mesa plateau between the two scarps. Site 2 showed greater variation in minimum and maximum reflectance at ROIs A and B, situated on dark rims than between RIO B and the mesa plateau (ROI C). Albedo was lowest at ROI A, the scarp that was highlighted as carbonates by the summary products. When compared, the spectra of ROI B and ROI C are virtually identical. It is clear that the illumination angle of the scarps results in different reflectance values between ROI A and those of ROI B and C. The troughs at ~2.85 and 3.35 µm are similar in reflectance for all ROIs.

4.2.3. Site 3

Site 3 (Figure 4.7) exhibits dark rims around most depressions and mesas independent of illumination angle. The dark rims are somewhat accentuated in shadowed areas and show up as more blue in the summary product visualisation, but overall the rims are largely green, indicating water ice.
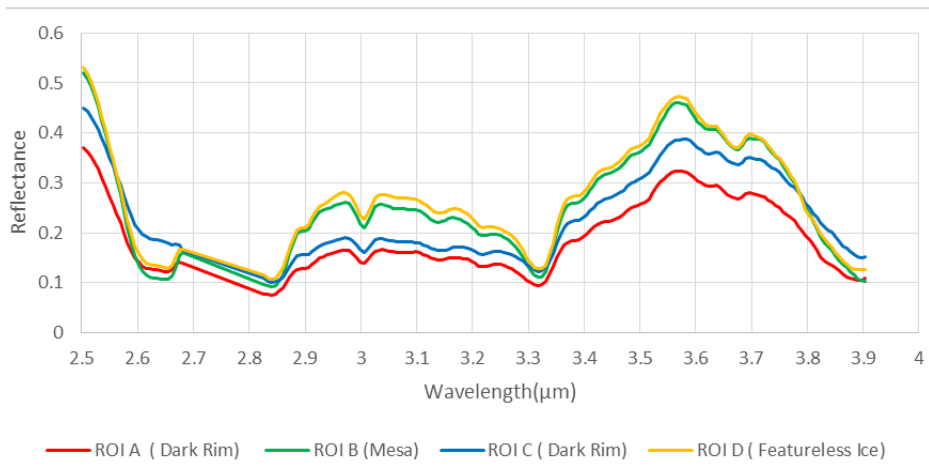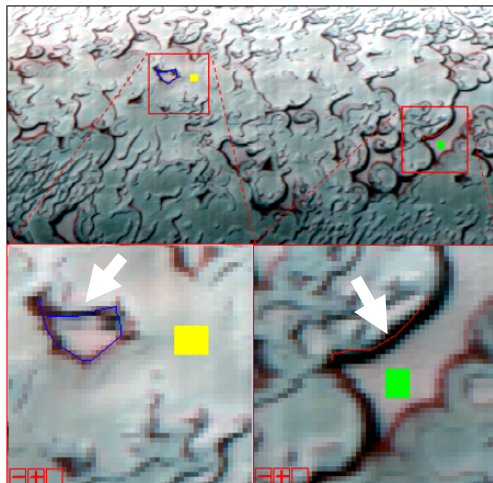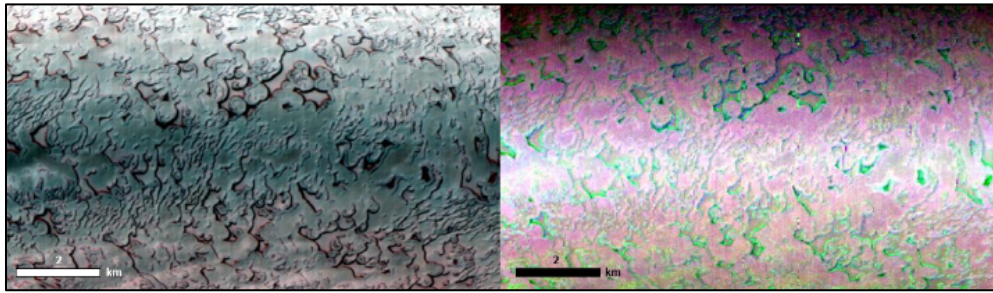
Figure 4.7: (Top left) False colour visualisation of Site 3 from CRISM bands R = 230 G = 75 B = 10. (Rop right) False colour visualisation of Site 3 using Pelkey (2007) summary products R = 1435 (CO_2 ice) G = 1500 (H_2O ice) B = BDCARB. (Centre) Locations and close ups of Site 3, ROI A (red line), B (green rectangle), C (blue polygon) and D (yellow rectangle). ROIs A and C highlighted by white arrows. Red squares are 1x1km. (Bottom) Reflectance spectra of Site 3 ROIs

117

Four ROIs were selected for this region. ROI A is a dark mesa rim that manifests as carbonate rich, while ROI C is from a mesa scarp rim that indicates water ice content. ROIs B and D are from a mesa plateau and featureless patch of ice respectively. ROIs A and C once again show that dark rim regions show greater variation between minimum and maximum reflectance while ROIs B and D show very little variation. The spectral profiles of flat, icy regions (ROIs B and D) are very similar. There is a rise in difference in reflectance between ROI A and ROI C beyond 3.4 μm, but overall the spectral profiles are similar. The dark rims show a broader, shallower absorption feature at 3 μm compared to the absorption feature for non-rim ROIs B and D.

4.2.4. Site 4

At Site 4, (Figure 4.8) ROI A is taken from the edge of a curled feature, while ROI B is within a curl feature. ROI C is situated on a featureless patch of ice between the curl features.
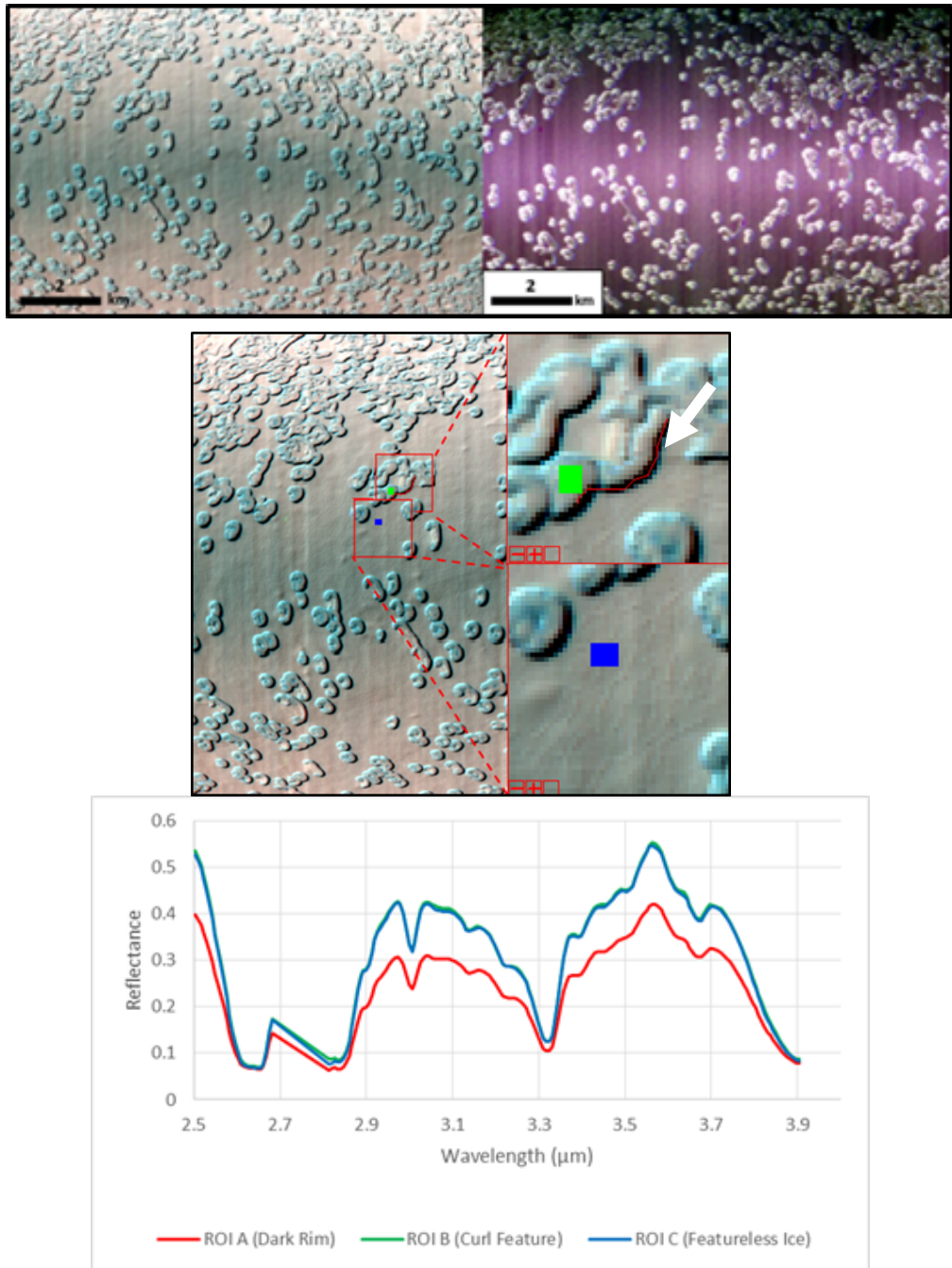
Figure 4.8: (Top left) False colour visualisation of Site 4 from CRISM bands R = 230 G = 75 B = 10. (Top right) False colour visualisation of Site 3 using Pelkey (2007) summary products R = 1435 (CO_2 ice) G = 1500 (H_2O ice) B = BDCARB. (Centre) Locations and close ups of Site 4, ROI A (red line), ROI B (green rectangle), and ROI C (blue rectangle). ROI A highlighted by white arrow. Red squares are 1x1km. Bottom: Reflectance spectra of Site 4 ROIs

As with the dark rim spectra from previous sites, the curl feature rim from ROI A exhibits greater variation in minimum and maximum reflectance values compared with smooth ice features. While there is less variation within the curl than at its edge, ROI B still shows greater min/max reflectance variation than ROI C. Despite differences in minimum and maximum reflectance variation, the curl feature (ROI B) and the featureless ice (ROI C) have virtually identical spectral profiles, to the point the green line can barely be seen in the graph; the dark rim of the curl feature (ROI A) has an overall lower reflectance.

4.2.5. Site 5

4 ROIs were investigated at Site 5; a 'blue' rim, a 'green' rim, a mesa plateau in between and a patch of featureless ice. Similarly to site 2 (Figure 4.2), Site 5's summary product false colour visualisation in Figure 4.9 shows shadowed rim areas as blue (carbonate rich) and illuminated scarps as green (water ice rich).
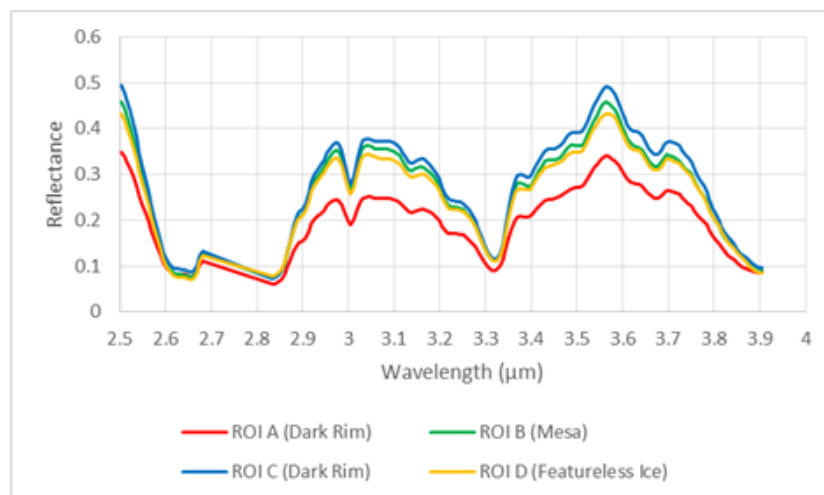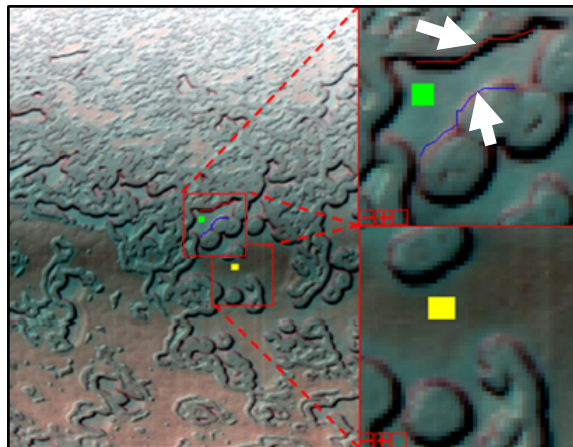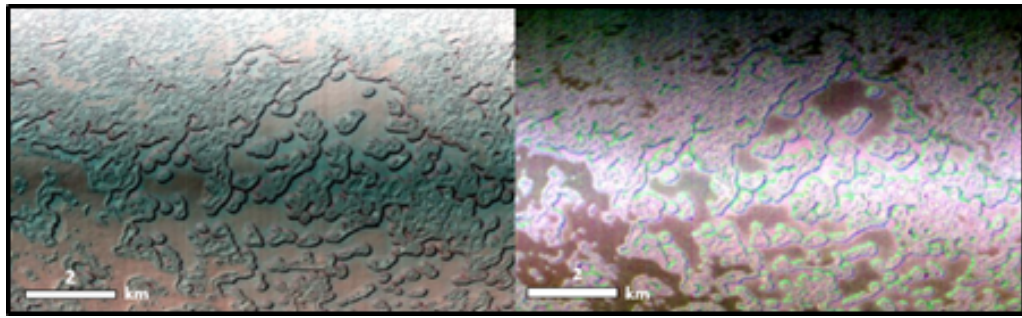
Figure 4.9: (Top left) False colour visualisation of Site 5 from CRISM bands

R = 230 G = 75 B = 10. (Top right) False colour visualisation of Site 3 using

Pelkey (2007) summary products R = 1435 (CO_2 ice) G = 1500 (H_2O ice) B =

BDCARB. (Centre) Locations and close ups of Site 5, ROI A (red line), ROI B

(green rectangle), and ROI C (blue line) and ROI D (yellow rectangle). ROIs

A and C highlighted by white arrows. Red squares are 1x1km. (Bottom)

Reflectance spectra of Site 5 ROIs

As with the previous investigation sites, there is higher variability in reflectance on dark rim ROIs and much more consistent reflectance across all pixels in ROIs B and D. As with site 3, the illuminated dark rim (ROI C) that was depicted as green (water ice) shows a very similar spectral profile to the mesa and featureless patch of ice (ROIs B and D) while the dark rim in shadow (ROI A) exhibits lower overall reflectance.

4.3. Analysis and Discussion

These initial results show that the dark rim sites consistently show a much wider variation in minimum and maximum reflectance across all ROI pixels than ROIs in non-rim locations. When the spectral profiles of all dark rims from all sites are plotted together, there are range of reflectance levels of spectral profiles (Figure 4.10).
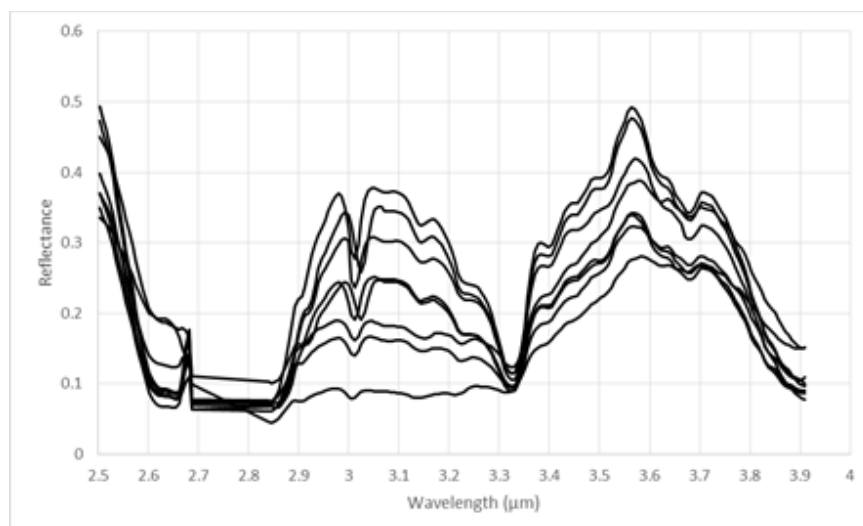
Figure 4.10: Reflectance spectra of Dark Rim ROIs from all 5 sites

The spectral profiles of all non-rim areas are more consistent with each other, particularly above 3.4 µm (Figure 4.11).
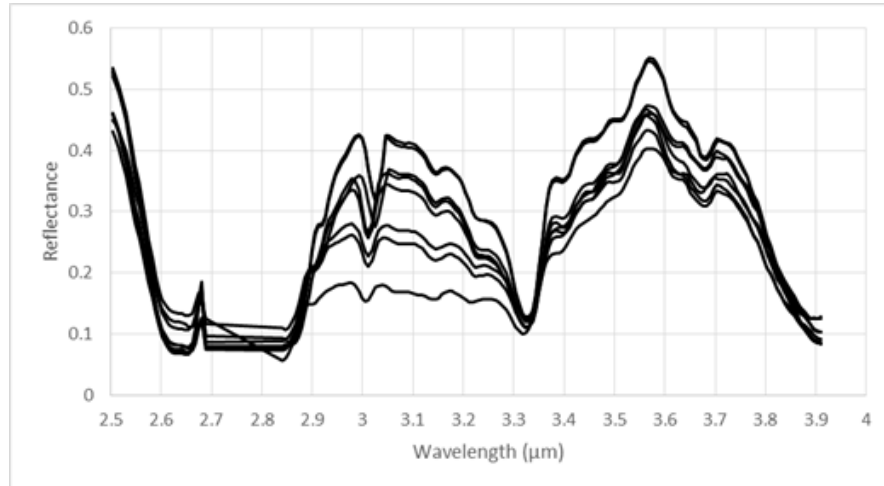
Figure 4.11: Reflectance spectra of Non-Rim ROIs from all 5 sites

In order to further analyse the overall characteristics of dark rim and non-rim regions, mean spectra were produced by averaging all rim spectra from Figure 4.10 for dark rims, and all non-rim spectra from Figure 4.11, to create two new spectral profiles (Figure 4.12).
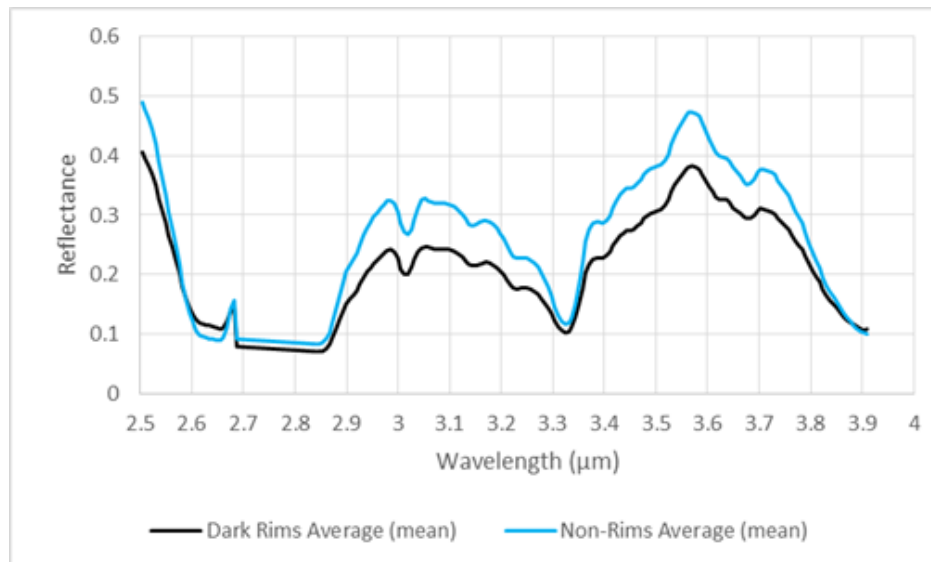
Figure 4.12: Average spectra of Dark Rim and Non-Rim ROIs for all 5 sites

Averaging the spectra of all regions is not particularly useful for examining individual, subtle characteristics of dark rim features, as any unique features will be lost. However, the average dark-rim and non-rim spectra are useful for looking at the effects of water and CO_2 ice on spectral profiles.

4.3.1. CO_2 Ice Spectral Features

Given that the SPRC is dominated by CO_2 ice, removing the spectral features of CO_2 ice from the ROI spectra enables residual features to be more effectively analysed.

CRISM-type spectra from the CRISM spectral library (Viviano-Beck et al., 2014) are used for comparison, but in addition, local spectra are used in order to minimise the effect of variables such as dust content in the atmosphere, angle of sunlight etc.; ROI band thresholds were used to identify the strongest

10% of CO_2 and H_2O ice signatures from each scene (Figure 4.13), and then

ROIs of a minimum of 25 pixels chosen from the same across-track region of

the scene as the dark-rim features to provide local 'purest' ice spectra.
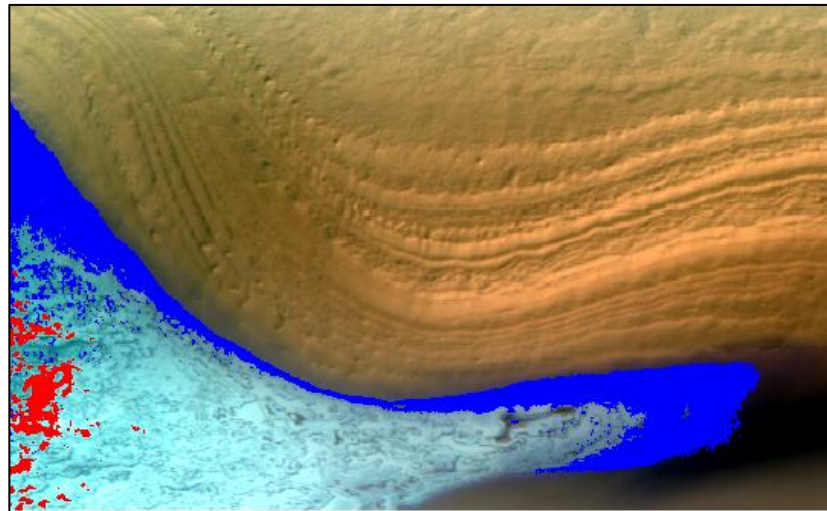
Figure 4.13: Site 1, strongest ROI band thresholds for strongest 10% of

signatures for summary products for H_2O ice (blues) and CO_2 ice (red)

Figure 4.14 shows the spectral profile for CO_2 ice CRISM type spectra

(Viviano-Beck et al., 2014) above the average spectra of the two types of ROI

from Figure 4.12. Below that is the mean spectrum for the strongest 10% of

CO_2 diagnostic summary product ROIs.
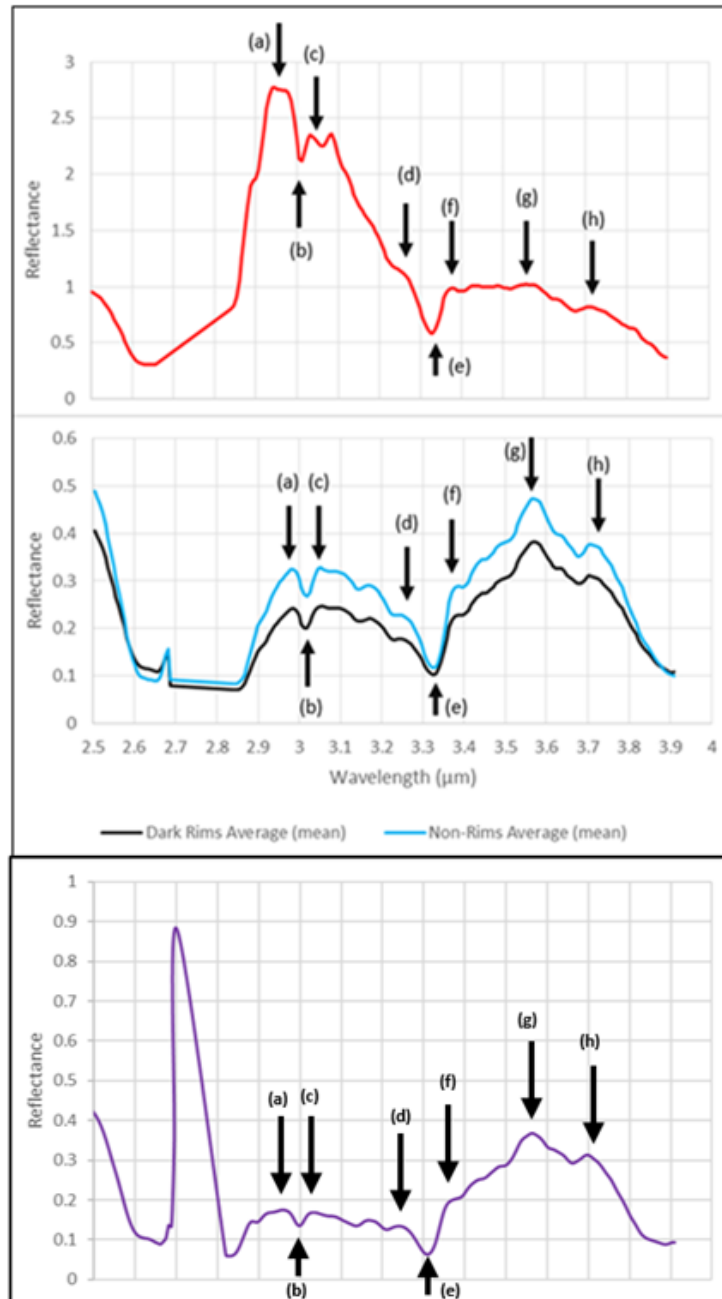
Figure 4.14: Comparison of peaks and troughs between Viviano-Beck CO$_2$ ice spectrum (top), average spectra of Dark Rims and Non-Rims (center) and mean strongest 10% of local CO$_2$ summary product spectra (bottom)

The Viviano-Beck profile of CO$_2$ is dominated by a region of very high reflectance made up of several peaks between 2.8 and 3.3 µm. This area of high reflectance is not duplicated in the ROI spectra of Dark Rim nor non-rim

ROIs. However, there are other features from the CO_2 spectrum that appear in the ROI spectra. The local 10% threshold ROI spectra (in purple) shows a more similar profile to the rim and non-rim regions (though with the spike at ~2.7 µm being more pronounced); this is thought to be an issue with spurious data from detector-type boundaries on the CRISM instrument and does not affect the wavelengths of interest. Figure 4.14 highlights eight peaks and troughs from the library and local CO_2 spectra that correlate with features in the dark rim and non-rim averaged spectra; the ROI spectra have been plotted on a separate scale in order to allow the spectral features to be seen in comparison to the high reflectance CO_2 spectrum. The 8 peaks and troughs (a-h) are only the most obvious features that can be seen on both the CO_2 and average ROI spectra to glean an overall idea of common distinctive attributes.

It would appear that CO_2 signatures contribute significantly to the dark-rim ROIs; this is to be expected in such a CO_2 ice rich environment. It is clear that there is a difference in overall reflectance values between dark rim and non-rim regions, which is likely to be a consequence of the lower albedo of the darker, textured scarp surfaces (Byrne, 2009).

The overwhelming influence of the CO_2 content of the ROIs must be removed in order to see any subtler compositional characteristics. In order to minimise the effects of CO_2 ice, the values for the two types of ROI were divided by both Viviano-Beck and local strongest 10% CO_2 spectra. The peaks between 2.8 and 3.3 µm were far too greatly reduced using the Viviano-Beck library spectrum (Figure 4.a, Appendix B), resulting in erroneously low reflectance

levels on the corrected rim spectra. Therefore, local spectra from each scene were used instead for individual corrections for each site.

Further processing of the ROI spectra may be necessary to highlight differences between dark rims and non-rim features. Back-wasting of scarps can expose higher concentrations of H_2O ice inside depressions (Thomas et al., 2009), and so it is prudent to attempt to account for the effects of water ice on ROI spectra to see if the rims are composed of more water ice than non-rims.

ROI thresholds for the strongest 10% of H_2O summary product parameters were used to obtain diagnostic water-ice rich spectra. The results (Figures 4.b-4.d, Appendix B) showed no discernible effect on the wavelengths of interest, with the local water ice rich regions still being largely overwhelmed by CO_2 ice signatures. It is concluded that local non-rim regions will suffice for removing the effect of ice from rim-feature spectra. In addition, given that the Viviano-Beck H_2O spectra were obtained from North Pole pure water ice, they are unlikely to be representative of SPRC non-rim regions.

Identification of PAH-like signatures on Iapetus and Phoebe relied on ice-free surface deposits of dark PAH-rich material; the Martian SPRC has no such extensive regions of low albedo material. The very small surface area of the depression scarps mean that the dust content is likely to be very low, and any organics are likely to be present in even lower concentrations. This problem is further exacerbated by the ~20 m spatial resolution of the CRISM

instrument, which cannot resolve homogeneous dark patches, and will almost always encompass some area of dust-free, icy surface material. However, Chapter 6 builds on work published by Buhler et al., (2017) to find more extensive areas of dust.

When the averaged ROI spectra are corrected for CO_2, there is no evidence of any PAH diagnostic absorption feature, indicating PAHs are not present in an abundance that can be detected using the well-known diagnostic spectral feature at 3.29 μm. Figure 4.15 shows the spectral region of interest of ice corrected spectra below the absorption profile of the mixture of 6 PAHs from Colangeli et al., (1992).
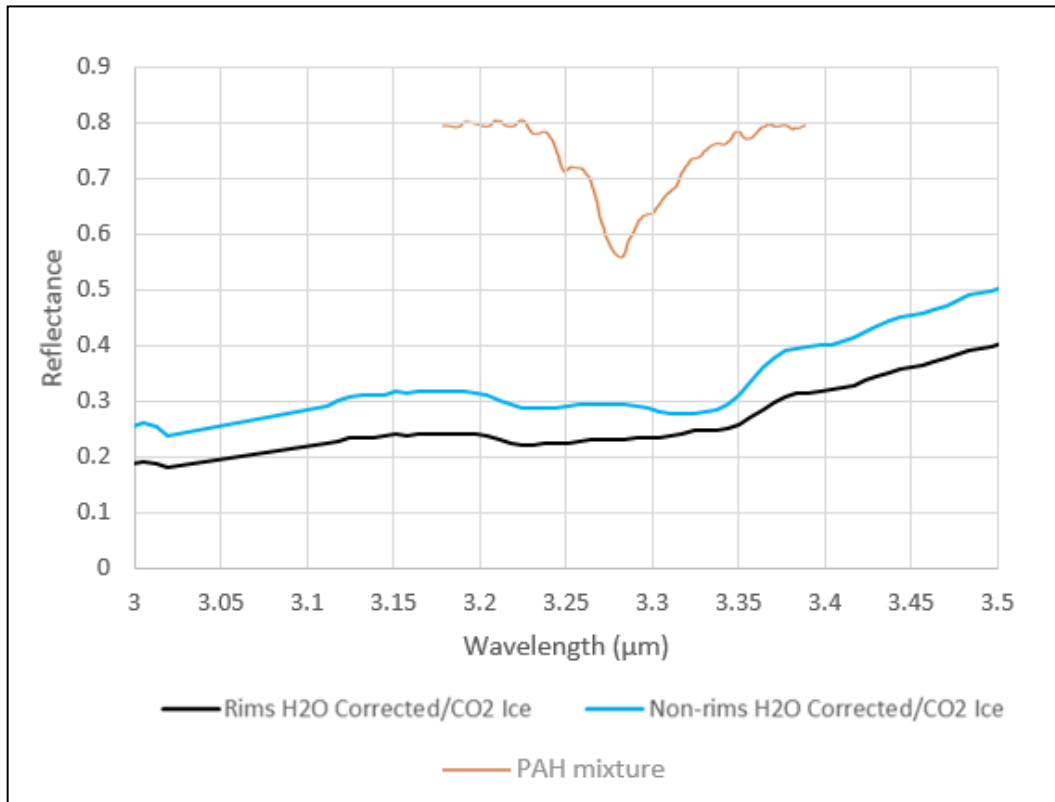
Figure 4.15: CO_2 corrected spectra for averaged Dark Rims and Non-Rims compared with average of Colangeli's averaged 6 PAHs

The presence of strong spectral responses of a CO_2 and water ice mix makes it very difficult to identify any weak absorption features that might be present at ~3.3 µm. The averaged ROI spectra by their very nature smooth out unique features. Examination of spectral features of PAHs at other wavelengths, particularly at lower wavelengths in the visible to near-infrared may be of use, where the effects of CO_2 ice are not so overwhelming.

While these generic spectra have been useful in establishing the overall common characteristics of dark rim and non-rim ROIs, and ascertaining the impact of water and CO_2 ice spectra on ROI features, it is necessary to examine individual ROIs for absorption features.

4.3.2. Analysis of Individual Spectra

Figure 4.16 shows all the spectral profiles of the dark rim ROIs. The 3 ROIs with the lowest reflectance in the PAH region of interest were chosen in order to minimise the effects of the impact of the steep shoulder into the CO_2 ice absorption feature at just above 3.3 µm. They are ROI A from Site 1, and ROIs A and C from Site 3. The non-rim features from the same sites are also analysed in order to examine the spectral differences of regions within the same CRISM scene.

These 3 dark rim sites are also interesting as they exhibit dark coverage around the whole rim regardless of illumination angle, suggesting dust coverage rather than simply shadow.
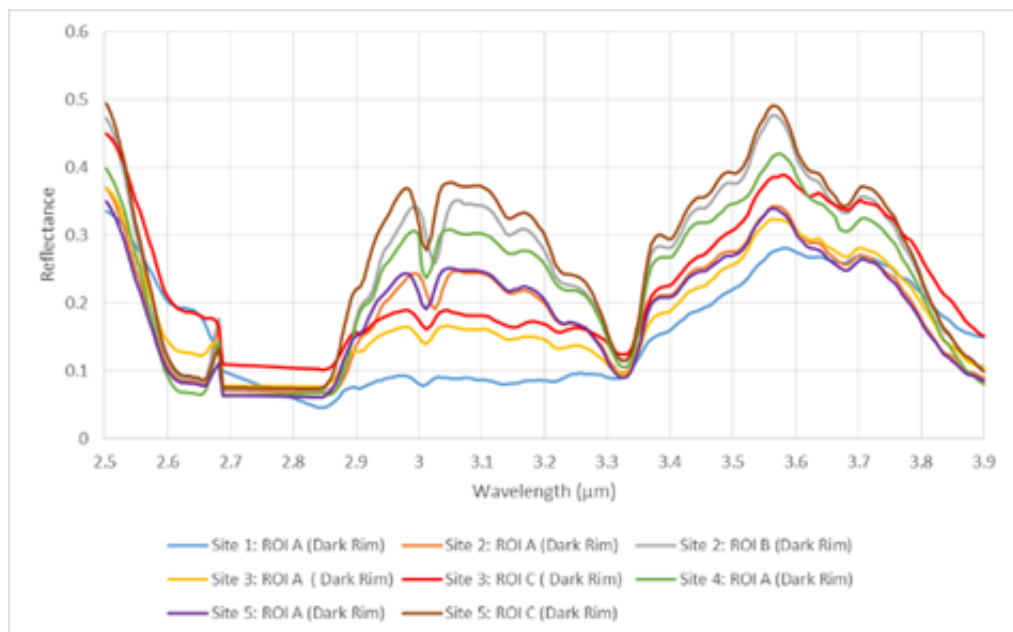
Figure 4.16: Spectral profiles of all Dark Rim ROIs

4.3.2.1. Site 1: ROIs A and B

Figure 4.17 shows the PAH spectral region of interest (3-3.5 µm) of Site 1, both CO_2 corrected and uncorrected ROI A (dark rim). There is a more pronounced feature between 3.30 and 3.35 µm for the corrected rim, suggesting that the non-rim region used for correction, i.e. a more CO_2 rich composition, had a significant effect on the 3.3 µm region.
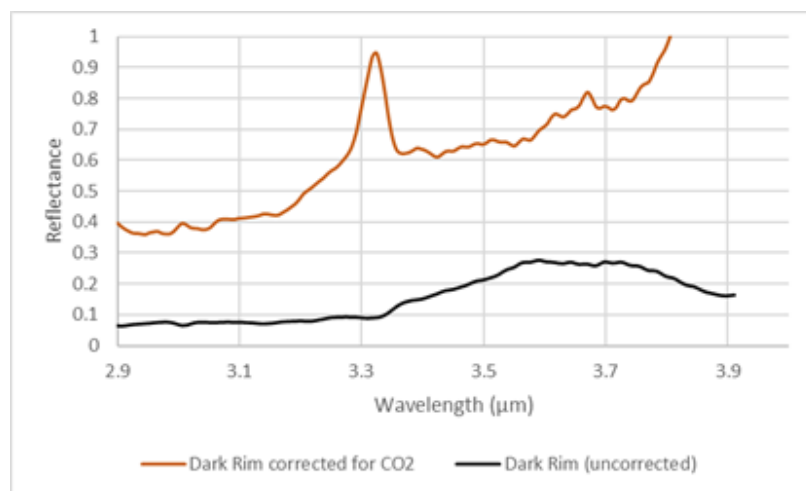
Figure 4.17: CO_2 corrected and uncorrected ROI A (Dark Rim)

In order to ascertain subtle differences between the two ROIs, PeakFit software was used to carry out a statistical fit to accentuate peaks by carrying out a Gaussian decomposition mentioned in Section 3.5, using an algorithm designed to smooth out noise. Corrected rim and non-rim profiles were compared to CO_2 and water ice as well as the 6 minerals of interest from section 3.5 (jarosite, magnesium carbonate, magnesium-rich olivine, high-calcium pyroxene, magnesium rich smectite clays, and talc).

Figures 4.18 and 4.19 show the PeakFit output for the spectra uncorrected for ices. An attempt was made to carry out peak fit for the corrected spectra, but it could not be done to an unacceptable R^2 value. Therefore, in this instance, the uncorrected profile for Site 1, ROI A was used, and was compared to CO_2 and water ice as well as the 6 minerals of interest. It was not possible to make any meaningful comparison of the 6 minerals because of the strong effects of CO_2 ice.
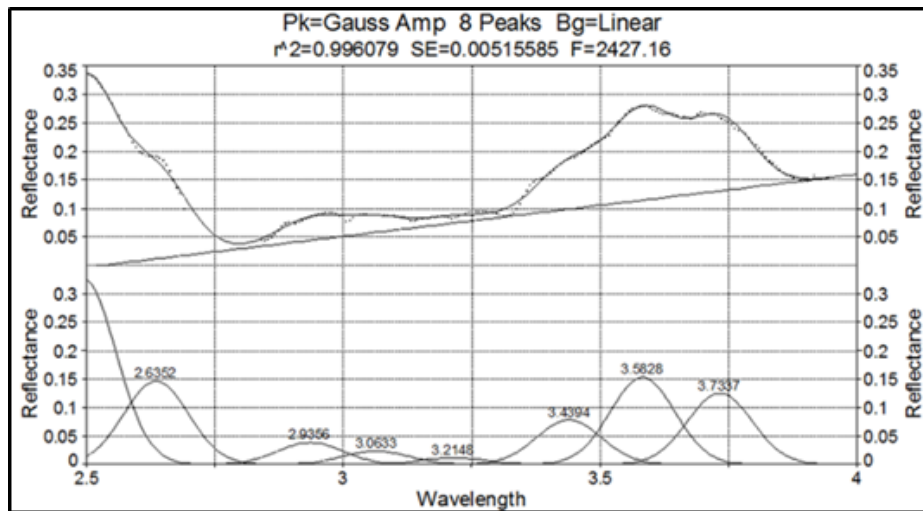
Figure 4.18: Gaussian decomposition for uncorrected Site 1, ROI A
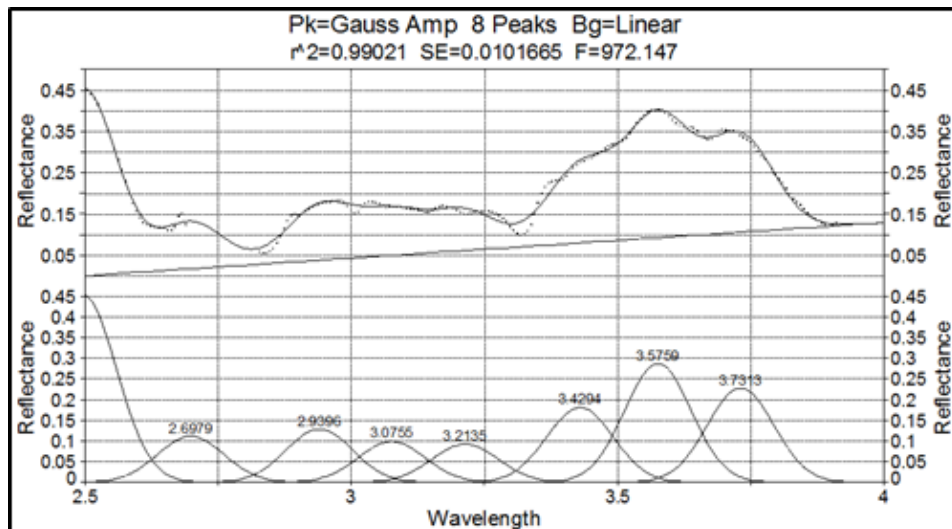
Figure 4.19: Gaussian decomposition for uncorrected Site 1, ROI B

Whilst there is an overall difference in reflectance intensity, with ROI B being more reflective, both regions show 8 peaks in very similar regions, indicating no significant compositional difference.

4.3.2.2. Site 3: ROIs A and B

At Site 3 the uncorrected spectra of ROIs A and B again show the strong CO_2 absorption feature (Figure 4.20). They are very similar, except for reflectance intensity.
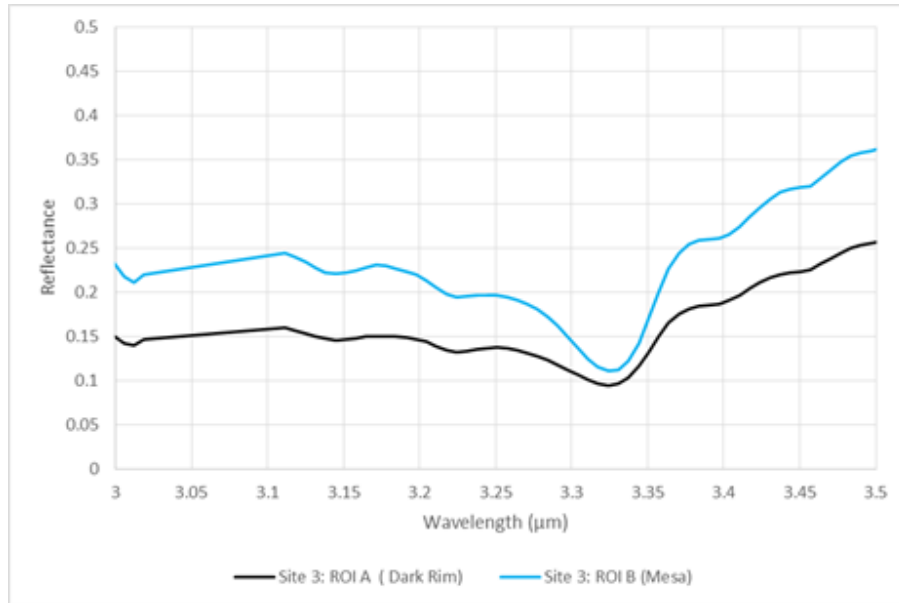
Figure 4.20: Spectral profiles of uncorrected Site 3 ROIs A and B

After correction for CO_2 ice, some subtle differences arise (Figure 4.21).
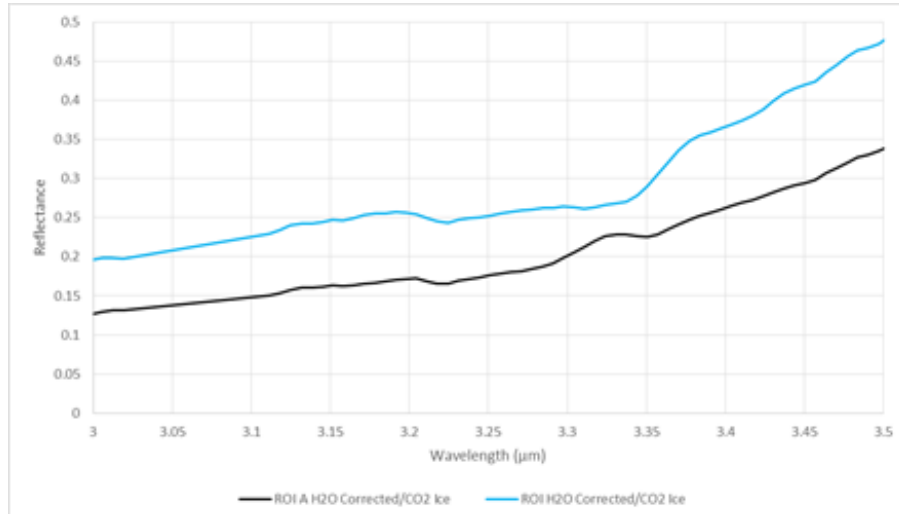
Figure 4.21: Spectral profiles of corrected Site 3 ROIs A and B

The Gaussian decomposition of dark rim ROI 3A (Figure 4.22) revealed far more individual peaks, with 17 distinct features, compared with the mesa

plateau of ROI B, which only shows 11, suggesting a significant compositional difference between the two regions.
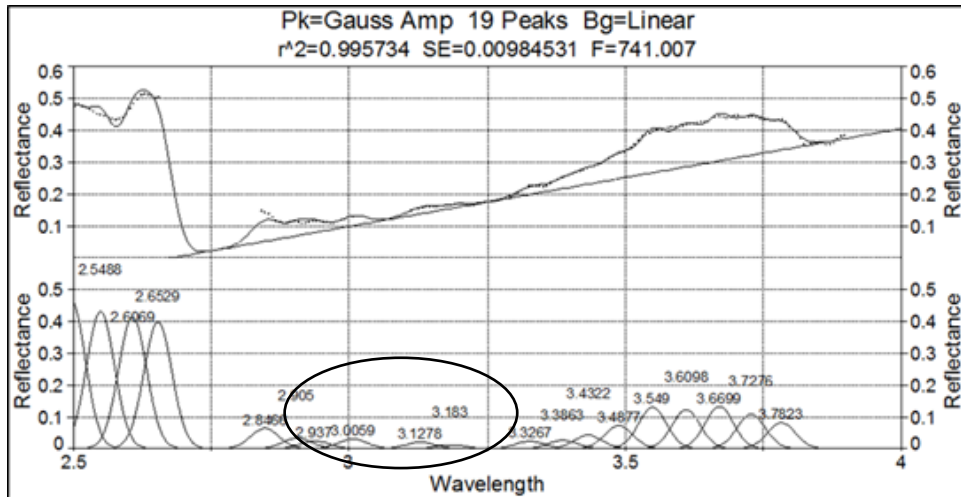
Figure 4.22: Gaussian decomposition for corrected Site 3 ROI A. Oval highlights peaks 2.8-3.2 μm

In the Gaussian decomposition for corrected spectra for ROI B (Figure 4,23), there are 3 peaks in this region, but they do not match the peaks in ROI A.
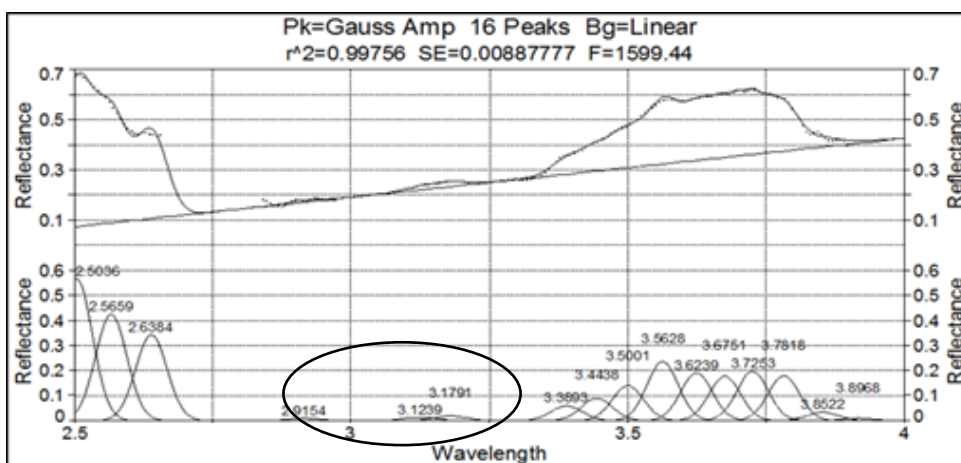
Figure 4.23: Gaussian decomposition for corrected Site 3 ROI B. Oval highlights peaks 2.8-3.2 μm

After comparison with the 6 minerals of interest, there is a similarity between ROI A and the spectrum for magnesium carbonate (Figure 4.24) suggesting some carbonate content. This is consistent with the results from spectral mapping which identified ROI A as having possible indications of carbonate overtones.
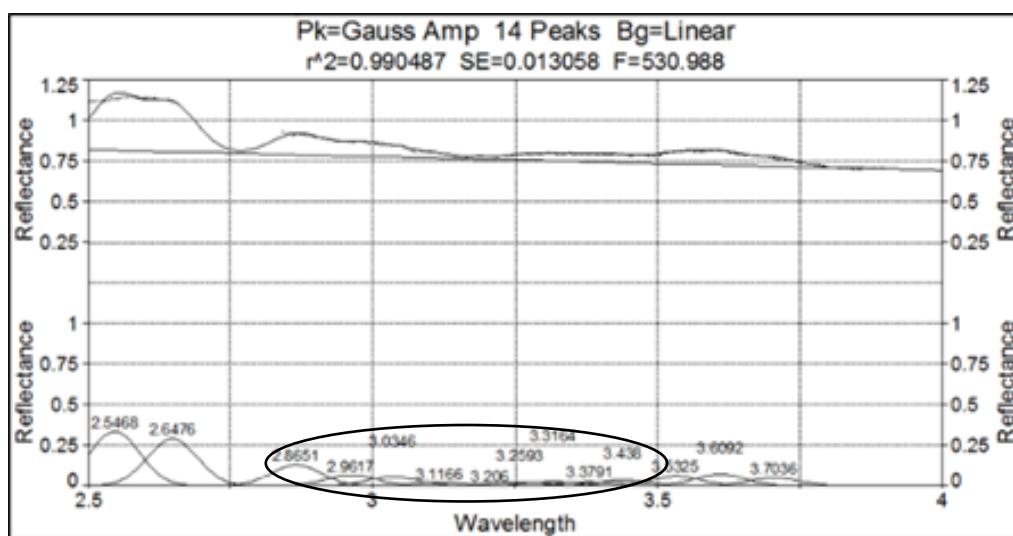
Figure 4.24: Gaussian decomposition for Mg carbonate spectrum. Oval highlights peaks 2.8-3.2 μm

4.3.2.3. Site 3: ROIs C and D

As with Site 3 ROIs 3A and 3B, ice correction of spectra highlights a compositional difference between ROI 3C and 3D (Figure 4.25).
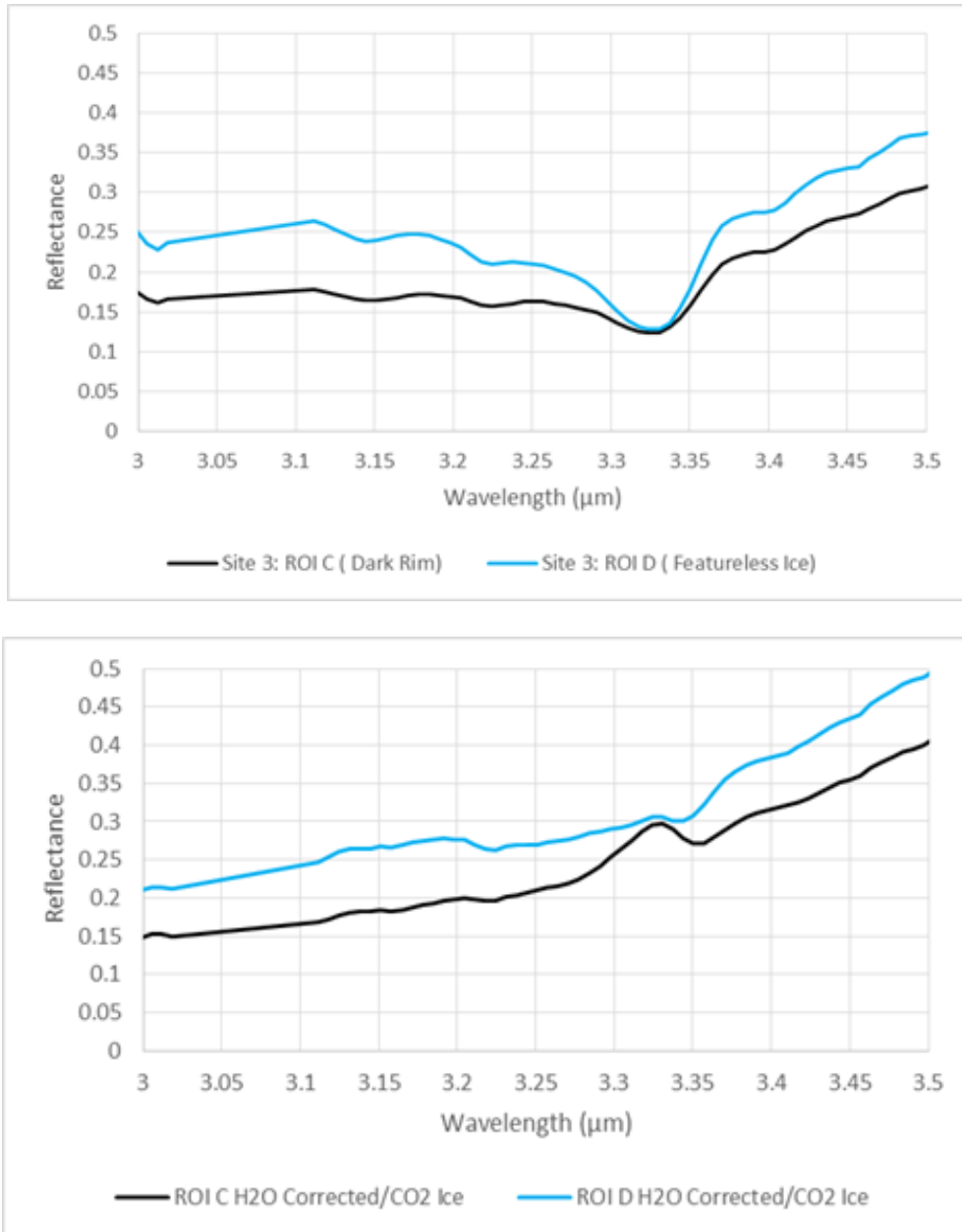
Figure 4.25: Uncorrected (top) and corrected (bottom) spectra of

Site 3 ROIs C and D

Following Gaussian decomposition, there is a feature at 2.85 μm in ROI 3C (Figure 4.26) that isn't reflected in ROI 3D (Figure 4.27). Upon comparison with the 6 minerals of interest, there is a tenuous similarity between ROI A and magnesium carbonate. The spectral map of Site 2 highlighted ROI C as water-

ice rich, and this is consistent with the weaker carbonate peaks when compared with Site 3, ROI A.
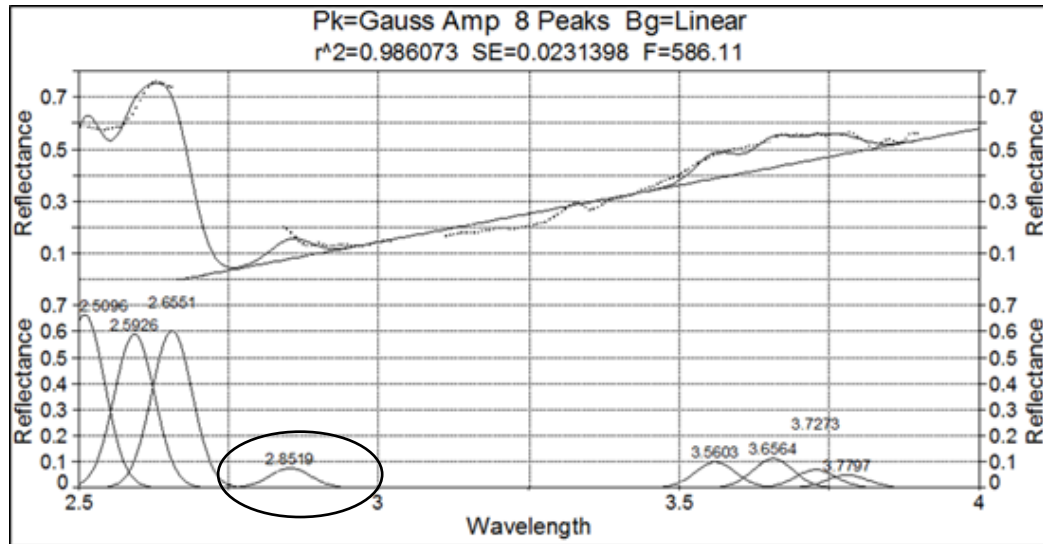
Figure 4.26: Gaussian decomposition for corrected Site 3 ROI C. Oval highlights peaks at 2.85 µm
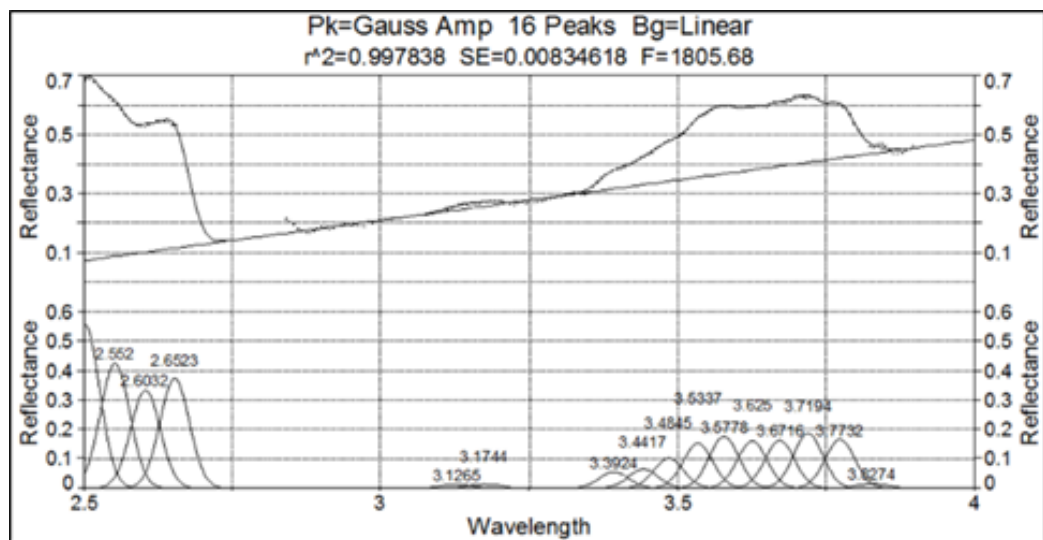
Figure 4.27: Gaussian decomposition for corrected Site 3 ROI D

4.4. Preliminary Conclusions

Spectral mapping has revealed that there is a distinct compositional difference between the majority of the SPRC and depression rims for all morphological units. Further analysis of ROI spectral features reveals that the compositional differences are highlighted when spectra are corrected for interference from ice absorption features.

Dark rims exhibit more variation in reflectance than non-rims. The influence of water ice is greater on rims and once removed, dark rim spectra more closely resemble the spectra of non-rims. CO_2 ice is a limiting factor due to the strong absorption feature between 3.3 and 3.4 µm, while water ice appears to have less of an impact, contrary to the findings of Cruikshank et al., (2008). This is likely due to the higher abundance of pure CO_2 on the SPRC than on icy moons of Saturn.

Other orbital spectrometers such as THEMIS, TES (Thermal Emission Spectrometer) and OMEGA could have been used to further investigate dark rims, but all these orbital spectrometers are limited by spatial resolution, as it will not be possible to resolve small SCT rim features nor analyse ice free pixels, given the paucity of dust on dark rims. In future, higher resolution orbital spectrometers, and ground based detectors may overcome this issue. However, following the failure of the Mars Polar Lander (Albee et al., 2000), there are no current plans to land on near the Martian ice caps.

Further analysis of the SPRC is outlined in Chapter 6, with more ROIs examined, and CRISM scenes utilised from various time periods included in order to try to monitor temporal changes in spectra. In addition, new work was published since the work in Chapter 4 regarding the origin of dust fans around A0 type morphology that sheds light on dust accumulation (Buhler et al., 2017) and this is discussed further in Chapter 6.

The spectral mapping of FRT scenes suggested magnesium carbonate may be present in some dust rims, with the Gaussian decomposition indicating that this may well be the case. It is possible that the non-targeted CRISM mode (which has global coverage) could be used to analyse the entire SPRC, as FRT only has ≈1% surface coverage, and much of the SPRC has not been imaged at high resolution. However, the 100-200m spatial resolution of non-targeted mode probably excludes effective perusal of small-scale features.

No sign of PAHs is yet found in detectable amounts; this may be because any organic content in SCT feature rims is less abundant than on Iapetus and Phoebe and may be beyond the detectability limits of the CRISM instrument, but a major issue is the use of the 3.29 µm diagnostic PAH feature and the fact that no detectability limit for PAHs existed, a problem that will be solved in Chapter 5. The ~3.3 µm wavelength region of SPRC CRISM spectra is very problematic when looking for subtle features due to the overwhelming effects of the CO_2 ice features. Experimental evidence of alternative PAH absorption features, and empirical evidence of the detectability limit of PAHs on or in CO_2 ice would have been very useful in determining what amount of PAH would

need to present in order to be discernible in CRISM-type spectra; laboratory experiments tackling these goals are the subject of the next chapter.

5. Laboratory Analysis of PAHs in Martian Analogues

This chapter outlines the results of a series of laboratory experiments carried out in order to generate a diagnostic spectrum for PAHs of astrobiological interest in the context of Martian analogues, to constrain the detectability limit of PAHs in CO_2 ice and briny soil, and to establish PAH spectral features at wavelengths other than the well-known absorption feature at 3.29 μm. This work was carried out over two 5-day sessions in 2017 and 2018 at the Institut de Planétologie et d'Astrophysique (IPAG) under the guidance of Dr. Bernard Schmitt and Dr. Olivier Brissaud, funded by Europlanet (please see acknowledgements). Detectability limits were ascertained for observing PAHs in SPRC and RSL analogues, with new PAH spectral features revealed that are easier to observe within CO_2 ice. Endmember spectra for all materials of interest were recorded, and it was found that the inclusion of partially dried brines within soil samples increased the detectability limit, suggesting increased transparency in the regolith due to salt crystals.

The need for empirical data on PAH detection limits pertinent to Mars environments spurred the development of a proposal that was submitted to the Europlanet Trans-National Access program [16]. As alluded to in Chapter 2, much of the existing literature on PAHs found on moons and comets references the laboratory spectra recorded by Colangeli et al., (1992), which is pertinent to PAHs of astrophysical interest, rather than astrobiological, or

specifically Martian. This distinction is important as some PAH compounds are more robust than others upon exposure to high UV flux; those that would survive or even catenate and become more complex within interstellar dust clouds may be unlikely to flourish in Martian conditions, and are therefore not especially pertinent to the search for life on Mars (Dartnell et al., 2012; Allamandola, 2011).

The proposal was to analyse a mixture of PAHs based on those found in Martian meteorites. The results of this chapter form two journal paper submissions, the SPRC part of which is currently under review by JGR Planets (Campbell et al., 2020); the RSL paper is in preparation.

5.1. Methods

The motivation for this set of experiments was to produce empirical observations to support the interpretation of data from orbital observations of the Martian SPRC and RSL-like environments by CRISM, which, as previously mentioned, obtains surface spatial resolution of around ~20 m/pixel (Murchie et al., 2007), with a spectral resolution of ~6 nm (see Section 3.1.4). It is, therefore, necessary to try to emulate CRISM's measurement parameters with laboratory instruments as closely as possible. In order to maximise the spectral resolution of the SHINE and SHADOWS instruments (see section 3.2) to bring it to ~10 nm (as close as possible to CRISM's resolution) the slit width was brought down to 0.3 nm for $\lambda > 2.0$ μm. Throughout the experiments, the CarboNIR cell temperature was kept at -100°C. The full spectral range

sampled was 0.4-3.6 μm with a fixed slit of width 1.5 mm at 10-20 nm resolution. Angular parameters were fixed as an incidence angle = 0° and observation angle = 20°. To complete the measurement of a full spectrum at the highest spectral resolution took >3 hours, so in order to effectively use the time available, multiple shorter spectra over the wavelength ranges of interest were taken. The angular parameters used were fixed incidence angle = 0°, and observation angle = 20°, optimized for the CarboN-IR cell. This is comparable with the median for 0-30° for CRISM (Ceamanos et al., 2013).

In order to produce a PAH spectrum more pertinent to Mars than those produced by Colangeli et al., (1992), we analysed our own mixture of PAHs based on those identified by Wright et al., (1989) and McKay et al. (1996) in the ALH84001 and EETA79001 Martian meteorites; The PAHs used were a mixture of anthracene, phenanthrene and pyrene in raw form, obtained from Sigma-Aldrich, and mixed into a 300 mg sample of equal parts of each PAH species. A ~1% mix of PAH mixture with room temperature, transparent powder (alumine) was tested to establish the minimum amount of PAH required for detection with CO_2 ice, and to define spectral ranges and resolution needed to detect the PAH mixture without interference from CO_2 ice spectra

We chose 3 different PAH concentrations (0.10, 0.54, 0.67% weight fractions) for our 3 PAH samples mixed with CO_2 ice, and various amounts of PAH with salts and brines in order to allow the detection limit to be determined by plotting band depth as a function of concentration. The salt used to create brines was

$MgCl_2$, and the rationale for this is initially discussed in Section 2.4.1, and further in section 5.3.

CO_2 ice was obtained from liquid decompression with a commercial device, SnowPack[©17]. This produces a granular snowpack of 312.5 cm^3 composed of small CO_2 ice grains. The average size of the grains, 150 μm, was estimated by measuring the true surface of the grains observed with a binocular microscope (Philippe et al. 2016). Part of the CO_2 ice snowpack was then manually crushed, weighed, and a known mass of PAH powder was added and thoroughly mixed in a stainless-steel container pre-cooled with liquid nitrogen to avoid CO_2 ice sublimation. The cell, also pre-cooled at 77 K, was filled up to its rim with the mixture (slightly compressed) and weighed before rapid installation inside the pre-cooled CarboN-IR environment chamber (-100°C). The sapphire windows of the cryogenic chamber and of the external chamber were then successively closed and air was completely evacuated from both volumes by pumping using a detailed protocol developed to avoid frost condensation on the windows. In addition, we measured one mixture of 1.5% PAH mixed with JSC-Mars 1 Mars simulant (Allen et al., 1998) as well as the simulant alone, as a reference.

For the RSL analogue experiments, $MgCl_2$, and $MgCl_2.6H_2O$, PAHs, and various mixes of these components at various ratios and under various environmental conditions were also recorded. Eighteen distinct samples were examined, with additional sub-samples examined in various stages of

---

[17] https://industry.airliquide.co.uk/snowpack

hydration. The objective of part of this study is to define the detectability limit of PAHs within RSL analogues, and diagnostic absorption features for higher concentrations of PAHs were recorded at a number of wavelengths. A number of series of spectra were recorded with varying ratios of PAH and salt content, and we found that drying brines within the soil sample increased the detectability of PAHs compared with soil samples devoid of salt.

The sample holder is 4.5 cm in diameter and 2 cm deep and has a total volume of 31.8 cm^3. Knowing the mass of the sample, measured just after filling the holder, and the density of bulk CO_2 ice allowed an estimate the initial density and porosity of the sample to be made.

The percentage of H_2O ice mixed in the CO_2 snow was estimated by comparison of its 1.5 μm band depth with that of the nearby CO_2 bands (at 1.44 and 1.58 μm) and relative to the spectra of a series of CO_2:H_2O ice mixtures previously measured and modelled (Philippe 2016).

After introduction of the sample holder containing the PAH-CO_2 ice mixture into the CarboN-IR cell and throughout the experiments, the cell and sample holder temperatures were kept at -100°C. Following initial measurements of the samples, sublimation experiments were conducted by pumping CO_2 gas into the cell to monitor spectral and detection limit changes with sublimation. Bi-directional reflectance spectra (at a single view geometry) on both full Vis-NIR and partial spectral ranges were recorded regularly during the sublimation

experiment to reflect regions of interest for later comparison to observational results from orbital sensors.

5.2. SPRC Material Analogue Results

A first guess of the detectability limit for PAHs in CO_2 ice was established with reference to levels detected on other planetary bodies such as Iapetus, 10^{-4} to 10^{-3} g/cm^3 (Cruikshank et al., 2008). This was then tested at room temperature with a ~1% mix of PAH mixture with a transparent powder (alumine) in order to estimate the minimum amount of PAH required for detection within CO_2 ice but outside its absorption bands. From this experiment, an approximate detection limit of about 0.1% by weight was determined. This experiment also allowed us to define spectral ranges and resolution needed to detect the PAH mixture without interference from CO_2 ice spectra. A spectrum of the 'pure' PAH mixture was also measured as a reference (grey line in Figure 5.1).

5.2.1. PAH/CO_2 = 0.1% - Sample 1

For the initial sample, an amount of PAH comparable to 10^{-4} to 10^{-3} g/cm^3, the amount detected on Iapetus by Cruikshank et al., (2008) was used. Table 5.1 shows the details of the sample used.

Table 5.1: Details of Sample 1

CO_2 Mass	31g
PAH Mass	32.7mg
Weight percentage of PAH to CO_2	0.10%
Weight percentage of H_2O to CO_2	~0.12%
Density	0.98 g/cm^3
Porosity	38.5%

During this experiment the speed with which the interior chamber was pumped out from the ambient air resulted in water frost particles condensing on the surface of the sample being blown onto the inside of the window, and could not be removed (in the subsequent experiments this was done more slowly and with additional heating of the window to avoid this problem) meaning that water contamination in the spectrum may be stronger in sample 1. A diagram of the environmental chamber can be seen in Figure 3.5, and for the remaining samples, the sapphire window was kept warm using a hair-dryer, and the securing of the window expedited by three people simultaneously securing the window bolts as quickly as possible to prevent condensation.

Two spectra were obtained from 0.4-3.6 µm with a spectral sampling of 20 nm. As the vacuum was very stable, to aid sublimation, a lamp was used to heat the sample surface, at 27cm distance from the window, resulting in 70W/m^2 equivalent to Mars at noon at 70°latitude, achieving a sample sublimation of ~3mm between two spectra. Upon examination of these spectra it was clear that the PAH feature at 3.3 µm was only very marginally evident on the side of

the strong and broad 3.1 µm water ice band, and so the following spectra were taken only between 0.6 and 2.0 µm at 20 nm sampling. Fig. 5.1 shows the results.
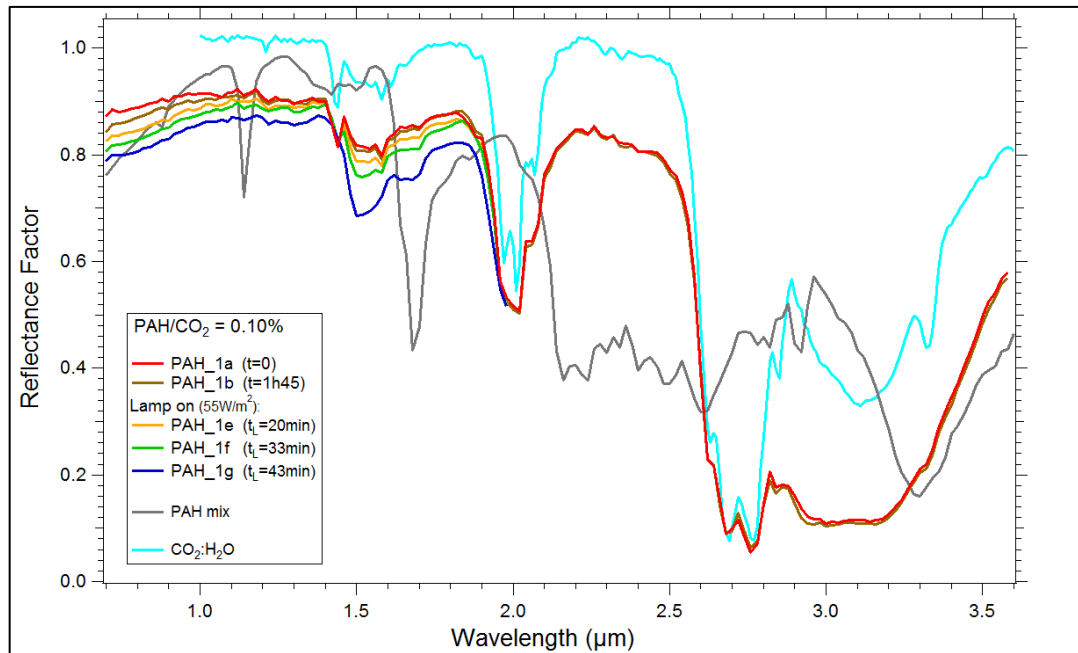
Figure 5.1: Spectra from sample 1, 0.10% PAH in CO_2 ice (with small amount of H_2O ice ~0.12%) during progressive sublimation of CO_2 (PAH_1a to 1g). The sublimation was at furst allowed to occur without any external heating, (1a, 1b) then triggered by illumination with a lamp (55W/m^2 at sample surface: 1e-1g) in order to cause more rapid sublimation as we feared the sample would remain in the same state for too long. The spectrum of the PAH mix and of CO_2 ice (with small amount of H_2O ice ~0.075%) are also shown for reference. Note the increasing slope below 1.1 µm and the bands at the limit of detection at 1.14 and 1.68 µm, but also at 3.29 µm.

It is clear that over time, the reflectance of the spectra (PAH1a-1g) becomes lower as the CO_2 ice sublimates, and the slope increases between 0.7 and 1.1

µm; this is likely to be associated with the steep slope in the corresponding pure PAH mixture spectrum (black line) as sublimation increased the ratio of PAH/CO_2 ice and probably concentrated the PAH at the surface of the sample. We also noticed that the water ice feature which dominates around 1.52 µm increases with sublimation, as the tiny frost particles present at very low level (~0.1%) in CO_2 ice are also segregated at the surface during sample sublimation (Philippe, 2016). A subtle absorption feature is visible in the in PAH 1a-1g series of spectra corresponding with the pure PAH feature at 1.14 µm, with a more ambiguous feature visible at 1.7 µm. It would seem that the 0.10% PAH/CO_2 ice ratio is actually at the detectability limit, and subsequent experiments used a higher ratio to confirm the detection of the PAH bands.

5.2.2. PAH/CO_2 = 0.67% - Sample 2

For this second experiment, more care was taken to limit frost condensation at the surface of the CO_2 ice sample during transfer to the CarboN-IR cell and the ambient air was pumped more slowly to avoid window condensation or frost particles blown onto it, and this proved to be successful. Details of the sample are shown in Table 5.2.

Table 5.2: Details of Sample 2

CO_2 Mass	23.5g
PAH Mass	158.1mg
Weight percentage of PAH to CO_2	0.67%
Weight percentage of H_2O to CO_2	~0.2%
Density	0.74 g/cm^3
Porosity	52%

A higher spectral resolution sampling, (10 nm) resulted in a longer time period to obtain spectra, so a spectral range of 0.7-2.2 µm was chosen to obtain multiple spectra at lower wavelengths to observe the features at 1.1 and 1.7 µm for the first 4 spectra (PAH2a-PAH2d) during the sublimation sequence. There was a small leak in the cell, increasing the sublimation rate, so a lamp was not used for sample 2 to avoid all CO_2 being lost too quickly. The spectral range was then increased to 0.7-2.75 µm and left to run overnight, resulting in total of 16 spectra, shown in Fig. 5.2.
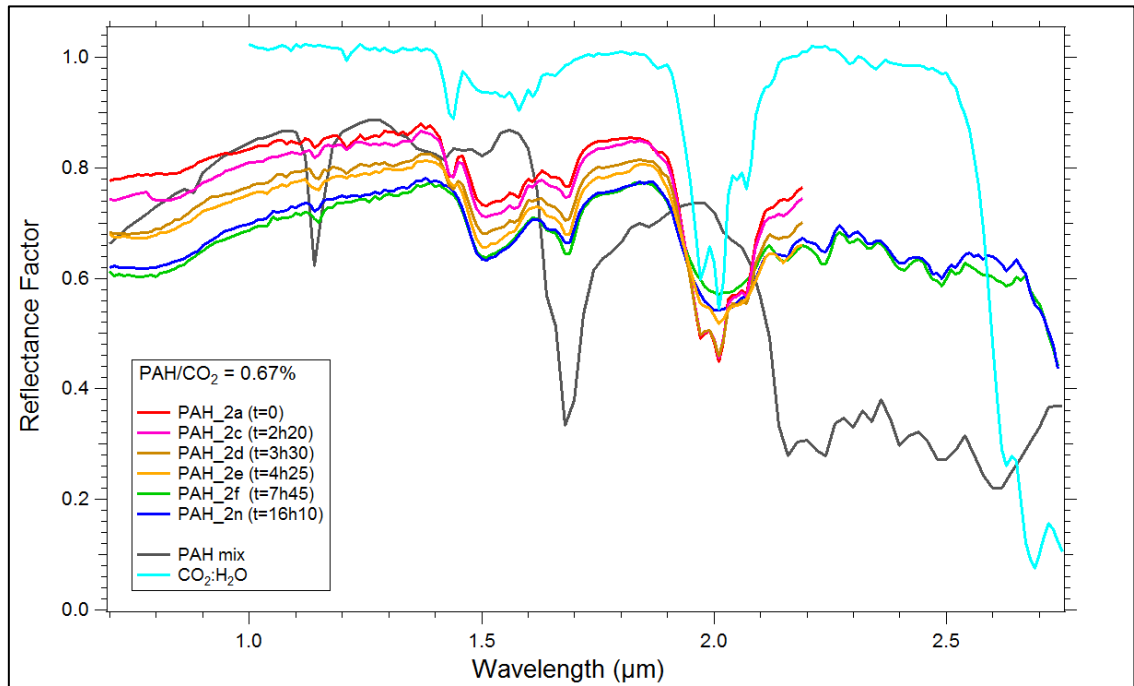
Figure 5.2: Spectra from sample 2, 0.67% PAH in CO_2 ice (with a small amount of H_2O ice ~0.2%) during progressive sublimation of CO_2 (PAH_2a to 2n). The sublimation continued until the complete disappearance of CO_2 ice. The spectrum of the PAH mix and of CO_2 ice (with small amount of H_2O ice ~0.075%) are also shown for reference. Note the increasing slope below 1.1 μm and the bands clearly appearing at 1.14 and 1.68 μm, but also in the 2.1-2.5 μm range

With the increased amount of PAH in the mixture, the absorption features at 1.14 and 1.68 μm are clearly visible throughout all PAH/CO_2 ice spectra, as well as the slope at 0.7-1.1 μm. In the extended spectra PAH2e-PAH2p, there are also corresponding features visible at 2.15, 2.24, 2.41, 2.49 and 2.62 μm in pure PAH and PAH/CO_2 ice spectra.

5.2.3. PAH/CO_2 = 0.54% - Sample 3

For this experiment, a spectral range of 0.4 -2.75 µm was chosen with a resolution of 10 nm. Details of the sample are shown in table 5.3.

Table 5.3: Details of Sample 3

CO₂ Mass	30g
PAH Mass	161.6mg
Weight percentage of PAH to CO_2	0.54%
Weight percentage of H_2O to CO_2	0.08%
Density	0.94 g/cm^3
Porosity	40%

16 spectra were taken throughout the day and overnight during the sublimation sequence. As with experiment 1, the vacuum was very stable, and little sublimation occurred, resulting in fairly homogenous spectra. Results are shown in Figure 5.3.
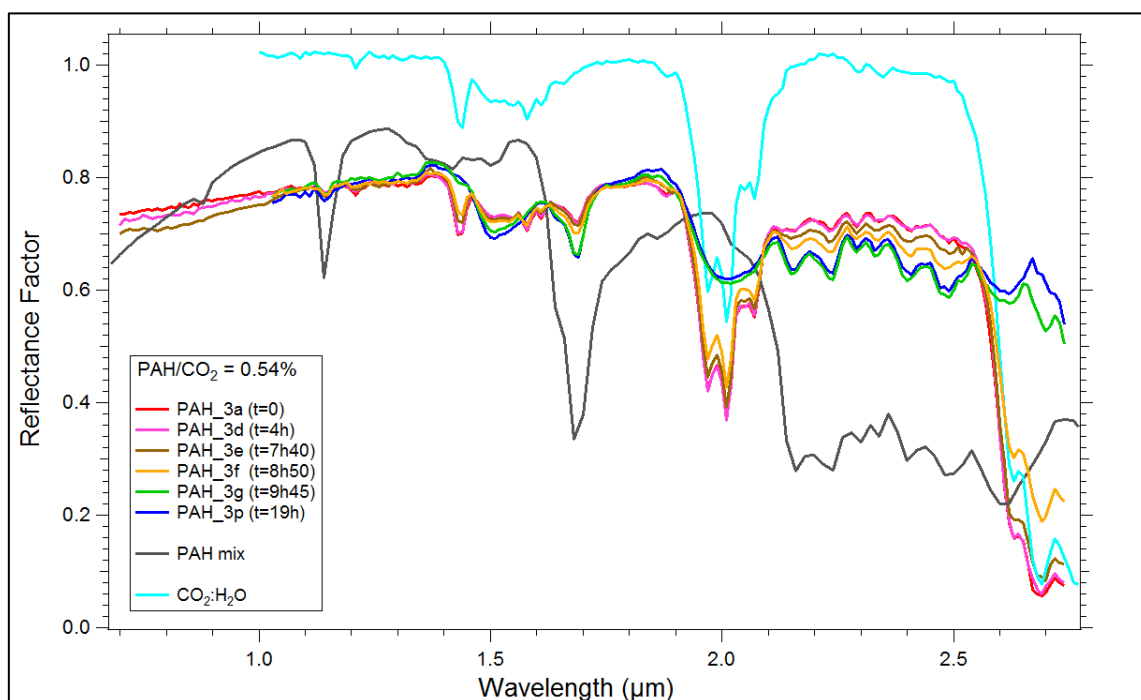
Figure 5.3: Spectra from sample 3, 0.54% PAH in CO_2 ice (with small amount of H_2O ice ~0.08%) during progressive sublimation of CO_2 (PAH_3a to 3p). The sublimation was free until the complete disappearance of CO_2 ice. The spectrum of the PAH mix and of CO_2 ice (with a small amount of H_2O ice ~0.075%) are also shown for reference. Note the increasing slope below 1.1 µm and the bands clearly appearing at 1.14 and 1.68 µm, but also in the 2.1-2.5 µm range

With 0.54% PAH, the features at 1.14, 1.685, 2.15, 2.24, 2.41, 2.49 and 2.62 µm are visible as with sample 2. With these higher signal-to-noise spectra, it is also possible to observe several other replicated PAH features at 2.29 and 2.33 µm, with the PAH/CO_2 ice mixture between 2.1 and 2.5 µm closely mirroring the shape of the spectrum for the pure PAH mixture. The change in the slope at 0.7-1.1 µm is also clear but unfortunately was not monitored until the end of the experiment due to time constraints.

5.2.4. JSC Mars-1 with and without PAH -Samples 4 and 5

An experiment, with two spectra ranging from 0.4-3.9 µm at a resolution of 10 nm, was taken of the PAH mixture in Mars simulant JSC Mars-1, weathered volcanic ash from Hawaii (Allen et al., 1998), as well as a pure dust spectrum for reference (Figure 5.5). Sample details are shown in Table 5.4.

Table 5.4: Details of Samples 4 and 5

	PAH/ JSC Mars-1 Dust Mix	JSC Mars-1 Dust
Dust Mass	7.7g	15.4 g
PAH Mass	117mg	-
Percentage of Dust to CO_2	1.5%	-
Density	1.895 g/cm^3	1.91 g/cm^3
Porosity	48.1%	49.3 %

Figure 5.4 shows the pure dust spectra alongside the PAH mixture and Mars regolith simulant with 1% PAH content.
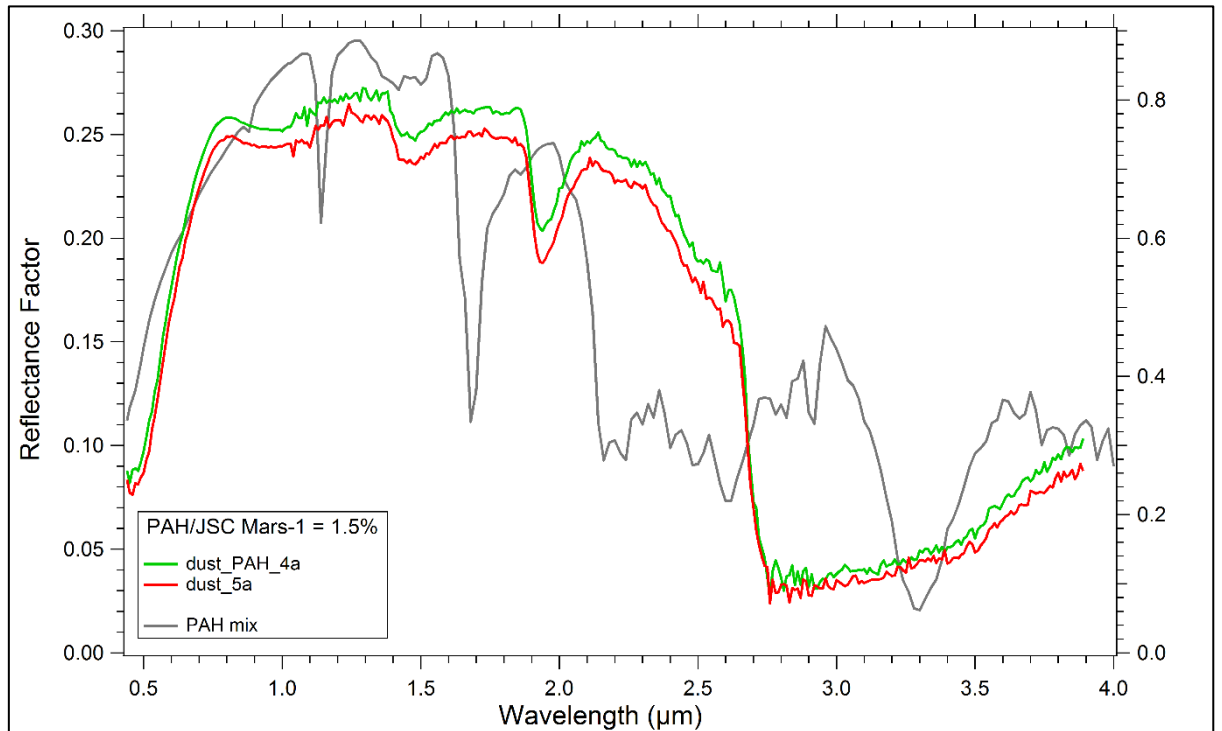
Figure 5.4: Spectra from samples 4 and 5, 1.5% PAH in JSC Mars-1 (dust_PAH_4a), and JSC Mars-1 (dust_5a). The spectrum of the PAH mix is also shown for reference. Note that no sign of increase in slope below 1.1 μm and no bands are detected at 1.14, 1.68 μm, nor at 3.29 μm

Despite PAH particles being clearly visible in the physical sample (see Figure 5.5), and the ratio of PAH to substrate being 2.5 to 3 times higher than in ice samples 2 and 3, (1.5% compared to 0.67% and 0.54%), no spectral features of PAHs are detectable in the dust spectrum.
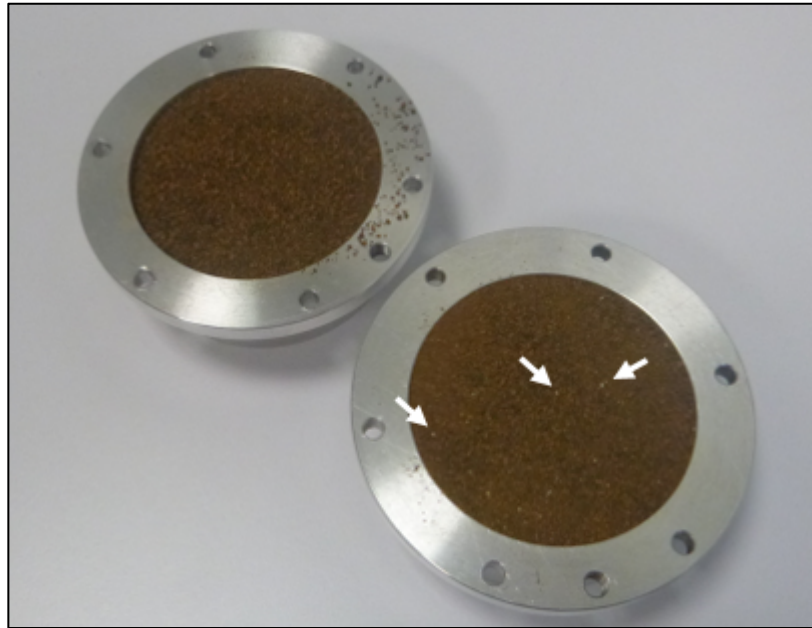
Figure 5.5: JSC Mars-1 samples. Upper left sample contains no PAH, bottom right contains 117 mg of PAH mix, with some individual grains visible on the surface (highlighted with white arrows)

Other than the pure dust sample being slightly lower in overall reflectance, there is no observable difference in spectra between pure dust and PAH/dust mix. This may be because of the relative opacity of dust compared with CO_2 ice, as well as its reflectance being three times lower. If PAHs are not discernible in Martian dust as ratios an order of magnitude higher than that detected on Iapetus, it is likely to be an extremely limiting factor in detecting PAHs on the SPRC if any potential PAHs are mixed with dust and not in pure form. No known segregation process can concentrate PAH in dust as is the case with PAH/CO_2 ice mixtures. In order to ascertain whether PAHs in small amounts of dust within CO_2 ice are detectable, further experiments would need to be carried out to better emulate the scarp wall dust deposits in the SCT. The next section deals with RSL analogue experiments.

5.3. RSL Analogue Experiments

This next set of experiments was designed to find endmembers and detectability limits of PAHs pertinent to Recurring Slope Lineae-like environments. As discussed in Section 2.4.1, various salts have been discussed as potential brine components in RSL, but based on the THEMIS detections (Osterloo et al.,2010) and the laboratory analogue experiments performed by Massé et al., (2014) magnesium chloride was chosen for these experiments. Both the non-hydrated ($MgCl_2$) and hexahydrate variants ($MgCl_2.6H_2O$) were considered, the latter of which would occur in any condition where magnesium chloride had been in contact with moisture (PubChem, 2004). The non-hydrated variant was examined, but the hydrated magnesium chloride used for most experiments based on the assumption that RSL's are a wet process, and given that near-surface thermal conditions on Mars are not known to have ever reached temperatures capable of dehydrating the molecules (Krasnopolsky, 2010; Dolezal, 1976)

To begin sample preparation, the large, ~0.5 cm flakes of $MgCl_2.6H_2O$ were ground down using a pestle and mortar and sorted to a range between 100-200 µm using sieves and vibration plates. It was not possible to grind to smaller sizes than this due to the spontaneous deliquescence exhibited by the magnesium chloride when kept at room temperatures and exposed to normal levels of humidity. After grinding, the samples were allowed to dry in an oven at ~50°C in order to recrystalise any wet material before sorting. In order to ensure the regolith analogue was a consistent grain size with the salts, the

JSC Mars-1 was sorted using sieves and vibration plates to sort between 100 and 200 µm. While these grain sizes are larger than typically found on the surface of Mars (20-80 µm; Dollfus and Deschamps, 1986), Martian sand dunes have been found to be significantly coarser (210 µm; Edgett, and Christensen, 1991). The decision to opt for relatively coarse regolith analogue grains was also informed by our aforementioned inability to grind the magnesium chloride any finer without deliquescence occurring, and our desire to keep the discrepancy between salt and dust particle size to a minimum.

Due to the large number of samples and spectra taken for the RSL analogue experiments, a sample by sample description is not the best way to present the results as with the small number of SPRC samples from the first part of this chapter. Instead, results have been combined into figures that best illustrate the results and how to they compare to each other, and the story they tell.

5.3.1. RSL Analogue Endmembers

Four distinct endmember spectra were obtained in sequence for RSL analogues; the PAH mixture discussed already in section 5.1, JSC Mars-1 simulant, and both hydrous and non-hydrous magnesium chloride ($MgCl_2.6H_2O$ and $MgCl_2$) variants described in the previous section.

Figure 5.6 shows the four endmembers established by these experiments.
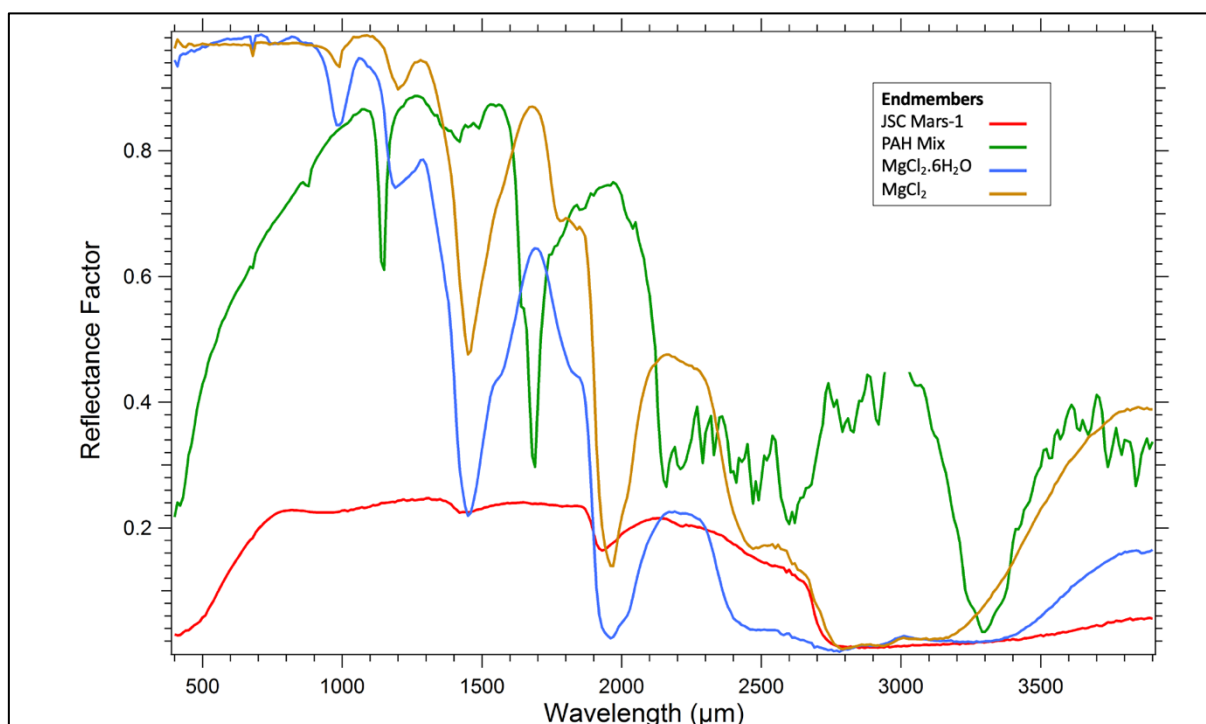
Figure 5.6: Endmember spectra for JSC- Mars-1, PAH mix, hydrous and non-hydrous magnesium chloride

Henceforth, we use only the hydrated form of magnesium chloride for these experiments, ($MgCl_2.6H_2O$) for the reasons discussed earlier in this section.

5.3.2. Increasing % of PAH mix in $MgCl_2.6H_2O$

The first set of RSL experiments were designed to ascertain whether the PAH mixture spectrum could be detected within the $MgCl_2.6H_2O$ spectrum. Figure 5.7 shows the spectra for $MgCl_2.6H_2O$ with PAHs mixed uniformly through the dry salt sample at various concentrations from 0-5% and then analysed with the spectro-goniometer radiometer.
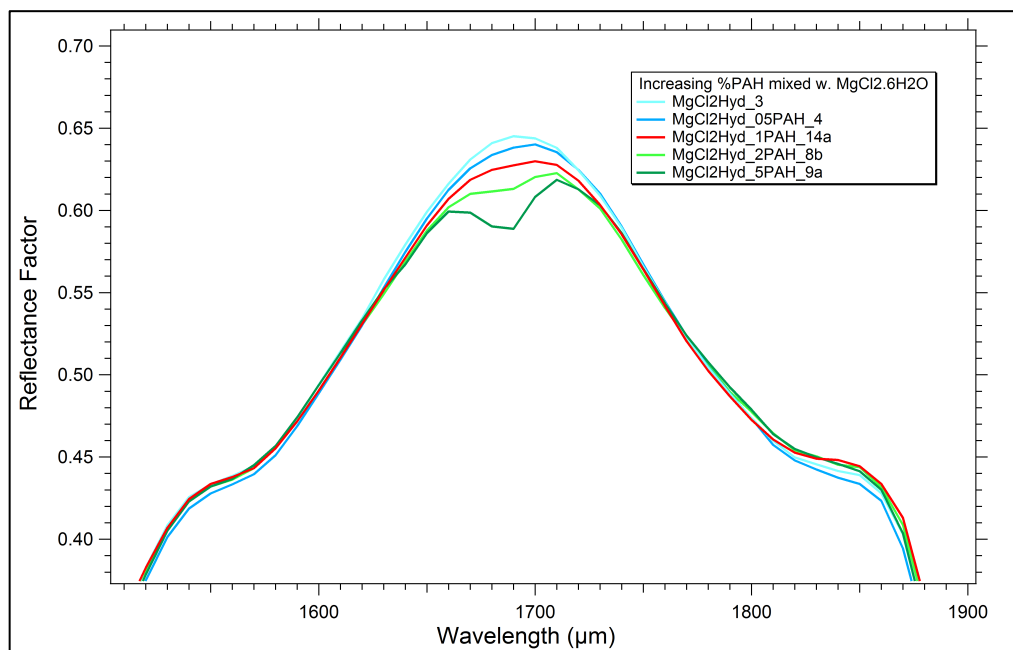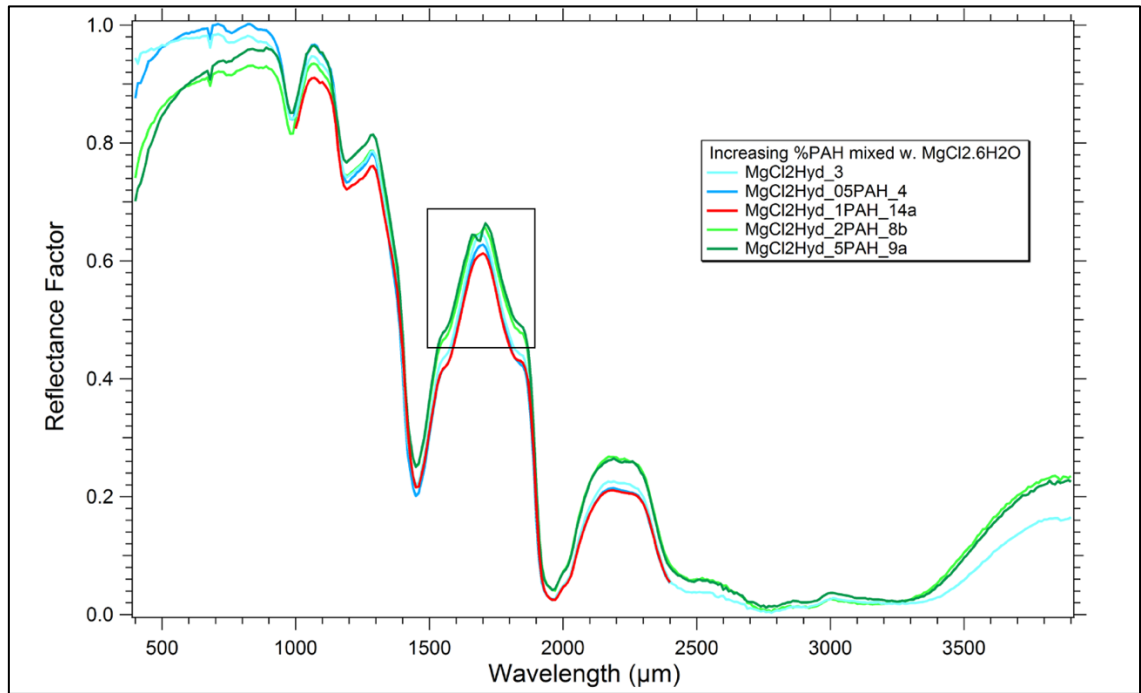
Figure 5.7: (Top) Entire range spectra for MgCl₂.6H₂O with concentrations of PAH mix at 0, 0.5, 1, 2 and 5% content. Black box indicates detail shown (bottom) of 1.5-1.9 µm

With an increase in PAH content it is clear that the PAH absorption feature at 1.7 µm deepens significantly. An obvious flattening of the magnesium chloride peak is clear with 1% PAH content, and so next this amount of PAH in

162

$MgCl_2.6H_2O$ was thoroughly mixed with varying amounts of JSC Mars-1 is shown in Figure 5.8.
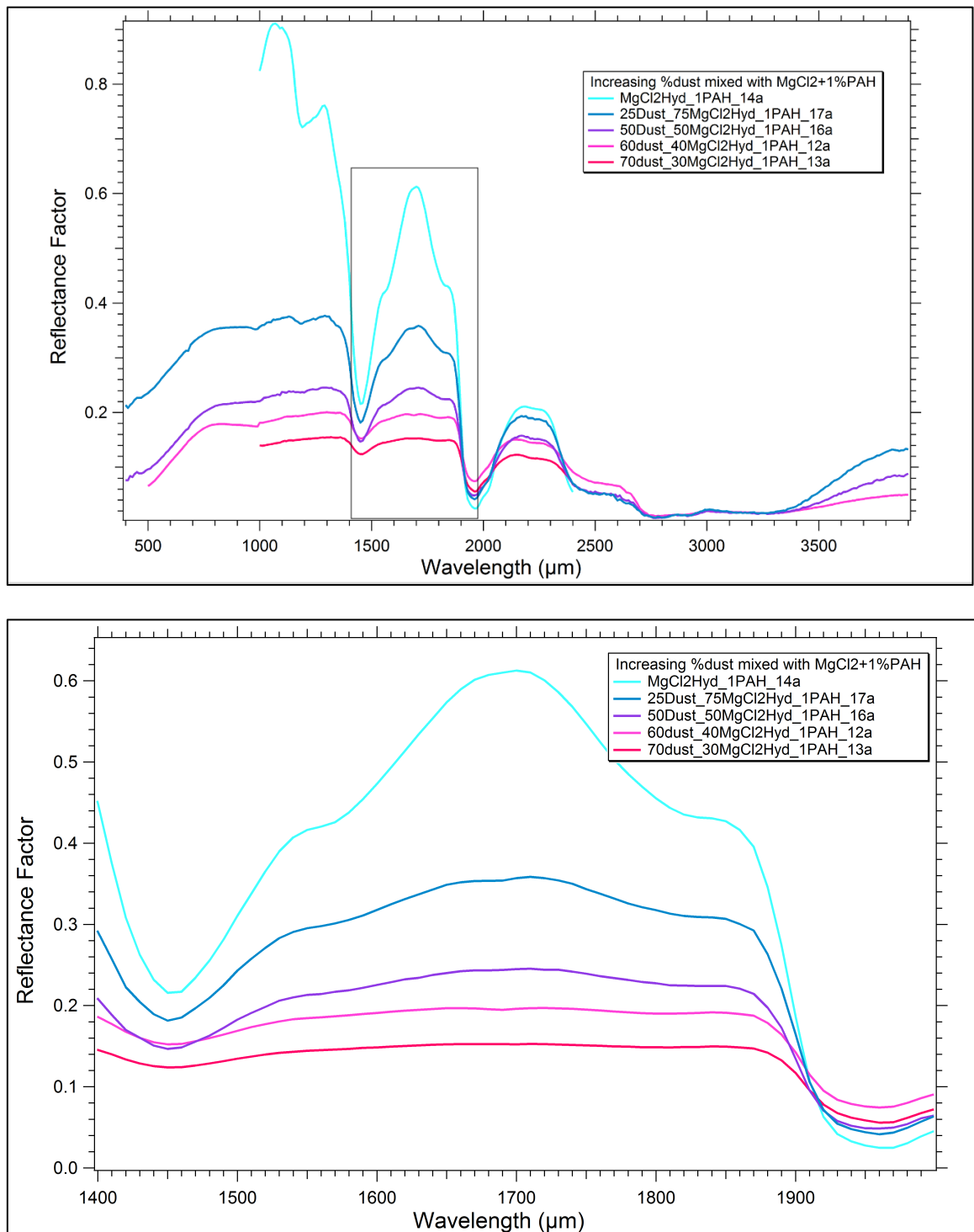
Figure 5.8: (Top) Entire range spectra for $MgCl_2.6H_2O$ with 1% PAH mix with 0. 25. 50. 60 and 70% JSC Mars-1. Black box indicates detail shown (bottom) of 1.4-2.0 μm

Up to 60% dust content mixed with the $MgCl_2.6H_2O$ + PAH still allows a very slight PAH absorption feature to be visible at 1.7 μm, despite the overall PAH content of the entire sample being <0.5%. This begs the question though why PAH signatures were not apparent in Sample 4, where 1.5% of PAH was included in JSC Mars-1. This is likely due to decreased opacity of the soil because of the presence of salt crystals, which allow light through.

5.3.3. Wet JSC Mars-1 with 1% of PAH mix in $MgCl_2.6H_2O$ observed until dry

So far, all the samples had been dry. Next we wanted to see how the PAH spectra might behave if the sample was wet. As the 1% PAH signature was still just visible in $MgCl_2.6H_2O$ mixed with 60%, we tried the 1% PAH with $MgCl_2.6H_2O$ at 70% to see if the wetting of the sample increased visibility of PAH at all. In order to acquire this spectrum, the salt and PAH mix was saturated with water. Figure 5.9 shows the wet sample at various stages of drying out and the same percentage mix that has never been moistened.
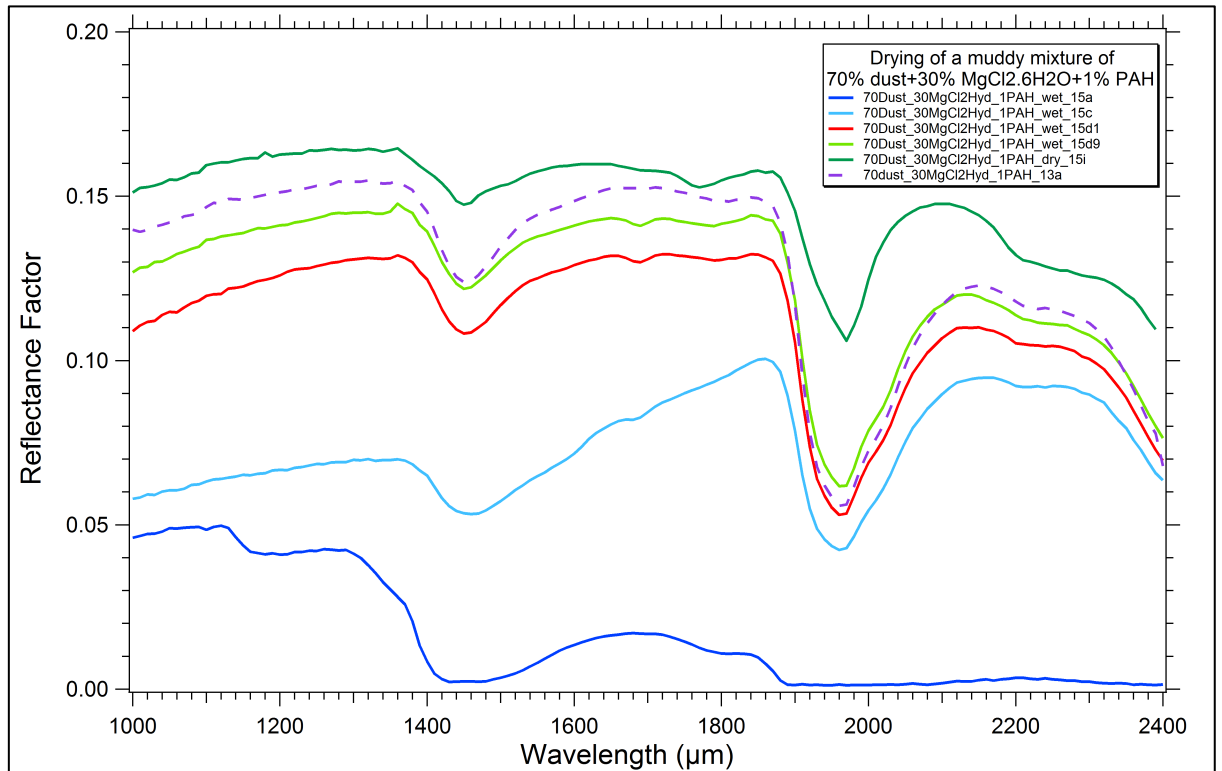
Figure 5.9: Spectra for MgCl₂.6H₂O with 1% PAH mix with 70% JSC Mars-1

In the early stages of spectra acquisitions where the sample is most wet, the H_2O overwhelms all other signatures, which is to be expected. It seems that when the sample is partially wet the PAH signature is more pronounced but only just visible in the sample that has dried out or never been moistened. For reference, the purple dotted line is the same content sample that had never been moistened is shown in Figure 5.9. It would appear that the drying out of the sample creates a crust once completely dry that slightly lowers the detectability of the PAH content compared to the slightly damp stage of spectral acquisition or the sample that was never moistened. Figure 5.10

shows the samples in various stages of wetness where the crust can be seen on the dried sample.

Figure 5.10: Samples of MgCl$_2$.6H$_2$O with 1% PAH mix with 70% JSC Mars-1at various stages of drying. Left is saturated with water, middle still slightly damp, right completely dry with hard crust formed

The centre stage of figure 5.10 was the optimum state of hydration, (slightly damp) for detecting PAH during spectra acquisition, which may give us insights about what time of year is best to analyse RSL in-situ. If indeed RSL is a wet process, the lengthening and darkening stage may mean water overwhelms any subtle signatures, while too late in the summer may mean a crust has formed and reduced any potential detectability.

5.4. Preliminary Conclusions

The results of these novel experiments are extremely useful to allow a future analysis of orbital observations from the infrared spectrometers at Mars, and establish a detection limit for PAHs in CO$_2$ ice, that can be applied not only to the poles, but in shadowed regions elsewhere, and in sub-surface ice that may

be sampled during future exploration as well as in RSL-type features. In addition, we ascertained the limitations of observing PAHs directly in Martian regolith, and how the presence of salts, particularly while the regolith is partially damp, may increase the detectability of subtle PAH features. This study also provides more relevant data in the near-infrared range on Mars regolith, brines and diagnostic PAH signatures of astrobiological importance to Mars, that are pertinent to planetary ices, while most previous literature uses mid-infrared transmission data from the 1990s which is more relevant to interstellar dust cloud PAH detection.

PAHs are a missing piece of the search for life on Mars, and despite their abundance in space, their detection on planetary bodies remains a primary objective for the field of planetary science. This work provides much needed PAH spectral signatures relevant to Mars, and features at wavelengths discernible in CO_2 ice and briny soil, which are extremely useful for the interpretation of Mars orbital hyperspectral data from polar, mid-latitude and equatorial regions. In particular, we have shown that the most interesting and sensitive signature of PAH for detection on the Mars residual CO_2 ice cap is at 1.68 μm, well outside the CO_2 and H_2O ice bands (Figure 5.1). The slope between 0.7 and 1.1 μm, and the absorption features at 1.14 and in the 2.1-2.5 μm range may also provide additional clues to confirm detection. On the other hand, the 'classical' strong 3.29 μm fundamental band is buried in the wing of the strong, and frequently saturated, water ice band at 3.1 μm. A detectability limit of ~0.1% has been established for observing PAH features in sublimation CO_2 ice while 1.5% PAHs yielded no discernible features in

Mars regolith analogue. The addition of $MgCl_2.6H_2O$ reduced the amount of PAH needed for detection to <0.5%, and slightly damp samples provide the optimum environment for PAH detection sensitivity. Figures 5.11 and 5.12 summarise the most interesting spectral results, and links to all the raw data from these experiments can be found in Appendix C.
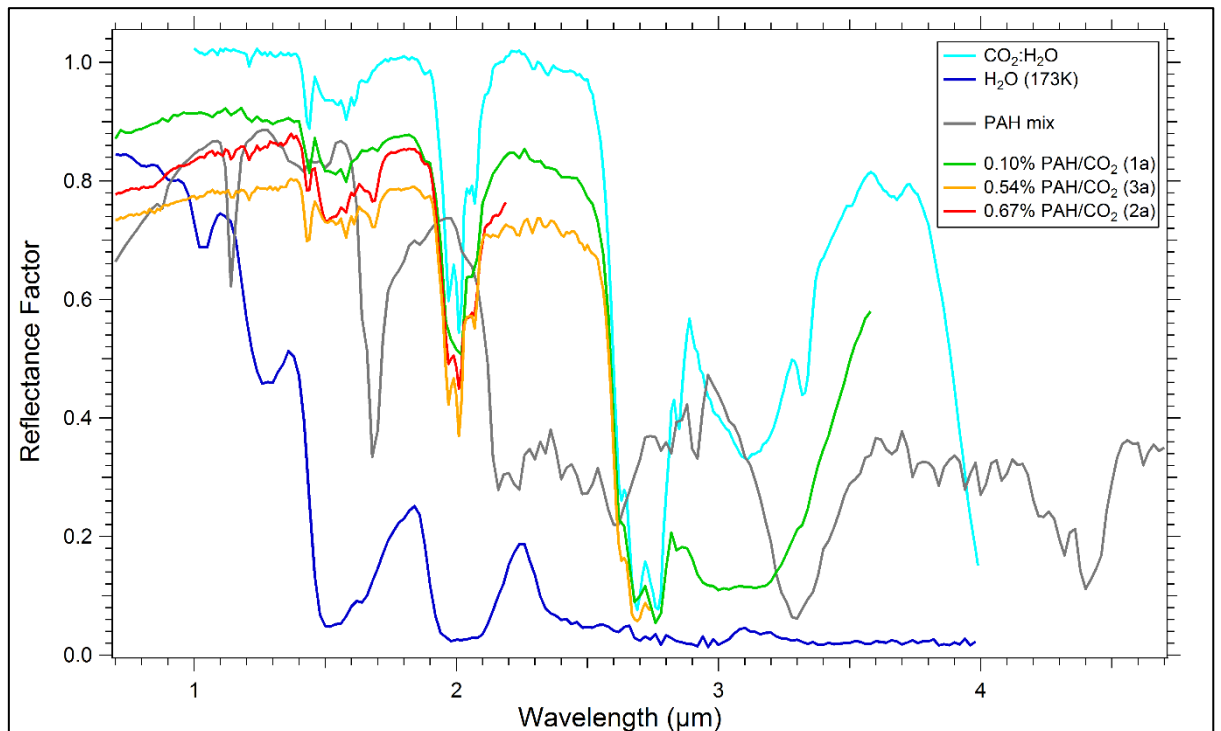
Figure 5.11: Spectra from three initial samples (1a, 2a, 3a) with varying

amount of PAH in CO_2 ice (with small amount of H_2O ice ~0.08-0.2%)

compared to the spectrum of the PAH mix and with those of CO_2 ice (with

~0.075%) H_2O ice) and pure H_2O ice at 173K (Philippe 2016).
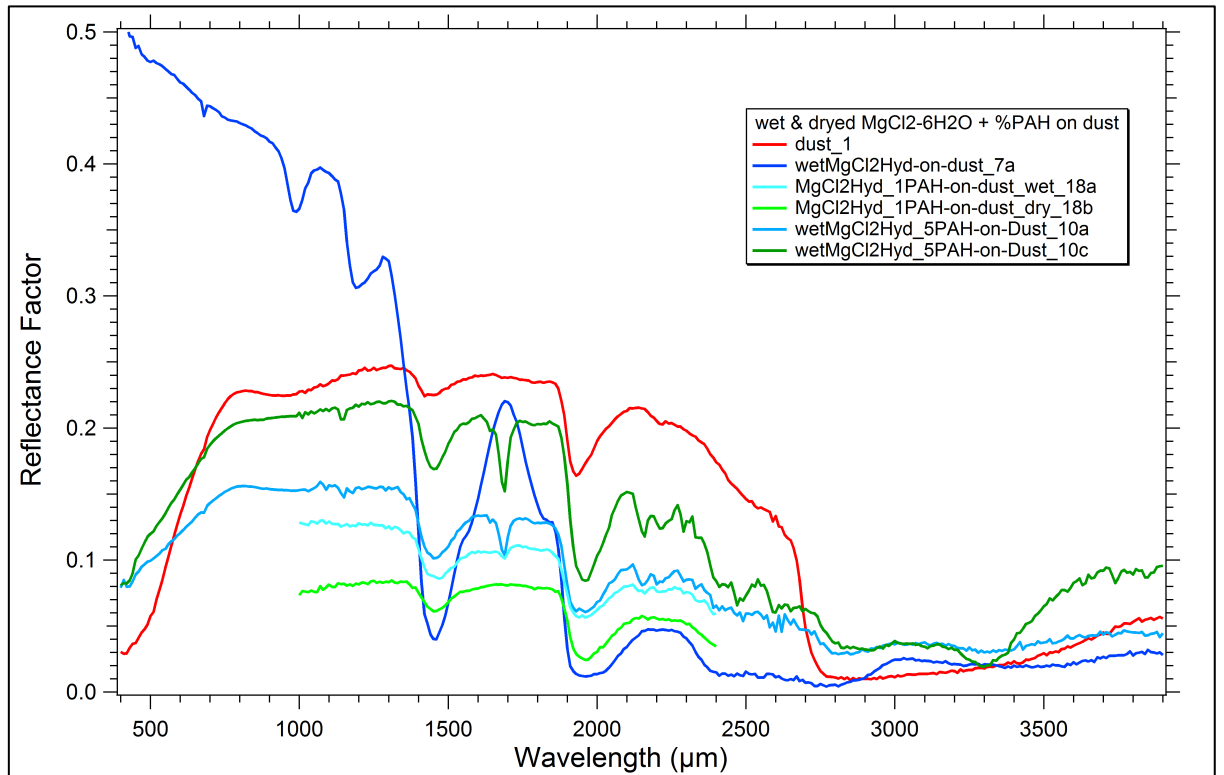
Figure 5.12: Spectra for JSC Mars-1, wet, damp and dry brine samples with 1% and 5% PAH content, illustrating that damp, briny samples are the prime conditions ofr PAH detection.

In the next two chapters, we will look at how these laboratory results can be applied to data over the SPRC, and to RSL sites at Valles Marineris.

6. Extended Analysis of SPRC to Search for PAH Candidate Site

As we discussed throughout the thesis, of utmost importance to this study is the presence of material uncovered from the subsurface. In the case of SCT, this means finding areas that are dustiest, and that are continuing to expose increasing amounts of dust, are of particular interest. Whilst it's clear that dust rims are present on various SCT pit morphologies, the regions examined so far give us only a snapshot of what is happening with dust exposure, and new information has since come to light about the dust's origin. All of the dustiest regions examined so far cover less than one 20 m CRISM pixel, and it is unclear what the source of the dust is and whether the dust is accumulating over time. Therefore, in this section, we will look at the different morphologies and changes over time to various SCT pit features, in order to gain some insight into the processes that are occurring and how these affect dust accumulation. The laboratory results from chapter 5 will then be used alongside analysis of the composition of dusty regions to search for evidence of PAHs.

6.1. Study Region

In a similar fashion to the survey carried out in Section 4.1, all CRISM FRT imagery was collated covering the SPRC, and manually assessed for quality and for repeat imagery providing seasonal or multi-year coverage (Figure 6.1).
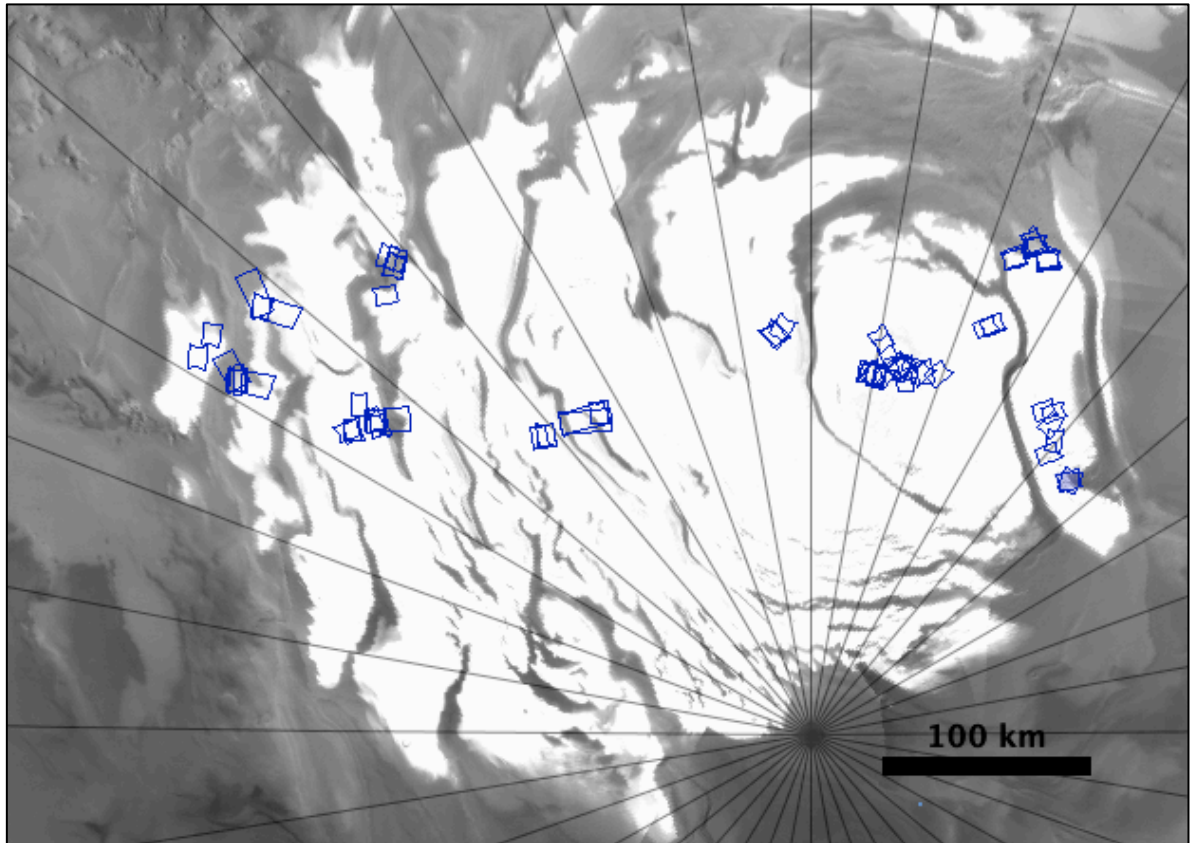
Figure 6.1: Distribution of multi-season and multi-year FRT CRISM coverage of the SPRC. Produced in JMARS, over MOC mosaic

Coverage by other instruments (HiRISE and CTX, see section 3.1) was also ascertained and quality assessments carried out. HiRISE imagery has been included that is as close as possible to the CRISM acquisition time and date, and with similar phase angles to make analysis as consistent as possible, though this was not always feasible.

Each group of CRISM imagery covering a specific region was analysed in detail to see what could be gleaned from the spectral and morphological changes over time. In the next section we will go through each morphology in

turn, and discuss results of interest. For a reminder of the morphology types described by Thomas et al., (2009), see section 2.3.2.

6.2. Spectral analysis of SCT Morphologies

As discussed in Section 2.3, Mars' surface is chiefly made up of mafic mineralogy, namely basalt. Spectral analysis using spectral profiles and summary products showed that on the SPRC, pyroxene, (a major constituent of basalt), both low and high calcium variants, were the easiest to recognise and seem to be abundant around particular morphologies. In Chapter 4, the summary product for carbonates was used but had mixed results. Given the subsequent publication by Buhler et al., (2017) about entrained dust ejection, the updated summary products devised by Viviano-Beck et al., (2014) which removed the carbonate summary product due to its unreliability, and my own better results using bands that look for mafic mineralogy, it seems that the summary products for pyroxene are better for looking for potential sites for PAHs. Therefore, it is pyroxene that we concentrate on when looking for the dustiest areas from now on. Please see Section 3.4 for a reminder of the details of summary products.

6.2.1. Fingerprint Terrain (A2 Type Morphology)

Figure 6.2 shows a region of Fingerprint Terrain (Type A2) as described by Thomas et al., (2009). It shows the site of CRISM and HiRISE imagery over a CTX background while Table 6.1 shows the imagery details.
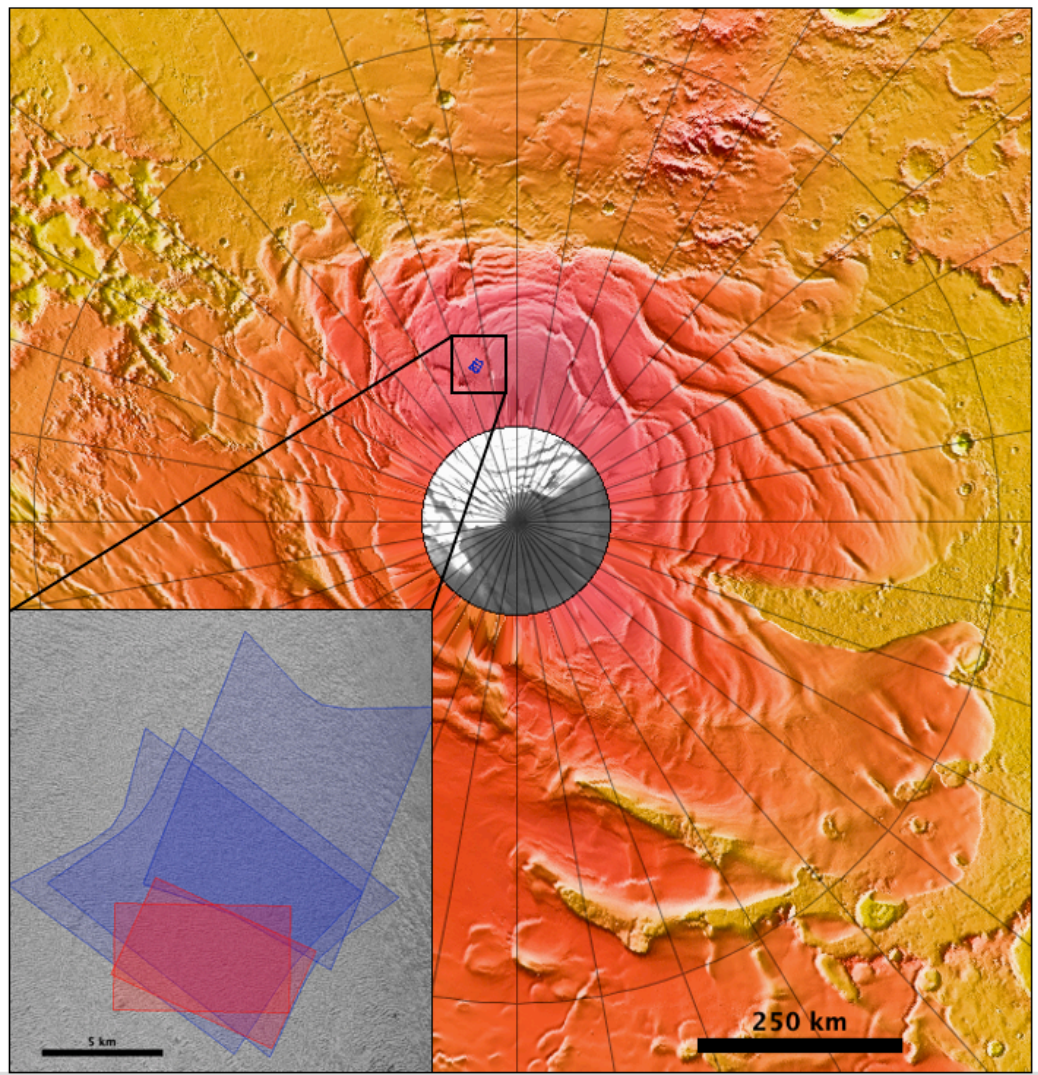
Figure 6.2: Location imagery of an example of A2 Type morphology; main figure shows location of CRISM and HiRISE products, (Lat: -86.6 Long: -23.9) over a colourised and hill-shaded 112m MOLA elevation map. Inset shows detail of footprints of CRISM (in blue).and HiRISE products (in red) used in this study over a CTX background image P13_005983_0879_XI_87S058W. Produced using JMARS

Table 6.1: Details of CRISM and HiRISE products covering A2 Type

Morphology

Instrument	Product ID	Acquisition Date	Mars Year	Solar Longitude°	Phase Angle°
CRISM	FRT00005FDB	31-May-2007	28	248	70
CRISM	FRT00011B05	22-March-2009	29	232	73
CRISM	FRT00011D89	02-April-2009	29	239	71
HiRISE	ESP_031244_0930_RED	27-March-2013	31	289	68
HiRISE	ESP_040357_0930_RED	07-March-2015	32	304	67

This type of terrain is thought to be the final stage of the SCT 'life-cycle'. The typical pit features of SCT are thought to be almost entirely eroded (Figure 6.3).
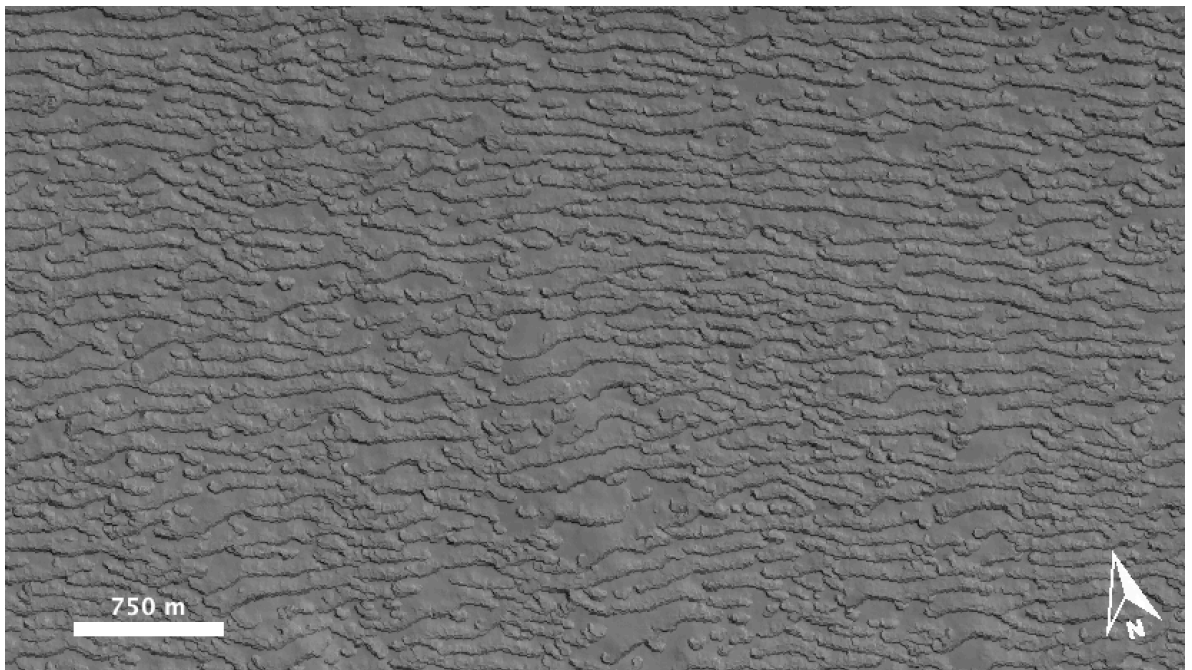
Figure 6.3: HiRISE image ESP_031244_0930_RED showing eroded

'Fingerprint Terrain', Type A2 morphology

As might be expected, the area shows virtually no dust content, certainly not concentrated around any vestigial rim features. Figure 6.4 shows that the region is almost entirely CO_2 ice-covered using CRISM summary products.
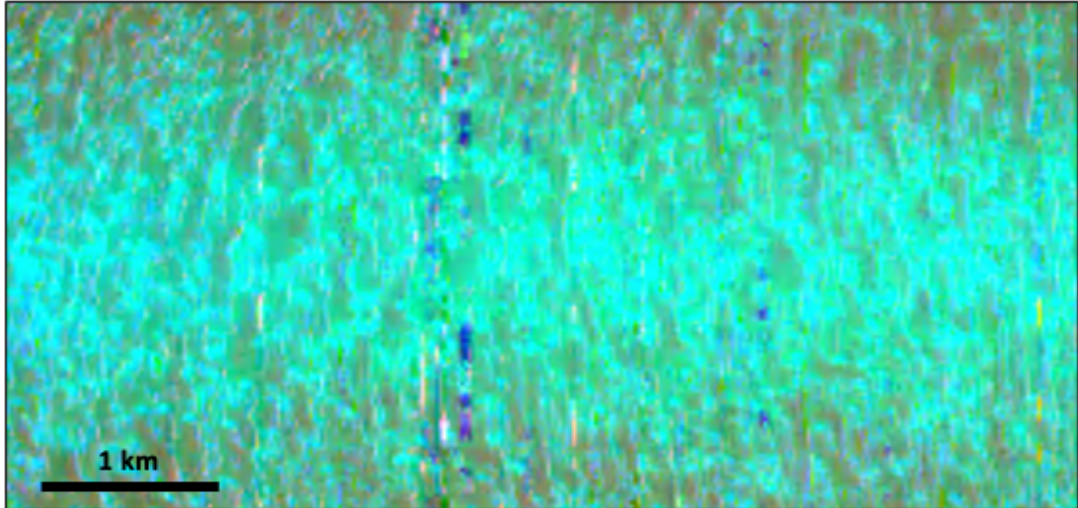
Figure 6.4: CRISM scene FRT00005FDB in RGB using Viviano-Beck et al.,(2014) summary products. Red = high-calcium pyroxene, Green= 1435 (CO_2 ice) and Blue = 1500 (H_2O ice).

This dearth of dust material was the case for every example of fingerprint terrain examined, and so Type A2 morphology will not be considered as a candidate site for dust left by sublimation, and therefore will not be examined for the presence of PAHs.

6.2.2. Circular Pits (Type B Morphology)

This is by far the most abundant SCT terrain type on the SPRC, and considered to be the middle stage of the SCT 'life-cycle'. Much of the terrain

examined in chapter 4 was Type B, and showed some areas of dust around rims, and higher levels of water ice than surrounding pit floors and mesa tops, which were largely CO_2 ice. This was also the case when examining a larger data set. Study of the same pits over time showed a slow increase in pit size between some images, while many others remained static over a number of years. There were no particularly interesting examples of dust content between multi-year images. Many pits exhibit little dust cover, and, as in chapter 4, the water-rich rims and especially CO_2 ice dominated the summary product analysis and spectra, with every pit examined having only sub-pixel dust coverage. Type B, while abundant, is not an ideal candidate for looking for dust coverage or PAHs.

Below is the location of some Type B morphology (Figure 6.5) while Table 6.2 shows the imagery details.
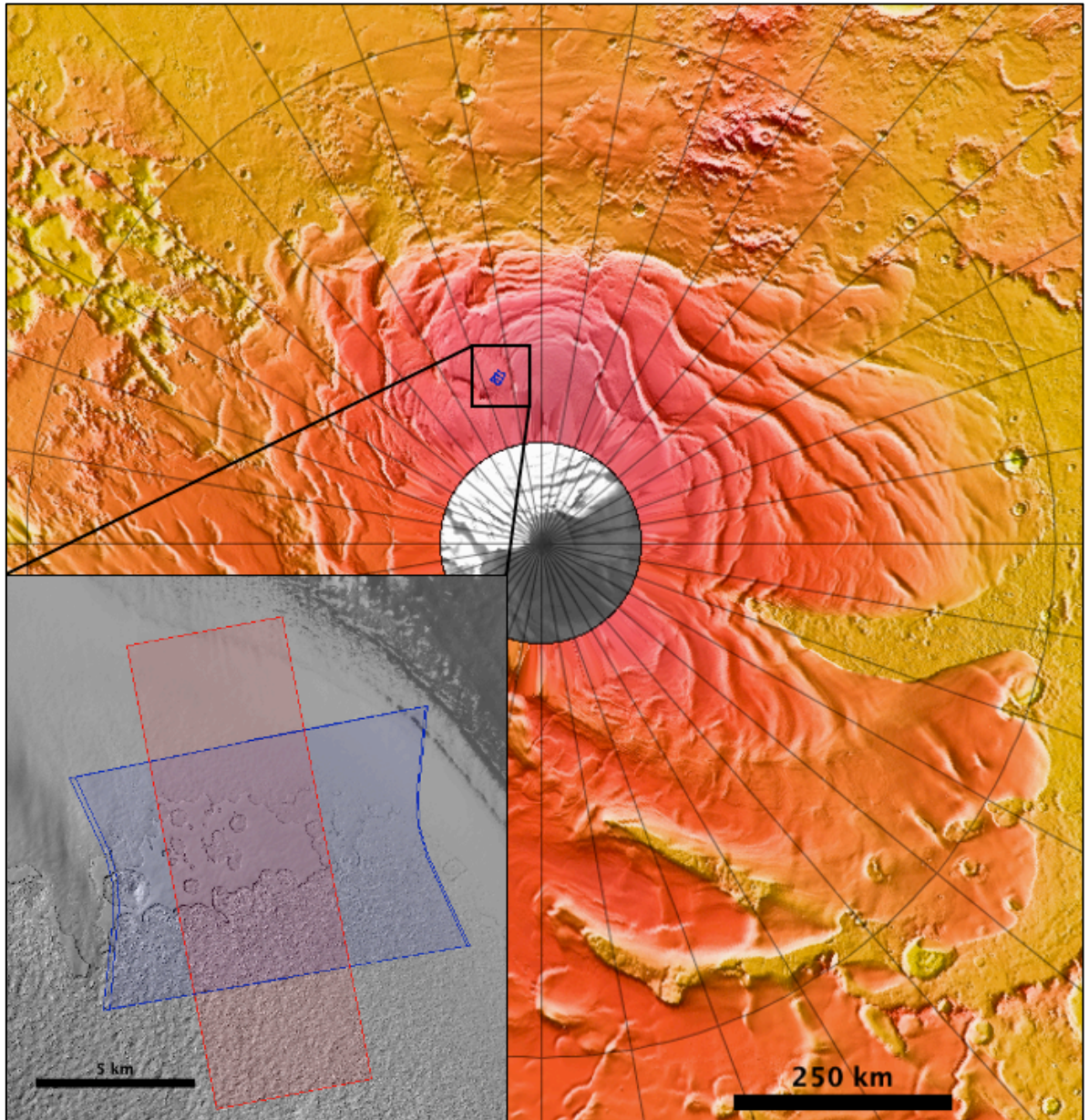
Figure 6.5: Location imagery of an example of B Type morphology; main figure shows location of CRISM and HiRISE products, (Lat: -85.6 Long: 6.4) over 112m colourised and hill-shaded MOLA elevation map. Inset shows detail of footprints of CRISM (in blue) and HiRISE products (in red) used in this study over a CTX background image G11_022421_0944_XN_85S353W. Produced using JMARS

Table 6.2: Details of CRISM and HiRISE products covering A2 Type

Morphology

Instrument	Product ID	Acquisition Date	Mars Year	Solar Longitude°	Phase Angle°
CRISM	FRT00006EC9	03-Aug-2007	28	289	67
HiRISE	PSP_004778_0945_RED	03-Aug-2007	28	289	65

Due to the extensive coverage of Type B morphology, it was not possible to manually examine each individual pit feature; Chapter 4 has a more in depth study of many of these features, but given the progression of this study, and the desire to find morphology with dust accrued by sublimation, and the spectral results of all Type B morphology that was examined, Type B morphology does not seem to be the best morphology to find large amounts of dust with multi-pixel coverage. Below in Figure 6.6 is a typical example of how Type B morphology responds spectrally when examined for pyroxene.
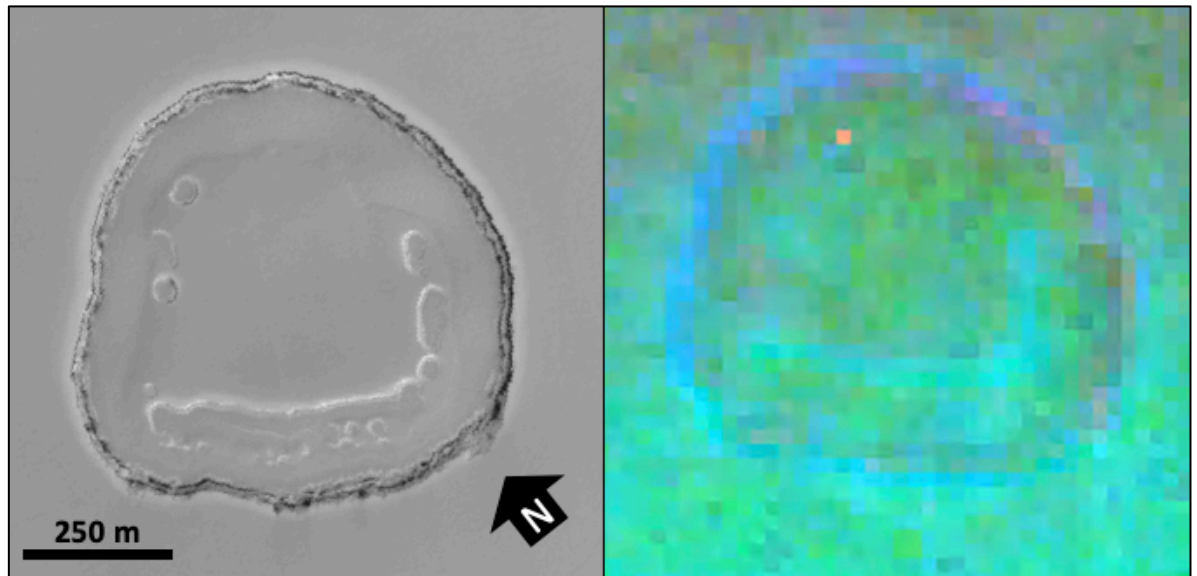
Figure 6.6: HiRISE image PSP_004778_0945_RED (left) CRISM scene FRT00006EC9 (right) in RGB using Viviano-Beck et al.,(2014) summary products. Red = high-calcium pyroxene, Green= 1435 (CO_2 ice) and Blue = 1500 (H_2O ice).

Type B morphology is interesting in that it tends to be rich in water ice around the rims but does not have a high dust content. Where rims are dust covered, examination of HiRISE imagery often shows areas of dust metres across in scale, which is insufficient to fill an entire 20m CRISM pixel, and therefore only adds to the problem of ice signatures interfering with any dust composition analysis. Water ice is also problematic for any comparisons with the laboratory results described in Chapter 5, as the experiments were based on primarily CO_2 mixed with PAH. Therefore, dusty areas over less H_2O rich rims would be preferred, another reason to eliminate Type B morphology.

6.2.3. Heart/Bean Shaped Curls (Type A1 Morphology)

This morphology is thought to be the earliest stage of SCT morphology, when pits have not yet formed circular shapes. Figure 6.7 shows the location of some CRISM imagery covering this type of SCT and below that is a table of the imagery details.

Figure 6.7: Location of coverage of Type A1 morphology; main figure shows location of CRISM and HiRISE products, (Lat: -86.8 Long: -6.2) over 112m colourised and hill-shaded MOLA elevation map. Inset shows detail of footprints of CRISM (in blue) and HiRISE products (in red) used in this study over a CTX background image G07_020800_0931_XN_86S006W.

Produced using JMARS

Table 6.3: Details of CRISM and HiRISE products

Instrument	Product ID	Acquisition Date	Mars Year	Solar Longitude°	Phase Angle°
CRISM	FRT00005AE3	14-May-2007	28	237.7	70
CRISM	FRT00007F62	30-Sept-2007	28	322.5	80
CRISM	FRT00011DA4	03-April-2009	29	239.2	69
HiRISE	PSP_005517_0930_RED	30-Sept-2007	28	322.5	79.6
HiRISE	ESP_029134_0930_RED	13-Oct-2012	31	329.7	87.3

Using the Summary Product specifications from Viviano-Beck et al., (2014); different RGB composites were generated for CRISM scenes to best highlight any dust deposits on SCT depression rims. Several combinations were tested to best highlight regions that appeared dark and dusty in the corresponding HiRISE imagery. The best combination was found to be:

• BD1435; diagnostic of CO_2 ice; displayed in the red channel

• BD1500; diagnostic of H_2O ice; displayed in the green channel

• LCPINDEX2; diagnostic of low calcium pyroxene; displayed in the blue channel

The red and green channels highlight the two most abundant units on the SPRC (CO_2 and water ice) while the blue channel is indicative of a common component of typical Martian mineralogy, in this case low calcium pyroxene ($[Mg,Fe]Si_2O_6$). Dust rims are also manifested clearly using summary products for other common Martian minerals, such as high-calcium pyroxene ($[MgCa,FeCa]Si_2O_6$) and olivine ($[Mg,Fe]_2SiO_4)$, but LCPINDEX manifests most strongly when combined with the ice summary products. 'False Colour' RGB composites were also generated for each CRISM scene, using bands 230 (2509.7 nm), 75 (1486.9 nm) and 10 (1060.3 nm) for red, green and blue channels, respectively as these most closely represent true colour.

Here we concentrate on a particular, irregular curl feature that shows signs of scarp collapse. Figure 6.8 shows the earliest CRISM scene (14/05/2007) from this study's region of interest, in which the irregular curl feature is in the centre of the inset. A clear region of blue pixels can be observed, indicating a dust accumulation.
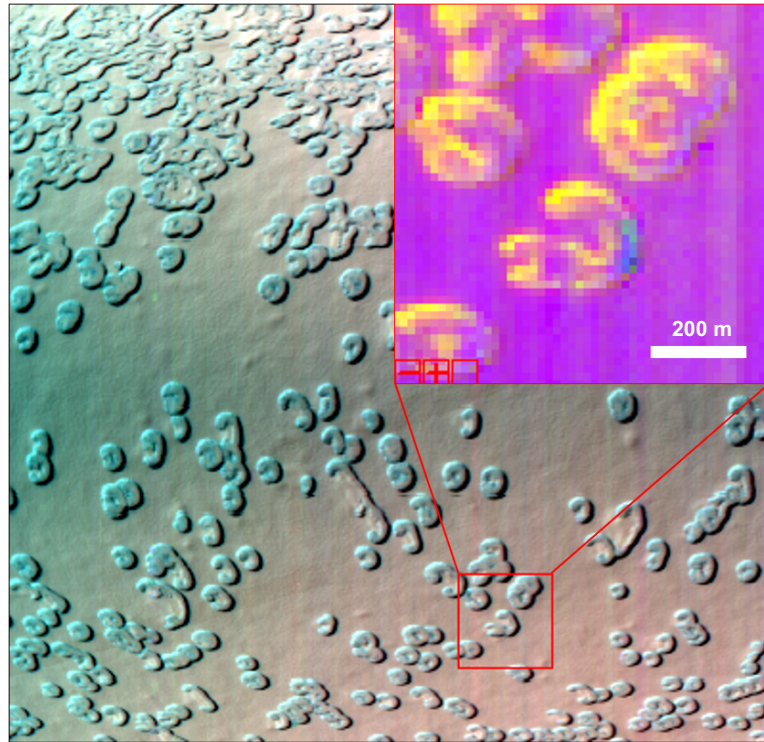
Figure 6.8: CRISM scene FRT00005AE3 on 14/05/2007 in 'False Colour'

bands R = 230 G = 75 B = 10. Inset shows detail false colour visualisation

using Viviano-Beck et al.,(2014) summary products R = 1435 (CO_2 ice) G =

1500 (H2O ice) B = LCPINDEX2 (High Calcium Pyroxene). Red box = 1 km

x 1 km

In a later image from 30/09/2007 (Figure 6.9), we can see the blue regions have diminished, while the green rim regions indicate water ice have increased.
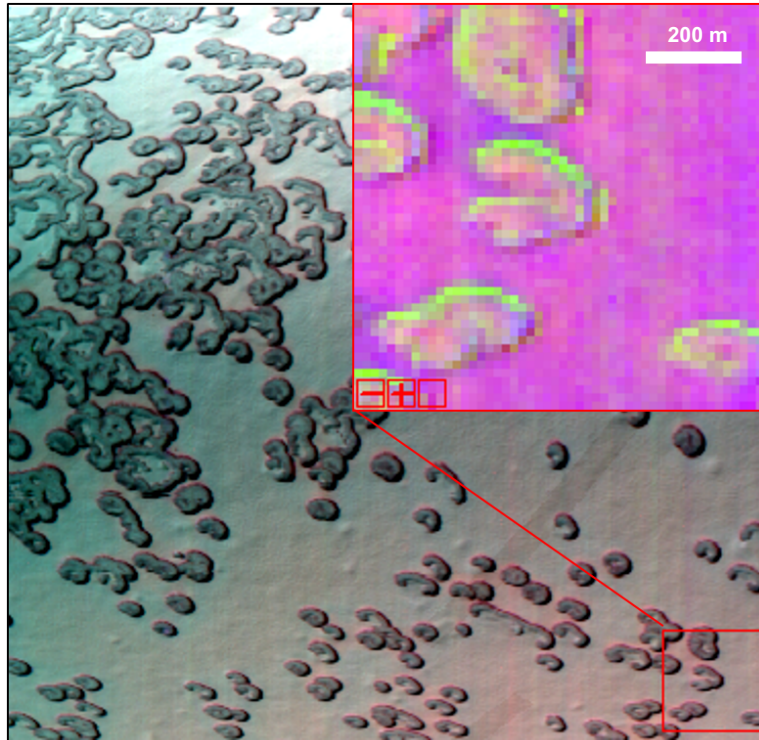
Figure 6.9: CRISM scene FRT00007F62 in 'True Colour' bands R = 230 G = 75 B = 10. Inset shows detail of the false colour visualisation using Viviano-Beck et al.,(2014) summary products R = 1435 (CO2 ice) G = 1500 (H2O ice) B = LCPINDEX2 (High Calcium Pyroxene),). Red box = 1 km x 1 km

In the most recent CRISM scene (03/04/2009, MY 29, L_s 239) from the study region (Figure 6.10), very little dust-rich material is observed in the curl, although the rounder feature directly above it, is beginning to manifest signs of water ice and dust.
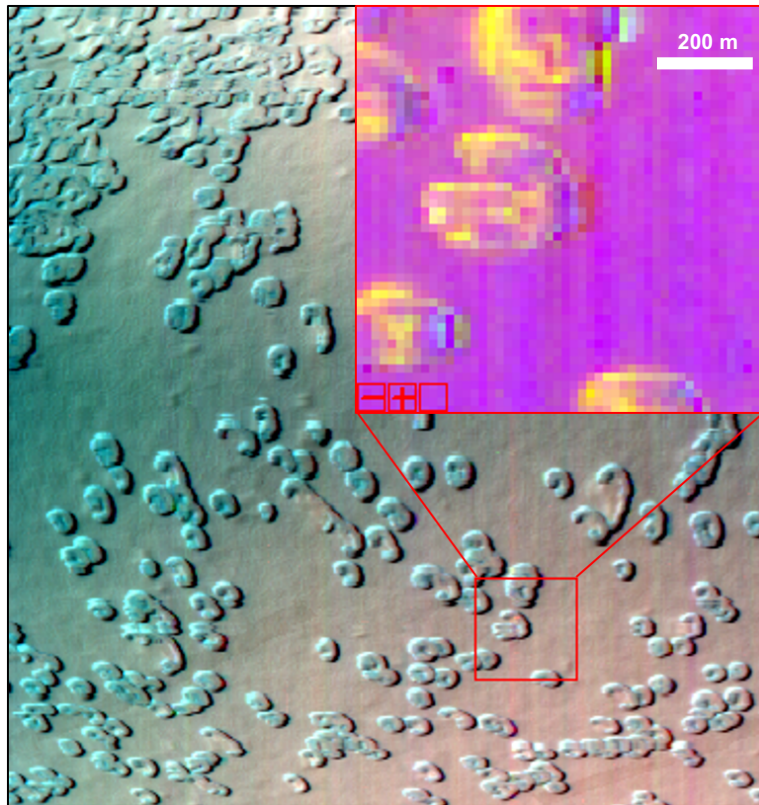
Figure 6.10: CRISM scene FRT00011DA4 on 03/04/2009 in 'False Colour'

bands R = 230 G = 75 B = 10. Inset shows detail false colour visualisation

using Viviano-Beck et al.,(2014) summary products R = 1435 (CO_2 ice) G =

1500 (H2O ice) B = LCPINDEX2 (High Calcium Pyroxene).). Red box = 1

km x 1 km

Analysis of individual spectra of pixels and regions of interest between the three CRISM scenes did not yield significant differences against the background of CO_2 ice spectra, largely due to the sub-pixel extent of dark, dusty regions, but they did show lower albedo in the younger images, indicating the presence of darker material. However, some morphological differences can be seen in the corresponding HiRISE imagery that might explain why pyroxene-like regions show up more strongly in earlier imagery.

Figure 6.11 shows two HiRISE images of the irregular curl feature taken 5 years apart, from 2007 and 2012 respectively.
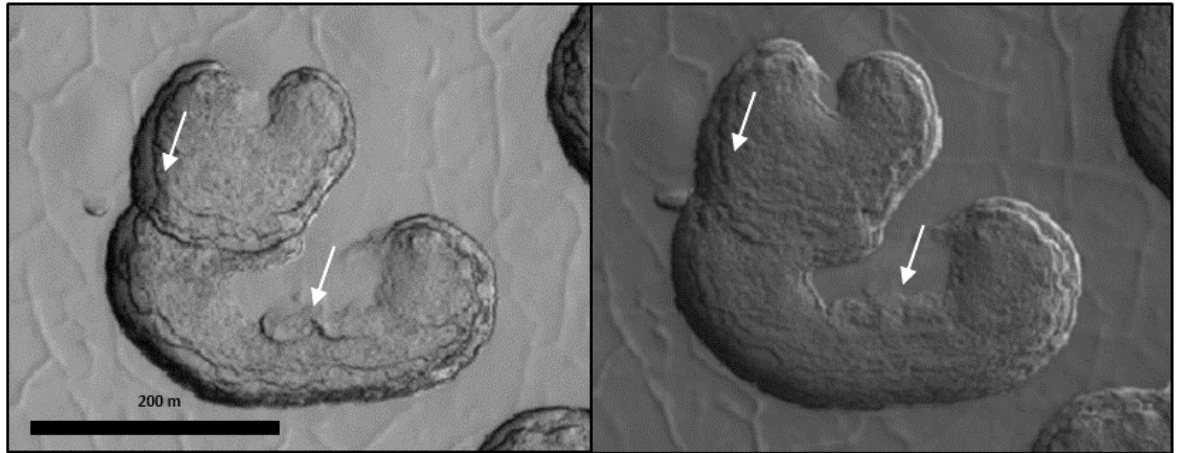
Figure 6.11: HiRISE imagery of irregular SCT curl feature. Left: PSP_005517_0930_RED (2007). Right: ESP_029134_0930_RED (2012). White arrows highlight changes in scarp wall morphology. Curl feature is inverted from CRISM imagery in Figs. 56-58

It appears that the sharpness of scarp terrace features has decreased over time. While some of this change in appearance may be attributable to lighting differences between the two images, the white arrows in Figure 6.11 show regions where the previously well delineated features clearly appear smoother and more eroded over time. Rounder, more well established SCT pits of late Unit A1 and Unit B terrain exhibit darkening rims over time (Jian and Ip, 2009; Byrne, 2009), and it may be that early, irregular pits which feature scarp and terrace collapse as they develop into rounder pits over time actually have lower concentrations of dust; this may be because the steep vertical walls are not simply receding laterally as they do in well-established pits, allowing for dust

concentration with sublimation, but collapsing and spreading out any dust exposure into less concentrated regions of dark material. This is consistent with the findings by Buhler et al., (2017) from their study of HiRISE imagery, which showed calving as well as sublimation on A1 pit walls.

Figure 6.12 highlights the difference in extent of the SCT pit wall between the two images.
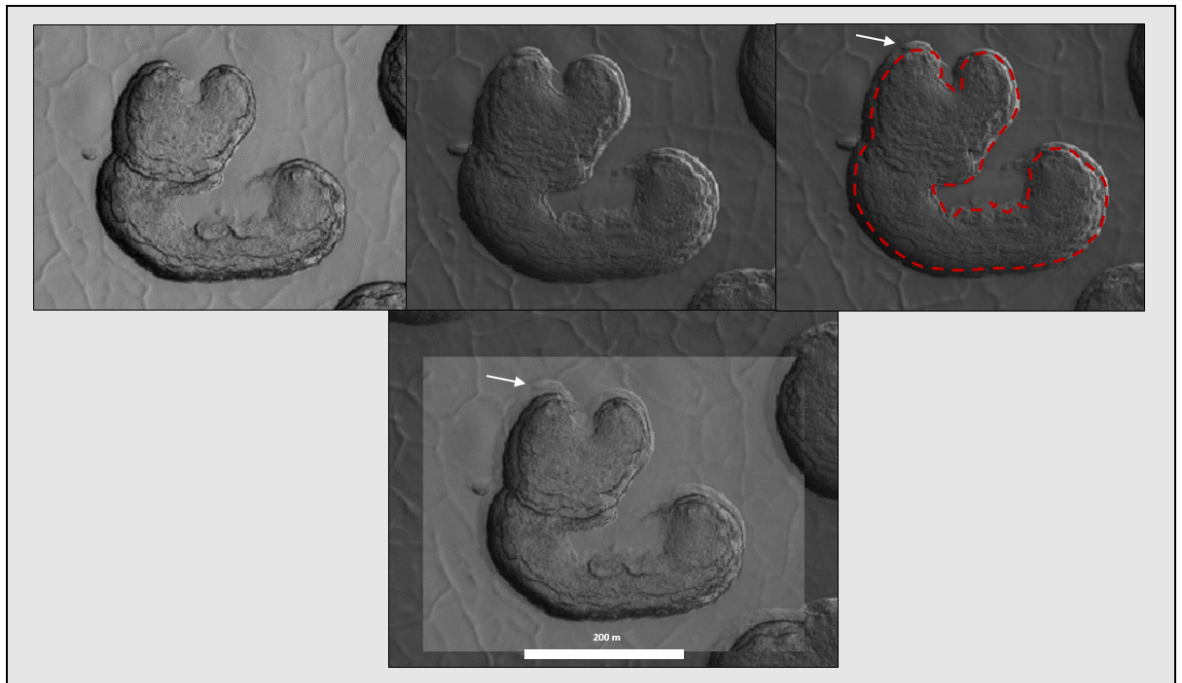
Figure 6.12: HiRISE imagery of irregular SCT curl feature. Top Left: PSP_005517_0930_RED. Top middle: ESP_029134_0930_RED. Top Right: ESP_029134_0930_RED with boundary of original pit from 2007 highlighted in red. Bottom shows transparency of the two images overlaid to show changes in scarp extent. White arrows highlight maximum change in extent of changes in scarp wall of ~11 m

The extension of the pit seems slightly offset with most of the growth occurring in the top and left of the pit as shown in Figure 6.12. The maximum amount of scarp retreat is in the top left of the pit, with a lateral change of ~11 m observed between 2007 and 2012. Consistent with the idea that collapsing walls show little dust accumulation and concentration is the fact that none of the summary product false colour RGB composites, nor the HiRISE imagery show dusty regions in the centre of the curl where there is erosion and collapse forming the notch in the curl. Again, these results are consistent with the findings of Buhler et al.,(2017) who found that a combination of sublimation and calving, where blocks fall and crumble away, can be observed on small, irregular pits.

6.2.4. Mixed and A0 Morphology

This next region was of interest as it contained a few different types of morphology (Figure 6.13).
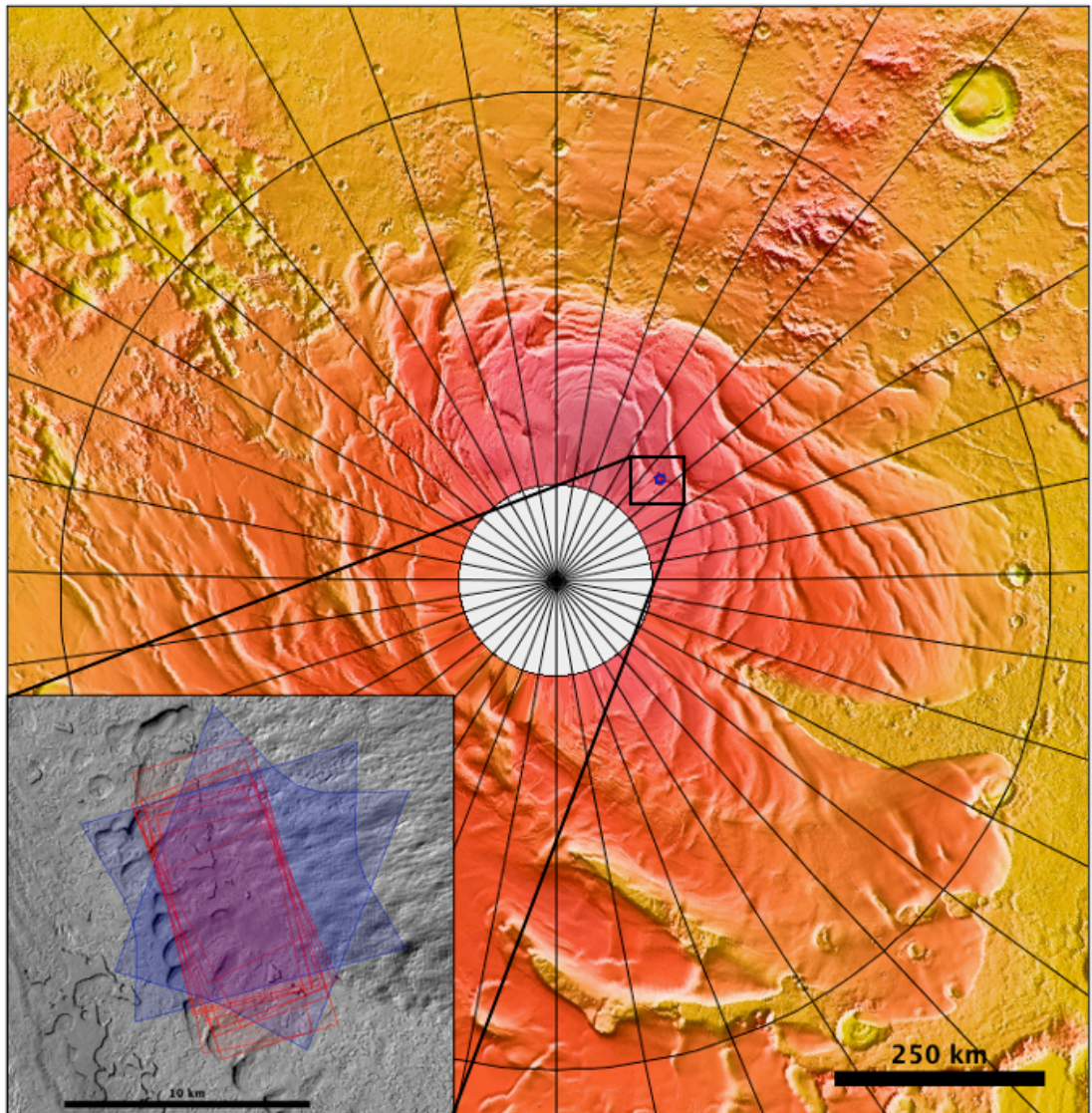
Figure 6.13: Location of coverage of mixed morphology; main figure shows location of CRISM and HiRISE products, (Lat: -87.0 Long: -25.2) over 112 m colourised and hill-shaded MOLA elevation map. Inset shows detail of footprints of CRISM (in blue) and HiRISE products (in brown) used in this study over a CTX background image B10_01369_0930_XN_87S334W. Produced using JMARS

The details of the products useful to this analysis are listed in Table 6.4.

Table 6.4: Details of Group 1 CRISM and HiRISE products

Instrument	Product ID	Acquisition Date	Mars Year	Solar Longitudeº	Phase Angleº
CRISM	FRT0001387A	06-July-2007	29	298	70
CRISM	FRT00013E4C	23-July-2009	29	308	70
HiRISE	ESP_013863_0930_RED	11-July-2009	29	301	69
HiRISE	ESP_013982_0930_RED	20-July-2009	29	307	69

The morphology type of this region is rather mixed, containing types B, A0 and A2 according to the classifications devised by Thomas et al., (2009).

Below in Figure 6.14 are the two HiRISE images taken as close in time as possible to the CRISM imagery, and as we might expect, there is virtually no visible change between the two images.
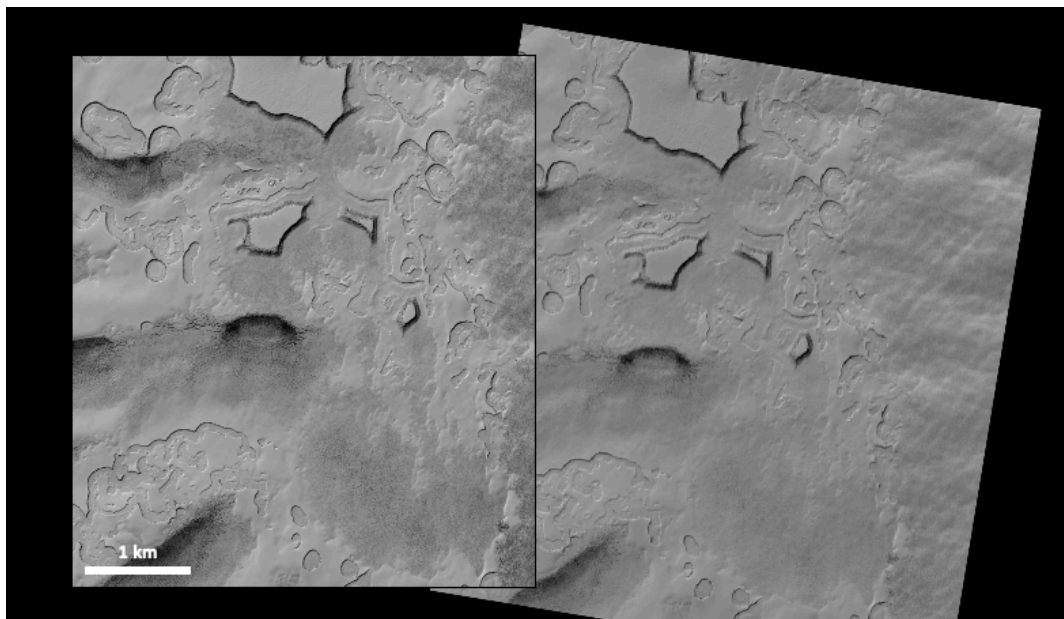
Figure 6.14: Side by side comparison of HiRISE images

ESP_013863_0930_RED (left) and ESP_013982_0930_RED (right)

When examined for spectral differences, other than slight differences in reflectance strength, the composition of the region varies very little. An example is shown below, where the brightest pixels indicate H_2O ice content around the rim of one of the mesas shown in Figure 6.15.
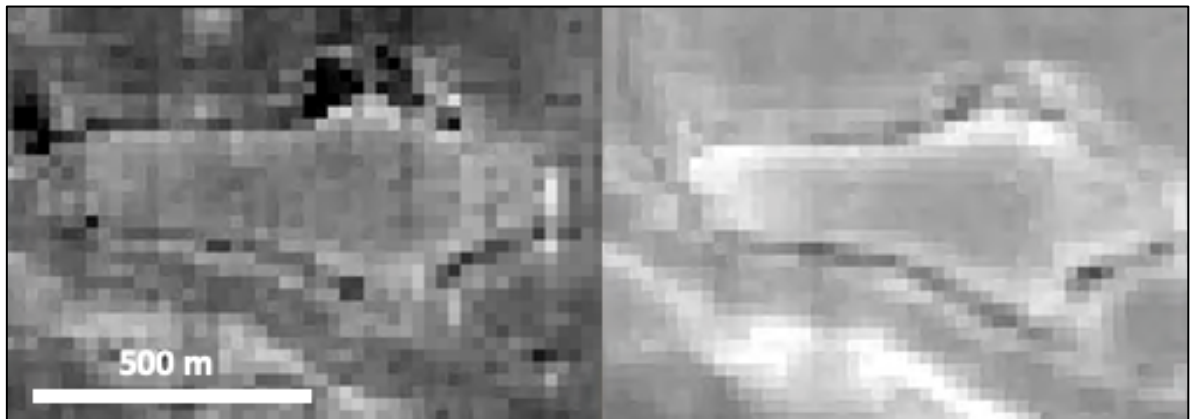
Figure 6.15: CRISM scenes FRT0001387A (left) and FRT00013E4C(right) in greyscale using Viviano-Beck et al.,(2014) summary product 1500 (H2O ice). Brightest pixels indicate strongest response for water ice spectrum signatures

Very little compositional difference was evident regardless of which summary product was examined. This region has been included to show how little variation there is over short time periods within the same season, but is also of interest as there is an area of gently sloped low topography that shows large amounts of dust. Many of the A0 features examined across the whole SPRC region showed uniform high-calcium pyroxene around the mesa edges, while other minerals were seen elsewhere. Unlike some of the dustier regions found around pit edges due to concentration of dust through sublimation as observed in the practical experiments, this area seems to be rather a large swathe of

dust, possibly accumulated there through aeolian processes rather than revealed from within the ice. Another nearby region shows a good example of this. This group unfortunately had very little overlap between CRISM scenes of good quality from different times, but it turned out to be one of the most spectrally interesting regions due to the unique mix of morphology in the area; therefore, we will take a closer look. Figure 6.16 shows the location of the area and the CRISM and HiRISE data available in the region; Table 6.5 shows their details.

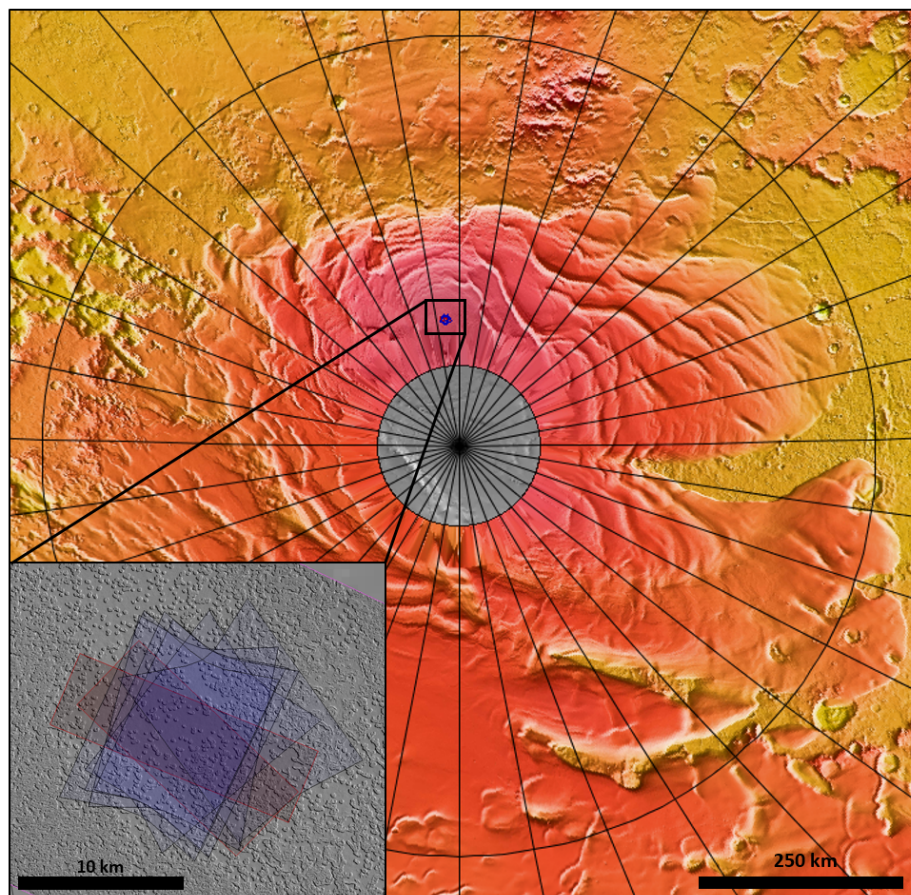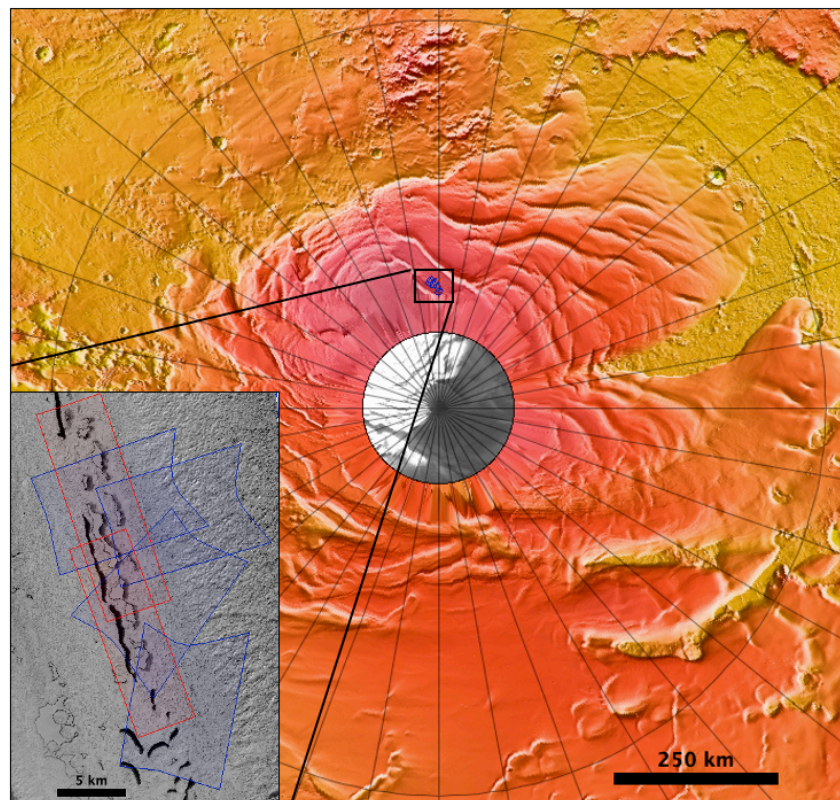*Figure 6.16: Location Type B and A0 morphology; main figure shows location of CRISM and HiRISE products, (Lat: -86.7 Long: 15.5) over MOLA elevation map. Inset shows detail of footprints of CRISM (in blue) and HiRISE products (in red) used in this study over a CTX background images B05_011661_0933_XN_86S344W and B12_014179_0932_XI_86S342W*

Table 6.5: Details of Group 2 CRISM and HiRISE products

Instrument	Product ID	Acquisition Date	Mars Year	Solar Longitudeº	Phase Angleº
CRISM	FRT00006CC3	27-July-2007	28	284	67
CRISM	FRT00006DFC	31-July-2007	28	287	74
CRISM	FRT0000741E	23-August-2007	28	301	72
CRISM	FRT00008490	18-October-2007	28	332	80
HiRISE	ESP_01124_0930_RED	17-July-2007	28	277	69
HiRISE	PSP_004686_0930_RED	27-July-2007	28	284	66

This region exhibits largely Type B morphology, but there are some plateaus (mesas) that have been almost completely removed with circular pits having joined up, more reminiscent of Type A0 morphology. Figure 6.17 shows a HiRISE image of this area of interest within the scene.
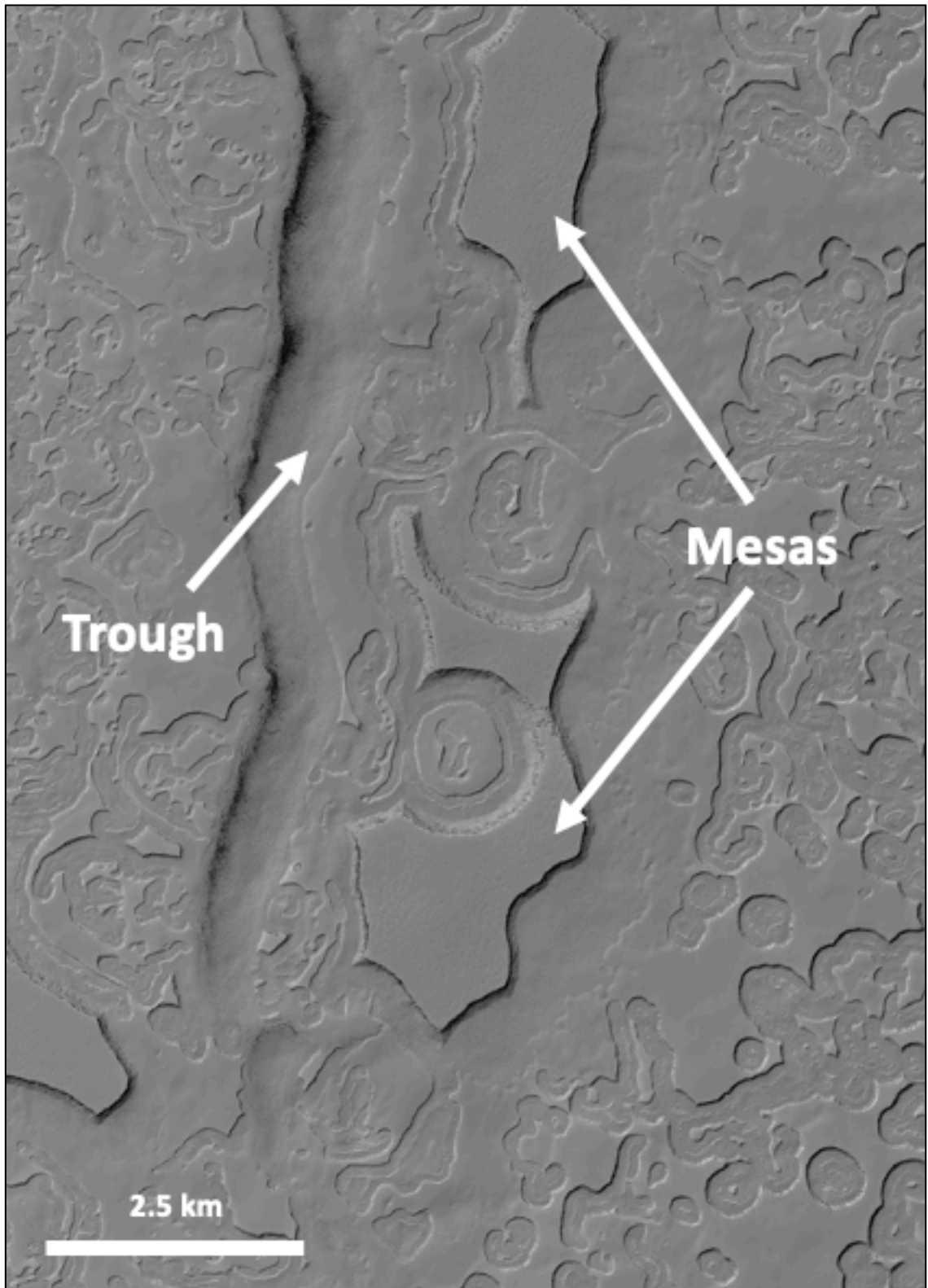
Figure 6.17: HiRISE Image ESP_01124_0930_RED of mixed morphology region showing A0 morphology and troughs

Of particular interest once examined spectrally, are the edges of the mesas and the long trough running from top to bottom of Figure 6.17. Initial examination (Figure 6.18) using indicators for CO_2 and water ice content reveal, as expected, a mix of CO_2 and water ice across the scene, with slightly more water ice content present around the mesa sublimation faces as was shown to be the case from pit rims in Chapter 4. However, these particular mesa rims seem to have a low response for either ice compared to others in the scene, which would be consistent with them being Type A0 rather than Type B morphology, and therefore may be older and have had more time to have concentrated dust on the scarp walls according to the 'life cycle' of SCT described in Chapter 2. The trough feature running diagonally across the right-hand side of the scene also shows low response for ices.
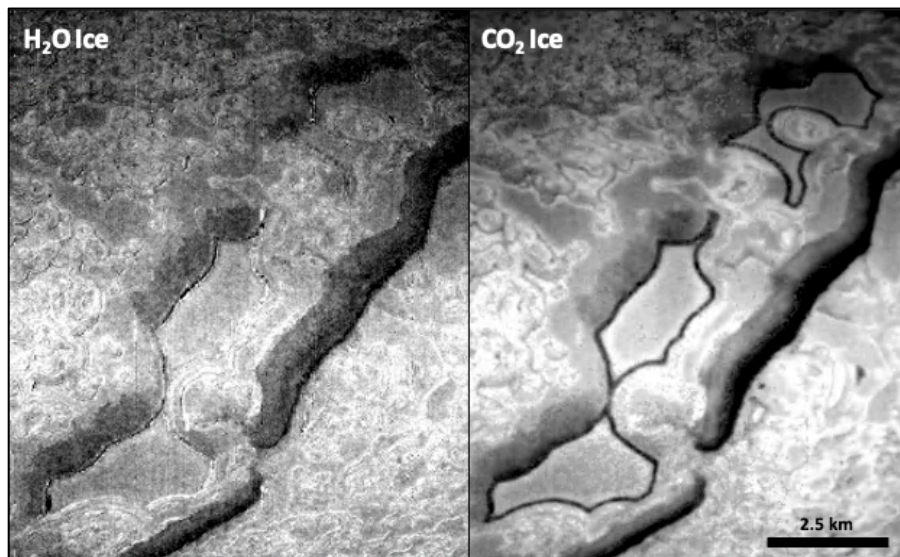
Figure 6.18: CRISM scene FRT0000741E close up of mesas and trough with summary products 1500 (H_2O ice) applied to left hand image, and 1435 (CO_2 ice) applied to right hand image. Brightest pixels indicate the highest concentration of the respective ices.

In order to have a better look at why there was low response for ices on the rims of the mesas, all summary products for known Martian minerals were applied to the scene (see VIviano-Beck et al., 2014). The three summary products that showed the strongest responses for a particular mineralogy in the scene were those for low-calcium pyroxene, high calcium pyroxene and olivine. Figure 6.19 shows grey scale imagery for these 3 mineral summary products, with the brightest pixels indicating the strongest response.
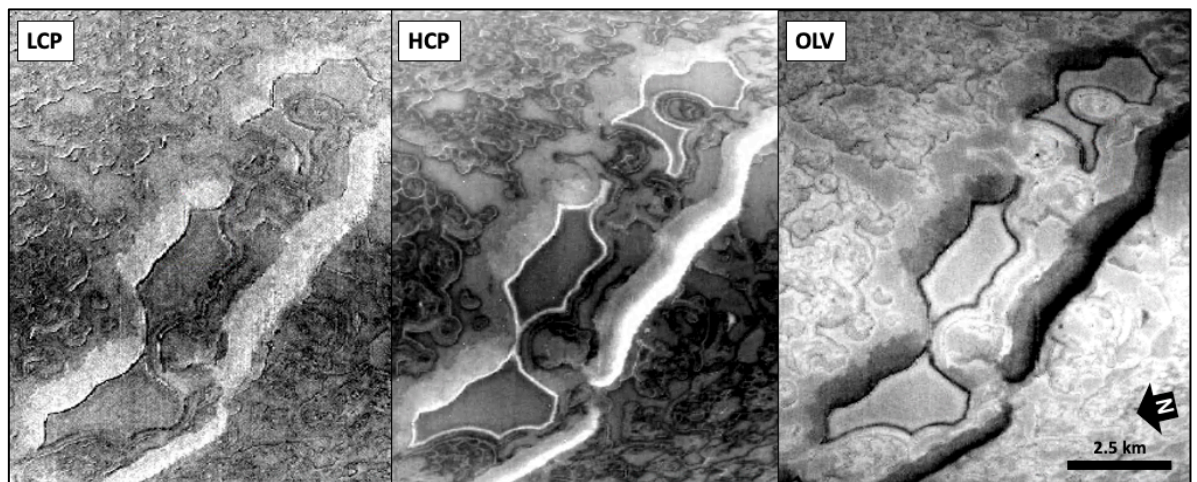
Figure 6.19: CRISM scene FRT000741E close up of mesas and trough with summary products LCPINDEX (low-calcium pyroxene) applied to the left hand image, HCPINDEX (high-calcium pyroxene) applied to the centre image, and OLINDEX2 (olivine) applied to the right hand image. Brightest pixels indicate the highest concentration of the respective minerals.

Interestingly, we can see that the minerals are responding most strongly within certain regions. The low calcium pyroxene is responding in what looks like a thin layer across a fairly large area to the north eastern approach to the mesa and trough scarp walls, becoming thicker closer to the vertical terrain. The high

196

calcium pyroxene also follows this pattern in a thin later, but very clearly has a very strong response around all edges of mesas, regardless of the direction scarp walls face, and an extremely bright band along the wall of the trough. The olivine, however, appears to be present all over the mottled mesa top and much of the surrounding area, although this ubiquitous presence of the strongest summary product response for olivine may well be spurious, and it very closely matches the distribution of strongest pixels for CO_2 ice. It's possible that olivine is mixed into the CO_2 ice fairly uniformly, but either way, it serves as a good background summary product to highlight the spatial difference in response for the two types of pyroxene. Figure 6.20 Shows the 3 mineral types in one RGB image, to give a better idea of their distribution.
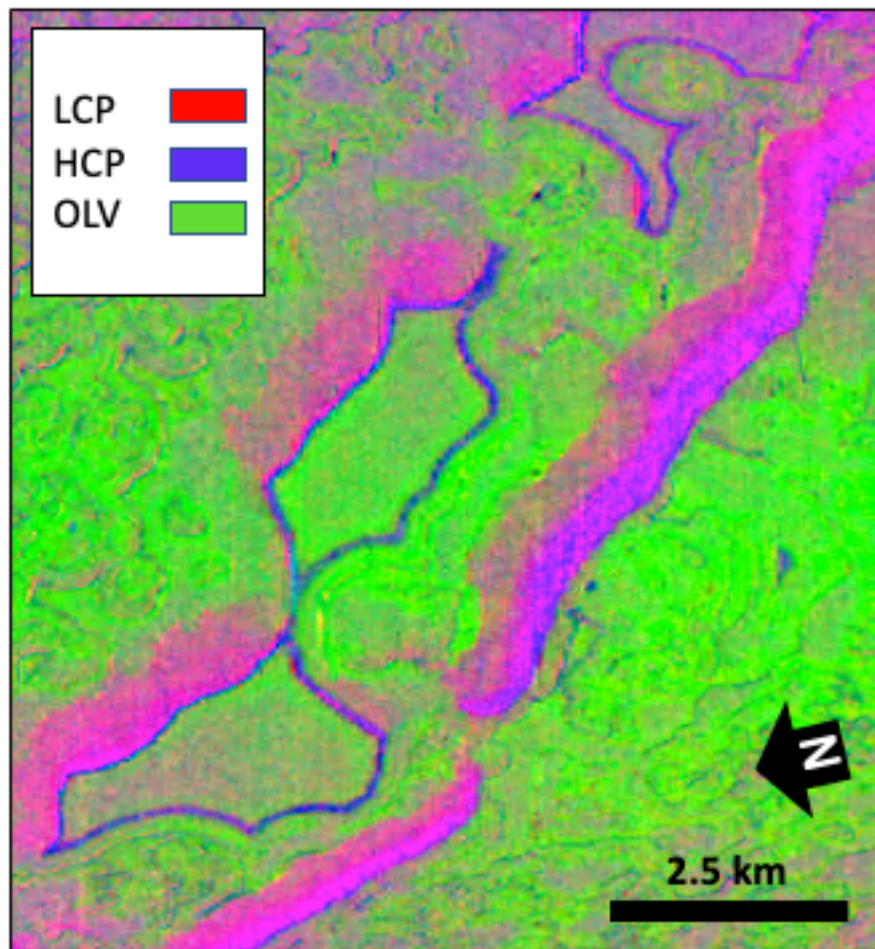
Figure 6.20: CRISM scene FRT000741E close up of mesas and trough RGB

false colour map of summary products LCPINDEX (low-calcium pyroxene,

Red), HCPINDEX (high-calcium pyroxene, Blue), and OLINDEX2 (olivine,

Green).

It would appear the olivine dust is fairly uniformly distributed around this region, while the two types of pyroxene (which form a mix and manifest as purple) are more clearly constrained to certain morphological features. Therefore, a new colour map was produced to more clearly see the differentiation between the two types of pyroxene on the ice cap (Figure 6.21).
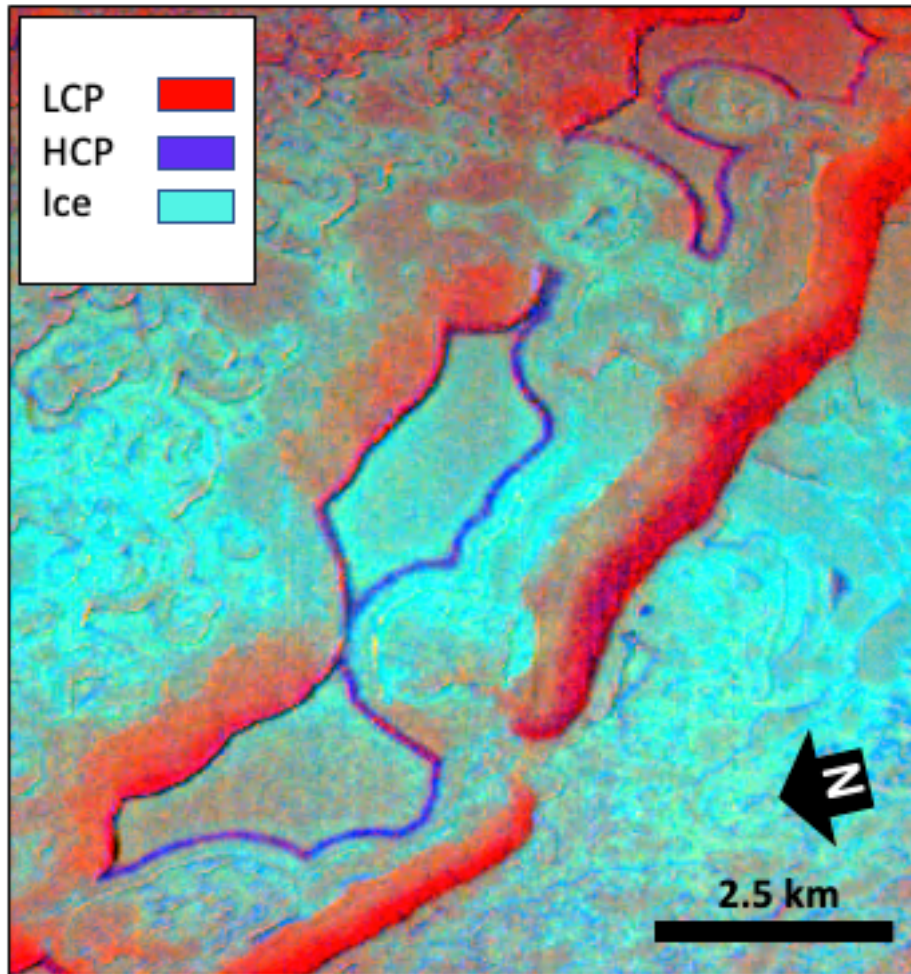
Figure 6.21: CRISM scene FRT000741E close up of mesas and trough. False colour map of summary products LCPINDEX (low-calcium pyroxene, Red), HCPINDEX (high-calcium pyroxene, Dark Blue), and ICER2 (CO_2 with small amounts of H_2O ice, Light Blue).

This analysis leads to the conclusion that the deposits of high-calcium pyroxene (blue) surrounding the mesas are more likely to have been exposed through sublimation due to their uniform presence around scarps walls that are known to sublimate from visible imagery, rather than deposited through aeolian processes and therefore accumulate from one particular direction; the next step was to analyse just the dust on the mesa walls. In order to do this, a

region of interest was created from the blue rim features shown in Figure 6.21 and a spectrum generated. The signature for high calcium pyroxene was then removed from the spectrum by ratioing it against Viviano-Beck's CRISM type spectra from high-calcium pyroxene. The remaining spectra still showed a lot of the features of CO_2 ice, as we might expect. Rather than remove these CO_2 spectral features, as was tried in Chapter 4, leaving us with a virtually featureless line, the CO_2 ice spectra with the dominant dust spectra removed was compared to the laboratory spectra described in Chapter 5 for 1% PAH content. The results are shown in Figure 6.22, and on indications of PAH signatures are present. A visual comparison of spectra was used rather than statistical as this was the most effective way to compare spectra, and the notable features were obvious to the eye. Statistical analysis was used in chapter 4 but in order to see the shape and depth of absorption features, a visual examination was more effective.
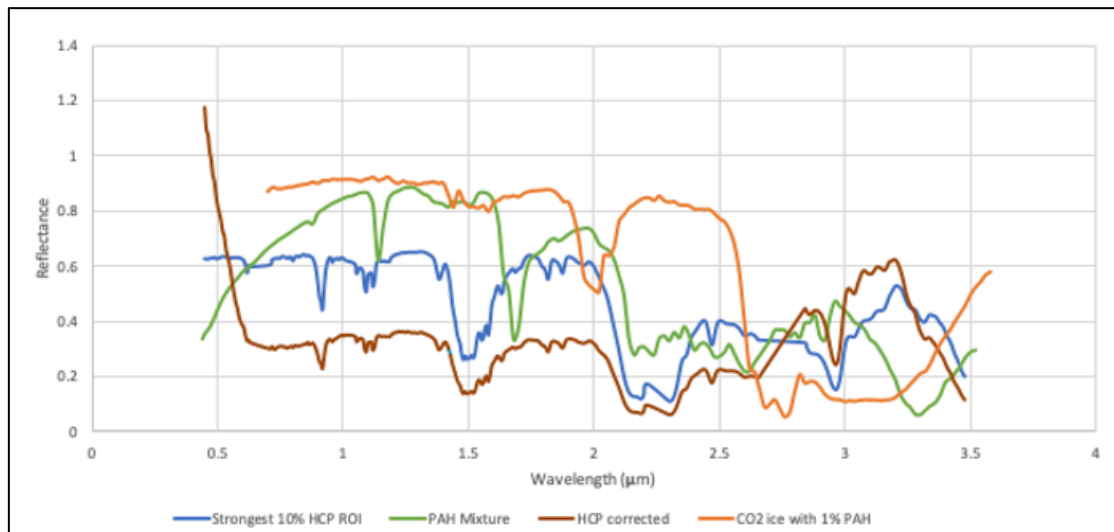
Figure 6.22: Graph showing CRISM scene FRT000741E's strongest 10% of signatures for high-calcium pyroxene, the mesa edges with high calcium pyroxene signatures corrected for, the laboratory spectra for the PAH mixture, and CO_2 ice with 1% PAH included.

Having looked carefully at this region, it was clear that at least the north-east scarp wall was well covered with low-calcium pyroxene, that may have collected there through deposition rather than accrued through sublimation, so it would be good to look at a region that perhaps did not have this issue and only contained dust left by sublimation. Fortunately, a neighbouring CRISM scene has an ideal feature.

6.3. Analysis of PAH Candidate Feature

Like the previous scene, FRT00008490, is largely a Type B morphology, but has a mesa typical of Type A0 morphology. In this case the mesa has been almost completely sublimated away and exhibits extended areas of terracing (Figure 6.23).
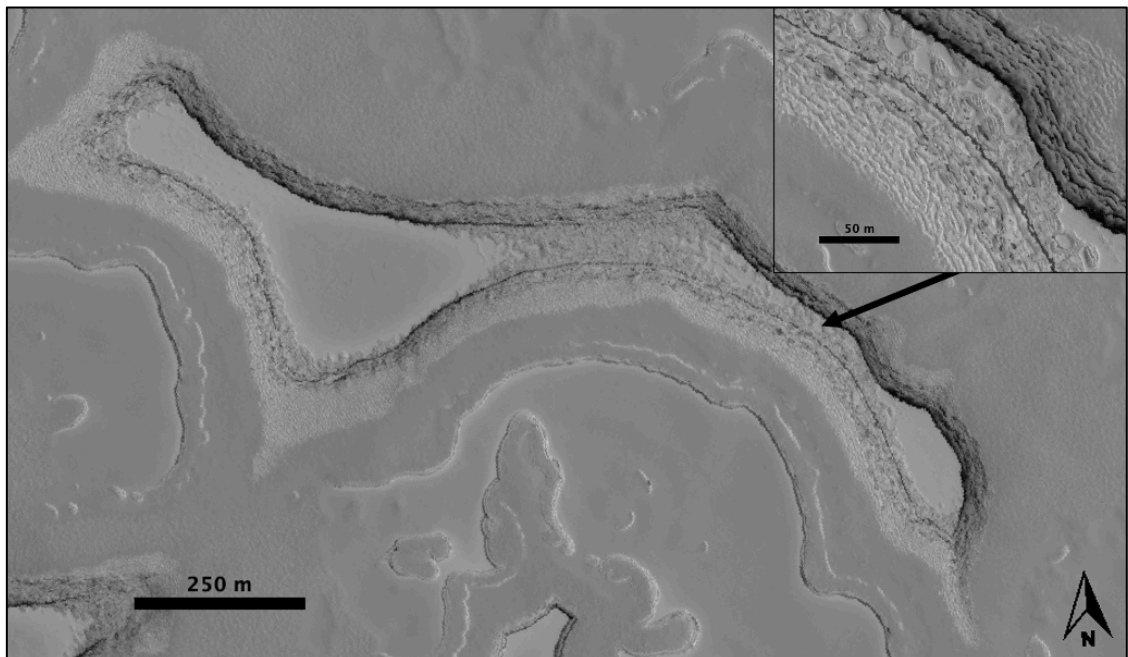
Figure 6.23: HiRISE image PSP_004686_0930_RED showing Type A0

mesa feature. Inset top right shows detail of terracing.

The above imagery is from 2007 (MY 28) and it's unfortunate that there isn't more recent high resolution CRISM FRT imagery available of this area, where more sublimation has taken place. However, HiRISE imagery does show that this region does indeed have quite rapid sublimation taking place (Figure 6.24).
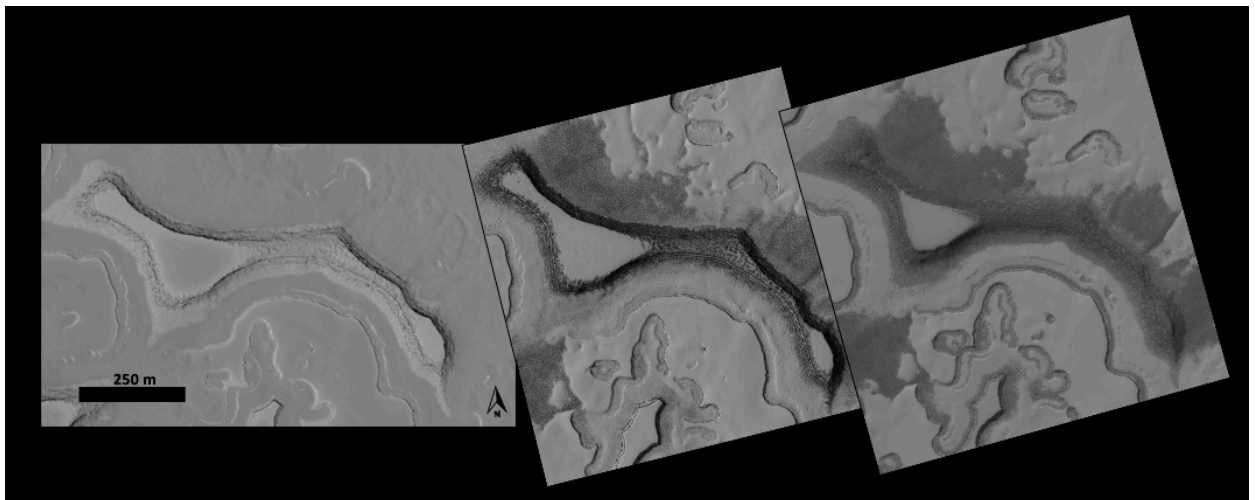
Figure 6.24: Time series of HiRISE imagery showing mesa sublimation over several years. Left: PSP_004686_0930_RED (2007). Centre: ESP_014390_0930_RED (2009). Right: ESP_049768_0930_RED,(2017)

The development of dark dust fans around the mesa are thought the be from sublimation occurring within the mesa and ejecting gas with entrained dust from within to the surrounding area (Buhler et al., 2017). Therefore, these dark, flat, dusty areas are prime candidates for looking for dust that has previously been protected within ice features.

These HiRISE images show a lot of detail with their 25 cm/pixel spatial resolution. But in order to get a better look at how these landforms really look,

some 3D imagery was produced for the region in the form of Digital Terrain Models (DTMs) that ascribe height values to each pixel (see Section 3.1.3). Please note that elevation values are negative due to the method by which the Areoid, the Martian equivalent of the Geoid, is measured (described in Section 2.3).

Below is a 3D visualization of the region made up of two HiRISE images from 2017 that have been processed into a DTM, [Putri and Yu, private communication 2020). This view more clearly shows the topographic highs of the mesa regions of SCT than just visual images.
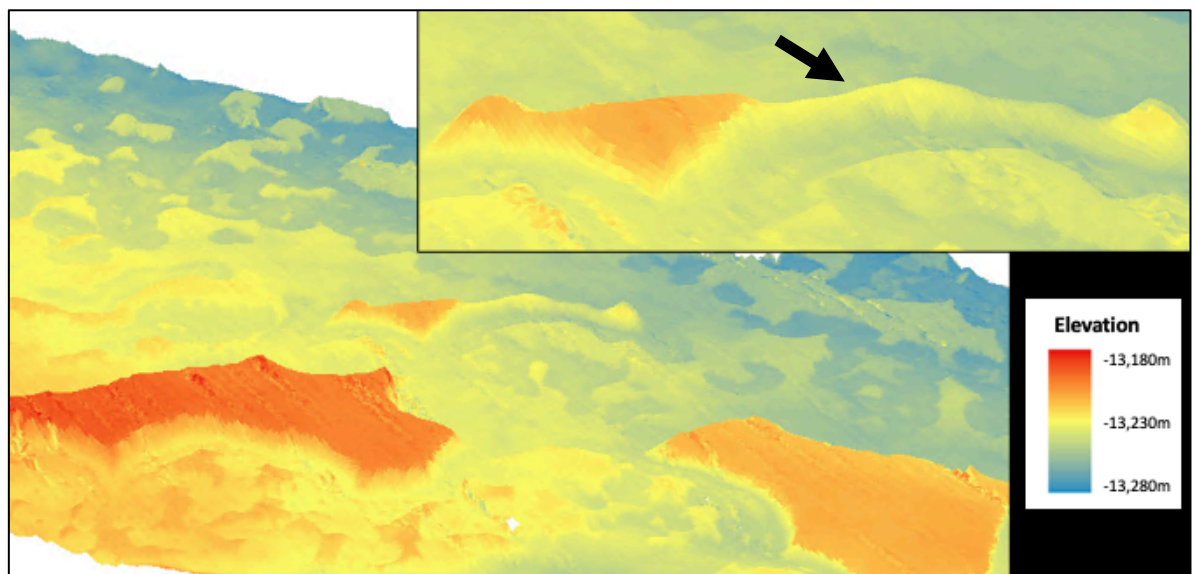
Figure 6.25: HiRISE DTM ESP_049768_0930_RED-ESP_049782_0930_RED of A0 mesa features, with red showing topographic highs, with close up of narrow mesa feature inset (top right). Dwindling ridge marked by black arrow. DTM (Putri and Yu, private communication 2020) colourised and visualised in ArcScene

This view makes it clear to see how Type A0 mesas can begin to erode into Type A2 Fingerprint Terrain, as we can see where the flat mesa top dwindles away to a thin, rounded, low ridge (black arrow, Figure 6.25). The same DTM is visualised below in Figure 6.26 from a top down view with an elevation profile taken across the central, narrow part of the mesa shown to have become increasingly narrow over time in Figure 6.24. As of 2017, it is clear the scarp is still present and probably still undergoing consistent sublimation to this day, having not completely sublimated away.
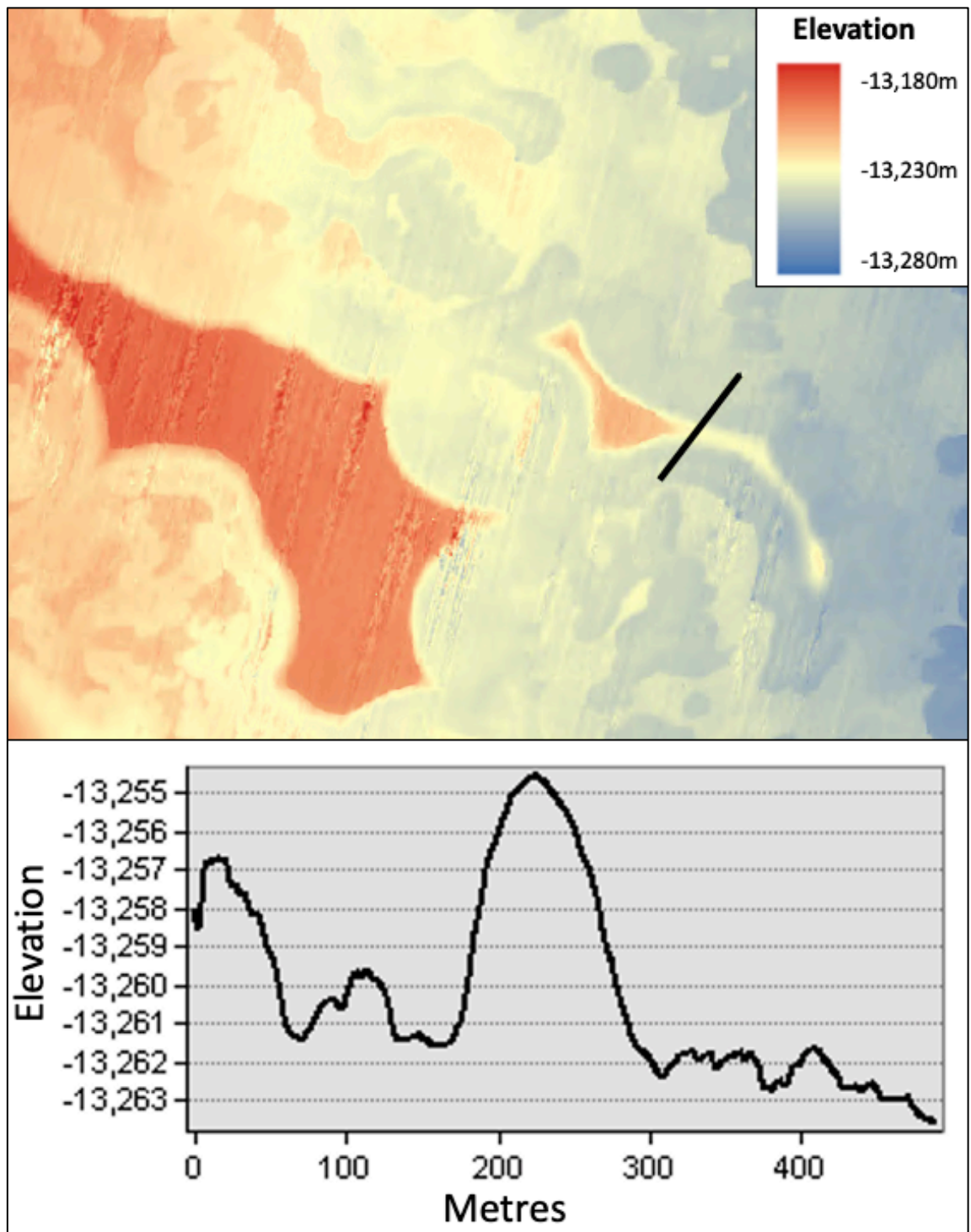
Figure 6.26: HiRISE DTM ESP_049768_0930_RED-

ESP_049782_0930_RED of A0 mesa features (top), with red showing

topographic highs and black line showing the location of the topographic

profile measurement. Elevation profile shown at bottom. DTM (Putri and Yu,

private communication 2020) colourised and visualised in ArcGis

Looking at the HiRISE visible imagery and 3D imagery, and with what we know of sublimation processes, it's fair to assume that this sublimation had been taking place prior to HiRISE and CRISM imagery becoming available in 2007 when MRO arrived at Mars and continues today, and so this is certainly an interesting region to look at, with extensive areas of dust likely left behind after sublimation rather than blown into place. While the HiRISE imagery seems to show dusty regions left surrounding the mesa on all sides, we will look at the CRISM spectral imagery to ascertain the composition, and therefore, hopefully, the source of the dust.

As noted previously, there is only CRISM FRT imagery available for this feature from 2007. In order to understand how the dust coalesces and its content, first the filter for CO_2 was applied and showed, as hoped, a CO_2 rich mesa top with almost no CO_2 surrounding the mesa walls. The real priority was to ensure that there wasn't a build-up of low-calcium pyroxene around the mesa, and the LCPINDEX summary product showed that there was no concentration of high-calcium pyroxene around all sides of the mesa. All of these results can be seen below in Figure 6.27 along with an RGB colour map showing the compositional context of the area for high-calcium pyroxene, CO_2 ice, and water ice which as expected is more abundant around the scarp sublimation faces of the mesa.
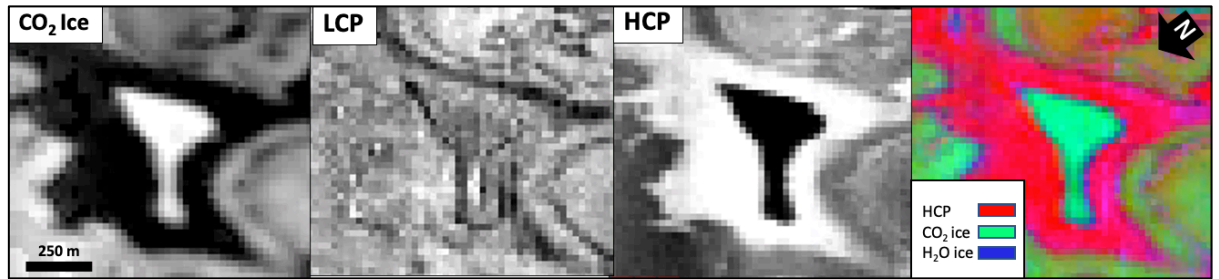
Figure 6.27: Greyscale maps of A0 Type mesa in CRISM scene FRT00008490. Left to right: CO_2 ice, low-calcium pyroxene, high-calcium pyroxene and RGB of high-calcium pyroxene, CO_2 ice and H_2O ice

All of the above analysis shows that this Type A0 feature seems to be the best place to look for dust deposits that are the result of sublimation or ejection, cover many CRISM FRT 20m pixels on relatively flat surfaces, and therefore the best place to look for PAH signatures. This is consistent with what is thought to be the 'life cycle' of SCT terrain; the Type A0 morphology uniformly sublimates rather than undergoes cliff collapse and has not been eroded away like A2 Type fingerprint terrain.

A manual 81-pixel region of interest was taken around the dustiest regions of the mesa indicating the highest levels of high-calcium pyroxene. Below, the candidate ROI can be seen alongside other pertinent spectra (Figure 6.28).
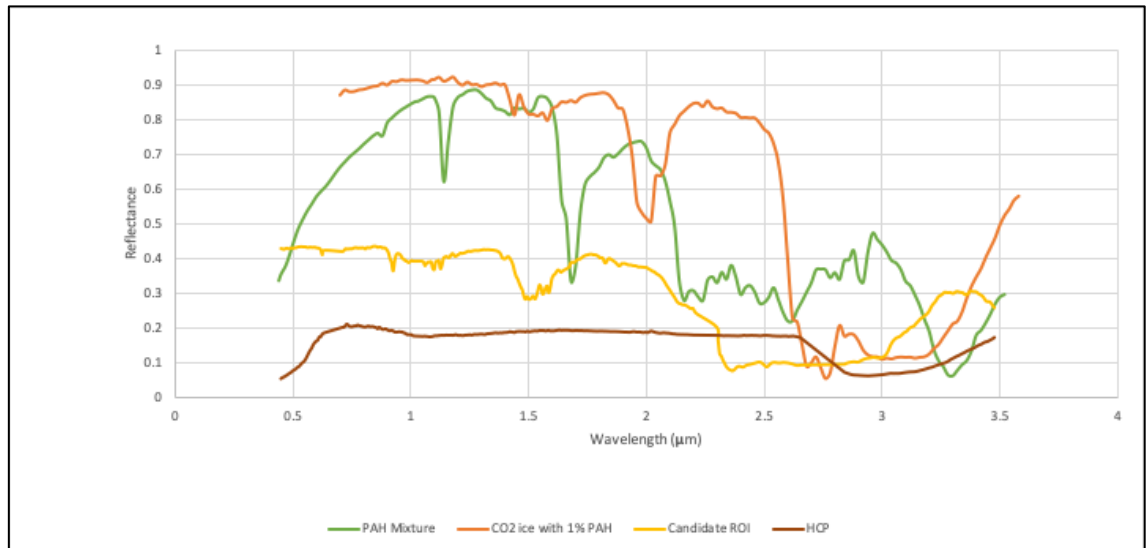
Figure 6.28: Graph showing CRISM scene FRT00008490's candidate ROI,

Viviano-Beck et a.l's CRISM type spectra for high-calcium pyroxene, the

laboratory spectra for the PAH mixture, and CO_2 ice with 1% PAH included.

It's clear that the candidate ROI spectrum has less obvious CO_2 ice features. Once corrected for high-calcium pyroxene signatures by spectral ratioing with the Viviano-Beck CRISM type spectra, the results can be seen below in Figure 6.29.
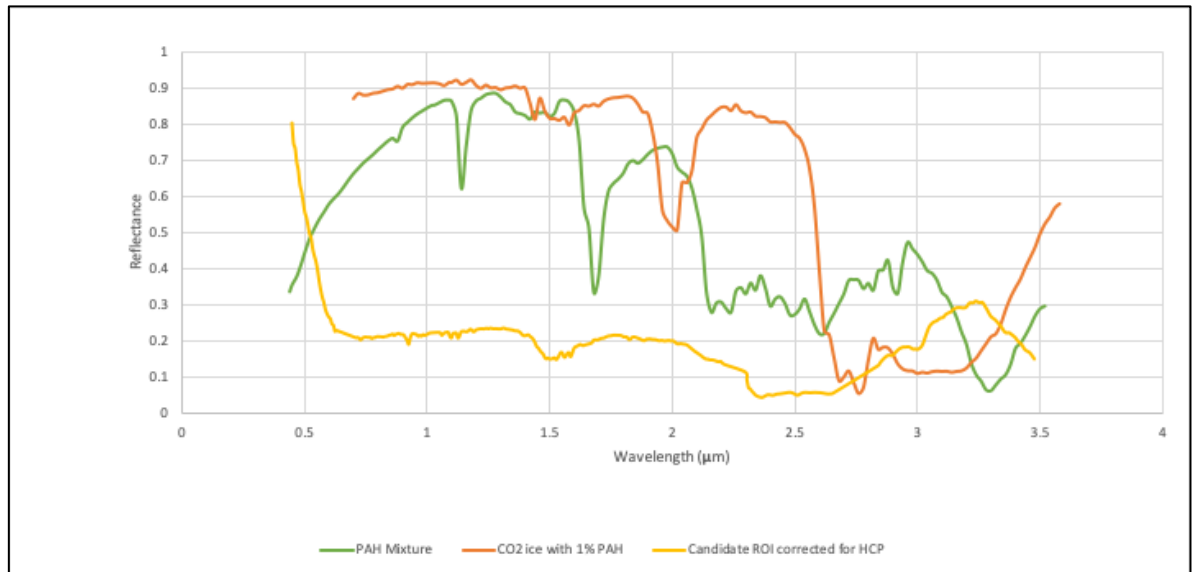
Figure 6.29: Graph showing CRISM scene FRT00008490's candidate ROI once corrected for high-calcium pyroxene features , the laboratory spectra for the PAH mixture, and CO2 ice with 1% PAH included.

There are none of the tell-tale PAH spectral features left in the corrected spectra, meaning that any PAHs present may be below the detection threshold established in laboratory experiments of 0.1% PAH within CO_2 ice.

In order to attempt to isolate some spectral endmembers from the region, linear spectral unmixing was also attempted for the candidate ROI using ENVI's SMACC endmember extraction tool (see section 3.5.3) with various numbers of endmembers employed, but no unique spectra were found, only various levels of reflectance were separated. Two examples are shown below for 3 and 30 endmembers respectively (Figure 6.30).
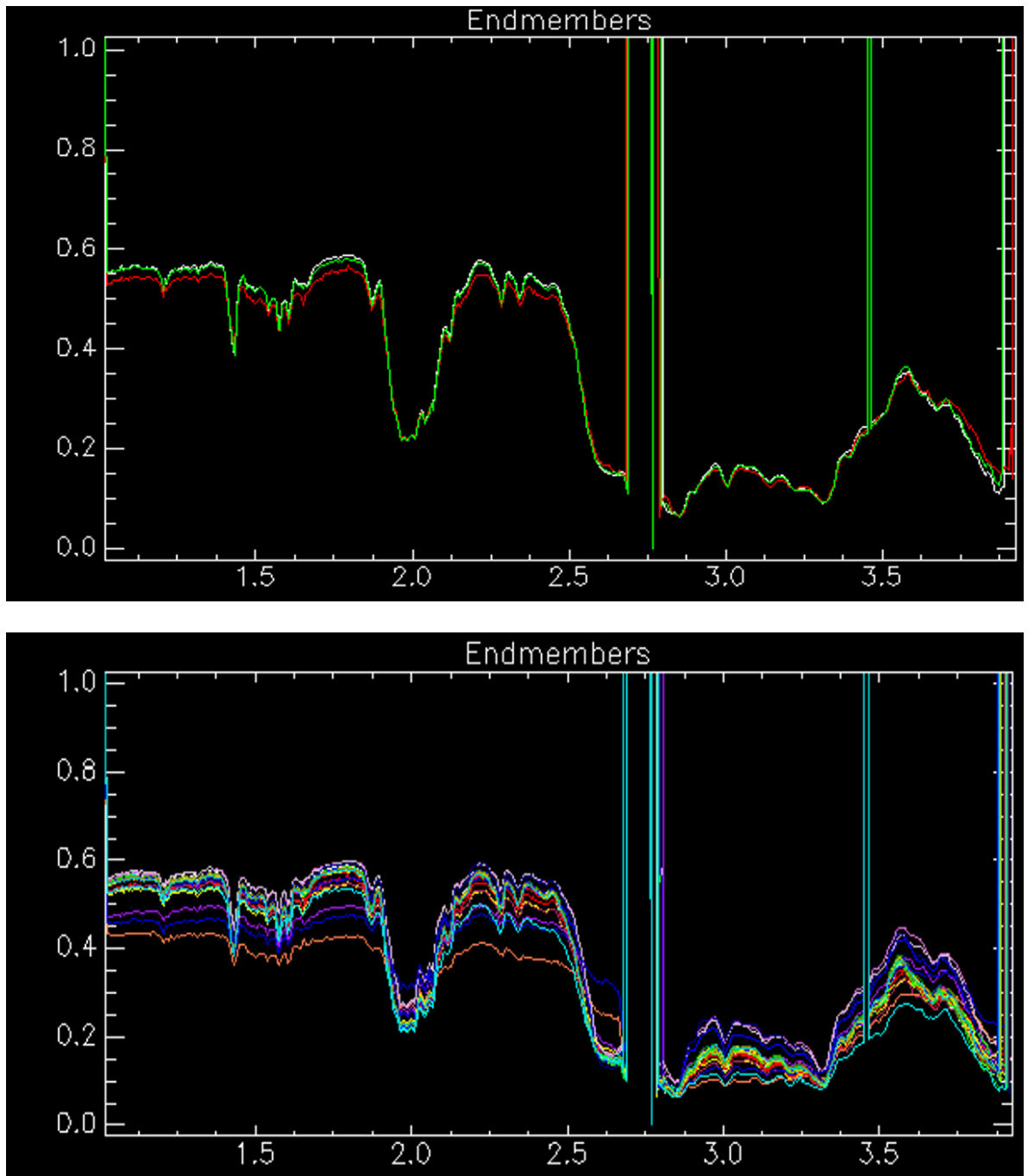
Figure 6.30: SMACC Linear spectral unmixing for endmembers from the

candidate ROI of 81 pixels around mesa feature from CRISM scene

FRT00008490. Top: 3 endmembers. Bottom: 30 endmembers

The spectra are dominated by CO_2 ice features, differing only in reflectance, and so a different method of endmember extraction was attempted. Using the

method devised by Rui Song, based on the NFINDR endmember extraction algorithm (see section 3.5.4), the dust rich region around the mesa was processed to look for unique spectra. The results are shown below in Figure 6.31.
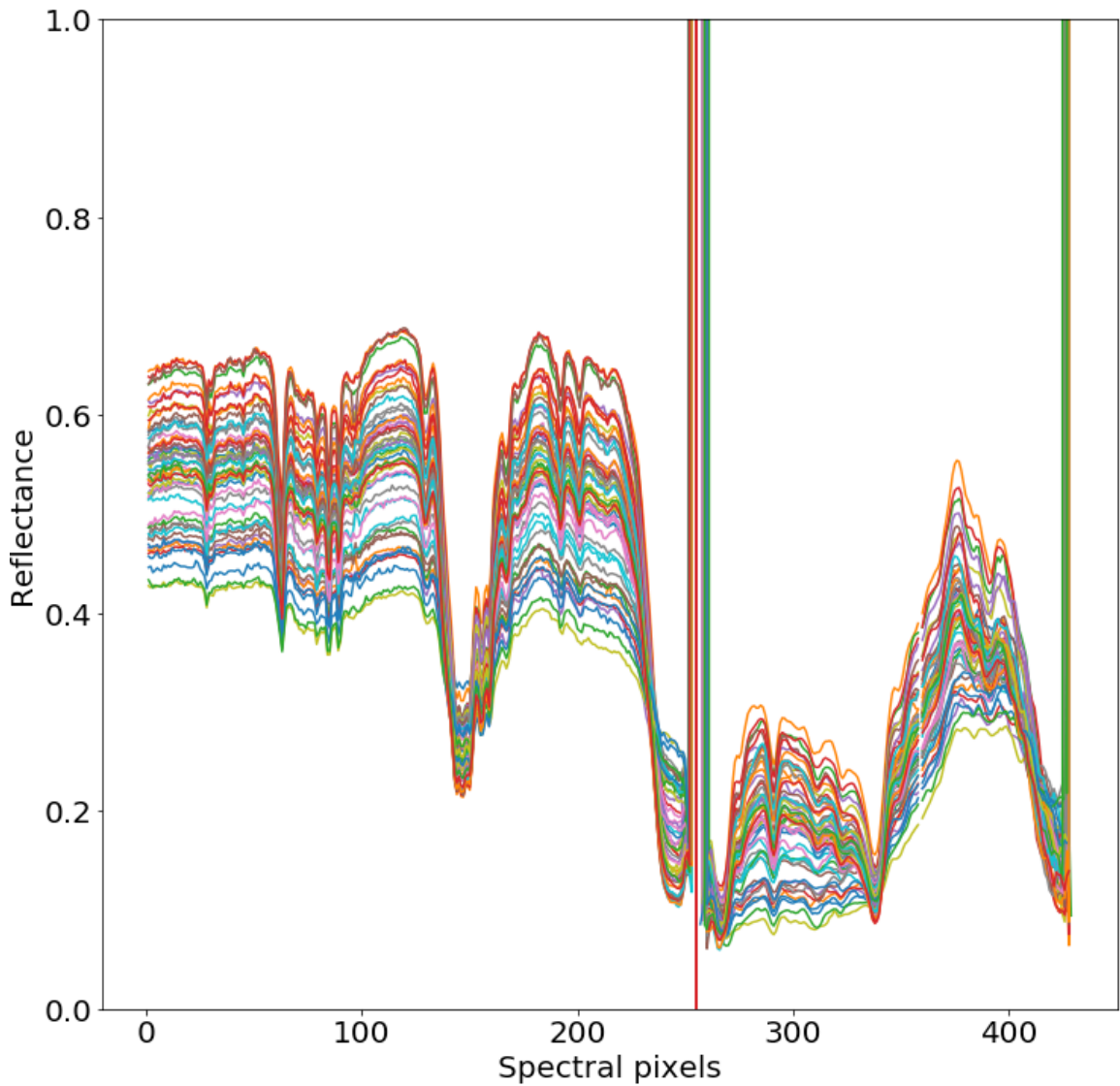
Figure 6.31: NFINDER endmember extraction algorithm applied to candidate ROI of 81 pixels around mesa feature from CRISM scene FRT00008490 by R. Song (private communication).

There are clear differences in overall reflectance, but no discrete endmembers were defined. CO_2 appears to be a severely limiting factor in discerning individual spectral features.

6.4. Preliminary Conclusions

The mechanisms by which SCT pits form and evolve have not been observed and are not well understood, but recent in-depth analysis of HiRISE imagery has shown that not just typical sublimation, but also calving and gas ejecta can lead to unique features (Buhler et al., 2017), and the spectral analysis shown here supports that. Analysis of the various existing morphologies leads to a better understanding of the decades to centuries long processes that we are unable to observe from the limited high-resolution imagery currently available. This allows us to understand the source of dust content on the SPRC, and which regions may be the best candidates to look for fragile organic molecules.

Fingerprint Type A2 morphology does not seem to coalesce dust in any particular regions, and represents the 'death throes' of the SCT morphology 'life-cycle'.

Type B pits are very abundant, and start to coalesce dust, but seem to expose more water ice than any mafic mineral of interest.

Spectral mapping of Type A1 proto-pit irregular features has shown that scarp collapse and calving may distribute rather than concentrate dusty regions as pits form. Sharp vertical walls in curl features show erosion and smoothing over time.

Topographic lows and vertical walls may collect dust deposited perhaps by aeolian processes, and while rich in mineralogy, particularly low-calcium pyroxene, do not show evidence that the dust accumulated there is the result of sublimation, and therefore any organic content would not have been afforded the protection for UV radiation that astrobiologists may be interested in.

A0 mesas seem to be the best terrain to look for dust accumulated through standard sublimation and the production of fans of previously entrained dust through gas ejection, which tends to be high in high-calcium pyroxene content. Mesas on the verge of being completely eroded, somewhere between Type B and Type A2 morphology seem to have the most dust, without the scarps and dust accumulations having undergone complete erosion and dispersal.

Spectral examination of the presumed sublimated dusty regions showed no evidence of PAH content above the 0.1% abundance established as the detectability limit of PAH in CO_2 ice in laboratory analogue experiments.

Even in the most dust rich regions, CO_2 ice signatures overwhelm the spectra, despite attempts at correction and endmember extraction, and therefore the

SPRC is a very difficult place to look for organic signatures, despite the many regions of A0 type morphology that would otherwise be excellent candidate sites for recently uncovered dusty material.

In the next chapter, we will move on to an equatorial region of dynamic surface features, unhindered by the ubiquitous presence of CO_2 ice; the Recurring Slope Lineae of Valles Marineris.

7. Analysis of Recurring Slope Lineae in Valles Marineris to Search for PAH Signatures

As we have seen in Chapters 4 and 6, CO_2 ice can be a major problem when looking for subtle spectral signatures. Therefore, following on from the laboratory experiments described in Chapter 5, this section will look at a non-polar environment in order to identify candidate sites for signature of PAHs.

As described in section 2.4, Recurring Slope Lineae (RSL) are of great interest to the search for life on Mars. While the debate still continues whether RSLs are caused by wet or dry processes (or a combination of both), they still remain of interest as a dynamic, seasonally active feature that re-occur year after year in the same L_s range in the same places in some of the warmest regions on Mars.

While there are many RSL sites around Valles Marineris, only a small number have CRISM FRT coverage that aligns with HiRISE imagery. This section will look at three sites around Valles Marineris, where RSL activity has been confirmed, and has coverage by both instruments, by examining CRISM scenes to try to identify surficial material where RSLs occur, both through spectral examination and through comparison to very high resolution visible imagery, and then compare spectra of those regions of interest to the laboratory spectra obtained in the analogue experiments described in chapter 5 in order to look for any evidence of PAHs in abundances above the detectability limit that has been established.

7.1. Study Regions

This section will look at the 3 individual sites identified by Edgar (MSc. Project, 2018) within the Valles Marineris. As described in section 2.4, Valles Marineris is an extremely large canyon feature near to the equator of Mars, and many sites around its perimeter have been identified as sites of confirmed and possible RSL activity (Stillman et al., 2017). The three sites that are examined are Coprates Montes, Nectaris Montes and Ganges Mensa, the locations of which are shown in Figure 7.1.
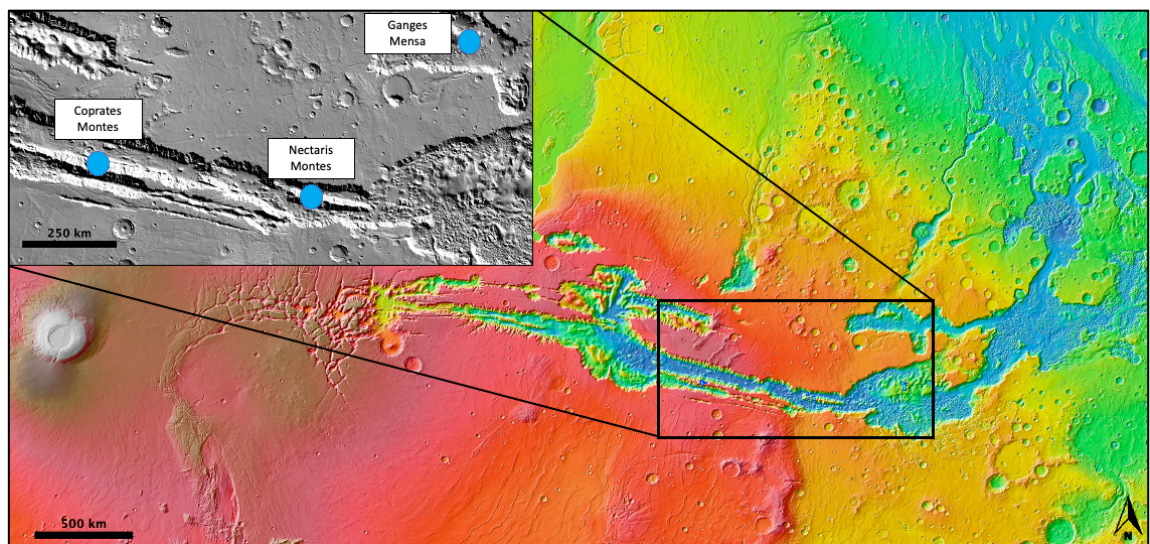
Figure 7.1: Location of 3 sites in Valles Marineris where analysis of RSL is carried out. Created in JMars over colour and greyscale hill-shaded MOLA 463 m elevation map. Inset shows Coprates Montes (Lat: -13.5, Long: 298.1), Nectaris Montes (Lat: -14.7, Long: 306.2) and Ganges Mensa (Lat: -7.6 Long: -48.0)

Edgar (2018) collated the CRISM and HiRISE imagery covering RSL locations identified by Stillman et al., (2017), and these areas will now be discussed in turn.

7.1.2. Coprates Montes

Figure 7.2 shows the location of the CRISM and HiRISE imagery of interest in this region, while Table 7.1 shows their details.
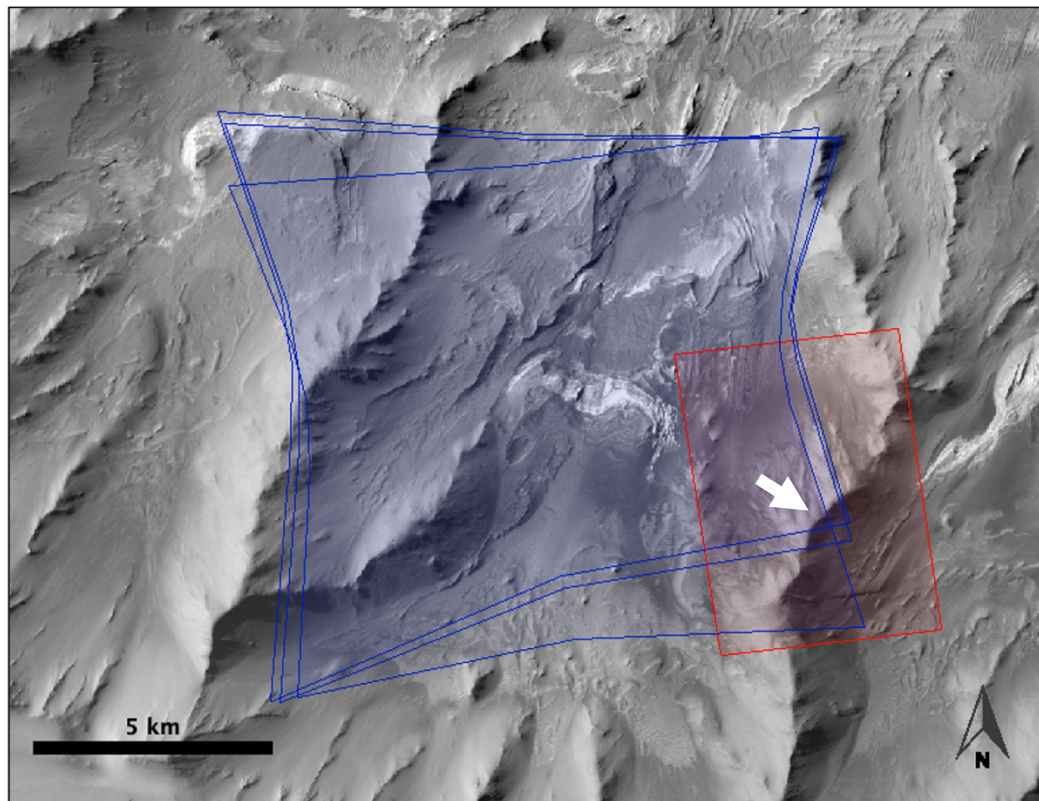
Figure 7.2: Coprates Montes study region (Lat: -13.0 Long: -64.9) CRISM
(FRT0000A16E, FRT0000A993 and FRT000186AC) and HiRISE
(ESP_033485_1670_RED) imagery locations draped over CTX image
P18_008194_1669_XN_13S065W. RSL location marked by white arrow.
Produced in JMARS

Table 7.1: Details of data products from Coprates Montes

Instrument	Product ID	Acquisition Date	Mars Year	Solar Longitude	Phase Angle (°)
CRISM	FRT0000A16E	24-Feb-2008	29	36	49
CRISM	FRT0000A993	25-April-2008	29	63	63
CRISM	FRT000186AC	30-April-2010	30	84	57
HiRISE	ESP_033485_1670_RED	17-Sept_2013	32	23	50

The 3 CRISM scenes analysed for Coprates Montes range from L_s 36-84, and occur on the NW facing slope. Figure 7.3 shows the detail from the HiRISE imagery of the RSL.
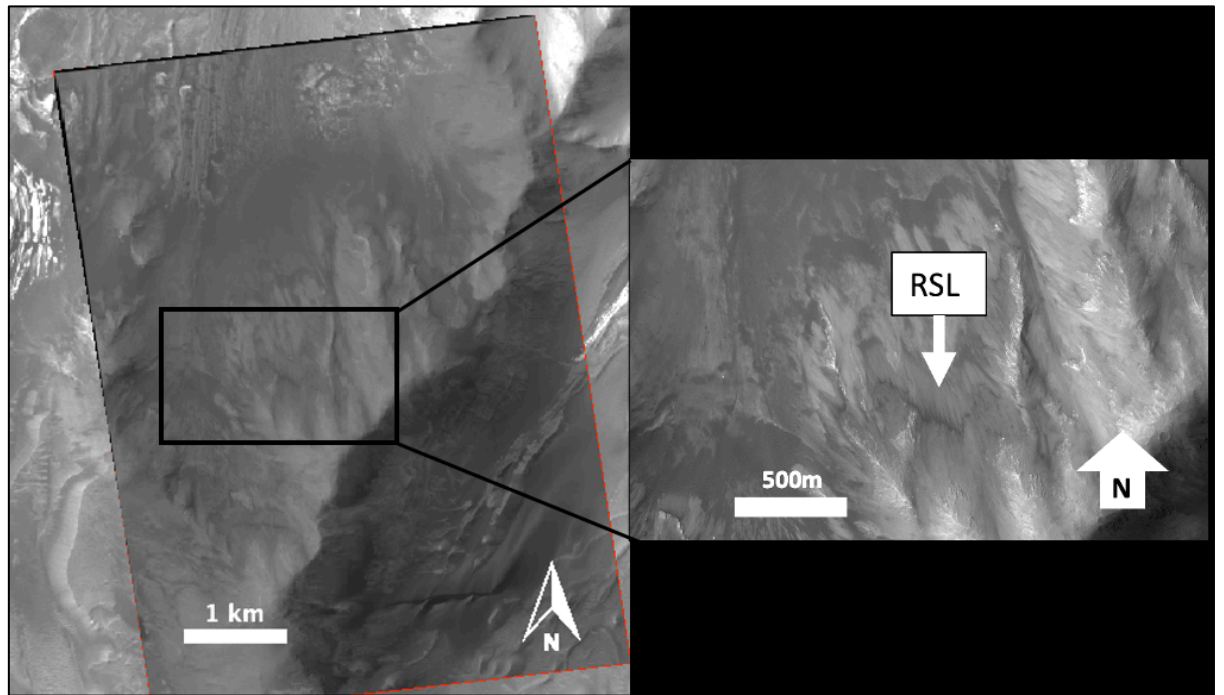
Figure 7.3: HiRISE image ESP_033485_1670_RED (left) of NW facing slope with inset from the same image (right) showing the RSL on the NW facing slope

Following on from the work of Edgar (2018), a region was identified that corresponded roughly to the locations of RSL imaged with HiRISE on the CRISM imagery; the same location was analysed with the two other CRISM scenes but one scene, FRT0000A993, was discarded as every pixel across the scene exhibited noise that interfered with crucial parts of the spectra.

In this case, the RSL locations occur right at the edge of the CRISM scenes. Edgar's RSL location for CRISM scene FRT0000A16E and a region manually located by finding the same spot visually for CRISM scene FRT000186AC are shown below in Figure 7.4.
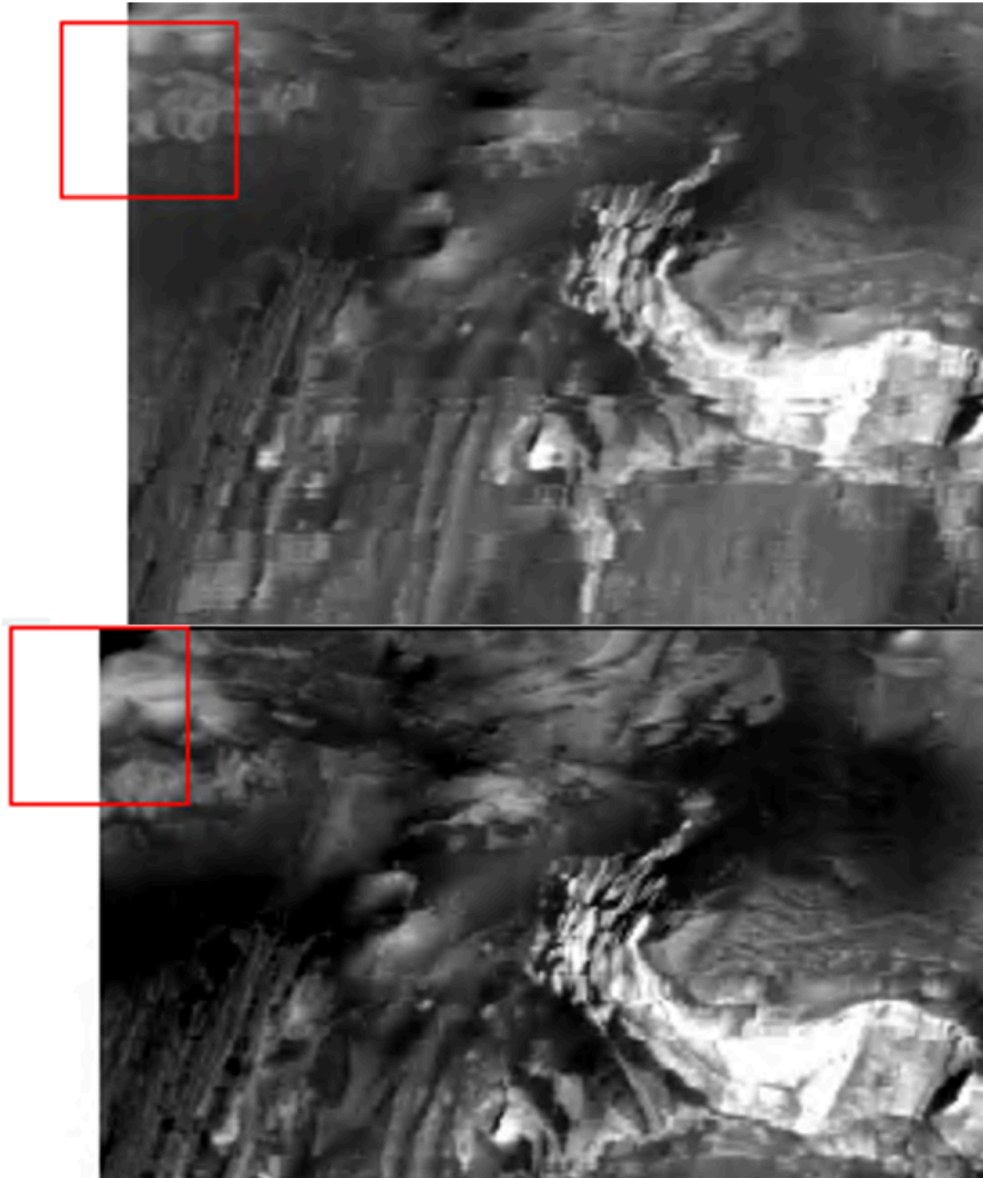
Figure 7.4: Location of RSL regions in CRISM scenes FRT0000A16E (top) and FRT000186AC (bottom). Red box is 1x1km.

An attempt was made to look for distinct endmembers using the pixels from within the red square in Figure 7.4 using an endmember extraction algorithm (R. Song, private communication, 2020), but much like the result of this technique on the SPRC, the spectra is overwhelmed by the background spectral response, in this case basalt rather than CO_2 ice (Figure 7.5).
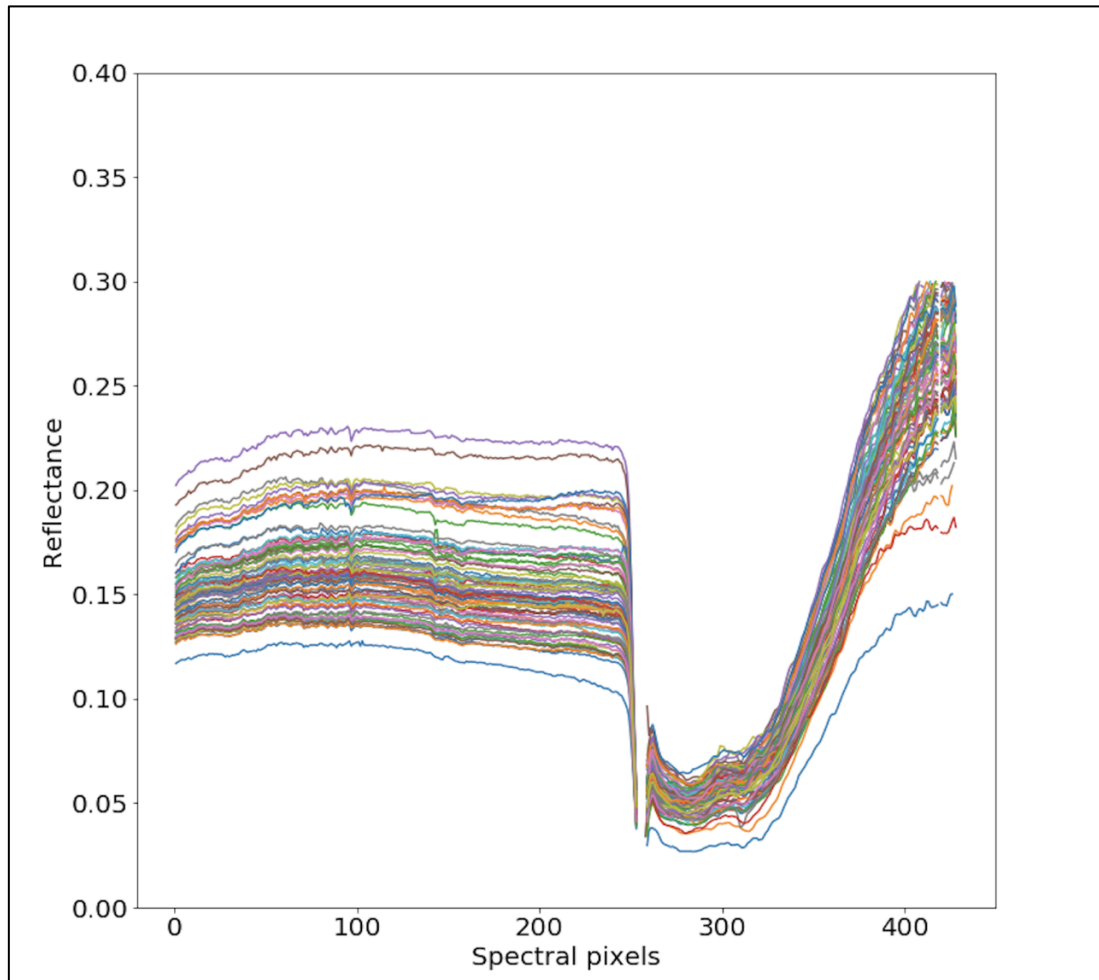
Figure 7.5: NFINDR endmember extraction algorithm applied to candidate ROI of area inside red square from Figure 7.4 around RLS location in CRISM scene FRT0000A16E by R. Song.

Examination using summary products of these scenes also failed to reveal anything unique for the RSL region or surrounding areas, but individual examination of the pixel locations identified by Edgar (ibid) can be seen compared to lab data in the graph below.

The resulting spectra from pixels over approximate RSL locations (according to HiRISE) were compared to the laboratory data from Chapter 5 for 70 % JSC

Mars-1 analogue dust mixed with 30% MgCL$_2$.6H$_2$O salt of which 1% of the salt was the PAH mix and these are plotted below in Figure 7.6.
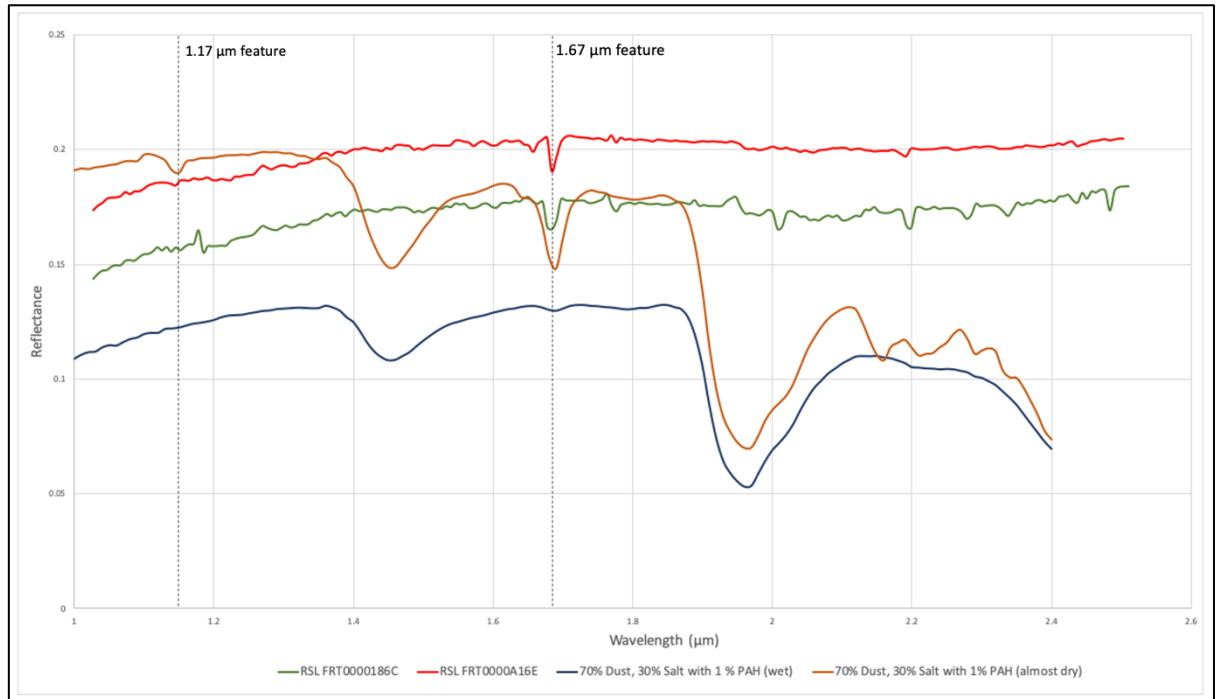
Figure 7.6: Graph showing spectra from two regions thought to overlay RSL features in CRISM scenes FRT000186AC (green) and FRT0000A16E (red) along with laboratory spectra of sample of 70 % JSC Mars-1 analogue dust mixed with 30% MgCL$_2$.6H$_2$O salt of which 1% of the salt was the PAH mixture when wet (dark blue) and almost dry (brown)

The RSL spectral features established at ~1.4 and 1.9 µm described by Ojha et al., (2015) and obvious in the laboratory magnesium chloride spectra, are not particularly visible for either of the CRISM spectra. What is obvious is the prominent feature at 1.67µm that occurs in all 4 spectra, this seems to closely resemble the strong diagnostic feature for the PAH in the RSL analogue mixture. The other diagnostic feature at 1.17 µm in the laboratory spectra

(which only becomes visible as the sample dries) can also be seen in the red spectra for FRT000A16E. This could indicate that the RSL was in a more dehydrated state at the time of the acquisition due to it being earlier in the spring. The 1.67 µm feature does not occur in nearby pixels outside of the region shown to have RSL activity by HiRISE. Figure 7.7 shows a sample of spectra for surrounding pixels alongside a pixel within the RSL region.
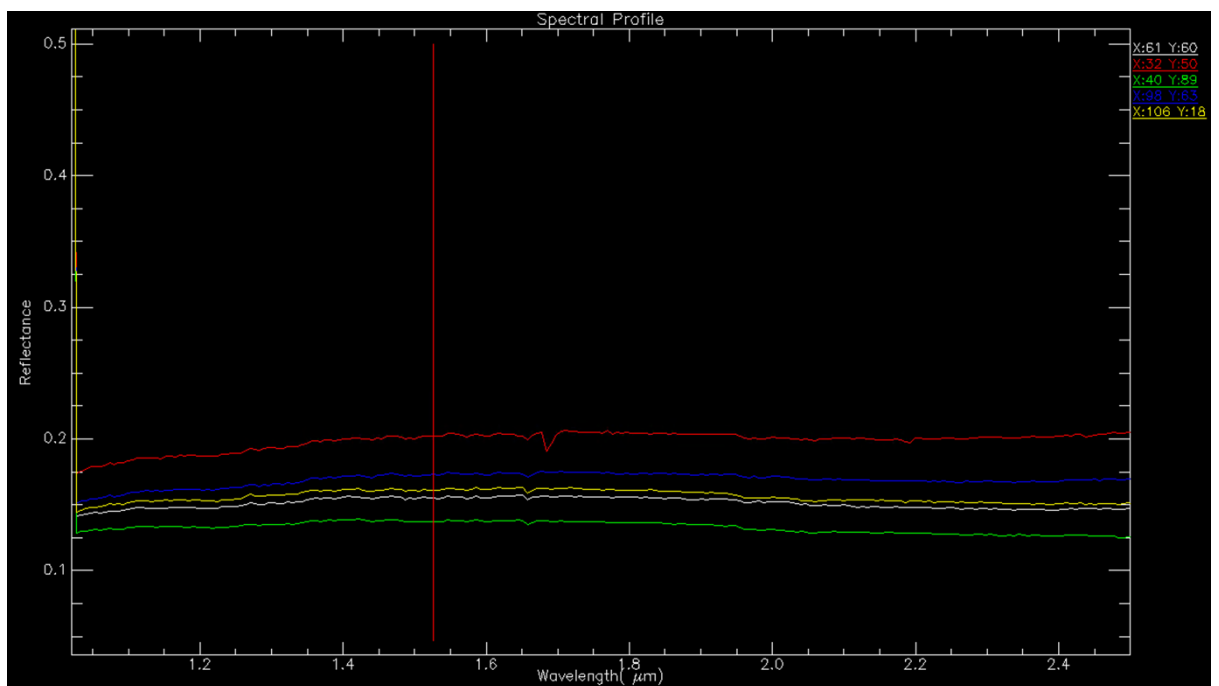
Figure 7.7: Spectra for pixels surrounding RSL region (blue, yellow, white and green) show no feature at 1.67 µm, while the pixel within the RSL (red) does

7.1.3. Nectaris Montes

The next area of interest is Nectaris Montes, further east along Valles Marineris, is also the site of RSL activity. Figure 7.8 shows the context for the imagery examined for this region, whilst Table 7.2 lists the product details.
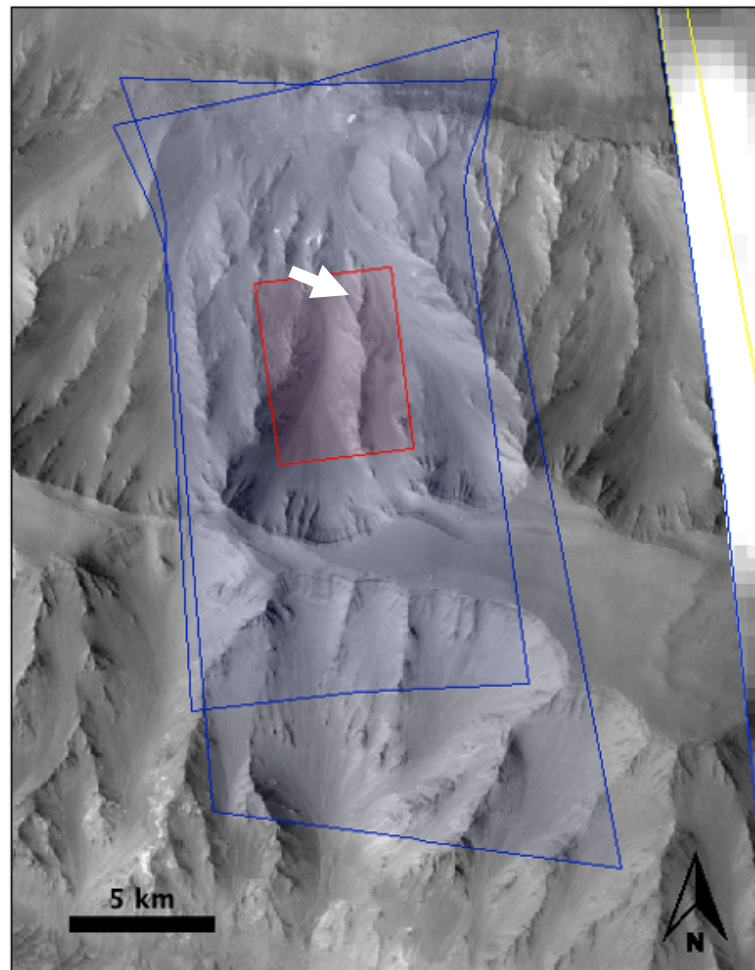
Figure 7.8: Nectaris Montes study region (Lat: -14.3 Long: -55.3) CRISM (FRT00024582 and FRT00024C3D) and HiRISE (ESP_034144_1655_RED) imagery locations over CTX image D07_030030_1651_XN_14S055W. RSL location marked by white arrow. Produced in JMARS

Table 7.2: Details of products from Nectaris Montes

Instrument	Product ID	Acquisition Date	Mars Year	Solar Longitude	Phase Angle (°)
CRISM	FRT00024582	13-April-2012	31	96	74
CRISM	FRT00024C3D	05-May-2012	31	106	57
HiRISE	ESP_034144_1655_RED	17-Sept_2013	32	46	56

The 2 CRISM scenes that cover the RSL are taken later in the CRISM mission after the gimbal issues materialised, hence the elongated footprint shape, but are still useable for analysis. The images are taken 10 L_s apart at the very beginning of southern hemisphere winter (although the near equatorial location of Valles Marineris means that it is not yet at extreme cold temperatures in this location). Figure 7.9 shows the detail from the HiRISE imagery of the RSL.
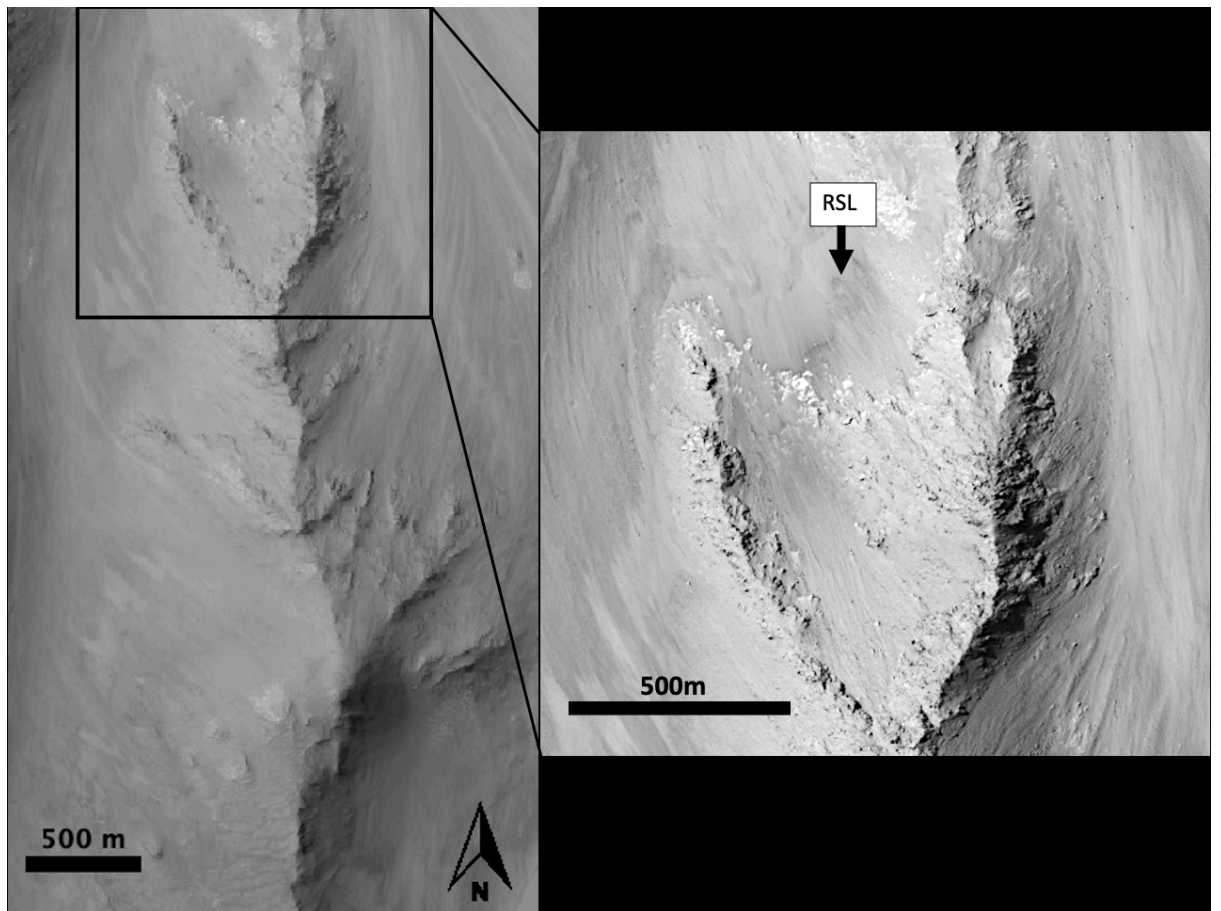
Figure 7.9: HiRISE image ESP_034144_1655_RED (left) of forked crests with inset from the same image (right) showing the RSL in between

As with the previous location, summary product evaluation of Nectaris Montes did not reveal anything that delineated the RSL area from the rest of the scene, but the location of the RSL corresponding to HiRISE visual identification is shown below in Figure 7.10.
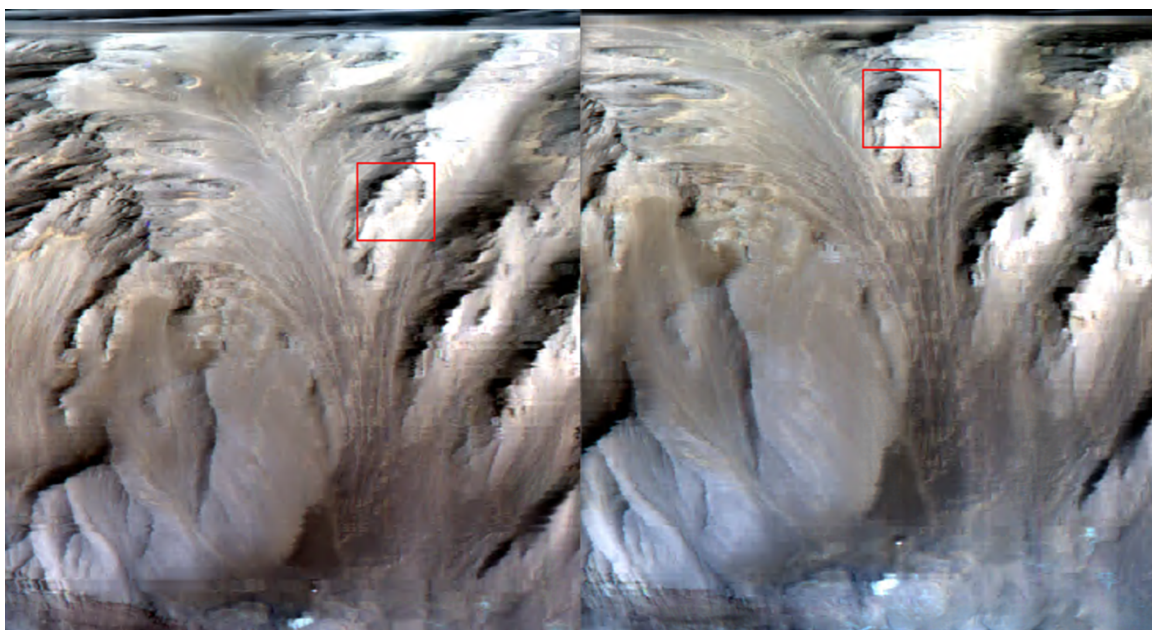
Figure 7.10: Location of RSL regions in CRISM scenes FRT00024582 (left) and FRT00024C3D (right). Red box is 1x1km.

There are some distortions due to differences in viewing geometry, and it is difficult because of this and the coarse spatial resolution to identify the exact spot where RSLs may be. Therefore, a pixel by pixel examination of the area between the two forked ridges was undertaken to look for signs of the telltale ~1.4 and 1.9 µm salt features, and of course, any PAH like signatures. In Figure 7.11, one pixel from the RSL region in scene FRT0000A16E (red line) shows a very subtle dip at 1.67 µm, and perhaps the same at 1.17 µm, but no other pixels in the scene showed any evidence of PAH like features; an example of the other RSL spectra is shown in green on the graph. No pixels at all show these features in scene FRT000186AC.
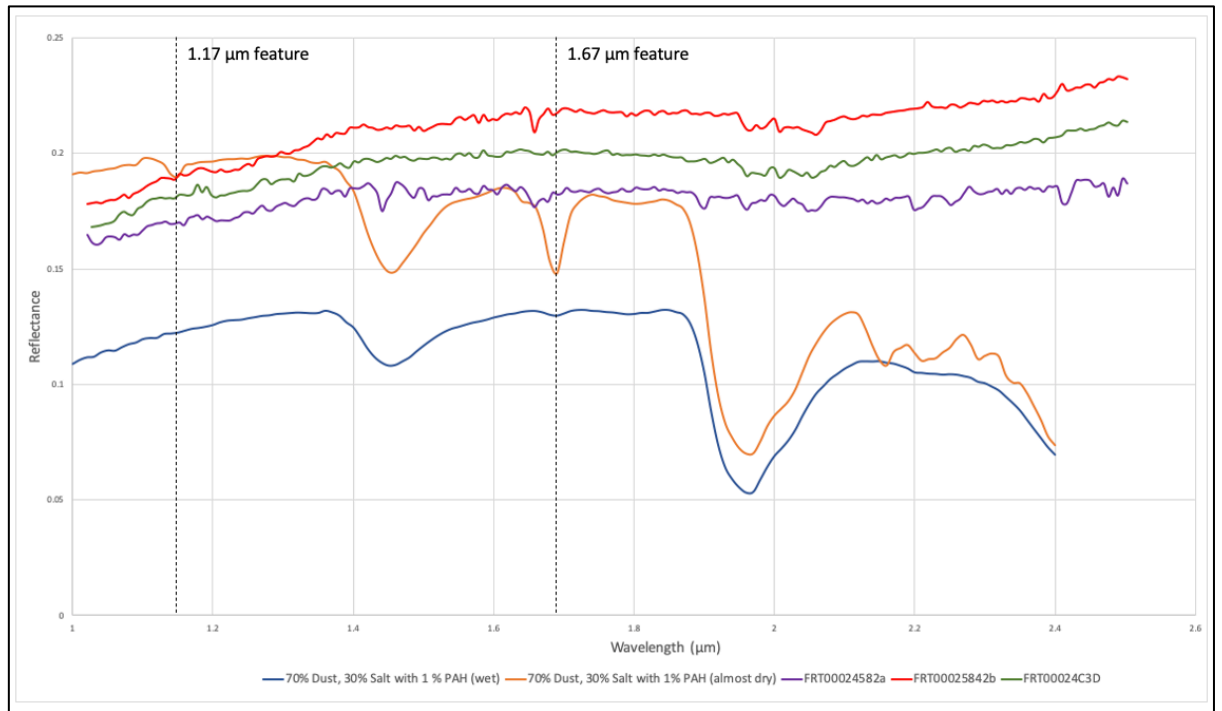
Figure 7.11: Graph showing spectra from two regions thought to overlay RSL features in CRISM scene FRT00024582 (red and purple) and one from FRT00024C3D (green) along with laboratory spectra of sample of 70 % JSC Mars-1 analogue dust mixed with 30% $MgCL_2.6H_2O$ salt of which 1% of the salt was the PAH mixture when wet (dark blue) and almost dry (rust)

There is a small absorption features at 1.67 µm; it is much smaller than the adjacent features at 1.65 µm but is distinct from it, The lack of any strong signature reminiscent of RSL spectral features at all may be due to the timings of these CRISM acquisitions. While it is still warmer at Valles Marineris compared to higher latitudes, the CRISM acquisitions are dated well into southern hemisphere winter (L_s 96 and 106), and so RSL activity is likely to have ceased. This implies that any organics that could have been exposed through RSL activity would have been exposed to too much UV radiation to be detected easily.

228

7.1.4. Ganges Mensa

Further east along and to the north of Valles Marineris is Ganges Mensa. Figure 7.12 shows the location of imagery used for this region, and Table 7.3 contains the imagery product details.
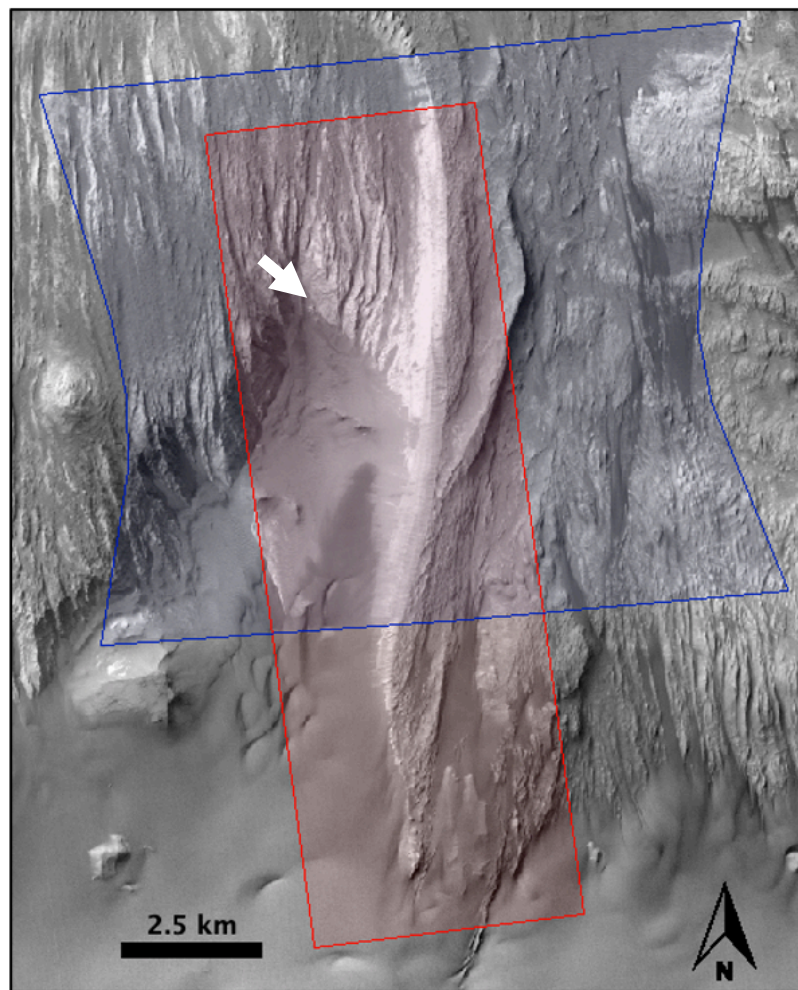
Figure 7.12: Ganges Mensa study region (Lat: -7.6 Long: -48.0) CRISM (FRT000125AD) and HiRISE (ESP_039933_1720_RED) imagery locations over CTX image F19_043124_1723_XN_07S048W. RSL location marked by white arrow. Produced in JMARS

Table 7.3: Details of products from Ganges Montes

Instrument	Product ID	Acquisition Date	Mars Year	Solar Longitude	Phase Angle (°)
CRISM	FRT000125AD	29-April-2009	29	256	52
HiRISE	ESP_039933_1720_RED	06_Feb_2016	32	283	36

There is only one FRT CRISM image available for this region, and the HiRISE

context is shown below in Figure 7.13.
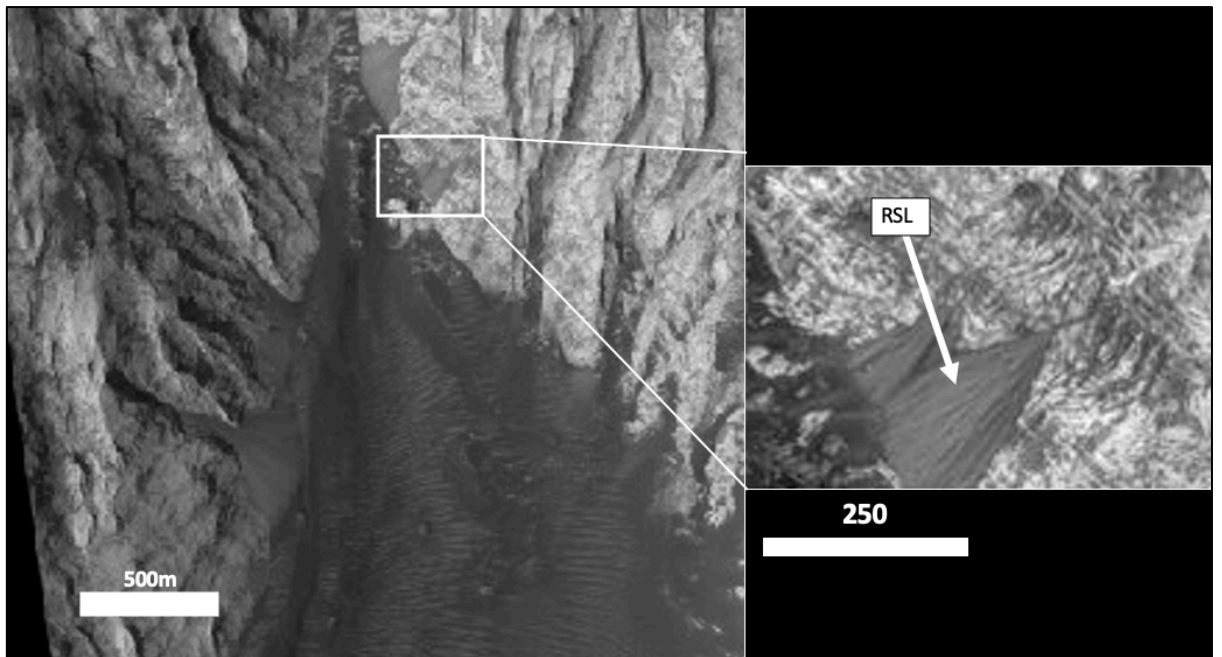
Figure 7.13: HiRISE image ESP_039933_1720_RED of Ganges Mensa

RSL region with detail from same image on the right

Figure 7.14 shows the corresponding CRISM scene for this region, with the

red box over the RSL region of interest.
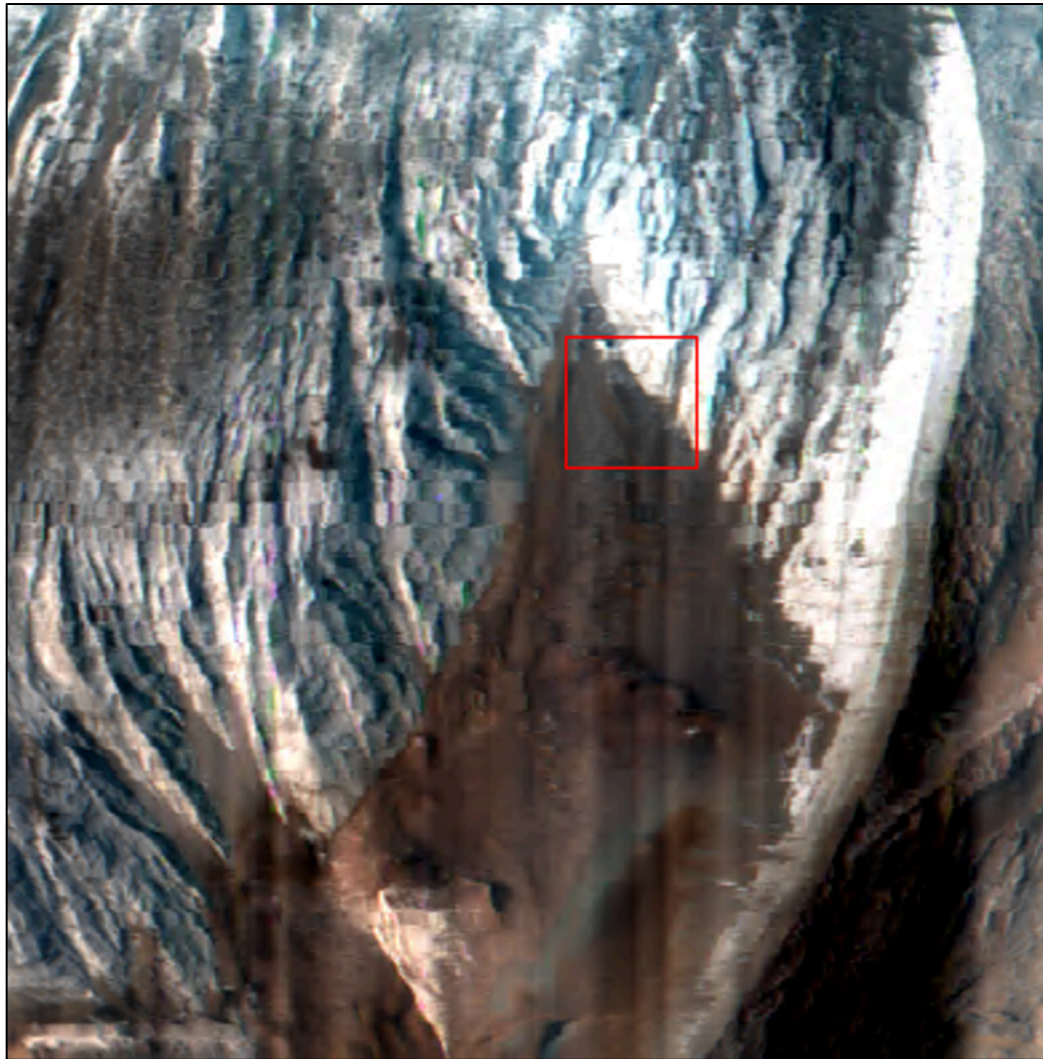
Figure 7.14: Location of RSL region in CRISM scene FRT000125AD.

Red box is 1x1km.

This region was quite interesting as there is stark contrast between the surface colour and albedo at the boundary where the RSL occur. Figure 7.15 shows the summary product for discerning between icy or highly reflective material and low albedo, possible mafic material (left) beside the summary product for high-calcium pyroxene (right).
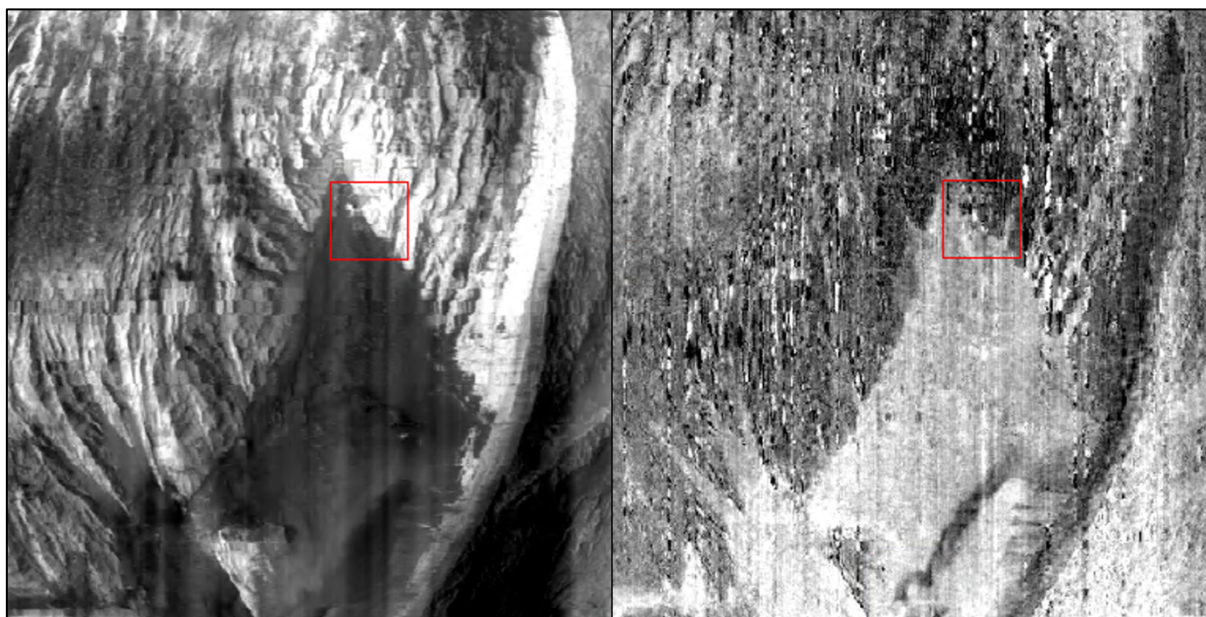
Figure 7.15: Location of RSL region in CRISM scene FRT000125AD with Viviano-Beck et al. summary products for albedo (R1130, left) and high-calcium pyroxene (HCPINDEX, right). Red box is 1x1km.

Following on from the work by Edgar (2018), the site that was identified as containing possible signatures of salt features at ~1.4 and 1.9μm was examined first. A pixel that was identified with quite a strong spectral feature at around ~1.7 μm was looked at first (line 256, sample 146) and then a region of interest was taken surrounding this pixel to include everywhere around this pixel, totalling 21 pixels, and both these spectra are shown alongside the laboratory spectra for wet and almost dry RSL analogues below (Figure 7.16).
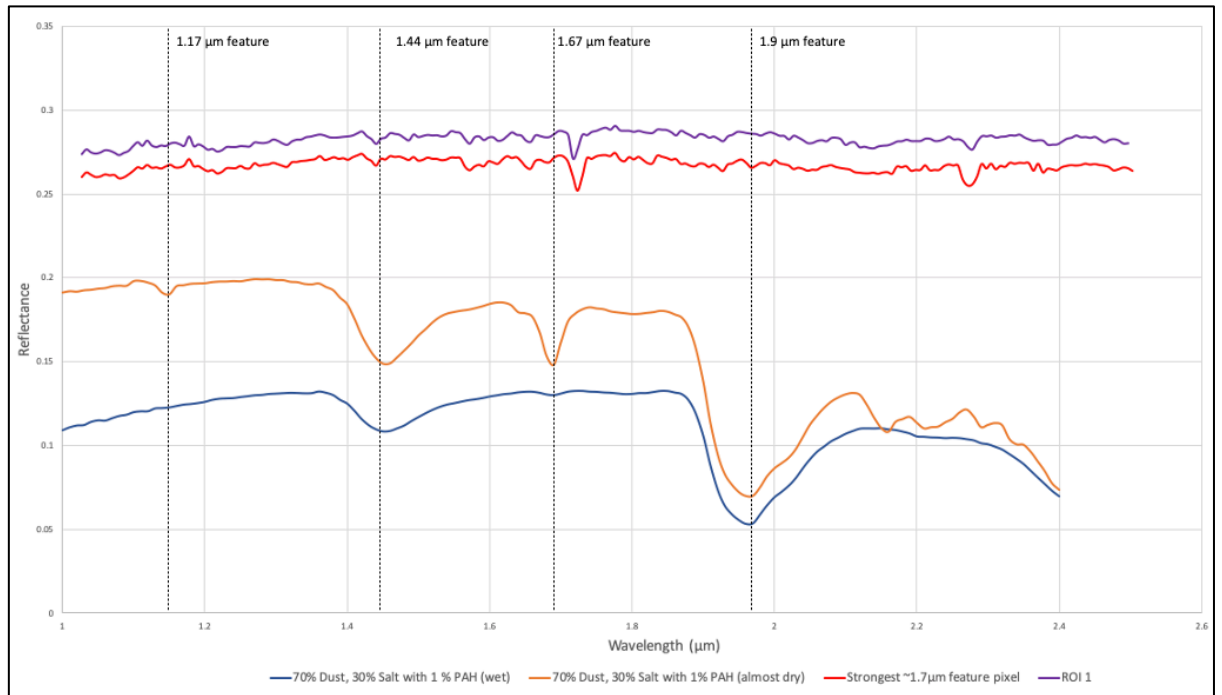
Figure 7.16: Graph showing spectra region thought to overlay RSL features in CRISM scene FRT000125AD (single pixel, red and ROI of 21 pixels averaged, purple) along with laboratory spectra of sample of 70 % JSC Mars-1 analogue dust mixed with 30% $MgCL_2.6H_2O$ salt of which 1% of the salt was the PAH mixture when wet (dark blue) and almost dry (rust)

We can see there does seem to be a slight dip in the single pixel (red line) at 1.9 μm, and a more significant absorption feature at 1.44 μm, indicating salts, but the feature at ~1.7 μm is at too long a wavelength to match the laboratory RSL analogues with PAH content. Taking a look at the location of this pixel and then looking at the surrounding pixels that exhibit the same RSL type features resulted in an average of the 21 pixels for ROI 1 (purple in Figure 7.16). When viewed in context on the image, ROI 1 doesn't seem to exactly

match up with the location of the RSL and is located over a much higher albedo, less dust rich region in the scene (Figure 7.17, red polygon).
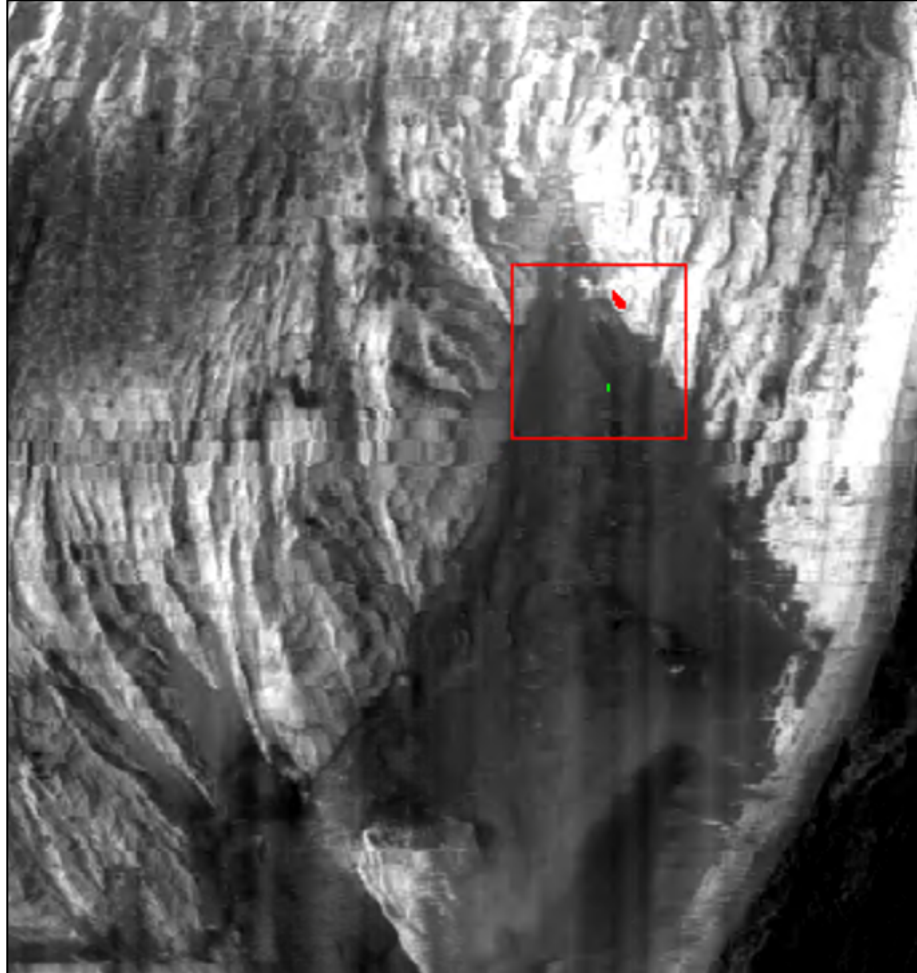
Figure 7.17: Location of ROI 1 (red) and ROI 2 (green) in CRISM scene

FRT000125AD

The adjacent low albedo region was examined pixel by pixel, and a region of interest (ROI 2) was made from 3 pixels that showed interesting spectral features (green rectangle, Figure 7.17). Below in Figure 7.18, the averaged spectra of these 3 green pixels from ROI 2 can be seen compared with ROI 1 and the laboratory spectra from RSL analogues with PAH content.
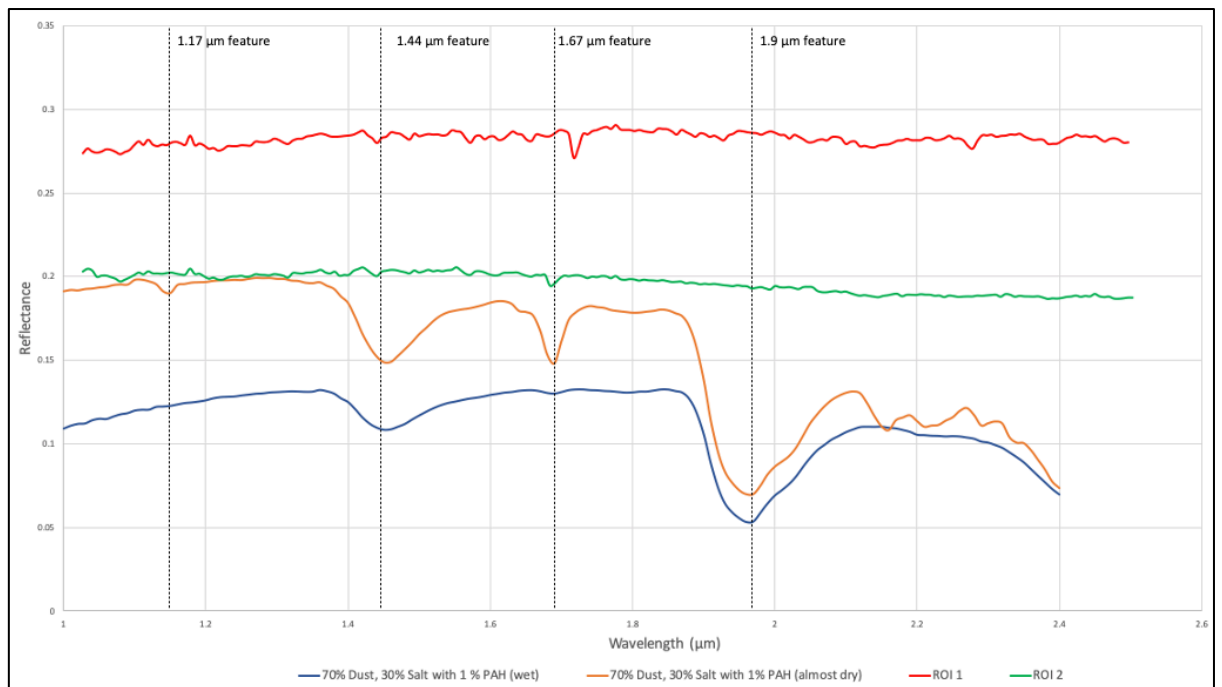
Figure 7.18: Graph showing spectra region thought to overlay RSL features

in CRISM scene FRT000125AD (ROI 1 of 21 pixels averaged, red and ROI 2

pf 3 pixels averaged, green) along with laboratory spectra of sample of 70 %

JSC Mars-1 analogue dust mixed with 30% $MgCL_2.6H_2O$ salt of which 1% of

the salt was the PAH mixture when wet (dark blue) and almost dry (rust)

Unlike ROI 1, ROI 2 does show an absorption feature at 1.67 µm consistent with the PAH feature from laboratory results but doesn't show any evidence of the 1.17 µm feature, or of any other RSL features.

7.2. Analysis of Results from All 3 Regions

Below are shown spectra of interest from all three RSL sites in one graph compared to laboratory analogue spectra (Figure 7.19).
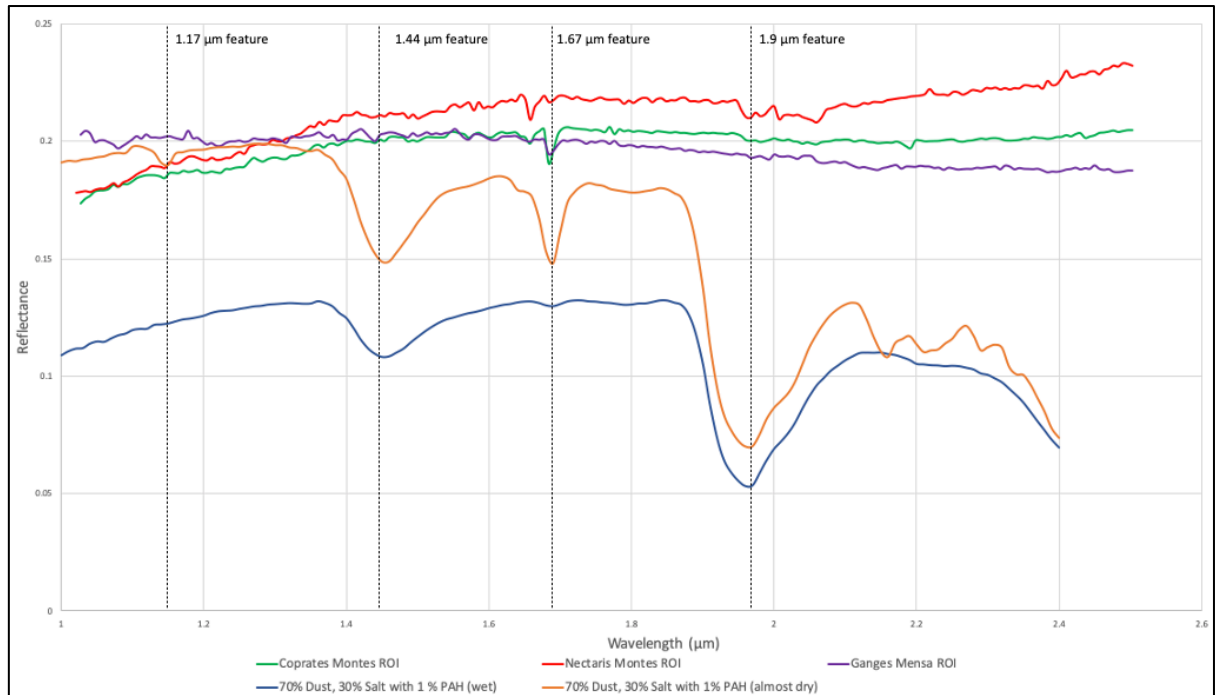
Figure 7.19: Graph showing spectra for regions thought to overlay RSL features in CRISM scene FRT0000A16E from Coprates Montes (green), FRT00024582 from Nectaris Montes (red) and FRT000125AD from Ganges Mensa (purple) along with laboratory spectra of sample of 70 % JSC Mars-1 analogue dust mixed with 30% $MgCL_2.6H_2O$ salt of which 1% of the salt was the PAH mixture when wet (dark blue) and almost dry (rust)

All three ROIs show a feature at 1.67 µm over confirmed RSL sites, and that feature was not present in nearby pixels over similar geology but not thought to host RSLs. However, while the ROIs from Coprates Montes and Nectaris Montes show a very subtle dip at 1.17 µm matching the almost dry RSL laboratory analogue with PAH content, the ROI from Ganges Mensa shows no match. None of the spectra showed any sign at all of the large feature at 3.29 µm, but as discussed in Chapter 2 and the SPRC analysis, this region is

not ideal to analyse for Mars due to the spectral features that occur at higher wavelengths that may mask any subtle features in these ranges.

Coprates Montes showed the strongest match with laboratory spectra, and so to try to isolate the unique RSL region features, spectral ratioing was carried out by dividing the ROI spectra with a non-RSL pixel spectrum from the same across-track region but covering similar geology; the results are shown below in Figure 7.20.
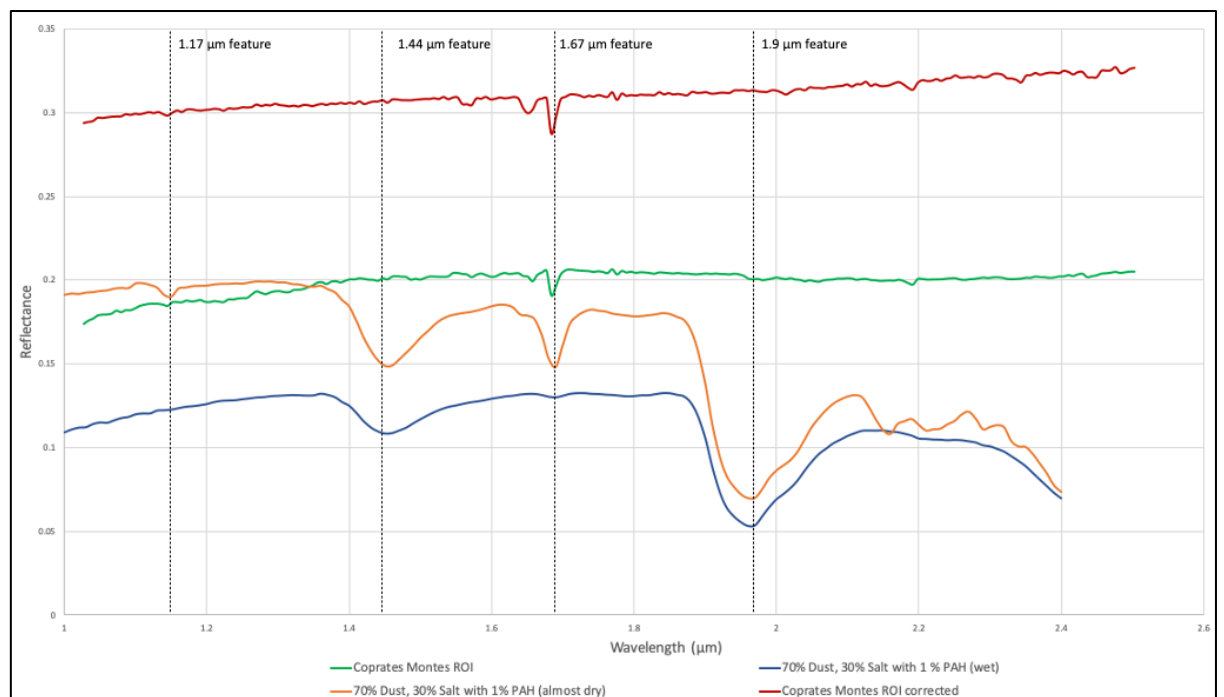
Figure 7.20: Graph showing ROI from CRISM scene FRT0000A16E from Coprates Montes (green) and the same ROI corrected by ratioing with a control spectrum from a nearby non RSL region (dark red) along with laboratory spectra of sample of 70 % JSC Mars-1 analogue dust mixed with 30% $MgCL_2.6H_2O$ salt of which 1% of the salt was the PAH mixture when wet (dark blue) and almost dry (rust)

This correction strengthens the features at 1.17 and 1.67 µm. Coprates Montes is certainly of great interest, and the presence of the features at 1.67 µm in all 3 sites over RSL regions matches well with laboratory results. It seems that the salt features at ~1.4 and ~1.9 µm are at least present where the 1.67 µm feature is strongest, being most obviously seen at Nectaris Montes, where the PAH-like feature was the weakest. This may be some feature of the life cycle of RSL, whatever the cause for the 1.67 µm signature. The time of year may shed some light on this; the Coprates Montes CRISM acquisition was at L_s 36, early autumn, Nectaris Montes in early Winter (L_s 96) while Ganges Mensa was acquired at L_s 256, the height of summer. Ganges Mensa has the weakest 1.67 µm feature, but the strongest salt signature at 1.9 µm, perhaps indicating that the RSL was more active at this stage, and that much like in the laboratory results, any PAH signature would become more pronounced with drying.

An assessment of the Viviano-Beck et al. CRISM type spectra found no known mineral on Mars to have features at both 1.17 and 1.67 µm, and there seems to be no real morphological, albedo or major geological or mineralogical unit boundary between pixels that do or don't exhibit the PAH like features, other than known locations of RSL activity. Therefore the consistency of these features across 3 known RSL sites hundreds of kilometres apart, and their match to laboratory RSL analogues, indicate that they are likely to be linked to RSL activity. The sites examined lack of any other features indicative of polycyclic aromatic hydrocarbons established in experiments, but the absorption features observed may be signs of some other unknown compound

238

hitherto not identified or associated with RSL activity. The absence of features at 1.17 and 3.29 µm indicate a lack of PAHs, but nonetheless, a study of all known RSL sites with CRISM coverage across Mars would be very interesting to see if this feature at 1.67 µm occurs elsewhere.

7.3. Preliminary Conclusions

Three sites with CRISM imagery over regions with RSL activity identified from visible imagery were examined, and all three showed a unique signature of varying strengths at ~1.67 µm, consistent with laboratory spectra for one known PAH absorption feature. There was no sign, however, of the other known PAH spectral features at 1.17 and 3.29 µm. It is interesting that the 1.67 µm feature occurs at all three sites, and comparison with known Martian mineralogy did not reveal a cause for what may be the source of this unidentified spectral feature. A further examination of more RSL sites outside of VM with corresponding CRISM FRT coverage would be of interest to see if this feature occurs at other sites of confirmed RSL activity.

Differences in spatial resolution between HiRISE (0.025 m/pixel) and CRISM (20 m/pixel) are a limiting factor in successfully finding overlapping small-scale features and obtaining pixel spectra with a pure signature, unobscured by surrounding non-RSL surface composition.

This chapter concludes the original research carried out in the search for candidate sites for PAH detection and their analysis and comparison with laboratory results. The next chapter will discuss and summarise the results of Chapters 4, 5, 6 and 7 and how well the research has answered the questions posed in Chapter 2.

8: Conclusions

PAHs are crucial to theories of abiogenesis, and despite their ubiquitous presence in space, their detection on planetary bodies remains a primary objective for the field of planetary science. The attempt to identify them on Mars is especially important given their conspicuous absence and the recent discoveries of other organic compounds and possible liquid water on the Red Planet (Freissinet et al., 2015; Lauro et al., 2020). In this final section the key results from each original research chapter will be discussed including their significance, implications and the limitations of the findings before finally discussing the impact of this study on future work.. This section will address the remaining questions from Chapter 1 that were not addressed during the review of existing literature from Chapter 2, namely:

- What would PAHs look like if they were present in these environments on Mars, and how much PAH would have to be there to be detectable at all?
- What processes occur, and what chemical and mineralogical components are present, on the SPRC and in RSL, and how might they affect attempts to detect PAHs?
- What implications does this study have on future work?

8.1: Conclusions of First Analysis of 5 SCT Pit Feature from 2007-2012

The work in Chapter 4 is the subject of a journal publication (Campbell et al, 2018) from which some of these conclusions are taken. The work undertaken in this section was extremely useful as a first step on how to go about analysis of the SPRC for signs of PAHs and was hugely influential to the course that the rest of the thesis would take. Wide-scale, low resolution mapping of the SPRC had been carried out by others using both OMEGA and CRISM spectrometers (Douté et al., 2007; Brown et al., 2010) and CRISM had been used to look at PLD and ice compositions (Pommerol et al., 2011). However, until now there has been no focus on the astrobiological importance of dust exposure and accumulation on SCT. The work in this chapter identified rim features that were most rich in water ice and those that had better dust coverage, as well as finding indications of magnesium carbonate on some rims. The diagnostic summary product for carbonates showed some unreliability, particularly with regard to angles of solar illumination, and it was removed as a product in Viviano-Beck et al.'s (2014) update of CAT summary products and was discarded as a tool in later chapters. However, the other summary products proved to be extremely useful for targeting compositional differences over the SPRC.

Spectral mapping revealed that there are distinct compositional differences between the majority of the SPRC and depression rims for all morphological units. Further analysis of ROI spectral features revealed that the compositional

differences are highlighted when spectra are corrected for interference from ices, with CO_2 ice being the crucial factor when looking for subtle spectral features.

Dark rims exhibit more variation in reflectance within spectra than non-rims. The influence of water ice is greater on rims and once removed, dark rim spectra more closely resemble the spectra of non-rims. CO_2 ice is a limiting factor in the detection of PAHs due to the strong absorption feature between 3.3 and 3.4 μm, while water ice appears to have less of an impact. The issue of the overwhelming influence of CO_2 ice informed my choice to look at some non-polar dynamic features, leading to the research described in Chapter 7 and the supporting RSL laboratory analogues discussed in Chapter 5.

A major limitation of this chapter was our lack of knowledge about the properties of the ice and frosts on the SPRC, which we can only infer from remote sensing; laboratory experiments and computer models may be used in future to improve the interpretation of remote sensing results (Singh and Flanner, 2016). Unfortunately, this is always going to be a limitation in planetary studies until such times as we are able to do in-situ polar analysis, whether that be with landers, rovers or people. Again, this was another motivator for the experiments in Chapter 5, so that we could have a controlled and complete record of the spectra of PAHs on CO_2 ice, which previously did not exist. It's almost impossible to find something if you don't know what you're looking for, and the work in Chapter 5 directly stemmed from the challenges faced in the work from Chapter 4.

I was also concerned about the effect of vertical surfaces like SCT scarp pits on both reflectance and elevation data during this chapter, and the sub-pixel dimensions of dust features; this contributed to the choice in Chapter 6 to look at A0 mesa features with large dust fans surrounding the plateaus, which cover multiple CRISM pixels and are relatively flat. The ability to analyse critically the influence of CO_2 and H_2O ice spectra on ROIs has paved the way for further in-depth analysis of spectral features of dust rims (Chapter 6). PAHs were not detected at the sensitivity level of the CRISM instrument, but this chapter highlighted the fact that the detectability limit of PAHs in ice was not known, and indeed a PAH spectrum pertinent to Mars did not exist, and as mentioned earlier, led directly to the work in Chapter 5 that addressed these problems, which we will talk about now.

8.2: Laboratory Analysis of PAHs in Martian Analogues

A series of novel experiments (described in Chapter 5) yielded some exciting results that will become publicly available (SSHADE; see Section 3) for free upon publication of the associated papers (SPRC analogue paper by Campbell et al., 2020, which is still under review by JGR Planets with an RSL paper in preparation).

This work is especially useful for anyone using CRISM data as the parameters of the SHINE and SHADOWS instruments replicated CRISM's spectral range and resolution, but the results are potentially useful for anyone looking for PAHs using infrared spectrometry.

A new spectrum was produced for a mix of anthracene, phenanthrene and pyrene PAHs which are pertinent to Mars (see Section 5.1) and absorption features at lower wavelengths than the typically used 3.29 µm were recorded (1.14 and 1.68 µm). Crucially, the detectability limit for PAHs in CO_2 was established as ~0.1% PAH and for magnesium chloride brines in Martian soil analogues as <0.5% PAH. We now know how the spectrum for PAHs in CO_2 ice and briny regolith evolves as the sample sublimates or dries, respectively. We can move from stating that PAHs were not detected, to stating that they are not present in concentrations above their empirically established detectability limits.

Although the importance of the RSL analogue experiments was somewhat diminished by the increasing evidence that RSLs may be a dry process (Schmidt et al., 2017), this matter is far from settled, and new discoveries of possible subterranean briny lakes (Lauro et al., 2020) mean that these experiments can still be of great importance to future studies of briny soils. RSLs may not be formed by brines, but if we are going to find wet environments on Mars, they are (because of the conditions on Mars, Section 2.3) very likely to be salty, and we now know how that affects the opacity of regolith with regard to the detection of some of the most important molecules in astrobiology.

8.3: Conclusions of Extended Analysis of SPRC to Search for PAH Candidate Site

This section also followed on from the work in Chapter 4, learning from the conclusions made there and taking into account a much wider pool of CRISM images, a new set of summary products (Viviano-Beck et al., 2014) and a brand-new set of spectra from the SPRC analogue experiments from Chapter 5. In addition, a study by Buhler et al., (2017) had shed some light on processes that might expose previously entrained dust that could now be examined spectrally.

Spectral evidence of a time series of suspected calving of A1 curl shaped pits was recorded, as well as evidence of a distinction between two types of pyroxene and their distribution across SCT features. There seems to be a preferential direction from which low-calcium pyroxene accumulates in some regions, which is very different from the uniform distribution of high-calcium pyroxene around A0 Type mesas.

A0 morphology appears to be the best candidate for accumulation of dust from sublimation around mesa edges and/or fans formed from previously entrained material through dust ejection. Type B morphology seems to be the most likely to expose water ice rich material and this fits with the assumed 'life cycle' of SCT where circular pit growth begins in earnest. CO_2 ice again is a massively limiting factor in finding subtle signatures, and even with the new laboratory data, no evidence of PAHs above the detectability limit of ~0.1% was found.

Additionally, endmember analysis using two different methods could not differentiate any unique signatures and simply showed slight variations in overall reflectance; summary products and individual pixel and ROI analysis was far more useful for looking at subtle characteristics of mineralogy distribution and spectra.

This work highlights the need to get in-situ measurements of polar ices. The CO_2 ice spectrum is, in particular, extremely difficult to separate from any subtle signature, and orbital remote sensing is just not up to the job with existing instrumentation. A spectrometer with higher spatial resolution is necessary as well as one that has high resolution at longer wavelengths where we can look for the stronger signatures at wavelengths above CRISM's 4 µm limit such as those routinely used to identify PAHs in the ISM (Allamandola, 2011). CRISM's FRT mode is no longer functioning properly and it's high time another high-resolution imaging spectrometer arrived at Mars. This along with high-resolution imagery of SCT over the coming years and decades will shed some light on the mysteries of the SPRC. This and other further work will be discussed in Section 8.5. Next are the conclusions for the final research chapter on RSL sites around Valles Marineris.

8.4: Analysis of Recurring Slope Lineae in Valles Marineris to Search for PAH Signatures

As discussed in Section 2.4.1, the mechanisms behind the formation of RSLs is still a matter of debate, and the brine hypothesis has somewhat fallen out of

favour since the inception of the experiments from Section 5.3. However, there are still some interesting results from the CRISM analysis of RSL regions surrounding Valles Marineris.

There is a real dearth of CRISM FRT imagery over confirmed RSL sites around Valles Marineris. Nevertheless, the 3 sites that did have imagery all had a unique signature of varying strengths at ~1.67 μm. However, none of the other known absorption features of PAHs was seen at any of the sites, so I would be very hesitant to ascribe the 1.67 μm feature to PAHs. Whatever this feature is, it only occurred over pixels thought to contain RSL features, and not in the surrounding pixels. It should be noted though that the massive difference in resolution between HiRISE and CRISM (0.025 m vs 20 m respectively) means that any meaningful comparison of individual pixels is impossible. Effective co-registration and even up-sampling of CRISM data to improve spatial resolution is currently underway by other members of MSSL's Imaging Group, but too late for inclusion within this work.

Returning to our list of unanswered questions, we now know what PAHs pertinent to Mars would look like in SPRC analogues and briny Martian soil, we know how much there needs to be in order to be detectable by CRISM. We have shed some light on SPRC processes that form different SCT morphologies, supporting findings for the interpretation of visible imagery, and have established how CO_2 ice and briny environments affect our ability to search for PAHs. We know that A0 SCT morphologies are the best places to look for large areas of dust on flat surfaces that may have been previously

entrained in ice. We know that the CO_2 ice spectrum is very difficult to work around, but that dried brines may actually increase our ability to see PAHs in soil. The final thing to address is what future work could be done to capitalise on these findings.

8.5: Future Work

Of course, my number one desire would be to send a lander to the SPRC and RSL environments to take samples, but this is unlikely to happen any time soon, especially for polar environments due to the failed Mars Polar Lander mission, and the current trend toward rover missions (which would be very difficult to operate on the SPRC's craggy and cold terrain). It is also extremely difficult to for landers to operate in Mars polar conditions due to the extremely low temperatures, absence of sunlight during winter for solar powered instruments, and landing on such uneven surface terrain would in itself be a huge challenge. However, there will soon be a mission (ExoMars Rosalind Franklin Rover) complete with a drill going to Mars (Vago et al., 2017) and a multispectral imager (PanCam; Coates et al., 2017) that will be able to tell us a lot more about the habitability of Mars and conditions at the surface and subsurface. In terms of remote sensing and this study, there are several other ways these results could be built upon. As mentioned earlier, a high-spatial resolution surface spectrometry mission that goes up to longer wavelengths would be of great utility in searching for PAHs. It would also be of interest to look at other areas of newly exposed material, for example new craters (Sidiropoulos and Muller, 2017) and see if there is any CRISM imagery over

these regions taken as short a time as possible after the impact to look at newly exposed material.

It would be interesting to see if local dust storm conditions and wind directions has any relationship to the directionally preferential accumulation of low-calcium pyroxene around SCT features, perhaps using historical Mars Colour Imager (MARCI) datasets which record daily, large-scale weather and climatic conditions on Mars (Bell et al., 2009). MARCI data could also be used to carry out scene specific CRISM correction to account for local differences when performing atmospheric corrections.

I would like to examine every known or suspected RSL site on Mars that has corresponding FRT CRISM imagery to look for similarities and differences in their spectra; more specifically, to see if there is evidence of salts and the absorption feature at 1.67 µm that was present in all three of the sites I looked at. I would also like to see the results of laboratory experiments that emulate brine-triggered granular flows as a possible cause of RSL as posited by the creators of the computer model that simulated this process (Wang et al., 2019). I would also like to perform experiments with Mars regolith simulant mixed with PAH and CO_2 ice to more fully simulate the conditions on A0 SCT regions; this was planned but unfortunately was not carried out due to shortages of CO_2 ice and time constraints.

Overall, this thesis stresses the importance of the detection of PAHs on Mars as a priority in astrobiology, identifies some of the best places to search for

them, and provides detectability constraints and data to help get the job done; until then, the search for PAHs on Mars continues.

References

Acke, B. (2011). *Observations of hydrocarbon emission in discs around young stars.* PAHS and the Universe. Joblin, C. Tielens, A.G.G.M. (eds). European Astronomical Society Publications Series. 46. 259-269

Africano, J. Kervin, P. Hall, D. Sydney, P. Ross, J. Payne, T. Gregory, S. Jorgensen, K. Jarvis, K. Parr-Thumm, T. Stansbery, G. Barker, E. (2005). *Understanding Photometric Phase Angle Corrections.* Proceedings of the 4th European Conference on Space Debris. 141-146

Albee, A., Battel, S., Brace, R., Burdick, G., Casani, J., Lavell, J., Leising, C., MacPherson, D., Burr, P. and Dipprey, D., (2000). *Report on the loss of the Mars Polar Lander and Deep Space 2 missions*

Allamandola, L.J., Tielens, A.G.G.M. and Barker, J., (1985). *Polycyclic aromatic hydrocarbons and the unidentified infrared emission bands-Auto exhaust along the Milky Way.* The Astrophysical Journal, 290, pp.L25-L28

Allamandola, L.J., (1990). *Benzenoid hydrocarbons in space: the evidence and implications*. In Advances in the Theory of Benzenoid Hydrocarbons (pp. 1-25). Springer, Berlin, Heidelberg

Allamandola, L.J., (2011). *PAHs and astrobiology*. EAS Publications Series, 46, pp.305-317

Allen, C.C.; Morris, R.V.; Jager, K.M.; Golden, D.C.; Lindstron, D.J.; Lindstrom, M.M.; Lockwood. J.P. (1998). *Martian Regolith Simulant JSC Mars-1*. Lunar and Planetary Sciences XXIX

Arey, J. and Atkinson, R., (2003). *Photochemical reactions of PAHs in the atmosphere.* PAHs: An ecotoxicological perspective, pp.47-63

Ball, P. (2004). *Astrobiology: Water, water everywhere?* Nature. 427. 19-20

Baratoux, D., Toplis, M.J., Monnereau, M. and Sautter, V., (2013). *The petrological expression of early Mars volcanism*. Journal of Geophysical Research: Planets, 118(1), pp.59-64

Becker, R.H. Pepin, R.O. (1984). *The case for a Martian origin of the shergottites: nitrogen and noble gases in EETA 79001.* Earth and Planetary Science Letters. 69. 2. 225-242

Bell III, J.F., Wolff, M.J., Malin, M.C., Calvin, W.M., Cantor, B.A., Caplinger, M.A., Clancy, R.T., Edgett, K.S., Edwards, L.J., Fahle, J. and Ghaemi, F., (2009). *Mars reconnaissance orbiter mars color imager (MARCI): Instrument description, calibration, and performance.* Journal of Geophysical Research: Planets, 114(E8)

Benner, S.A., Devine, K.G., Matveeva, L.N. and Powell, D.H., (2000). *The missing organic molecules on Mars*. Proceedings of the National Academy of Sciences, 97(6), pp.2425-2430

Bibring, J.P. Langevin, Y. Poulet, F. Gendrin, A. Gondet, B. Berthe, M. Soufflot, A. Drossart, P. Comes, M. Bellicci, G. Moroz, V. Mangold, N. Schmitt, B and the OMEGA team. (2004a). *Perennial water ice identified in the south polar cap of Mars.* Nature. 428**.** pp.627-630

Bibring, J.P., Soufflot, A., Berthé, M., Langevin, Y., Gondet, B., Drossart, P., Bouyé, M., Combes, M., Puget, P., Semery, A. and Bellucci, G., (2004b), August. *OMEGA: Observatoire pour la Minéralogie, l'Eau, les Glaces et l'Activité*. In Mars Express: the scientific payload (Vol. 1240, pp. 37-49)

Bibring, J.P., Langevin, Y., Gendrin, A., Gondet, B., Poulet, F., Berthé, M., Soufflot, A., Arvidson, R., Mangold, N., Mustard, J. and Drossart, P., (2005). *Mars surface diversity as revealed by the OMEGA/Mars Express observations*. Science, 307(5715), pp.1576-1581

Blackburn, D.G., Bryson, K.L., Chevrier, V.F., Roe, L.A. and White, K.F., (2010). *Sublimation kinetics of CO_2 ice on Mars*. Planetary and Space Science, 58(5), pp.780-791

Bonnefoy N., Brissaud O., Schmitt B., Douté S., Fily M., Grundy W., Rabou P., (2000). *Experimental system for the study of planetary surface materials - BRDF*. Remote Sensing Reviews, Vol. 19, 59-74

Borel and Gerstl, (1994). *Nonlinear spectral mixing model for vegetative and soil surfaces*. Remote Sens. Environment, vol. 47, no. 3, pp. 403–416, 1994

Botta O. and Bada J. (2002). *Extraterrestrial organic compounds in meteorites.* Surveys in Geophysics 23. pp.411–467

Botta, O. Martins, Z. Emmenegger, C. Dworkin, J.P. Glavin, D.P. Harvey, R.P. Zenobi, R. Bada, J.L. Ehrenfreund, P. (2008). Polycyclic *aromatic hydrocarbons and amino acids in meteorites and ice samples from LaPaz Icefield, Antarctica*. Meteoritics & Planetary Science. 43. 1465-1480

Brissaud, O., B. Schmitt, N. Bonnefoy, S. Douté, P. Rabou, W. Grundy, and M. Fily (2004). *Spectrogonio radiometer for the study of the bidirectional reflectance and polarization functions of planetary surfaces*: I. Design and tests. Appl. Optics, 43 (9), 1926-1937

Brown, R.H. Baines, K.H. Bellucci, G. Bibring, J-P. Buratti, B.J. Capaccioni, F. Cerroni, P. Clark, R.N. Coradini, A. Cruikshank, D.P. Drossart, P. Formisano, V. Jaumann, R. Langevin, Y. Matson, D.L. McCord, T.B. Mennella, V. Miller, E. Nelson, R.M. Nicholson, P.D. Sicardy, B. Sotin, C. (2004). *The Cassini Visual and Infrared Mapping Spectrometer (VIMS) investigation.* Space Science Reviews. 115. 111-168

Brown, A.J., Calvin, W.M., McGuire, P.C. and Murchie, S.L., (2010). *Compact Reconnaissance Imaging Spectrometer for Mars (CRISM) south polar mapping: First Mars year of observations.* Journal of Geophysical Research: Planets, 115(E2)

Buhler, P.B., Ingersoll, A.P., Ehlmann, B.L., Fassett, C.I. and Head, J.W., (2017). *How the Martian residual south polar cap develops quasi-circular and heart-shaped pits, troughs, and moats.* Icarus, 286, pp.69-93

Buratti, B.J. Cruikshank, D.P. Brown, R.H. Clark, R.N. Bauer, J.M. Jaumann, R. McCord, T.B. Simonelli, D.P. Hibbitts, C.A. Hansen, G.B. Owen, T.C. Baines, K.H. Bellucci, G. Bibring, J-P. Capaccioni, F. Cerroni, P. Coradini, A. Drossart, P. Formisano, V. Langevin, Y. Matson, D.L. Mennella, V. Nelson, R.M. Nicholson, P.D. Sicardy, B. Sotin, C. Roush, T.L. Soderund, K. Muradyan, A. (2005). *Cassini Visual and Infrared*

Mapping Spectrometer observations of Iapetus: Detection of CO_2. The Astrophysical Journal. 622**.** 149-152

Burke, K., Steinberger, B., Torsvik, T.H., Werner, S.C. and Wilkinson, J., (2012). *Why are the Geoid and the Areoid so similar*?. EGUGA, p.14126

Byrne, S. and Ingersoll, A.P., (2003). *A sublimation model for Martian south polar ice features.* Science, 299(5609), pp.1051-1053

Byrne, S., (2009). *The polar deposits of Mars*: Annual Reviews of Earth and Planetary Science, v. 37

Calvin, W.M. James, P.B. Cantor, B.A. Dixon, E.M. (2015). *Interannual and seasonal changes in the north polar ice deposits of Mars: Observations from MY 29-31 using MARCI.* Icarus. 251**.** pp.181-190

Campbell, J.D., Sidiropoulos, P. and Muller, J.P., (2018). *A search for polycyclic aromatic hydrocarbons over the Martian South Polar Residual Cap.* Icarus, 308, pp.61-70

Campbell, J.D., Schmitt, B. Brissaud, O., and Muller, J-P (2020). *The Detectability Limit of Organic Molecules within Mars South Polar Laboratory Analogues.* JGR Planets (under review)

Carroll, D., (2012). *Rock Weathering*. Springer Science & Business Media. Ch.2 pp. 7-16

Ceamanos, X. and Douté, S., (2010), June. *Calibration of CRISM/MRO apparent wavelengths using synthetic data*. In 2010 2nd Workshop on Hyperspectral Image and Signal Processing: Evolution in Remote Sensing (pp. 1-4). IEEE.

Ceamanos, X., Douté, S., Fernando, J., Schmidt, F., Pinet, P. and Lyapustin, A., (2013). *Surface reflectance of Mars observed by CRISM/MRO: 1. Multi-angle Approach for Retrieval of Surface Reflectance from CRISM observations* (MARS-ReCO). Journal of Geophysical Research: Planets, 118(3), pp.514-533

Chevrier, V.F. and Rivera-Valentin, E.G., (2012). *Formation of recurring slope lineae by liquid brines on present-day Mars.* Geophysical Research Letters, 39(21)

Christensen, P.R.; Engle, E.; Anwar, S.; Dickenshied, S.; Noss, D.; Gorelick, N.; Weiss-Malik, M. (2009) *JMARS – A Planetary GIS,* http://adsabs.harvard.edu/abs/2009AGUFMIN22A..06C

Ciarletti, V., Corbel, C., Plettemeier, D., Cais, P., Clifford, S.M. and Hamran, S.E., (2011). *WISDOM GPR designed for shallow and high-resolution sounding of the Martian subsurface*. Proceedings of the IEEE, 99(5), pp.824-836

Clark, R.N. and Roush, T.L. (1984). Reflectance spectroscopy: *Quantitative analysis techniques for remote sensing applications.* J. Geophys. Res., vol. 89, no. 7, pp. 6329–6340

Clark, R.N. Brown, R.H. Jaumann, R. Cruikshank, D.P. Nelson, R.M. Buratti, B.J. McCord, T.B. Lunine, J. Hoefen, T.M. Curchin, J.M. Hansen, G. Hibbitts, C. Matz, K.-D. Baines, K. Bellucci, H.G. Bibring, J.-P. Capaccione, F. Cerroni, P. Coradini, A. Formisano, V. Langevin. Y.,Matson, D.L., Mennella, V. Nicholson, P.D. Sicardy, B. Sotin, C. (2005). *Compositional mapping of Saturn's moon Phoebe with imaging spectroscopy*. Nature. 435. 66–69

Coates, A.J., Crary, F.J., Lewis, G.R., Young, D.T., Waite, J.H. and Sittler, E.C., (2007). *Discovery of heavy negative ions in Titan's ionosphere.* Geophysical Research Letters, 34(22).

Coates, A.J., Jaumann, R., Griffiths, A.D., Leff, C.E., Schmitz, N., Josset, J.L., Paar, G., Gunn, M., Hauber, E., Cousins, C.R. and Cross, R.E., (2017). *The PanCam instrument for the ExoMars rover.* Astrobiology, 17(6-7), pp.511-541

Cockell, C.S. Catling, D.C. Davis, W.L. Snook, K. Kepner, R.L. Lee, P. McKay, C.P. (2000). *The ultraviolet environment of Mars: Biological Implications past, present and future.* Icarus. 146. 343-359

Cockell, C.S., Bagshaw, E., Balme, M., Doran, P., McKay, C.P., Miljkovic, K., Pearce, D., Siegert, M.J., Tranter, M., Voytek, M. and Wadham, J., (2011). *Subglacial environments and the search for life beyond the Earth.* Antarctic Subglacial Aquatic Environments, 192, pp.129-148

Colangeli, L. Mennella, V. Baratta, G.A. Bussoletti, E. Strazzulla, G. (1992). *Raman and infrared spectra of polycyclic aromatic hydrocarbon molecules of possible astrophysical interest.* Astrophysics Journal. 396. 369–377

Couper, H. Henbest, N. (2001). *Mars: The Inside Story of the Red Planet.* Headline Book Publishing. pp. 45-47

Crovisier, J. and Bockelée-Morvan, D., (2008). *Comment on "Comparison of the composition of the Tempel 1 ejecta to the dust in Comet C/Hale–Bopp 1995 O1 and YSO HD 100546"* by CM Lisse, KE Kraemer, JA Nuth III, A. Li, D. Joswiak [2007. Icarus 187, 69–86]. Icarus, 195(2), pp.938-940

Cruikshank, D.P. Wegryn, E. Dalle Ore, CM. Brown, R.H. Bibring, J-P. Buratti, B.J. Clark, R.N. McCord, T.B. Nicholson, P.D. Pendleton, Y.J. Owen, T.C. Filacchione, G. Coradini, A. Cerroni, P. Capaccioni, F. Jaumann, R. Nelson, R.M. Baines, K.H. Sotin, C. Bellucci, G. Combes, M. Langevin, Y. Sicardy, B. Matson, D.L. Formisano, V. Drossart, P. Mennellao, V. (2008). *Hydrocarbons on Saturn's satellites Iapetus and Phoebe.* Icarus. 193. 334-343

Cruikshank, D.P., Dalle Ore, C.M., Clark, R.N. and Pendleton, Y.J., (2014). *Aromatic and aliphatic organic materials on Iapetus: Analysis of Cassini VIMS data*. Icarus, 233, pp.306-315

Dartnell, L.R. Patel, M.R. Storrie-Lombardi, M.C. Ward, J.M. Muller. J.P. (2012). Experimental determination of photostability and fluorescence-based detection of PAHs on the Martian surface. Meteorics and Planetary Science. 47. 5. pp.806-819

de Pater, I. Lissauer, J.J. (2007). *Planetary Sciences*. 2nd Edition. Cambridge University Press. pp.163-170

Derenne, S. Coelho, C. Anquetil, C. Szopa, C. Rahman, A.S. McMillan, P.F. Cora, F. Pickard, C.J. Quirico, E. Bonhomme, C. (2012). *New insights into the structure and chemistry of Titan's tholins via ^{13}C and ^{15}N solid state nuclear magnetic resonance spectroscopy.* Icarus. 221**.** 844-853

Dickson, J.L., Kerber, L.A., Fassett, C.I. and Ehlmann, B.L., (2018). A *global, blended CTX mosaic of Mars with vectorized seam mapping: a new mosaicking pipeline using principles of non-destructive image editing*. In Lunar and Planetary Science Conference (Vol. 49, pp. 1-2)

Dolezal, H., US Department of the Interior, (1976). *Dehydration of magnesium chloride*. U.S. Patent 3,962,408

Dollfus, A. and Deschamps, M., (1986). *Grain-size determination at the surface of Mars.* Icarus, 67(1), pp.37-50

Douté, S., Schmitt, B., Langevin, Y., Bibring, J.P., Altieri, F., Bellucci, G., Gondet, B. and Poulet, F., (2007). *South Pole of Mars: Nature and composition of the icy terrains from Mars Express OMEGA observations*. Planetary and Space Science, 55(1-2), pp.113-133

Draine, B.T. Li, A. (2007). *Infrared emission from the interstellar dust. IV. The silicate-graphite-PAH model in the post-Spitzer era.* The Astrophysical Journal. 657**.** 810-837

Draine, B.T. (2011). *PAHS and the Universe*. Joblin, C. Tielens, A.G.G.M. (eds). European Astronomical Society Publications Series. 46**.** 29-42

Dullemond, P. Henning, T.H. Visser, R. Geers, V.C. van Dishoeck, E.F. Pontoppidan, K.M. (2007). *Dust sedimentation in protoplanetary disks with polycyclic aromatic hydrocarbons.* Astronomy and Astrophysics. 473. 457-466

Dundas, C.M., McEwen, A.S., Chojnacki, M., Milazzo, M.P., Byrne, S., McElwaine, J.N. and Urso, A., (2017). *Granular flows at recurring slope lineae on Mars indicate a limited role for liquid water.* Nature Geoscience, 10(12), pp.903-907

Dworkin, J.P., Deamer, D.W., Sandford, S.A. and Allamandola, L.J., (2001). *Self-assembling amphiphilic molecules*: *Synthesis in simulated interstellar/precometary ices.* Proceedings of the National Academy of Sciences, 98(3), pp.815-819

Edgar, B. (2018). *Mapping the composition of RSLs in the Valles Marineris area of Mars: an assessment using CRISM imaging spectroscopy.* Planetary Science MSc thesis. UCL Dept. Physics and Astronomy.

Edgett, K.S. and Christensen, P.R., (1991). *The particle size of Martian aeolian dunes*. Journal of Geophysical Research: Planets, 96(E5), pp.22765-22776

Ehrenfreund, P. and Charnley, S.B., (2000). *Organic molecules in the interstellar medium, comets, and meteorites: a voyage from dark clouds to the early Earth*. Annual Review of Astronomy and Astrophysics, 38(1), pp.427-483

Fairén, A.G., Davila, A.F., Lim, D., Bramall, N., Bonaccorsi, R., Zavaleta, J., Uceda, E.R., Stoker, C., Wierzchos, J., Dohm, J.M. and Amils, R., (2010). *Astrobiology through the ages of Mars: the study of terrestrial analogues to understand the habitability of Mars*. Astrobiology, 10(8), pp.821-843

Fassett, C.I. Head, J.W. (2010). *Sequence and timing of conditions on early Mars.* Icarus. 211. pp.1204-1214

Finlayson-Pitts, B.J. and Pitts, J.N., (1997). *Tropospheric air pollution: ozone, airborne toxics, polycyclic aromatic hydrocarbons, and particles*. Science, 276(5315), pp.1045-1051

Flynn G. (1996). *The delivery of organic matter from asteroids and comets to the early surface of Mars*. Earth, Moon, and Planets 72. pp.469–474.

Flynn, G.J., Keller, L.P., Miller, M.A., Jacobsen, C. and Wirick, S., (1998), March. *Organic compounds associated with carbonate globules and*

rims in the ALH 84001 meteorite. In Lunar and Planetary Science Conference (Vol. 29)

Freissinet, C. Glavin, D.P Mahaffy, P. R. Miller, K. E. Eigenbrode, J. L. Summons, R. E. Brunner, A. E. Buch, A. Szopa, C. Archer Jr., P. D. Franz, H. B. Atreya, S. K. Brinckerhoff, W. B. Cabane, M. Coll, P. Conrad, P. G. Des Marais, D. J. Dworkin, J. P. Fairén, A. G. François, P. Grotzinger, J. P. Kashyap, S. ten Kate, I. L. Leshin, L. A. Malespin, C. A. Martin, M. G. Martin. Torres, F. J. McAdam, A. C. Ming, D. W. Navarro-González, R. Pavlov, A. A. Prats, B. D. Squyres, S. W. Steele, A. Stern, J. C. Sumner, D. Y. Sutter, B. Zorzano, M.-P. The MSL Science Team. (2015). *Organic molecules in the Sheepbed Mudstone, Gale Crater, Mars*. Journal of Geophysical Research: Planets. 120. 3. 495-514

Gaffey, S.J., (1986). *Spectral reflectance of carbonate minerals in the visible and near infrared (0.35-2.55 microns); calcite, aragonite, and dolomite.* American Mineralogist, 71(1-2), pp.151-162

Gibson, Jr, E.K. McKay D.S. Thomas-Keprta, K.L. Wentworth, S.J. Westall, F. Steele, A. Romanek, C.S. Bell, M.S. Toporski, J. (2001). *Life on Mars: evaluation of the evidence within Martian meteorites ALH84001, Nakhla, and Shergotty.* Precambrian Research. 106. 15-34

Greaves, J.S., Richards, A.M., Bains, W., Rimmer, P.B., Sagawa, H., Clements, D.L., Seager, S., Petkowski, J.J., Sousa-Silva, C., Ranjan, S. and Drabek-Maunder, E., (2020). *Phosphine gas in the cloud decks of Venus*. Nature Astronomy, pp.1-10

Gwinner, K.; Jaumann, R.; Hauber, E.; Hoffmann, H.; Heipke, C.; Oberst, J.; Neukum, G.; Ansan, V.; Bostelmann, J.; Dumke, A.; Elgner, S.; Erkeling, G.; Fueten, F.; Hiesinger, H.; Hoekzema, N. M.; Kersten, E.; Loizeau, D.; Matz, K.-D.; McGuire, P. C.; Mertens, V.; Michael, G.; Pasewaldt, A.; Pinet, P.; Preusker, F.; Reiss, D.; Roatsch, T.; Schmidt, R.; Scholten, F.; Spiegel, M.; Stesky, R.; Tirsch, D.; van Gasselt, S.; Walter, S.; Wahlisch, M.; Willner, K. (2016). *The High Resolution Stereo Camera (HRSC) of Mars Express and its approach to science analysis and mapping for Mars and its satellites. Planetary and Space Science*, *126*, 93–138

Gwinner, K. (2019). HRSC CoI Proceedings. (Private communication)

Harner, P.L. and Gilmore, M.S., (2015). *Visible–near infrared spectra of hydrous carbonates, with implications for the detection of carbonates in hyperspectral data of Mars*. Icarus, 250, pp.204-214

Hecht, M.H., (2002). *Metastability of liquid water on Mars*. Icarus, 156(2), pp.373-386

Hecht, M.H., Kounaves, S.P., Quinn, R.C., West, S.J., Young, S.M.M., Ming, D.W., Catling, D.C., Clark, B.C., Boynton, W.V., Hoffman, J. and DeFlores, L.P., (2009). *Detection of perchlorate and the soluble chemistry of Martian soil at the Phoenix lander site*. Science, 325(5936), pp.64-67

Herbst, E. and van Dishoek, E.F. (2009). *Complex Organic Interstellar Molecules. Annual Review of Astronomy and Astrophysics*. 47. 427-480

Herd, C.D., Borg, L.E., Jones, J.H. and Papike, J.J., (2002). *Oxygen fugacity and geochemical variations in the Martian basalts: Implications for*

Martian basalt petrogenesis and the oxidation state of the upper mantle of Mars. Geochimica et Cosmochimica Acta, 66(11), pp.2025-2036.

Herr, K.C., Forney, P.B. and Pimentel, G.C., (1972). *Mariner Mars 1969 infrared spectrometer*. Applied Optics, 11(3), pp.493-501

Ifegwu, O.C. and Anyakora, C., (2015). *Polycyclic aromatic hydrocarbons*: part I. Exposure. In Advances in Clinical Chemistry (Vol. 72, pp. 277-304). Elsevier

Jakosky, B.M. and Phillips, R.J., (2001). *Mars' volatile and climate history*. nature, 412(6843), pp.237-244

Jakosky, B.M., Lin, R.P., Grebowsky, J.M., Luhmann, J.G., Mitchell, D.F., Beutelschies, G., Priser, T., Acuna, M., Andersson, L., Baird, D. and Baker, D., (2015). *The Mars atmosphere and volatile evolution (MAVEN) mission*. Space Science Reviews, 195(1-4), pp.3-48

James, P.B. Kieffer, H.H. Paige, D.A. (1992). *The seasonal cycle of carbon dioxide on Mars.* Mars. University of Arizona Press. pp.934-968

Jaumann, R., Neukum, G., Behnke, T., Duxbury, T.C., Eichentopf, K., Flohrer, J., Gasselt, S.V., Giese, B., Gwinner, K., Hauber, E. and Hoffmann, H., (2007). *The high-resolution stereo camera (HRSC) experiment on Mars Express: Instrument aspects and experiment conduct from interplanetary cruise through the nominal mission.* Planetary and Space Science, 55(7-8), pp.928-952

Jian, J.J. and Ip, W.H., (2009). *Seasonal patterns of condensation and sublimation cycles in the cryptic and non-cryptic regions of the South Pole*. Advances in Space Research, 43(1), pp.138-142.

Joblin, C., Tielens, A.G.G.M. and Kamp, I., (2011). *Evolution of PAHs in protoplanetary disks.* European Astronomical Society Publications Series, 46, pp.271-283

Johnson, R.E. Liu, M. Kass, D.M. Yung, Y.L. (1996). *The loss of atmosphere from Mars.* Science. **274.** 1932-1933

Johnson, T.V. Lunine, J.I. (2005). *Saturn's moon Phoebe as a captured body from the outer Solar System.* Nature. 435. 69-71

Johnston, M.D., Graf, J.E., Zurek, R.W., Eisen, H.J. and Jai, B., (2005). *The Mars reconnaissance orbiter mission.* In 2005 IEEE Aerospace Conference (pp. 447-464). IEEE

Kass, D.M. and Yung, Y.L., (1995). *Loss of atmosphere from Mars due to solar wind-induced sputtering.* Science, 268(5211), pp.697-699

Keshava, N. and Mustard, J.F., (2002). *Spectral unmixing.* IEEE signal processing magazine, 19(1), pp.44-57

Klein, H.P., (1978). *The Viking biological experiments on Mars.* Icarus, 34(3), pp.666-674

Krasnopolsky, V.A., (2010*). Solar activity variations of thermospheric temperatures on Mars and a problem of CO in the lower atmosphere.* Icarus, 207(2), pp.638-647

Kreisch, C.D., O'Sullivan, J.A., Arvidson, R.E., Politte, D.V., He, L., Stein, N.T., Finkel, J., Guinness, E.A., Wolff, M.J. and Lapotre, M.G.A., (2017). *Regularization of Mars Reconnaissance Orbiter CRISM along-track oversampled hyperspectral imaging observations of Mars.* Icarus, 282, pp.136-151

Lammer, H. Selsis, F. Penz, T. Amerstorfer, U.V. Lichtenegger, H.I.M. Kolb, C. Ribas, I. (2005). *Atmospheric Evolution and the History of Water on Mars.* Water on Mars and Life. Tokano, T. (ed.). 25-43. Springer

Langevin, Y., Poulet, F., Bibring, J.P., Schmitt, B., Douté, S. and Gondet, B., (2005). Summer evolution of the north polar cap of Mars as observed by OMEGA/Mars express. Science, 307(5715), pp.1581-1584

Lauro, S.E., Soldovieri, F., Orosei, R., Cicchetti, A., Cartacci, M., Mattei, E., Cosciotti, B., Di Paolo, F., Noschese, R. and Pettinelli, E., (2019). *Liquid Water Detection under the South Polar Layered Deposits of Mars—A Probabilistic Inversion Approach.* Remote Sensing, 11(20), p.2445

Lauro, S.E., Pettinelli, E., Caprarelli, G., Guallini, L., Rossi, A.P., Mattei, E., Cosciotti, B., Cicchetti, A., Soldovieri, F., Cartacci, M. and Di Paolo, F., (2020). *Multiple subglacial water bodies below the South Pole of Mars unveiled by new MARSIS data.* Nature Astronomy, pp.1-8

Leger, A. and Puget, J., (1984*). Identification of the 'unidentified' IR emission features of interstellar dust?*. Astronomy and Astrophysics, 137, pp.L5-L8

Levy, J., (2012). *Hydrological characteristics of recurrent slope lineae on Mars: Evidence for liquid flow through regolith and comparisons with Antarctic terrestrial analogs.* Icarus, 219(1), pp.1-4

Li, A., (2009*). PAHs in comets: an overview*. In Deep Impact as a World Observatory Event: Synergies in Space, Time, and Wavelength (pp. 161-175). Springer, Berlin, Heidelberg

Lisse, C.M., Kraemer, K.E., Nuth III, J.A., Li, A. and Joswiak, D., (2007). *Comparison of the composition of the Tempel 1 ejecta to the dust in*

Comet C/Hale–Bopp 1995 O1 and YSO HD 100546. Icarus, 191(2), pp.223-240

Lopez-Puertas, M. Dinelli, B.M. Adriani. A. Funke, B. Garcia-Comas, M. Moriconi, M.L. D'Aversa, E.D. Boersma, C. Allamandola, L.J. (2013). *Large abundances of polycyclic aromatic hydrocarbons in Titan's upper atmosphere.* The Astrophysical Journal. 770**.**132. 1-8

Lovas, F.J. McMahon, R.J. Grabow, J-U. Schnell, M. Mack, J. Scot, L.T. Kuczkowski, R.L. (2005). *Interstellar Chemistry: A Strategy for detecting polycyclic aromatic hydrocarbons.* Journal of the American Chemical Society. 127**.** 12. 4245-4349

Malin, M.C. and Edgett, K.S., (2001). *Mars global surveyor Mars orbiter camera: interplanetary cruise through primary mission.* Journal of Geophysical Research: Planets, 106(E10), pp.23429-23570

Malin, M.C. Caplinger, M.A. Davis, S.D. (2001). Observational evidence for an active surface reservoir of solid carbon dioxide on Mars. Science. 294. 2146-2148

Malin, M.C., Bell, J.F., Cantor, B.A., Caplinger, M.A., Calvin, W.M., Clancy, R.T., Edgett, K.S., Edwards, L., Haberle, R.M., James, P.B. and Lee, S.W., (2007). *Context camera investigation on board the Mars Reconnaissance Orbiter.* Journal of Geophysical Research: Planets, 112(E5)

Massé, M., Beck, P., Schmitt, B., Pommerol, A., McEwen, A., Chevrier, V., Brissaud, O. and Séjourné, A., (2014). *Spectroscopy and detectability of liquid brines on Mars.* Planetary and space science, 92, pp.136-149.

McEwen, A.S., Eliason, E.M., Bergstrom, J.W., Bridges, N.T., Hansen, C.J., Delamere, W.A., Grant, J.A., Gulick, V.C., Herkenhoff, K.E., Keszthelyi, L. and Kirk, R.L., (2007). *Mars reconnaissance orbiter's high resolution imaging science experiment (HiRISE).* Journal of Geophysical Research: Planets, 112(E5)

McEwen, A.S., Ojha, L., Dundas, C.M., Mattson, S.S*., Byrne, S., Wray, J.J., Cull, S.C., Murchie, S.L., Thomas, N. and Gulick, V.C., (2011). Seasonal flows on warm Martian slopes. Science*, 333(6043), pp.740-743

McEwen, A.S., Dundas, C.M., Mattson, S.S., Toigo, A.D., Ojha, L., Wray, J.J., Chojnacki, M., Byrne, S., Murchie, S.L. and Thomas, N., (2014). *Recurring slope lineae in equatorial regions of Mars*. Nature geoscience, 7(1), pp.53-58

McEwen, A., Chojnacki, M., Dundas, C., Ojha, L., Masse, M., Schaefer, E. and Leung, C., (2015*). Recurring slope lineae on Mars: Atmospheric origin.* EPSC Abstracts, 10

McGuire, P.C., Bishop, J.L., Brown, A.J., Fraeman, A.A., Marzo, G.A., Morgan, M.F., Murchie, S.L., Mustard, J.F., Parente, M., Pelkey, S.M. and Roush, T.L., (2009). *An improvement to the volcano-scan algorithm for atmospheric correction of CRISM and OMEGA spectral data*. Planetary and Space Science, 57(7), pp.809-815

McKay, D.S., Gibson, E.K., Thomas-Keprta, K.L., Vali, H., Romanek, C.S., Clemett, S.J., Chillier, X.D., Maechling, C.R. and Zare, R.N., (1996). *Search for past life on Mars: possible relic biogenic activity in Martian meteorite ALH84001*. Science, 273(5277), pp.924-930

Melosh, H.J. and Vickery, A.M., (1989). *Impact erosion of the primordial atmosphere of Mars*. Nature, 338(6215), pp.487-489

Milkovich, S.M., Head III, J.W., Neukum, G. and HRSC Co-Investigator Team, (2008). *Stratigraphic analysis of the northern polar layered deposits of Mars: Implications for recent climate history*. Planetary and Space Science, 56(2), pp.266-288

Monnard, P.A. and Deamer, D.W., (2002). *Membrane self-assembly processes: Steps toward the first cellular life*. The Anatomical Record: An Official Publication of the American Association of Anatomists, 268(3), pp.196-207

Morgan, F. Seelos, F. Murchie, S and The *CRISM* Team. (2009). *CRISM* Data Users' Workshop CAT Tutorial (on-line). NASA/JPL/John Hopkins University. http://pds-geosciences.wustl.edu/missions/mro/*CRISM*_Workshop_090322_CAT_MFM.pdf. (Accessed 23 January 2019)

Mulas, G. Malloci, C. Joblin, C. Toublanc, D. (2005). *Estimated IR and phosphorescence emission fluxes for specific Polycyclic Aromatic Hydrocarbons in the Red Rectangle.* Astronomy and Astrophysics. 446. pp.537-549

Murchie, S. Arvidson, R. Bedini, P. Beisser, K. Bibring, J-P. Bishop, J. Boldt, J. Cavender, P. Choo, T. Clancy, R.T. Darlington, E.H. Des Marais, D. Espiritu, R. Fort, D. Green, R. Guinness, E. Hayes, J. Hash, C. Heffernan, K. Hemmler, J. Heyler, G. Humm, D. Hutcheson, J. Izenberg, N. Lee, R. Lees, J. Lohr, D. Malaret, E. Martin, T. McGovern, J.A. McGuire, P. Morris, P. Mustard, J. Pelkey, S. Rhodes,

E. Robinson, M. Roush, T. Schaefer, E. Seagrave, G. Seelos, F. Silverglate, P. Slavney, S. Smith, M. Shyong, W.J. Strohbehn, K. Taylor, H. Thompson, P. Tossman, B. Wirzburger, M. Wolff, M. (2007). *Compact Reconnaissance Imaging Spectrometer for Mars (CRISM) on Mars Reconnaissance Orbiter (MRO).* Journal of Geophysical Research. 112. E05S03, doi:10.1029/2006JE002682

NASA MRO Website: Spacecraft and instruments. (https://www.nasa.gov/mission_pages/MRO/spacecraft/sc-instru-crism.html) (Accessed 21/09/2019)

NASA/JPL. (2019). Mars Reconnaissance Orbiter: Mission Overview (on-line). NASA. http://mars.jpl.nasa.gov/mro/mission/overview/. Accessed 24 March, 2019

Navarro-González, R., Vargas, E., de La Rosa, J., Raga, A.C. and McKay, C.P., (2010). *Reanalysis of the Viking results suggests perchlorate and organics at midlatitudes on Mars*. Journal of Geophysical Research: Planets, 115(E12)

Neukum, G. and Jaumann, R., (2004), August. HRSC: *The high resolution stereo camera of Mars Express*. In Mars Express: The Scientific Payload (Vol. 1240, pp. 17-35)

Neumann, G. A., Rowlands, D. D., Lemoine, F. G., Smith, D. E., & Zuber, M. T. (2001). Crossover analysis of Mars Orbiter Laser Altimeter data. *Journal of Geophysical Research, 106*(E10), 23753–23768

Oberg, K.I. Garrod, R.T. van Dishoek, E.F. Linnartz, H. (2009). *Formation rates of complex organics in UV irradiated CH_3OH-rich ices*. Astronomy and Astrophysics. 504. 3. 891-913

Ojha, L. Willhelm, M.B. Murchie,. S.L. McEwen, S.S. Wray, J.J. Hanley, J. Masse. M. Chojnacki, M. (2015). *Spectral evidence for hydrated salts in recurring slope lineae on Mars.* Nature Geoscience. 8. 829-832

Orosei, R.O., Lauro, S.E., Pettinelli, E., Cicchetti, A., Coradini, M., Cosciotti, B., Di Paolo, F., Flamini, E., Mattei, E., Pajola, M. and Soldovieri, F., (2018). *Radar evidence of subglacial liquid water on Mars.* Science, 361(6401), pp.490-493.

Osterloo, M.M., Anderson, F.S., Hamilton, V.E. and Hynek, B.M., (2010). *Geologic context of proposed chloride‐bearing materials on Mars.* Journal of Geophysical Research: Planets, 115(E10)

Owen, T.C. Cruikshank, D.P. Dalle Ore, C.M. Geballe, T.R. Roush, T.L. de Bergh, C. Pendleton, Y.J. Khare, B.N. (2001). *Decoding the domino: The dark side of Iapetus*. Icarus 149. 160–172

Paige, D. Herkenhoff, K. Murray, B. (1990). *Mariner 9 observations of the south polar cap of Mars: Evidence for residual CO_2 frost.* Journal of Geophysical Research. 95. pp.1319-1335

Parker, D.S., Zhang, F., Kim, Y.S., Kaiser, R.I., Landera, A., Kislov, V.V., Mebel, A.M. and Tielens, A.G.G.M., (2012). *Low temperature formation of naphthalene and its role in the synthesis of PAHs (polycyclic aromatic hydrocarbons) in the interstellar medium*. Proceedings of the National Academy of Sciences, 109(1), pp.53-58

Patel, M. Zarnecki, J. Catling, D.C. (2002). *Ultraviolet radiation on the surface of Mars and the Beagle 2 UV sensor.* Planetary and Space Science 50. pp.915–927

Pelkey, S.M., Mustard, J.F., Murchie, S., Clancy, R.T., Wolff, M., Smith, M., Milliken, R., Bibring, J.P., Gendrin, A., Poulet, F. and Langevin, Y., (2007). *CRISM multispectral summary products: Parameterizing mineral diversity on Mars from reflectance.* Journal of Geophysical Research: Planets, 112(E8)

Perovich, D.K., (2006). *The interaction of ultraviolet light with Arctic sea ice during SHEBA.* Annals of glaciology, 44, pp.47-52

Philippe S. (2016*). Microphysique des processus saisonniers des glaces de Mars et Pluton : suivi par télédétection hyperspectrale et étude expérimentale.* PhD thesis, Université Grenoble Alpes, Grenoble. https://tel.archives-ouvertes.fr/tel-01560378/document]

Piqueux, S., Edwards, C.S. and Christensen, P.R., (2008). *Distribution of the ices exposed near the south pole of Mars using Thermal Emission Imaging System (THEMIS) temperature measurements*. Journal of Geophysical Research: Planets, 113(E8)

Plaxco, K.W. Gross, M. (2011). *Astrobiology: A Brief Introduction*. 2nd Edition. John Hopkins University Press. pp.19-20

Poch, O. Pommerol, A. Jost, B. Carrasco, N. Szopa, C. Thomas, N. (2016). *Sublimation of ice–tholins mixtures: A morphological and spectrophotometric study.* Icarus. 266**.** 288-305

Pommerol, A. Portyankina, G. Tomas, N. Aye, K-M. Hansen, C.J. Vincendon, M. (2011). *Evolution of the south seasonal cap during Martian Spring: Insights from the high-resolution observations by HiRISE and CRISM on Mars Reconnaissance Orbiter.* Journal of Geophysical Research. 116**.** pp.898-910

Potin, S., Brissaud, O., Beck, P., Schmitt, B., Magnard, Y., Correia, J.J., Rabou, P. and Jocou, L., (2018). *SHADOWS: a spectro-gonio radiometer for bidirectional reflectance studies of dark meteorites and terrestrial analogs: design, calibrations, and performances on challenging surfaces*. Applied optics, 57(28), pp.8279-8296

Press, F., Siever, R., Grotzinger, J. and Jordan, T.H., (2004). *Understanding earth*. Macmillan. pp. 56-61

PubChem [Internet]. Bethesda (MD): National Library of Medicine (US), National Center for Biotechnology Information; (2004) *PubChem Compound Summary for CID 24644, Magnesium chloride hexahydrate;* [cited 2020 Oct. 4]. Available from: https://pubchem.ncbi.nlm.nih.gov/compound/Magnesium-chloride-hexahydrate

Putri, A.R.D., Sidiropoulos, P. and Muller, J.P., (2019). *Anomaly detection performance comparison on anomaly-detection based change detection on Martian image pairs.* In International Archives of the Photogrammetry, Remote Sensing and Spatial Information Sciences-ISPRS Archives (Vol. 42, No. 2/W13, pp. 1437-1441). International Society of Photogrammetry and Remote Sensing (ISPRS)

Quinn R. and Zent A. (1999). *Peroxide-modified titanium dioxide: A chemical analog of putative Martian soil oxidants.* Origins of Life and Evolution of Biospheres. 29. pp.59–72

Rice, M.S., Gupta, S., Treiman, A.H., Stack, K.M., Calef, F., Edgar, L.A., Grotzinger, J., Lanza, N., Le Deit, L., Lasue, J. and Siebach, K.L., (2017). *Geologic overview of the Mars Science Laboratory rover*

mission at the Kimberley, Gale crater, Mars. Journal of Geophysical Research: Planets, 122(1), pp.2-20

Ricks, A.M., Douberly, G.E. and Duncan, M.A., (2009). *The infrared spectrum of protonated naphthalene and its relevance for the unidentified infrared bands.* The Astrophysical Journal, 702(1), p.301

Sagan, C. and Fox, P., (1975). *The canals of Mars: an assessment after Mariner 9.* Icarus, 25(4), pp.602-612

Sagan, C. Khare, B.N. (1979). *Tholins – Organic chemistry of interstellar grains and gas.* Nature. 277. (5692). 102-107

Salama, F., (2008). *PAHs in astronomy-a review.* Proceedings of the International Astronomical Union, 4(S251), pp.357-366

Samanta, S.K., Singh, O.V. and Jain, R.K., (2002). *Polycyclic aromatic hydrocarbons: environmental pollution and bioremediation.* TRENDS in Biotechnology, 20(6), pp.243-248

Schmidt, F., Andrieu, F., Costard, F., Kocifaj, M. and Meresescu, A.G., (2017). *Formation of recurring slope lineae on Mars by rarefied gas-triggered granular flows.* Nature Geoscience, 10(4), pp.270-273

Schuerger, A.C. and Clark, B.C., (2008). *Viking biology experiments: Lessons learned and the role of ecology in future Mars life-detection experiments.* In Strategies of Life Detection (pp. 233-243). Springer, Boston, MA.

Schuhmann, M., Altwegg, K., Balsiger, H., Berthelier, J.J., De Keyser, J., Fiethe, B., Fuselier, S.A., Gasc, S., Gombosi, T.I., Hänni, N. and Rubin, M., (2019). *Aliphatic and aromatic hydrocarbons in comet*

67P/Churyumov-Gerasimenko seen by ROSINA. Astronomy & Astrophysics, 630, p.A31

Seelos, K. (2017). *A Brief History of CRISM Observing Modes*. 3rd Planetary Data Workshop. http://crism.jhuapl.edu/data/CRISM_workshop_2017/Presentations/Ancillary/CRISM_Workshop2017_CRISM_obs_mode_history.pdf

Sidiropoulos, P. and Muller, J.P., (2015). *On the status of orbital high-resolution repeat imaging of Mars for the observation of dynamic surface processes*. Planetary and Space Science, 117, pp.207-222.

Sidiropoulos, P. and Muller, J.P., (2016). *Batch co-registration of Mars high-resolution images to HRSC MC11-E mosaic*. The International Archives of Photogrammetry, Remote Sensing and Spatial Information Sciences, 41, p.491

Sidiropoulos, P. and Muller, J.P., (2017). *Automatic detection of changes on Mars surface from high-resolution orbital images*. EGUGA, p.18300.

Singh, D. and Flanner, M.G., (2016). *An improved carbon dioxide snow spectral albedo model: Application to Martian conditions*. Journal of Geophysical Research: Planets, 121(10), pp.2037-2054

Sironi, L. and Draine, B.T., (2009). *Polarized infrared emission by polycyclic aromatic hydrocarbons resulting from anisotropic illumination*. The Astrophysical Journal, 698(2), p.1292

Smith, D. E., Zuber, M. T., Frey, H. V., Garvin, J. B., Head, J. W., Muhleman, D. O., Pettengill, G. H., et al. (2001). *Mars Orbiter Laser Altimeter—Experiment summary after the first year of global mapping of*

Mars. Journal of Geophysical Research, 106*(E10), 23689–23722*. https://doi.org/10.1029/2000JE001364

Squyres, S. (2005). *Roving Mars: Spirit, Opportunity and the Exploration of the Red Planet.* Hyperion Press. 54-60

Stillman, D.E., Michaels, T.I., Grimm, R.E. and Hanley, J., (2016). *Observations and modeling of northern mid-latitude recurring slope lineae (RSL) suggest recharge by a present-day Martian briny aquifer*. Icarus, 265, pp.125-138

Stillman, D.E., Michaels, T.I. and Grimm, R.E., (2017). *Characteristics of the numerous and widespread recurring slope lineae (RSL) in Valles Marineris,* Mars. Icarus, 285, pp.195-210

Stuart, B.H. (2004). *Organic Molecules. Infrared Spectroscopy: Fundamentals and Applications.* Wiley Press. pp. 46-48

Tao, Y., Muller, J.P., Sidiropoulos, P., Xiong, S.T., Putri, A.R.D., Walter, S.H.G., Veitch-Michaelis, J. and Yershov, V., (2018). *Massive stereo-based DTM production for Mars on cloud computers*. Planetary and Space Science, 154, pp.30-58

Taylor, G. J. (2009) *Mars Crust: Made of Basalt*. Planetary Science Research Discoveries. http://www.psrd.hawaii.edu/May09/Mars.Basaltic.Crust.html (Accessed 20/05/2020).

ten Kate, I.L., (2010). *Organics on Mars?.* Astrobiology, 10(6), pp.589-603.

Thomas, P.C. James, PB. Calvin, W.M. Haberle, R. Malin, M.C. (2009). *Residual south polar cap of Mars: Stratigraphy, history, and implications of recent changes.* Icarus. 203**.** pp.352-375

Thomas, P.C. Malin, M.C. James, P.B. Cantor, B.A. Williamns, R.M.E. Gierasch, P. (2005), *South polar residual cap of Mars: Features, stratigraphy, and changes.* Icarus. 174**.** pp.535-559

Titus, T.N. Kieffer, H.H. Christensen. P.R. (2003). *Exposed water ice found near the south pole of Mars.* Science. 299**.** 1048-1051

Tokunaga, A.T., Sellgren, K., Smith, R.G., Nagata, T., Sakata, A. and Nakada, Y., (1991). *High-resolution spectra of the 3.29 micron interstellar emission feature-A summary*. The Astrophysical Journal, 380, pp.452-460

Touma, J. and Wisdom, J., (1993). *The chaotic obliquity of Mars.* Science, 259(5099), pp.1294-1297

UoA (University of Arizona, HiRISE Team. (2016). Private Communication

Vago, J.L., Westall, F., Coates, A.J., Jaumann, R., Korablev, O., Ciarletti, V., Mitrofanov, I., Josset, J.L., De Sanctis, M.C., Bibring, J.P. and Rull, F., (2017). *Habitability on early Mars and the search for biosignatures with the ExoMars Rover*. Astrobiology, 17(6-7), pp.471-510

Vincent, W.F. Rae, R. Laurion, I. Howard-Willimans, C. Priscu, J.C. (1998). *Transparency of Antarctic ice-covered lakes to solar UV radiation.* Limnology and Oceanography. 43. 4. 618-624

Vita-Finzi, C. Fortes, D. (2013). *Planetary Geology: An Introduction.* 2nd edition. Dunedin Academic Press. 16-30

Viviano-Beck, C.E., Seelos, F.P., Murchie, S.L., Kahn, E.G., Seelos, K.D., Taylor, H.W., Taylor, K., Ehlmann, B.L., Wiseman, S.M., Mustard, J.F. and Morgan, M.F., (2014). *Revised CRISM spectral parameters and*

summary products based on the currently detected mineral diversity on Mars. Journal of Geophysical Research: Planets, 119(6), pp.*1403-1431*

Waite, J.H., Young, D.T., Cravens, T.E., Coates, A.J., Crary, F.J., Magee, B. and Westlake, J., (2007). *The process of tholin formation in Titan's upper atmosphere.* Science, 316(5826), pp.870-875.

Wang, A., Ling, Z., Yan, Y., McEwen, A.S., Mellon, M.T., Smith, M.D., Jolliff, B.L. and Head, J., (2019). *Subsurface Cl-bearing salts as potential contributors to recurring slope lineae (RSL) on Mars.* Icarus, 333, pp.464-480

Ward, W.R., (1973). *Large-scale variations in the obliquity of Mars.* Science, 181(4096), pp.260-262

Wilson, J.T., Eke, V.R., Massey, R.J., Elphic, R.C., Feldman, W.C., Maurice, S. and Teodoro, L.F., (2018). *Equatorial locations of water on Mars: Improved resolution maps based on Mars Odyssey Neutron Spectrometer data.* Icarus, 299, pp.148-160

Wing, M.R. Bada, J.L. (1991). *The origin of the polycyclic aromatic hydrocarbons in meteorites*. Origins of life and evolution of the biosphere. 21**.** 5. 375-383

Winter, M.E. (1999) *N-FINDR: an algorithm for fast autonomous spectral endmember determination in hyperspectral data*. Imaging Spectrometry V, Proc. SPIE 3753, pp. 266-277, 1999

Wright, I.P., Grady, M.M. and Pillinger, C.T., (1989). *Organic materials in a Martian meteorite.* Nature, 340(6230), pp.220-222

Yung, Y.L., Russell M.J., Parkinson, C.D. (2010). *The search for life on Mars*. Journal of Cosmology. 5. 1121-1130

Zhao, L., Kaiser, R.I., Lu, W., Xu, B., Ahmed, M., Morozov, A.N., Mebel, A.M., Howlader, A.H. and Wnuk, S.F., (2019). *Molecular mass growth through ring expansion in polycyclic aromatic hydrocarbons via radical–radical reactions*. Nature communications, 10(1), pp.1-7

Zolotov, M. and Shock, E., (1999). *Abiotic synthesis of polycyclic aromatic hydrocarbons on Mars*. Journal of Geophysical Research: Planets, 104(E6), pp.14033-14049

Zurek, R.W. and Smrekar, S.E., (2007). *An overview of the Mars Reconnaissance Orbiter (MRO) science mission*. Journal of Geophysical Research: Planets, 112(E5)

Appendices

Appendix A: Generalised Workflow for CRISM Data Processing and Analysis
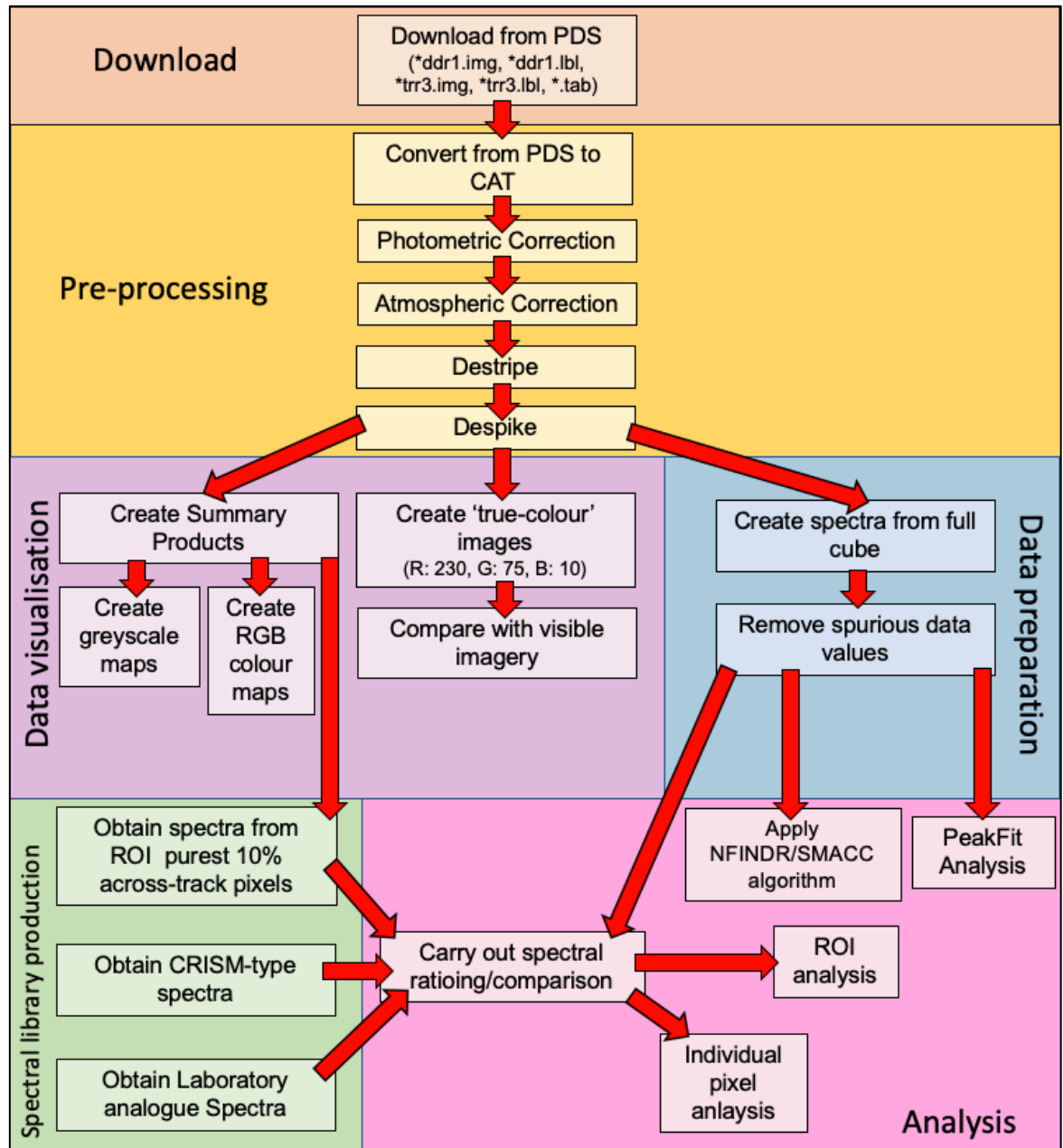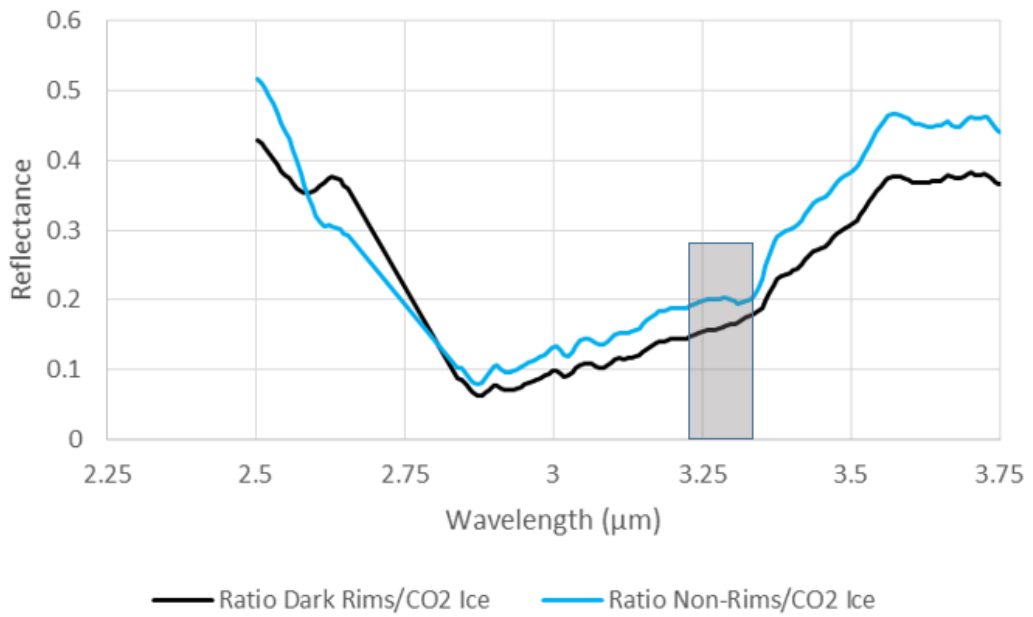
Figure 4.a Comparison of absorption feature for ROI on Phoebe (Cruikshank et al., 2008) compared with CO_2 corrected average spectra from Mars
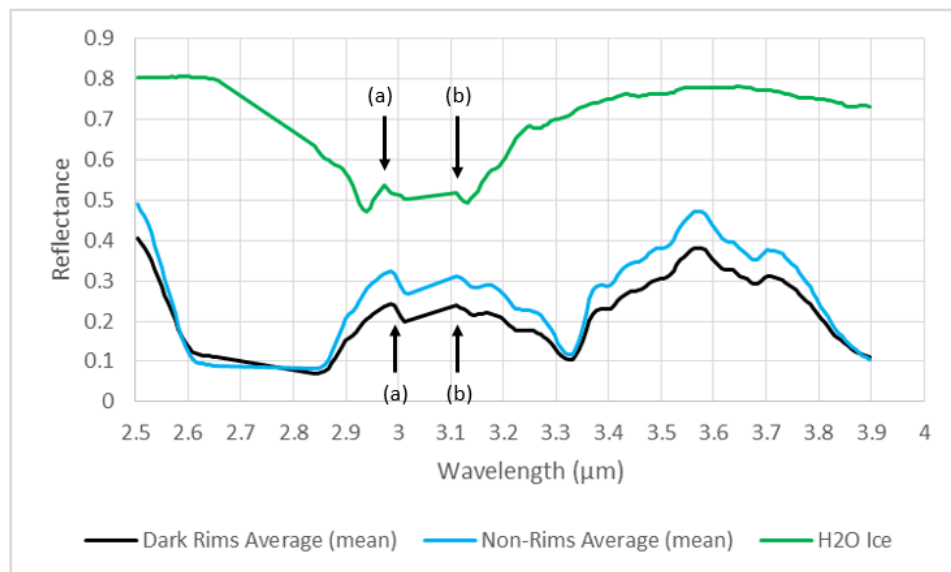
Figure 4.b: Comparison of peaks and troughs between H₂0 ice spectrum

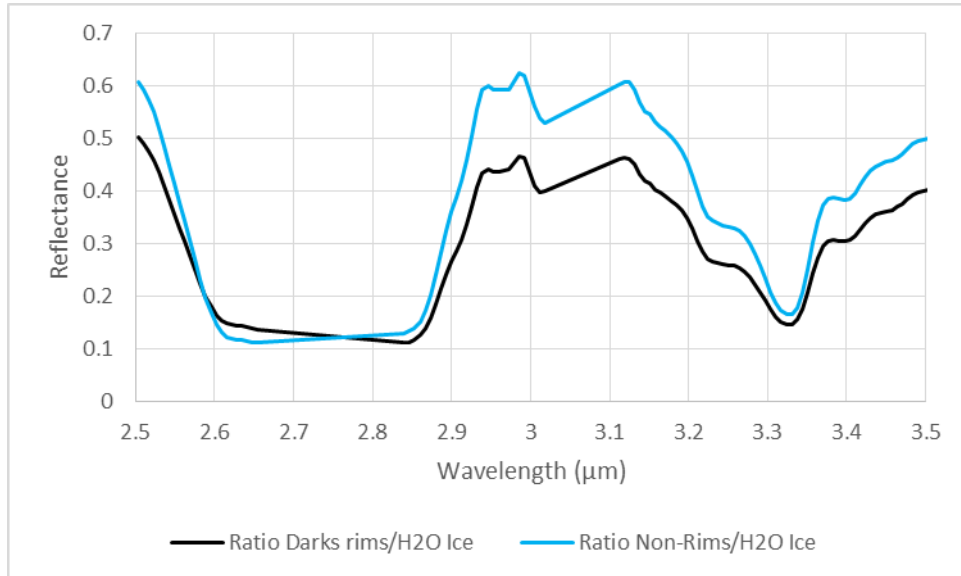*and average spectra of Dark Rims and Non-Rims*

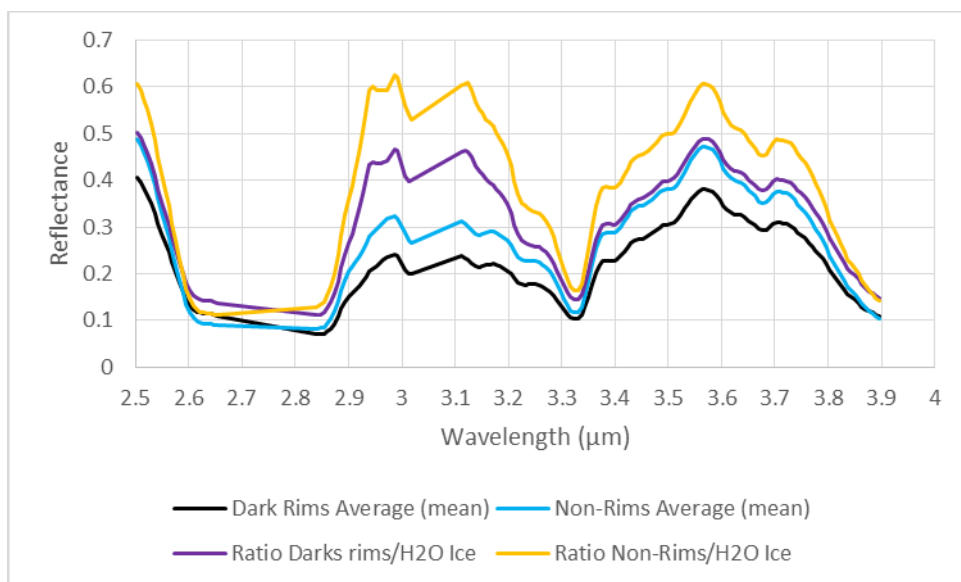*Figure 4.c: H₂O corrected mean spectra of Dark Rims and Non-Rims*

Figure 4.d: H20 corrected and non-corrected spectra of Dark Rims and Non-

Rims

Appendix C: Data from Laboratory Experiments from Chapter 5

The data from the SPRC analogue experiments from Section 5.2 can be accessed here:

https://www.sshade.eu/data/EXPERIMENT_BS_20181101_001

user login: 'ForThe.Reviewers@gmail.com'

password: 'jgr-planets'

The data from the RSL analogue experiments from Section 5.3 are yet to be uploaded into the SSHADE database as the paper is in preparation, but the raw data can be accessed here along with the SPRC data:

https://drive.google.com/drive/folders/1ksL5bRxfn4RWJIlj74-ZP_Jxo93jkwwo?usp=sharing

Appendix D: List of Publications

Journal Papers

Campbell, J.D., Sidiropoulos, P. and Muller, J.P., (2018). *A search for polycyclic aromatic hydrocarbons over the Martian South Polar Residual Cap.* Icarus, 308, pp.61-70

Campbell, J.D., Schmitt, B. Brissaud, O., and Muller, J-P., (2020). *The Detectability Limit of Organic Molecules within Mars South Polar Laboratory Analogues.* JGR Planets (under review)

Xiong, S., Tao, Y., Persaud, D.M., Campbell, J.D., Putri, A.R.D., and Muller, J-P., (2020*). Subsurface Reflectors Detected by SHARAD Reveal Stratigraphy and Buried Channels over Central Elysium Planitia*, Mars. Earth and Space Science (in press)

A paper on the RSL laboratory analogue experiments from the second part of Chapter 5 and another from the results of chapter 6 are currently in preparation.

Conference Paper Highlights

Campbell, J., Sidiropoulos, P. and Muller, J.P., (2016). *IR Spectral Mapping Of The Martian South Polar Residual Cap Using CRISM*. International Archives of the Photogrammetry, Remote Sensing and Spatial Information Sciences, 7.

Campbell, J., Sidiropoulos, P. and Muller, J.P., (2016). *The Search for Polycyclic Aromatic Hydrocarbons in the Martian South Polar Residual Cap Using CRISM Infrared Spectra*. LPI, (1903), p.2110.

Campbell, J.D., Sidiropoulos, P. and Muller, J.P., (2017). *Compositional Mapping of the Martian South Polar Residual Cap Using CRISM Infrared Spectra.* LPI, (1964), p.2684.

Campbell, J.D., Sidiropoulos, P. and Muller, J.P., (2017). *Hyperspectral characterisation of the Martian south polar residual cap using CRISM*. EPSC, pp.EPSC2017-1008.

Campbell, J., Sidiropoulos, P. and Muller, J.P., (2018*). Detection of Polycyclic Aromatic Hydrocarbons on the Martian South Polar Residual Cap.* EGU, p.1112.

Campbell, J., Schmitt, B., Brissaud, O. and Muller, J.P., (2019). *Laboratory analysis of Martian analogues for comparison with CRISM observations for detection of polycyclic aromatic hydrocarbons.* EPSC, 2019, pp.EPSC-DPS2019

Campbell, J.D., Schmitt, B., Brissaud, O. and Muller, J.P., (2020). *Hyperspectral Mapping of the Martian South Polar Residual Cap Using Laboratory Analogues and Orbital Imagery.* LPICo, 2099, p.6021.

Campbell, J.D., Schmitt, B., Brissaud, O. and Muller, J.P., (2020). *Detection of Polycyclic Aromatic Hydrocarbons in Mars Analogues.* LPI, (2326), p.1928